DISSERTATION

submitted to the
Combined Faculties for the Natural Sciences and for Mathematics
of the Ruperto-Carola University of Heidelberg, Germany
for the degree of
Doctor of Natural Sciences

Put forward by
Dipl.-Phys. Grzegorz Leszek Bauman
Born in: Lubaczów, Poland

Oral examination: 7th July 2010

Development of a non-contrast-enhanced method for spatially resolved lung ventilation and perfusion measurement using Magnetic Resonance Imaging

Referees: Prof. Dr. Lothar Rudi Schad
Prof. Dr. Wolfgang Schlegel

Development of a non-contrast-enhanced method for the spatially resolved lung ventilation and perfusion measurement using Magnetic Resonance Imaging
Assessment of the pulmonary function remains a challenge for the development of suitable MRI techniques due to the unique lung tissue structure and its short effective transverse relaxation time ($T_2^* \approx 1$ ms). In this work, a new method of non-contrast-enhanced lung ventilation and perfusion MRI is presented. A 2D bSSFP pulse sequence ($TR/TE/TA = 1.9/0.8/116$ ms, 3-7 images/s, $FA = 75°$, $ST = 10$ mm, $matrix = 128$ x 128, GRAPPA 3) was implemented on a 1.5 T MR-scanner. The method uses fast image acquisition and submillisecond echo sampling to enhance the signal intensity in the pulmonary tissue. The proposed technique does not rely on respiratory and ECG-triggering. Application of non-rigid image registration was mandatory to compensate for the breathing motion. The rapid acquisition of time-resolved MR-data allowed observing intensity changes in corresponding lung areas modulated with respiratory and cardiac frequencies. Two different spectral analysis methods, Fourier decomposition (FD) and wavelet analysis (WA) were used to produce ventilation- and perfusion-weighted images by retrieving information associated with both physiological frequencies (FD/WA-MRI). The imaging technique was used in volunteers to test the technical and medical reproducibility. For validation purposes a group of cystic fibrosis patients was examined using FD-MRI and dynamic Contrast-Enhanced MRI. A good correlation between both methods ($\rho = 0.82$, $P < 0.05$) was determined. Animal experiments were conducted for validation of FD-MRI against other imaging modalities (CT and SPECT/CT).

Entwicklung einer kontrastmittelfreien Methode zur räumlich aufgelösten Messung der Lungenventilation und -perfusion mittels Magnetresonanztomographie
Die Untersuchung der Lungenfunktion stellt auf Grund der besonderen Struktur des Lungenparenchyms und dessen kurzer, effektiver transversaler Relaxationszeit ($T_2^* \approx 1$ ms) eine Herausforderung für die Entwicklung passender MRT Verfahren dar. In dieser Arbeit wird ein neues Verfahren zur kontrastmittelfreien Ventilations- und Perfusionsmessung mittels MRT vorgestellt. Eine 2D bSSFP Pulssequenz ($TR/TE/TA = 1.9/0.8/116$ ms, 3-7 Bilder/s, $FA = 75°$, $ST = 10$ mm, $Matrix = 128$ x 128, GRAPPA 3) wurde auf einem 1.5 T MR-Tomographen implementiert. Diese Technik nutzt eine schnelle Bildaquisition und Echozeiten im Submillisekundenbereich zur Verstärkung der Signalintensität des Lungenparenchyms. Das vorgeschlagene Verfahren benötigt keine Atem- oder EKG-Triggerung. Eine nicht-rigide Bildregistrierung war notwendig für die Kompensation der Atembewegung. Die schnelle zeitaufgelöste Datenaufnahme ermöglichte die Beobachtung von Intensitätsänderungen in bestimmten Lungenbereichen, die durch Atem- und Herzfrequenz moduliert sind. Mit Hilfe zweier spektraler Analysemethoden, Fourier-Analyse (FD) und Wavelet-Analyse (WA), wurden Informationen über diese beiden physiologischen Frequenzen gewonnen, um ventilations- und perfusionsgewichtete Bilder zu erzeugen (FD/WA-MRT). Anhand einer Studie an Probanden wurde die medizinische und technische Reproduzierbarkeit der vorgestellten Bildgebungsmethode untersucht. Zur Validierung wurde eine Gruppe von Patienten mit zystischer Fibrose mittels FD-MRT und dynamischer, kontrastmittelverstärkter MRT untersucht. Hierbei konnte eine gute Korrelation ($\rho = 0.82$, $P < 0.05$) zwischen beiden Methoden nachgewiesen werden. Tierexperimente wurden durchgeführt um das FD-MRT Verfahren mit anderen Modalitäten zu vergleichen (CT und SPECT/CT).

Opracowanie bezkontrastowej metody przestrzennego pomiaru wentylacji i perfuzji płuc przy użyciu obrazowania rezonansem magnetycznym

Ocena funkcji płuc w obrazowaniu rezonansem magnetycznym (MR) jest wyzwaniem z powodu unikalnej struktury tkanki płucnej oraz krótkiego efektywnego czasu relaksacji poprzecznej ($T_2^* \approx 1$ ms). W niniejszej pracy przedstawiona została nowa metoda bezkontrastowego obrazowania wentylacji i perfuzji płuc przy użyciu MR. Sekwencja 2D bSSFP ($TR/TE/TA = 1.9/0.8/116$ ms, 3-7 obrazy/s, $FA = 75°$, $ST = 10$ mm, $macierz = 128$ x 128, GRAPPA 3) została zaimplementowana w 1.5 T tomografie MR. Metoda bazuje na szybkiej akwizycji obrazów oraz próbkowaniu echa w zakresie sub-milisekundowym, co jest konieczne do wzmocnienia intensywności sygnału z tkanki płucnej. Zaproponowana technika nie wymaga wstrzymywania oddechu ani zastosowania metody wyzwalania EKG. Niesztywna korekcja obrazów była konieczna do skompensowania ruchu płuc. Szybka czasowo-rozdzielcza akwizycja danych MR umożliwiła zaobserwowanie zmian intensywności sygnału w odpowiednich rejonach płuc, modulowanego częstością rytmów oddechowego oraz serca. Dwie różne metody analizy spektralnej, dekompozycja fourierowska (FD) oraz analiza falkowa (WA) zostały zastosowane do uzyskania informacji związanej z obiema częstościami fizjologicznymi i wygenerowania obrazów ważonych wentylacją i perfuzją (FD/WA-MR). Medyczna oraz techniczna odtwarzalność powyższych metod obrazowania została sprawdzona na grupie ochotników. Grupa pacjentów z mukowiscydozą została przebadana przy użyciu obrazowania FD-MR oraz dynamicznego kontrastowego MRI w celu walidacji metody. Analiza statystyczna potwierdziła dobrą korelację pomiędzy ($\rho = 0.82$, $P < 0.05$) dwiema metodami. Eksperymenty na zwierzętach zostały przeprowadzone w celu porównania techniki FD-MR z innymi metodami obrazowania (TK oraz SPECT/TK).

In memory of my sister Krystyna

Contents

Chapter 1

Introduction

Magnetic Resonance Imaging (MRI) has become a highly-valued diagnostic tool in the modern clinical medicine. This technique is commonly used in radiology, and allows for the spatially resolved visualization of internal body structures. Additionally, it provides a broad range of functional information. MRI is based on the scientific principles of Nuclear Magnetic Resonance (NMR). The range of clinical applications of MRI is constantly growing, and new ideas with significant potential emerge on a regular basis since its discovery [Lauterbur, 1973]. The first studies on humans were performed by Hinshaw et al. [1977] and Damadian et al. [1977]. Nowadays, MRI represents a breakthrough in medical diagnostics, treatment, and follow-up.

This modality uses the magnetic properties of hydrogen and its interaction with both a large external magnetic field and radio frequency (RF) waves to produce images of the human body. A powerful magnetic field aligns the nuclear magnetization of hydrogen nuclei. RF pulses applied perpendicular to the external magnetic field are used to disturb the alignment of the magnetization and produce a rotating magnetic field detectable as a complex signal. This signal can be manipulated by additional magnetic fields to create spatial information, and sampled by the MR-scanner. Fourier analysis and various postprocessing techniques are used to create an image from the acquired data. MRI offers better contrast quality between the different soft tissues of the body than other imaging modalities e.g. computed tomography (CT). The contrast is given by the difference in local density of the observed nucleus, by spin-spin, or spin-lattice relaxation times. A huge variety of contrasts can be produced mixing those parameters. Technical flexibility offered by MRI is reflected in a possibility of providing not only the detailed anatomical images in various contrast-weighting but also functional information of the internal organs. The functional aspect of MRI with regard to the lung is in the main focus of this work.

The lung is a highly specialized vital organ providing gas exchange by sustaining regional ventilation and perfusion. The lung parenchyma has an unique delicate structure and limited regenerative capacity. Lung diseases remain one of the main causes of morbidity and mortality worldwide. Thus, the evaluation of the pulmonary function plays a key role as an indicator of the tissue vitality and gas exchange. Early detection of regional defects of the lung function, monitoring of disease progression, as well as assessing the impact of therapeutic interventions are the most significant goals in modern pulmonary radiology.

Many different imaging techniques have been developed for the assessment of lung function. Currently, the standard approaches for lung imaging approaches comprise the following imaging modalities: nuclear scintigraphy, single-photon emission computer tomography (SPECT), position-emission tomography (PET), CT, and MRI [van Beek and Hoffman, 2008; Zhang et al., 2008]. Methods based on application of radioactive nuclides (aerosols or macroaggregates labeled with ^{99,m}Tc, ^{81,m}Kr or ^{133}Xe) such as scintigraphy and SPECT remain the gold-standard for functional lung imaging. However, the dilemma of exposure to radiation remains. Limitations of a cumulative radiation dose is particularly important in children and young adults requiring long periods of follow-up. Prolonged exposition to ionizing radiation has a strong association with the risk of developing cancer [Diederich and Lenzen, 2000]. The most significant advantages of functional MRI are the lack of harmful ionizing radiation, improved tissue contrast compared to CT, higher spatial and temporal resolution than in nuclear medicine imaging techniques. Thus, MRI offers a new insight into fast functional changes. Moreover, a deeper understanding of the human physiology appears possible.

Despite great advances in the field of proton-based MRI during the past decades, its clinical application for assessment of regional pulmonary functions is still limited. There are several technological and methodological reasons for which proton-based MRI of the lung is difficult. Lungs have a unique foam-like structure and the MR signal from the pulmonary parenchyma is hampered by low proton density. A large number of air-tissue interfaces within alveoli induce local gradients affecting magnetic field homogeneity. High susceptibility differences on intravoxel scales are responsible for phase dispersion of spins and signal loss. The sophisticated lung structure results in extremely short effective transverse relaxation time in a 1.5 T magnetic field, T_2^* of $1-2$ ms and T_2 of $30-80$ ms, influenced by a significant molecular diffusion [Hatabu et al., 1999a,b]. On the other hand, the longitudinal relaxation time T_1 of $1100-1500$ ms is relatively long [Stadler et al., 2005]. In addition, factors contributing in image artifacts comprise respiratory, cardiac motion, pulsation, and blood flow. To overcome these restrictions, very short TE gradient-echo and spin-echo imaging sequences were developed [Stock et al., 1999; Hatabu et al., 1999b; Deimling, 2000]. Application of parallel imaging techniques helps minimizing the acquisition time, which is crucial to reduce the influence of motion artifacts Blaimer et al. [2004]. A combination of minimal interecho spacing with asymmetric echo sampling and parallel MRI can remarkably increase the visibility of lung structure as well as the spatial and temporal resolution.

Dynamic Contrast-Enhanced MRI (DCE-MRI) has recently become popular to study lung perfusion. The method is based on enhancement of lung parenchyma by shortening the T_1 relaxation time using intravenously injected paramagnetic contrast agent. DCE-MRI allows for quantitative perfusion assessment [Hatabu et al., 1999c]. Three-dimensional (3D) imaging of the whole chest volume is performed during the first pass of the contrast at inspiratory breath-hold [Fink et al., 2003]. Subtraction of images before and after contrast injection creates an image representing perfused areas and major vessels.

Several studies have shown an association between the development of the nephrogenic systemic fibrosis (NSF) and the administration of gadolinium based contrast agents in patients with renal failure [Grobner, 2006]. Since there is no established curative treatment to NSF, the only option would be prevention and application of non-contrast-based imaging method. Furthermore, there

is a relevant risk of any intra-venous contrast media to develop an allergic reaction. Another disadvantage of DCE-MRI is high price of contrast agents.

Alternative techniques such as arterial spin labeling (ASL) MRI can be used to evaluate perfusion in the lung tissue [Mai and Berr, 1999]. The ASL technique uses magnetically-tagged water protons in arterial blood as a contrast bolus to measure blood delivery to the lung parenchyma. Blood in tagged by application of RF pulses to invert the magnetization. Albeit the method is noninvasive, it suffers from low temporal resolution, making it inapplicable to cover the whole volume of the lung in a reasonable time.

Visualization of regional lung ventilation can be performed using oxygen-enhanced MRI [Edelman et al., 1996]. The method relies on the paramagnetic properties of the molecular oxygen, which serves as a T_1-shortening contrast agent. This technique require complicated double measurement and suffers from low signal-to-noise ratio (SNR).

Non-proton-based lung imaging techniques employ hyperpolarized noble gases like ^{3}He or ^{129}Xe [Middleton et al., 1995; Ebert et al., 1996; Mugler et al., 1997]. Imaging is performed after inhalation of a tracer gas and allows measuring ventilated lung areas but also dynamic ventilation, apparent diffusion coefficient, or partial oxygen pressure. Clinical applications of those imaging techniques are unfortunately impeded by high cost of tracers gases, polarizers, limited availability of ^{3}He, and requirement for experienced technical staff.

The aim of this work was to develop a method of non-Contrast-Enhanced perfusion and ventilation MRI, which is not dependent on the application of intravenous contrast agents or gaseous media. It was shown that using fast acquisition with a balanced steady-state free-precession (bSSFP) sequence at a low magnetic field of 0.2 T combined with non-rigid image registration, it is possible to observe regional changes of parenchyma density and visualize local tissue alterations [Zapke et al., 2006]. An alternative method was developed at a low magnetic field of 0.35 T by the application of Fourier decomposition MRI (FD-MRI) to spectrally separate and retrieve perfusion- and ventilation-related information [Deimling et al., 2008]. The above mentioned imaging technique was implemented on a 1.5 T whole-body MR scanner using fast acquisition and submillisecond echo sampling with the bSSFP sequence to produce time-resolved two-dimensional (2D) MR data sets [Bauman et al., 2009]. Imaging scheme and parameters were optimized using proper simulations and tested experimentally. This imaging method allows covering the whole lung volume using a multi-slice acquisition in a complete acquisition time shorter than 10 minutes being applicable in a clinical routine. Postprocessing methods were extended by the use of wavelet analysis (WA) to produce perfusion- and ventilation-weighted images. The proposed imaging technique requires only minimal patient compliance and is not dependent on any triggering or gating technique.

Chapter 2

Basic principles

2.1 Nuclear Magnetic Resonance

Nuclear Magnetic Resonance (NMR) is a physical phenomenon used in Magnetic Resonance Imaging (MRI). The first successful NMR experiment was independently performed by Felix Bloch and Edward Purcell in 1946 [Bloch et al., 1946; Purcell et al., 1946]. Both physicists were awarded the Nobel price in 1952. This section briefly covers the theoretical basics of the Nuclear Magnetic Resonance. More intricate description of the NMR phenomena can be found in classic textbooks of Abragam [1961] and Slichter [1989].

2.1.1 Nuclear spin and magnetic moment

Protons and neutrons composing an atomic nucleus posses a quantum mechanical property called the spin, which is the intrinsic angular momentum. The magnitude of the spin is determined by the spin quantum number I. It is known from quantum mechanics, that the angular momentum is quantized in half-integer or integer multiples of $\hbar$ (here $\hbar = 1.055 \cdot 10^{-34}\ \frac{\mathrm{m^2kg}}{\mathrm{s}}$ is the Planck's constant). The maximum observable component of angular momentum is given by:

$$p = I\hbar \tag{2.1}$$

The nucleus can be considered to be rotating about an axis at a constant rate. All atoms with an odd number of protons or neutrons have a non-zero value of the spin. The nuclear magnetic moment $\vec{\mu}$ is collinear with the angular momentum vector and related to the spin $\vec{I}$ with the formula:

$$\vec{\mu} = \gamma\vec{p} = \gamma\hbar\vec{I} \tag{2.2}$$

where the proportionality constant γ called gyromagnetic ratio is a characteristic measure for every nuclei. The atom of hydrogen has the largest value of the gyromagnetic ratio among stable nuclei $\gamma = 2.675 \cdot 10^8 \frac{\mathrm{rad}}{\mathrm{Ts}}$. High NMR sensitivity and very large abundance of hydrogen atoms in biological tissues make it ideal for medical imaging purposes. In fact, NMR signal can be measured in all nuclei with a non-zero spin. Values of γ for other NMR sensitive isotopes are

shown in table 2.1. The gyromagnetic ratio of a nucleus can be expressed as:

$$\gamma = \frac{g_I \mu_N}{\hbar} \tag{2.3}$$

where μ_M is the nuclear magneton, and g_I - dimensionless Landé g-factor associated with certain nuclei. The magnetic moments are measured in nuclear magnetons, and can be defined as a ratio between electron charge e and proton mass m_p:

$$\mu_N = \frac{e\hbar}{2m_p} \tag{2.4}$$

Nuclear magnetic moments have a negligibly small contribution to the magnetization of materials, because the nuclear magneton is smaller than the Bohr magneton (where the proton mass is replaced by the electron mass) by the factor of $\frac{m_p}{m_e} \approx 1863$.

Table 2.1: *A list of selected NMR-active isotopes of interest in biomedical applications. Data in the table is adapted from the "Encyclopedia of Nuclear Magnetic Resonance" [Harris, 1996].*

Nucleus	Spin [$\hbar$]	Magnetic moment [μ_N]	γ [$\frac{rad}{s \cdot T}$]	Natural abundance [%]
^{1}H	1/2	2.793	$2.675 \cdot 10^8$	99.98
^{3}He	1/2	-3.685	$-2.038 \cdot 10^8$	0.00013
^{17}O	5/2	-1.893	$-0.368 \cdot 10^8$	0.037
^{19}F	1/2	2.627	$2.518 \cdot 10^8$	100
^{23}Na	3/2	2.216	$0.708 \cdot 10^8$	100
^{31}P	1/2	1.131	$1.084 \cdot 10^8$	6.88
^{41}K	3/2	0.277	$0.686 \cdot 10^8$	6.88
^{129}Xe	1/2	-1.345	$-0.744 \cdot 10^8$	26.44

An arbitrary state of a nucleus $|\Psi\rangle$ can be written in terms of a linear combination of basis states labelled by m:

$$|\Psi\rangle = \sum_m a_m |m\rangle \tag{2.5}$$

with complex amplitudes a_m. The angular momentum can be expressed as an operator $\hat{I}$, which satisfies the commutation relationships:

$$\begin{aligned} [\hat{I}_i, \hat{I}_j] &= i\epsilon_{ijk}\hbar\hat{I}_k \\ [\hat{I}^2, \hat{I}_i] &= 0 \end{aligned} \tag{2.6}$$

One can construct eigenfunctions that are common to the operators $\hat{I}^2$ and $\hat{I}_z$ for the arbitrary chosen z-axis. The eigenvalue equations for those operators are given by:

$$\begin{aligned} \hat{I}^2|I,m\rangle &= I(I+1)\hbar^2|I,m\rangle \\ \hat{I}_z|I,m\rangle &= m\hbar|I,m\rangle \end{aligned} \tag{2.7}$$

where the possible values of quantum numbers I and m are:

$$-I \leq m \leq I, \qquad I = 0, \frac{1}{2}, 1, \frac{3}{2}, \ldots \tag{2.8}$$

with the eigenvalue m increasing in units of one and called the magnetic number. In the absence of magnetic fields the $2I+1$ values of m are degenerated. However, when a magnetic field $\vec{B}$ is applied, nuclear spin may take on different orientations with respect to the z-axis, and m is no longer degenerated. This accounts for the spectral line splitting into several components, so-called the nuclear Zeeman effect.

2.1.2 The nuclear Zeeman effect

The phenomenon of the NMR results from the interaction of the magnetic moment of an atomic nucleus $\vec{\mu}$ with an external magnetic field. The dynamics of the system is described by the Schrödinger equation:

$$i\hbar\frac{\partial}{\partial t}|\Psi(t)\rangle = H|\Psi(t)\rangle \tag{2.9}$$

The total Hamiltonian $\hat{H}$ of a single spin system in a external magnetic field is given by:

$$\hat{H} = \hat{H}_0 + \hat{H}_1 \tag{2.10}$$

where H_0 is an unperturbated Hamiltonian and H_1 is a perturbation caused by the magnetic field:

$$\hat{H}_1 = -\hat{\mu}\vec{B} = -\gamma\hbar\hat{I}\vec{B} \tag{2.11}$$

In a uniform z-directed field $\vec{B} = [0, 0, B_0]$ this problem simplifies to:

$$\hat{H}_1 = -\gamma\hbar I_z\vec{B} \tag{2.12}$$

Since the quantum operators $\hat{I}$ and $\hat{H}$ have simultaneous eigenvectors one can use the eigenstates of $\hat{I}$ to calculate the eigenvalues E_m of the Schrödinger equation:

$$\hat{H}_1|I, m\rangle = E_m|I, m\rangle \tag{2.13}$$

$$E_m = -\gamma\hbar m B_0 \tag{2.14}$$

For a nucleus with a nuclear spin I, a discrete number of $2I+1$ different energy levels arise. The energy difference ΔE between two neighboring levels is given by:

$$\Delta E = E_m - E_{m-1} = \gamma\hbar B_0 = \hbar\omega_0 \tag{2.15}$$

where ω_0 is Larmor frequency describing the precession rate of the magnetic moment about the external field axis. In case of hydrogen atom with the nuclear spin of $I = \frac{1}{2}$, only two energy levels are allowed:

$$E = \begin{cases} -\hbar\omega_0/2 & \text{for } |\beta\rangle \text{ (if } \vec{\mu} \text{ is parallel to } \vec{B_0}) \\ \hbar\omega_0/2 & \text{for } |\alpha\rangle \text{ (if } \vec{\mu} \text{ is anti-parallel to } \vec{B_0}) \end{cases} \tag{2.16}$$

The lower and the upper level correspond to $m = +\frac{1}{2}$ (state $|\alpha\rangle$) and $m = -\frac{1}{2}$ (state $|\beta\rangle$), respectively. The energy gap between them is proportional to the applied magnetic field strength, at $B_0 = 1.5$ T the Larmor frequency is $\omega_0 = 2\pi \cdot 63.86$ MHz and $\Delta E = 2.6 \cdot 10^{-7}$ eV (Fig. 2.1).

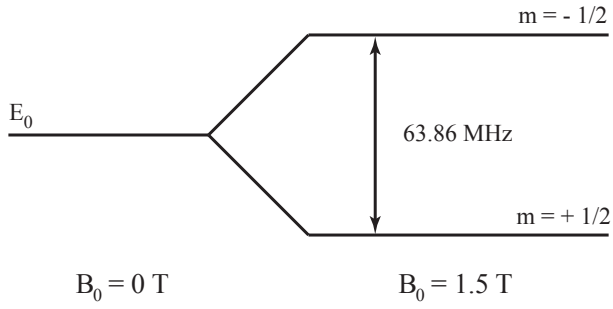

Figure 2.1: *Zeeman splitting of energy level in the hydrogen nuclei under the influence of* 1.5 T *magnetic field. A transition between energy levels, the lower corresponding to* $m = +\frac{1}{2}$ *and the upper to* $m = -\frac{1}{2}$*, can be induced by application of an external alternating magnetic field at the Larmor frequency* ω_0*.*

2.1.3 Macroscopic magnetization and nuclear polarization

A single spin system offers a straightforward model to understand the behavior of the nucleus in the presence of an external magnetic field. However, NMR measurements are made on collections of similar spins rather than on an individual spin. It is possible to define a macroscopic magnetization $\vec{M}$ as a vector sum of individual magnetic moments. This macroscopic quantity can be treated by the classical mechanics. The amplitude M_0 of the $\vec{M}$ in a macroscopic sample placed in a homogeneous static magnetic field $\vec{B}_0$ is proportional to the population difference between spin states (Fig. 2.2). In thermal equilibrium, when the temperature is high enough, and density low enough to render quantum effect negligible, the population of the $2I + 1$ spin states is described by the Boltzmann statistics:

$$p_m = \frac{1}{Z} \exp\left(-\frac{\gamma \hbar m B_0}{k_B T}\right) = \frac{1}{Z} \exp\left(-\frac{E_m}{k_B T}\right), \quad Z = \sum_{m=-I}^{I} \exp\left(-\frac{E_m}{k_B T}\right) \tag{2.17}$$

where k_B is the Boltzmann constant ($1.38 \cdot 10^{-23} \mathrm{m^2 kg/s^2 K}$), T the absolute temperature and Z the partition function.

Consider a system comprising nuclei with the spin $I = 1/2$ (e.g. ^{1}H or ^{3}He). The distribution of the spin states can be described using the density matrix $\hat{\rho}$ formalism:

$$\hat{\rho} = \langle I, m | p_m | I, m \rangle = \begin{bmatrix} p_\alpha & 0 \\ 0 & p_\beta \end{bmatrix} \tag{2.18}$$

The expectation values of the components $\hat{I}_i$ where $i = \{x, y, z\}$ can be calculated as:

$$\langle \hat{I}_i \rangle = \mathrm{Tr}[\hat{\rho} \cdot \hat{I}_i] \tag{2.19}$$

where the individual spin components are represented by Pauli matrices:

$$\hat{I}_i = \frac{\hbar}{2} \cdot \hat{\sigma}_i \tag{2.20}$$

with:

$$\hat{\sigma}_x = \begin{bmatrix} 0 & 1 \\ 1 & 0 \end{bmatrix}, \quad \hat{\sigma}_y = \begin{bmatrix} 0 & -i \\ i & 0 \end{bmatrix}, \quad \hat{\sigma}_z = \begin{bmatrix} 1 & 0 \\ 0 & -1 \end{bmatrix} \tag{2.21}$$

The expectation values are presented below:

$$\begin{aligned} \langle \hat{I}_x \rangle &= \langle \hat{I}_y \rangle = 0 \\ \langle \hat{I}_z \rangle &= \frac{\hbar}{2} \tanh\left(-\frac{\hbar\omega_0}{2k_B T}\right) \end{aligned} \tag{2.22}$$

The macroscopic magnetization $\vec{M}$ for a sample volume V containing N spins can be represented as the sum of the expectation values for the single magnetic moments $\vec{\mu}$:

$$\vec{M} = \frac{1}{V}\sum_{i=1}^{N} \langle \vec{\hat{\mu}}_i \rangle = \frac{1}{V}\sum_{i=1}^{N} \gamma \langle \vec{\hat{I}}_i \rangle \tag{2.23}$$

Since the expectation values of the transverse components $\langle \hat{I}_x \rangle, \langle \hat{I}_y \rangle$ are equal to zero, the magnetization is directed parallel to the z-axis and can be written as:

$$M_0 \equiv \langle M_z \rangle = \frac{\gamma\hbar N}{2V} \tanh\left(-\frac{\hbar\omega_0}{2k_B T}\right) \tag{2.24}$$

For $k_B T \gg \gamma\hbar B_0$ at room temperature conditions ($\sim$ 296 K) the Eq. 2.24 reduces to:

$$M_0 \approx \frac{\gamma\hbar N}{2V}\left(-\frac{\hbar\omega_0}{2k_B T}\right) = \frac{\gamma^2\hbar^2 B_0 N}{4k_B T V} \tag{2.25}$$

In our simple spin system described by the Boltzmann statistics the nuclear polarization P is defined as a ratio of the number of atoms n_α, n_β occupying two possible energy states $|\alpha\rangle, |\beta\rangle$:

$$\frac{n_\beta}{n_\alpha} = \exp\left(-\frac{\gamma\hbar B_0}{k_B T}\right), \quad P = \frac{n_\beta - n_\alpha}{n_\beta + n_\alpha} \tag{2.26}$$

which simplifies at room temperature to:

$$P_0 \approx \frac{\gamma\hbar B_0}{2k_B T} \tag{2.27}$$

According to the Eq. 2.27 at a 1.5 T magnetic field the nuclear polarization of hydrogen atoms is equal to 0.0005%. This value can be increased by application of a higher magnetic field or lowering temperature. Despite the marginal value of the nuclear polarization, the NMR signal is detectable for relative dense and rich in water samples like biological tissues. Various methods to increase the nuclear polarization have been developed over the years. One of the methods is based on optical pumping of noble gases like ^{3}He or ^{129}Xe. The optical pumping is a process in which spin alignment is generated by a transfer of the angular momentum from circularly polarized photons to the spin system. Spin-exchange optical pumping can be used to hyperpolarize both ^{3}He and ^{129}Xe, while metastability-exchange optical pumping applies only to ^{3}He. Optical pumping of noble gases allows achieving polarization up to 80%, which is 10^5 times higher than the thermal polarization. For detailed information on this topic further reading of Gentile and McKeown [1993]; Appelt et al. [1998]; Ruth et al. [1999] and Nikiel et al. [2007] is recommended.

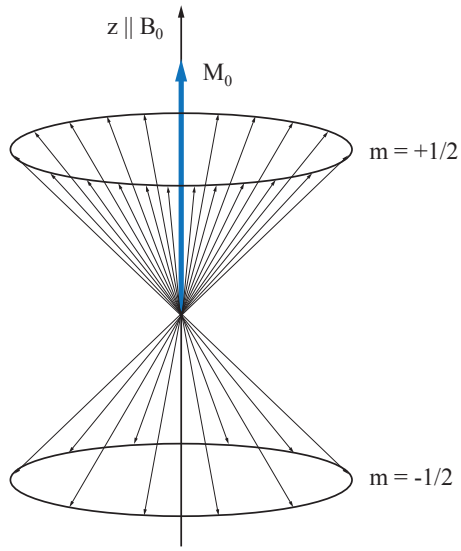

Figure 2.2: *The amplitude of the macroscopic magnetization M_0 in thermal equilibrium represented as a sum of magnetic moments of spins occupying two allowed energy states $m = -\frac{1}{2}$ and $m = +\frac{1}{2}$. The external magnetic field B_0 is parallel to the z-axis.*

2.1.4 Macroscopic magnetization in an external magnetic field

The time-dependent Schrödinger equation describes the behavior of a nuclear spin in the presence of an external magnetic field. The temporal evolution of the macroscopic magnetization vector $\vec{M}$ can be treated using simple laws of the classical mechanics. The time derivative of angular momentum of the spin system is equal to the torque ($\vec{\tau} = d\hbar\vec{I}/dt$) acting on a magnetic moment. For a magnetic moment $\vec{\mu}$ placed in an external magnetic field $\vec{B}$ the torque is defined as $\vec{\tau} = \vec{\mu}\times\vec{B}$ and the equation of precession is given by the formula:

$$\begin{aligned} \frac{d}{dt}(\hbar\vec{I}) &= \vec{\mu} \times \vec{B} \\ \frac{d}{dt}(\vec{\mu}) &= \gamma\vec{\mu} \times \vec{B} \end{aligned} \tag{2.28}$$

The macroscopic magnetization vector defined by the Eq. 2.23 satisfies a similar equation:

$$\frac{d\vec{M}(t)}{dt} = \gamma\vec{M}(t) \times \vec{B}(t) \tag{2.29}$$

In case of thermal equilibrium, in the absence of alternating magnetic fields the macroscopic magnetization vector $\vec{M}$ does not precess, and is parallel to the direction of the external static magnetic field:

$$\vec{M} = [0, 0, M_0]^T \tag{2.30}$$

2.1.5 Signal excitation by radio frequency pulses

An application of an external electromagnetic field $\vec{B}_1(t)$ alternating at the Larmor frequency $\omega_1 = \omega_0$ disturbs the equilibrium of the spin system. The circularly polarized resonant field

$\vec{B}_1(t)$ is perpendicularly oriented to the static magnetic field $\vec{B}_0 = [0, 0, B_0]^T$ and given by:

$$\vec{B}_1(t) = B_1 \cdot [\cos(\omega_1 \cdot t), \sin(\omega_1 \cdot t), 0]^T \tag{2.31}$$

Then, the Bloch equation Eq. 2.29 describes the precession of the magnetization vector about the directions of fields $\vec{B}_0$ and $\vec{B}_1$:

$$\frac{d\vec{M}(t)}{dt} = \vec{M}(t) \times (\vec{B}_0 + \vec{B}_1) = \vec{M}(t) \times \begin{bmatrix} B_1 \cos(\omega_1 \cdot t) \\ B_1 \sin(\omega_1 \cdot t) \\ B_0 \end{bmatrix} \tag{2.32}$$

An introduction of the rotating frame of reference simplifies the mathematical treatment of the motion equations, and allows eliminating the precession and time dependence of the field $\vec{B}_1$. The new coordinate system (x', y', z') rotates at the Larmor frequency ω_0 about the z-axis:

$$\begin{bmatrix} x' \\ y' \\ z' \end{bmatrix} = \begin{bmatrix} \cos(\omega_0 \cdot t) & -\sin(\omega_0 \cdot t) & 0 \\ \sin(\omega_0 \cdot t) & \cos(\omega_0 \cdot t) & 0 \\ 0 & 0 & 1 \end{bmatrix} \begin{bmatrix} x \\ y \\ z \end{bmatrix} \tag{2.33}$$

The equation 2.32 simplifies to:

$$\frac{d\vec{M}'(t)}{dt} = \vec{M}'(t) \times \gamma \begin{bmatrix} B_1 \\ 0 \\ B_0 - \frac{\omega_1}{\gamma} \end{bmatrix} = \vec{M}'(t) \times \vec{B}_{eff} \tag{2.34}$$

where the magnetization vector $\vec{M}'$ rotates about the effective magnetic field $\vec{B}_{eff}$. When the resonance condition is met $\omega_1 = \omega_0$ the difference $B_0 - \frac{\omega_1}{\gamma} = 0$, and the effective magnetic field is aligned along the x'-axis:

$$\vec{B}_{eff}^{res} = [B_1, 0, 0]^T \tag{2.35}$$

The solution of equations 2.32 and 2.34 is given by:

$$\begin{aligned} \vec{M}(t) &= M_0 \begin{bmatrix} -\sin(\omega_1 \cdot t)\sin(\omega_0 \cdot t) \\ \sin(\omega_1 \cdot t)\cos(\omega_0 \cdot t) \\ \cos(\omega_1 \cdot t) \end{bmatrix} && \text{for the laboratory coordinates} \\ \vec{M}'(t) &= M_0 \begin{bmatrix} 0 \\ \sin(\omega_1 \cdot t) \\ \cos(\omega_1 \cdot t) \end{bmatrix} && \text{for the rotating coordinates} \end{aligned} \tag{2.36}$$

The flip angle α is defined as the angle to which the net magnetization $\vec{M}$ is tipped relative to the direction of the magnetic field $\vec{B}_0$ via the application of a radio frequency (RF) excitation field $\vec{B}_1$:

$$\alpha = \gamma \int_0^T B_1(t) dt \tag{2.37}$$

Two widely utilized flip angles in NMR experiments rotate the net magnetization by 90° or 180°. The 90° pulse flips the magnetization into the xy-plane, and 180° pulse inverts the magnetization to the $-z$ direction.

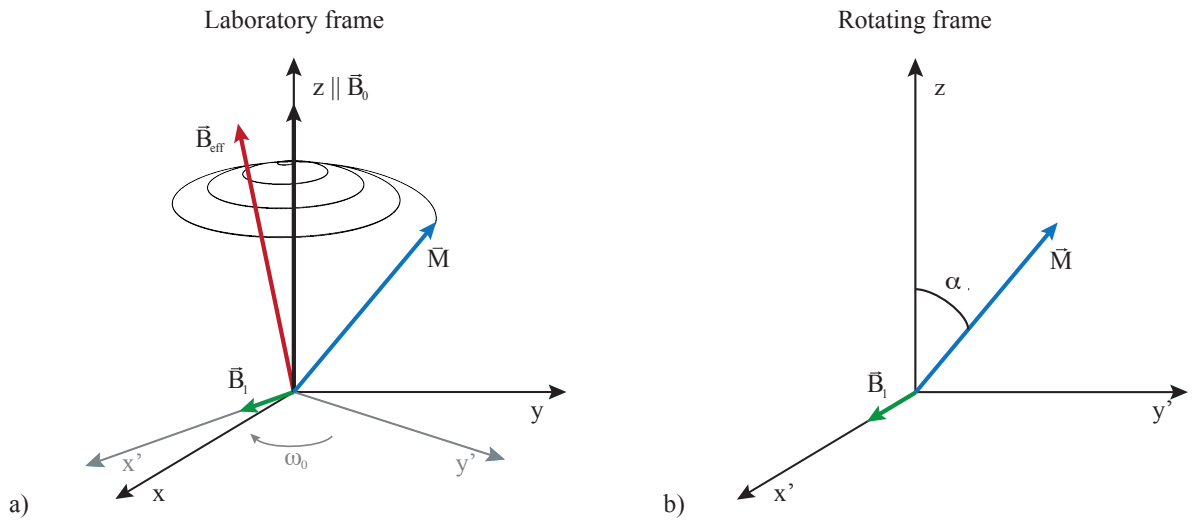

Figure 2.3: *The application of the radio frequency field $\vec{B}_1$ matching exactly the Larmor frequency of the nuclei $\omega_1 = \omega_0$ flips the net magnetization $\vec{M}$ away from the longitudinal direction z. In the laboratory frame (a) the magnetization precess about the direction of the $\vec{B}_{eff}$ vector. However, in the coordinates rotating at the Larmor frequency (b) the magnetic field $\vec{B}_1$ appears stationary, the motion can be interpreted as a precession of the magnetization $\vec{M}$ about $\vec{B}_1$.*

2.1.6 Relaxation in a magnetic field

The application of an RF pulse flips a macroscopic magnetization, and creates a transverse magnetization component M_{xy}. In the equation 2.29 it was assumed that inter-nuclear and inter-molecular forces can be neglected. Thus, the transverse magnetization component will persist indefinitely in its state. Nuclear interactions cause a loss of phase coherence among the spins, and decay of the transverse magnetization called *Free Induction Decay* (FID). The system returns to the original steady-state after a certain amount of time. This phenomenon of temporal evolution of the macroscopic magnetization was observed by Bloch et al. [1946].

Let:

$$\vec{M}(t) = [M_x(t), M_y(t), M_z(t)]^T \tag{2.38}$$

Then, the equations originally proposed by Bloch read:

$$\begin{aligned}
\frac{dM_x(t)}{dt} &= \gamma(M_y(t)B_z(t) - M_z(t)B_y(t)) - \frac{M_x(t)}{T_2} \\
\frac{dM_y(t)}{dt} &= \gamma(M_z(t)B_x(t) - M_x(t)B_z(t)) - \frac{M_y(t)}{T_2} \\
\frac{dM_z(t)}{dt} &= \gamma(M_x(t)B_y(t) - M_y(t)B_x(t)) + \frac{M_0 - M_z(t)}{T_1}
\end{aligned} \tag{2.39}$$

The above form can be further simplified assuming that:

$$M_{xy} = M_x + iM_y \quad and \quad B_{xy} = B_x + iB_y \tag{2.40}$$

which leads to the formulas:

$$\begin{aligned} \frac{dM_{xy}(t)}{dt} &= -i\gamma(M_{xy}(t)B_z(t) - M_z(t)B_{xy}(t)) - \frac{M_{xy}(t)}{T_2} \\ \frac{dM_z(t)}{dt} &= i\gamma(M_{xy}(t)\overline{B}_{xy}(t) - \overline{M}_{xy}(t)B_{xy}(t)) + \frac{M_0 - M_z(t)}{T_2} \end{aligned} \tag{2.41}$$

where:

$$\overline{M}_{xy} = M_x - iM_y \quad and \quad \overline{B}_{xy} = B_x - iB_y \tag{2.42}$$

In a homogeneous static magnetic field $\vec{B}_0 = [0, 0, B_0]^T$ solutions of the Bloch equations are given by:

$$M_{xy}(t) = M_{xy}(0)\ e^{i\omega_0 t} e^{-\frac{t}{T_2}} \tag{2.43}$$

$$M_z(t) = M_0 - (M_0 - M_z(0))\ e^{\frac{t}{T_1}} \tag{2.44}$$

The two decay constants T_1 and T_2 describe the relaxation of the macroscopic magnetization. The T_1 is called longitudinal or spin-lattice relaxation time, and the T_2 the transverse or spin-spin relaxation time. Solutions of the Bloch equations in form of a temporal evolution of the transverse and longitudinal magnetization components are depicted in figure 2.4.

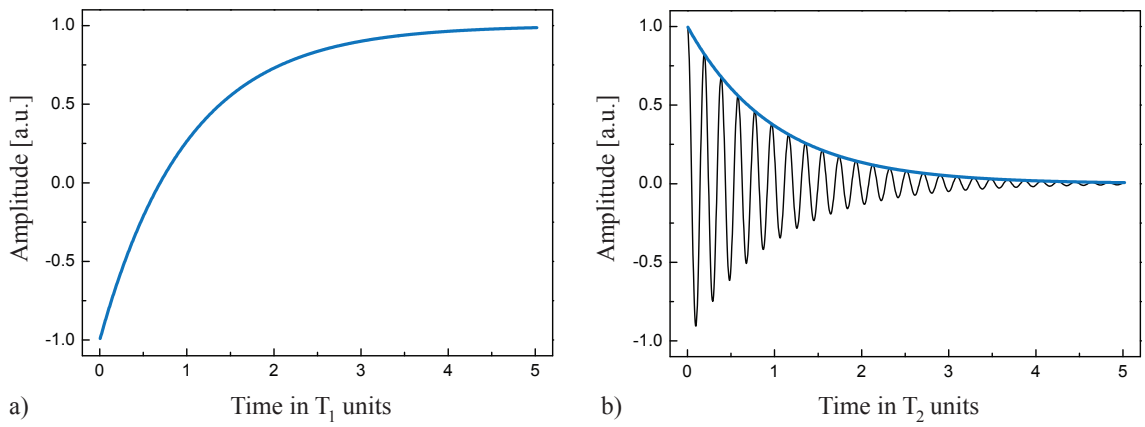

Figure 2.4: *Recovery of the longitudinal component of the magnetization with the spin-lattice relaxation time T_1 (a) after the application of a 180° excitation pulse. Temporal evolution of the real part of the measured signal (black line) and decay of the transverse magnetization component with the spin-spin relaxation time T_2 (blue line) (b).*

2.1.6.1 Spin-lattice relaxation

When a sample is placed in an external magnetic field, the net magnetization develops along the direction of $\vec{B}_0$. At thermal equilibrium in a spin system, populations of the energy levels are

given by the Boltzmann distribution (Eq. 2.26). After the longitudinal magnetization has been totally inverted $\vec{M}(0) = [0, 0, -M_0]^T$ by the application of a 180° excitation pulse, the disturbed system starts to return to the original state (Eq. 2.30). The redistribution of populations comes from an interaction of the nuclei with its surroundings (i.e. the lattice). This process is characterized by the spin-lattice relaxation rate $R_1 = 1/T_1$, and depends on the rate at which the spin system can transfer energy to its surroundings [Becker, 1999].

Let $n = n_\beta - n_\alpha$, $n_0 = n_\beta + n_\alpha$, W_+ be the probability of transition from the lower to the upper energy level and W_- probability for the downward transition. The number of upward and downward transitions are equal at equilibrium:

$$W_+ n_\beta = W_- n_\alpha \tag{2.45}$$

Combining the equations 2.26 and 2.45 yields the following:

$$\frac{W_+}{W_-} = \frac{n_\beta}{n_\alpha} = e^{\frac{\gamma\hbar B_0}{k_B T}} \tag{2.46}$$

For $k_B T \gg \gamma\hbar B_0$ and $W = (W_+ + W_-)/2$ the above formula modifies to:

$$\begin{aligned} \frac{W_+}{W} &= \frac{(n_\alpha)_{eq}}{n_0/2} = 1 - \frac{\gamma\hbar B_0}{k_B T} \\ \frac{W_-}{W} &= \frac{(n_\beta)_{eq}}{n_0/2} = 1 + \frac{\gamma\hbar B_0}{k_B T} \end{aligned} \tag{2.47}$$

The total change of n is given by:

$$\frac{dn}{dt} = \frac{dn_\beta}{dt} - \frac{dn_\alpha}{dt} = 2\frac{dn_\beta}{dt} \tag{2.48}$$

then using the probabilities W_- and W_+ yields:

$$\frac{dn_\beta}{dt} = n_\alpha W_- - n_\alpha W_+ \tag{2.49}$$

From equations 2.47 and 2.49:

$$\frac{dn}{dt} = -2W\left(n - n_0\frac{\gamma\hbar B_0}{k_B T}\right) = -\frac{1}{T_1}(n - n_{eq}) \tag{2.50}$$

where the time constant T_1 is a measure for the transition probability between the Zeeman-levels. The relaxation time T_1 is dependent on the strength of the magnetic field $\vec{B_0}$.

2.1.6.2 Spin-spin relaxation

Immediately after an excitation with a 90° pulse, all spins precess synchronously in the xy-plane. The coherent spin movement results as the transverse magnetization. Dephasing of the transverse magnetization component is characterized by the spin-spin relaxation rate $R_2 = 1/T_2$, and caused by the mutual energy exchange between the spins. The spins influence each other in a variety of processes, among other things through to the Brownian motion. Molecular movements alter the magnetic field in the vicinity of every spins. This implies that the speed of each spin's precession frequency changes, thus, the initial phase coherence will be lost. This process will be observed as an exponential decay of the transverse magnetization with the time constant T_2 (Eq. 2.43).

2.1.7 Measurement of signal in NMR

In an NMR experiment, the oscillating transverse component of the magnetization M_{xy} induces a voltage in a receiving coil (or a set of coils) positioned transversely to the main magnetic field $\vec{B}_0$. The measured signal is proportional to the transverse magnetization. The longitudinal component M_z cannot be directly measured. The induced voltage is digitized using an Analog Digital Converter, which is combined with the quadrature detection. This allows measuring the x- and y-components of the signal independently. The signal is demodulated by the multiplication with a sine and cosine function, synchronized with the Larmor frequency.

The precession frequency of the magnetization in a sample is a position-dependent variable. The local magnetization of a spin packet at position $\vec{r}$ becomes an additional phase factor:

$$\phi(\vec{r}, t) = \int_t (\omega(\vec{r}, t') - \omega_0) dt' \tag{2.51}$$

The local transverse magnetization is not detectable in an NMR experiment, but only the magnetization averaged over the whole sample volume V:

$$M_{xy}(t) = \int_V m_{xy}(\vec{r}, t)\ e^{i\phi(\vec{r},t)} d\vec{r} \tag{2.52}$$

Therefore, the detectable signal is given by:

$$S(t) \propto \int_V m_{xy}(\vec{r}, t)\ e^{i\phi(\vec{r},t)} \cdot e^{-\frac{t}{T_2}} d\vec{r} \tag{2.53}$$

An example of a measured signal envelope decaying exponentially with the T_2 time constant is shown in figure 2.4.

2.1.8 T_2^* relaxation

Dipol-dipol interactions between neighboring spins cause local variations of the magnetic field, and lead to the T_2 relaxation. The local magnetic field variations can be also present due to imperfections in the main magnetic field $\vec{B}_0$, or, as a result of magnetic inhomogeneities of the measured objects placed in a magnetic field.

The magnetization $\vec{M}$ is related to the magnetic field strength $\vec{B}_0$ by the relationship:

$$\vec{M} = \chi \vec{H} \tag{2.54}$$

where χ is the magnetic susceptibility of the material. If χ has a positive value, the material can be paramagnetic, ferromagnetic, ferrimagnetic or antiferromagnetic, and the magnetic field is strengthened by the presence of the material. For the negative values of χ the field is weakened, and the material is diamagnetic. In fact, studied objects contain materials of different properties, which leads to local variations of the magnetic susceptibility $\chi(\vec{r})$. The local magnetic field induction $\vec{B}(\vec{r})$ can be described using the (cgs) convention as:

$$\vec{B}(\vec{r}) = \vec{H} + 4\pi\vec{M}(\vec{r}) = (1 + 4\pi\chi(\vec{r}))\vec{H} \tag{2.55}$$

The form of the magnetic field distribution as a function of position $\vec{r}$ and susceptibility difference $\Delta\chi(\vec{r})$ is given by:

$$B_s(\vec{r}) = f(\vec{r}, \Delta\chi(\vec{r})) \tag{2.56}$$

An additional time-evolving phase in the local magnetization M_{xy} appears, and is described by:

$$\phi(\vec{r}, t) = \gamma B_s(\vec{r})\ t \tag{2.57}$$

Taking the above into account, the total measured signal can be expressed as:

$$S(t) \propto \int_V m_{xy}(\vec{r}, t_0)\ e^{i\gamma B_s(\vec{r})t} \cdot e^{-\frac{t}{T_2}} d\vec{r} \tag{2.58}$$

As a result, in an inhomogeneous object the overall relaxation time is shortened due to the additional spin dephasing. The equation 2.58 can be simplified to:

$$S(t) \propto M_{xy}(t_0)\ e^{-\frac{t}{T_2'}} \cdot e^{-\frac{t}{T_2}} \tag{2.59}$$

where T_2' is referred to as the reversible relaxation time. The dephasing time T_2^*, also known as the effective transverse relaxation T_2^* time can be defined as a combination of both T_2 and T_2' components:

$$\frac{1}{T_2^*} = \frac{1}{T_2} + \frac{1}{T_2'} \tag{2.60}$$

The effective transverse relaxation can be measured from the FID decay:

$$T_2^* = \frac{1}{\pi w_{\frac{1}{2}}} \tag{2.61}$$

where $w_{\frac{1}{2}}$ is the full width at half-maximum of the Lorentzian spectral line.
In general, the following always holds true: $T_2^* \leq T_2 \leq 2T_1$ [Levitt, 2008]. For a perfectly homogeneous magnetic field $T_2^* = T_2$. However, in real MRI measurements T_2^* is much shorter, this situation concerns lung parenchyma where a large number of air/soft tissue interfaces creates high local susceptibility differences. For this reason, very short acquisition times and specially adapted pulse sequences are required to obtain a sufficient signal intensity. This topic will be covered in chapter 3.

2.1.9 Spin echo

In 1950 Erwin Hahn astonished the scientific community with his discovery of the spin echoes [Hahn, 1950]. The phenomenon of spin echo occurs when an additional RF pulse is applied following a certain time delay after a first RF pulse. The generated FID signal decays quickly due to the short T_2^* relaxation time. The second RF pulse applied after a time interval $TE/2$ creates a spin echo of the original signal at a time TE. In the first spin echo experiments Hahn used the configuration of $90° - 90°$ flip angles. However, the application of $90° - 180°$ pulses creates the strongest echo. After the initial $90°$ RF pulse flips the magnetization into

the xy-plane, the individual magnetic moments immediately start to dephase. There are two fundamentally different processes contributing to the transverse magnetization dephasing, spin-spin interactions and field inhomogeneities. Hahn recognized that this loss of coherence due to the static field inhomogeneities was inherently reversible, in contrast the spin-spin interactions are random and irreversible. If a 180° pulse is applied at some point in time $TE/2$ after the first RF pulse, the fan of vectors is rotated by 180°, converting the acquired phase ϕ into a negative phase $-\phi$. Each spin will precess at the same rate as before. After an additional time, at TE each spin will have acquired the same additional phase that was acquired before the 180° pulse. This means that the spins are back in phase and create an echo. Formation of the spin echo is depicted in Fig. 2.5. The pulse sequence can be extended with the application of further 180° pulses to produce a chain of echoes with. This pulse sequence is called CPMG after its inventors Carr and Purcell [1954], Meiboom and Gill [1958], and allows acquiring the whole decay curve to determine the T_2 relaxation time. Amplitudes of echoes are modulated by the T_2 exponential decay curve (Fig. 2.6). The amplitude of n-th echo at time $t = n \cdot TE$ is $M(t) = M_0\, e^{-\frac{t}{T_2}}$.

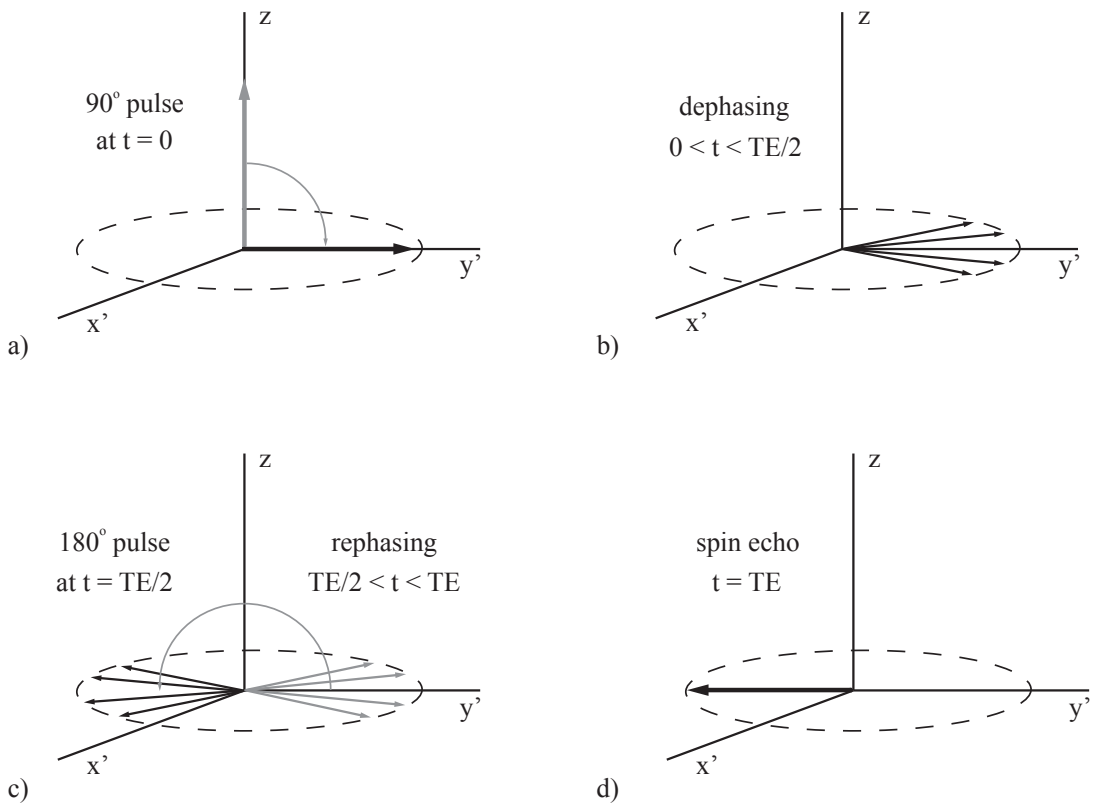

Figure 2.5: *The concept of the spin echo. The initial macroscopic magnetization is flipped into the xy-plane by the* 90° *RF excitation pulse (a). Due to the* T_2^* *effects, spins start to dephase and the measured signal decays. Some spins slow down, some speed up and start getting ahead of the others (b).* 180° *RF pulse inverts the acquired phase (c). Complete refocusing and spin echo creation occurs at* $t = TE$ *(d).*

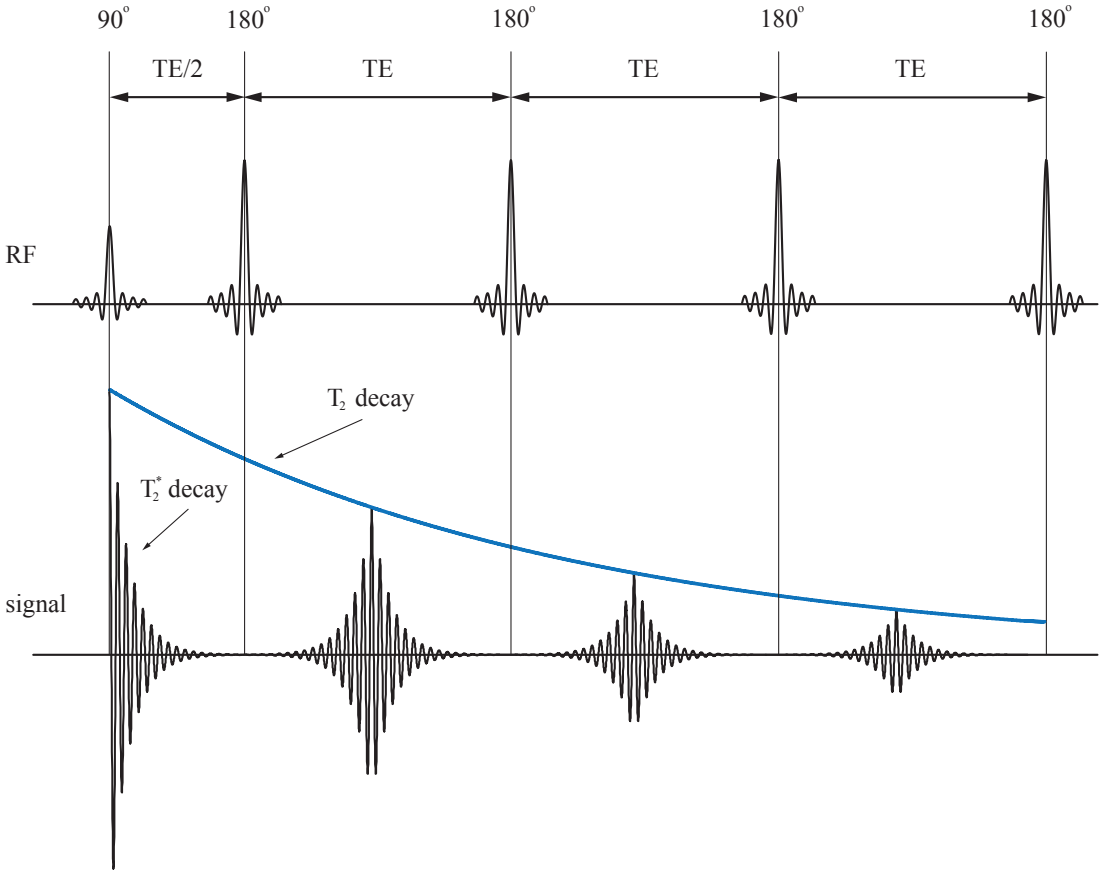

Figure 2.6: *Carr-Purcell Meiboom-Gill sequence. A train of* 180° *RF pulses following the first* 90°*pulse is used to produce a set of spin echoes. The transverse magnetization decay is characterized by the* T_2 *relaxation time and can be estimating by measuring the amplitudes of the echoes.*

2.1.10 Gradient echo

Additional to the static homogeneous $\vec{B}_0 = [0, 0, B_z]^T$ magnetic field, linear magnetic field gradients (referred to as gradient fields or gradients) can be applied to achieve a spatial variability of the B_z amplitude:

$$\vec{G}(t) = \left[\frac{\partial B_z(t)}{\partial x}, \frac{\partial B_z(t)}{\partial y}, \frac{\partial B_z(t)}{\partial z}\right]^T \tag{2.62}$$

In the next section, it will be shown that gradient fields can be used to recover the spatial information from the measured signal. The z-directed gradient field and the precession frequency associated with this field are given by the relations:

$$B_z(\vec{r}, t) = B_0 + \vec{G}(t) \cdot \vec{r} \tag{2.63}$$

$$\omega(\vec{r}, t) = \omega_0 + \gamma \vec{G}(t) \cdot \vec{r} \tag{2.64}$$

Through an addition of the gradient fields, the Bloch equations are modified to the form:

$$\begin{aligned}
\frac{dM_x(t)}{dt} &= \gamma \vec{G}(t) \cdot \vec{r}\, M_y(t) - \frac{M_x(t)}{T_2} \\
\frac{dM_y(t)}{dt} &= -\gamma \vec{G}(t) \cdot \vec{r}\, M_x(t) - \frac{M_y(t)}{T_2} \\
\frac{dM_z(t)}{dt} &= \frac{M_0 - M_z(t)}{T_1}
\end{aligned} \tag{2.65}$$

Solutions of those equations are shown below:

$$\begin{aligned}
M_{xy}(t) &= M_{xy}(t_0)\; e^{i\phi(\vec{r}(t),t)}\; e^{-\frac{t}{T_2}} \\
M_z(t) &= M_z(t_0)\; e^{-\frac{t}{T_1}} + M_0(1 - e^{-\frac{t}{T_1}})
\end{aligned} \tag{2.66}$$

The accumulated phase $\phi(\vec{r}(t), t)$ is defined by:

$$\phi(\vec{r}(t), t) = \gamma \int_0^t \vec{G}(\tau) \cdot \vec{r}(\tau) d\tau + \phi(0) \tag{2.67}$$

where $\gamma = \frac{\gamma}{2\pi}$. The measured demodulated signal is proportional to the integral over the whole sample volume:

$$S \propto \int_V m_{xy}(\vec{r}) e^{-2\pi i \phi(\vec{r}(t),t)} e^{-\frac{t}{T_2}}\; d\vec{r} \tag{2.68}$$

Presence of the gradient field after the RF excitation pulse leads to the accelerated signal dephasing. Additional phase accumulated by a spin packet is directly proportional to the time integral of the gradient. To generate a gradient echo, the signal has to be refocused. A second gradient of an equal strength and duration but opposite in polarity, brings the spins back into the focus. If the reversed gradient is maintained, the spins rephase again creating the gradient echo. For this kind of echo the local variations of the main magnetic field $\vec{B}_0$ are not compensated. The amplitude of the gradient echo is proportional to $\exp(-t/T_2^*)$, which results in a very fast dispersion of transverse magnetization and loss of signal. The signal decays fast when large differences between magnetic susceptibilities in a studied object distort the local magnetic field. The great advantage of the gradient echo sequence comparing to the spin echo sequence is no requirement for 180° RF pulses. As a consequence, the echo can be created more rapidly shortening the acquisition time.

2.2 Magnetic Resonance Imaging

THIS SECTION COVERS basics of the Magnetic Resonance Imaging (MRI), a technique providing noninvasive tools to investigate the internal anatomy, and physiology of a living subject. During the last decades MRI has become one of the most powerful imaging modalities. For its discovery Paul Lauterbur and Peter Mansfield were awarded the Nobel Prize in Physiology or Medicine in 2003. Readers wishing to study this technique in more detail are advised to read the textbooks of Haacke et al. [1999], Vlaardingerbroek and den Boer [2003], or Bernstein et al. [2004].

2.2.1 Spatial encoding and k-space formalism

The encoding of the spatial information required to reconstruct an image is achieved by the application of linear magnetic field gradients perpendicular to the main magnetic field $\vec{B}_0(t)$ (Eq. 2.62). By neglecting the relaxation effects, the time-domain signal created by the transverse magnetization is expressed by the modified Eq. 2.68 as:

$$S \propto \int_V m_{xy}(\vec{r}, t_0) e^{-2\pi i \gamma \int_0^t \vec{G}(\tau)\vec{r}(\tau)d\tau} \, d\vec{r} \tag{2.69}$$

Assuming that position $\vec{r}$ of the spin packets is time-independent:

$$\gamma \int_0^t \vec{G}(\tau)\vec{r}(\tau)d\tau = \gamma \vec{r} \int_0^t \vec{G}(\tau)d\tau = 2\pi \vec{k} \cdot \vec{r} \tag{2.70}$$

where $\vec{k}$ is defined as a gradient integral:

$$\vec{k}(t) \equiv \gamma \int_0^t \vec{G}(\tau)d\tau \tag{2.71}$$

the measured MR signal is given by:

$$S\left(\vec{k}(t)\right) \propto \int_V m_{xy}(\vec{r}) \; e^{-2\pi i \vec{k}(t) \cdot \vec{r}} \, d\vec{r} \tag{2.72}$$

The signal $S(\vec{k}(t))$ is proportional to the Fourier transform of the spatially distributed transverse magnetization. The space that $\vec{k}(t)$ resides in is called k-space and has units of inverse distance. The k-space formalism was introduced in 1983 by Ljunggren [1983] and Twieg [1983] independently, and proved to be an invaluable tool in unifying different MRI techniques. Equations 2.71 and 2.72 show that the signal traces a path $\vec{k}(t)$. A distance covered in the k-space for any time interval is determined by the duration and amplitude of the applied gradient. The inverse Fourier transform can be used to restore the spatial distribution of the transverse magnetization:

$$m_{xy}(\vec{r}) \propto \int S(\vec{k}(t)) \; e^{2\pi i \vec{k}(t) \cdot \vec{r}} \, d\vec{k} \tag{2.73}$$

The goal of the data acquisition is to manipulate gradient waveforms in such a way that the k-space is sampled sufficiently to satisfy the Nyquist criterion, which is necessary for correct image reconstruction. An activation of appropriate gradient configurations allows for sampling

any points in the k-space. Low amplitude or short duration of the gradient event encodes low frequency information, and, alternatively, high amplitude or long duration of a gradient event allows for retrieving high frequency information. Since the Fourier conjugate of $\vec{k}$ is the spatial vector $\vec{r}$, the Fourier transform of the k-space produces a spatially resolved image. The signal in the k-space center $S(\vec{k} = 0)$ corresponds to the mean intensity (baseline) in the whole image. The low frequencies around the k-space center have the highest amplitude, and contain information about the general shape and the contrast of the image. Peripheries of the k-space with high frequency components have lower amplitudes. They encode rapid changes of image signal as a function of position, and contain detailed image information (sharpness and edges). The contribution of the low and high spatial frequencies on the image appearance is shown in figure 2.7.

In theory, any trajectory to cover the k-space is possible to obtain through the temporal modulation of the gradient fields. However, the simplest and the most common method to fill the k-space is sampling on a Cartesian grid in an equidistant manner.

2.2.2 Gradient moments

Moving spins experience difference phase evolution than the stationary spins under the influence of a gradient field. The position vector $\vec{r}(t)$ of a spin packet can be expanded using the Taylor series:

$$\vec{r}(t) = \sum_{n=0}^{\infty} \frac{1}{N!} \frac{d^n \vec{r}}{dt^n} \cdot t^n = \vec{r}_0 + \vec{v}_0 \cdot t + \vec{a}_0 \cdot t^2 + \dots \tag{2.74}$$

where $\vec{r}_0$ is the initial position, $\vec{v}_0$ velocity and $\vec{a}_0$ acceleration at time $t = 0$. Substituting the expanded location vector 2.74 into the equation 2.70 yields:

$$\begin{aligned} \gamma \int_0^t \vec{G}(\tau)\vec{r}(\tau)d\tau = \gamma \vec{r}_0 \int_0^t \vec{G}(\tau)d\tau + \gamma \vec{v}_0 \int_0^t \vec{G}(\tau)\tau d\tau + \gamma \vec{a}_0 \int_0^t \vec{G}(\tau)\tau^2 d\tau + \dots = \\ = \gamma \vec{r}_0 m_0(t) + \gamma \vec{v}_0 m_1(t) + \gamma \vec{a}_0 m_2(t) + \dots \end{aligned} \tag{2.75}$$

where $m_0(t)$, $m_1(t)$ and $m_2(t)$ are the zeroth, first, and second gradient moments. The nth gradient moment is given by:

$$m_n(t) = \int_0^t G(\tau)\tau^n d\tau \tag{2.76}$$

The zeroth gradient moment is equivalent to the definition of $\vec{k}(t)$ (Eq. 2.71). Non-zero values of higher moments generated by the moving spin packets can produce image flow artifacts.

2.2.3 Field of view

Two important image parameters, namely, resolution and field of view (FOV) depend on the size of the covered k-space and on the sampling interval. The field of view defines the size of the

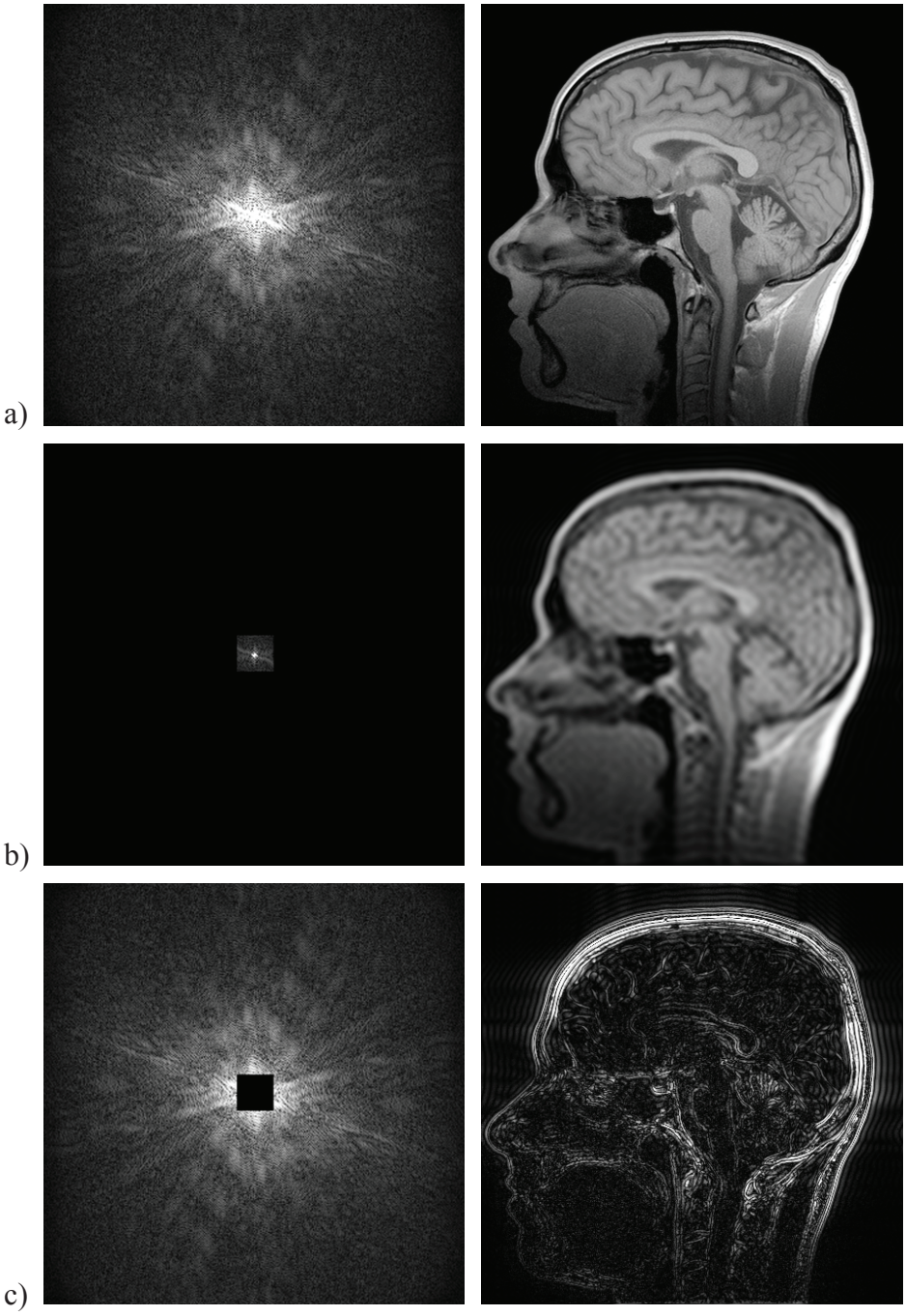

Figure 2.7: *Sagittal T_1-weighted image of a volunteer's head. The left column shows the data acquired in the k-space (the square root scaled look-up table), and the right column a corresponding image in the spatial domain. In the first row fully sampled k-space and the reconstructed image are shown (a). The second row shows the image reconstructed using only the low frequency components of the k-space (b). In the third row the image created from the high frequency components are shown (c).*

two or three dimensional spatial encoding area of the image. As mentioned before, the discrete number of k-space points has to be sampled in order to create an image. The discretization of

the continuous image $S(\vec{k})$ can be performed with the help of the Shah function $^3\text{Ш}$ [Bracewell, 1999]. The 1D and 3D Shah functions can be defined as:

$$\begin{aligned} {}^1\text{Ш}\left(\frac{k_i}{\Delta k_i}\right) &= \Delta k_i \sum_{n=-\infty}^{\infty} \delta(k_i - n\Delta k_i) \\ {}^3\text{Ш}(k_x, k_y, k_z) &= {}^1\text{Ш}(k_x){}^1\text{Ш}(k_y){}^1\text{Ш}(k_z). \end{aligned} \tag{2.77}$$

where $i \in \{x, y, z\}$. The function has two important properties:

$$\begin{aligned} {}^1\text{Ш}(k_i)\ S(k_i) &= \sum_{n=-\infty}^{\infty} S(n)\delta(k_i - n) \quad \text{(sampling property)} \\ {}^1\text{Ш}(k_i) * S(k_i) &= \sum_{n=-\infty}^{\infty} S(k_i - n) \quad \text{(replicating property)} \end{aligned} \tag{2.78}$$

A discrete image is obtained using the sampling property of the Shah function:

$$S_d(k_x, k_y, k_z) = S(k_x, k_y, k_z) \cdot {}^3\text{Ш}\left(\frac{k_x}{\Delta k_x}, \frac{k_y}{\Delta k_y}, \frac{k_z}{\Delta k_z}\right) \frac{1}{\Delta k_x \Delta k_y \Delta k_z} \tag{2.79}$$

Using the convolution theorem, the Fourier transform of the above equation can be written as:

$${}^3\mathcal{F}[S_D(k_x, k_y, k_z)] = {}^3\mathcal{F}[S(k_x, k_y, k_z)] * {}^3\mathcal{F}\left[{}^3\text{Ш}\left(\frac{k_x}{\Delta k_x}, \frac{k_y}{\Delta k_y}, \frac{k_z}{\Delta k_z}\right)\right] \frac{1}{\Delta k_x \Delta k_y \Delta k_z} \tag{2.80}$$

The Fourier transform of the Shah function is also the Shah function (Fig. 2.8):

$$\mathcal{F}\left[\text{Ш}\left(\frac{k_i}{\Delta k_i}\right)\right] = \Delta k_i \text{Ш}(\Delta k_i n) \tag{2.81}$$

Thus, the discrete image in the spatial domain is given by:

$$\tilde{S}_d(x, y, z) = \tilde{S}(x, y, z) * {}^3\text{Ш}(\Delta k_x x, \Delta k_y y, \Delta k_z z) \tag{2.82}$$

The convolution of the continuous image $\tilde{S}$ with the Shah function replicates the discrete image $\tilde{S}_d$ periodically according to the Eq. 2.78. The period of the replication in each direction is equal to $\frac{1}{\Delta k_i}$. The maximal dimensions of the studied object are restricted by the field of view (FOV), and defined as:

$$FOV_x = \frac{1}{\Delta k_x}, \quad FOV_y = \frac{1}{\Delta k_y}, \quad FOV_z = \frac{1}{\Delta k_z} \tag{2.83}$$

The larger the FOV, the smaller is the sampling interval $\frac{1}{\Delta k_i}$. Due to the periodicity of the Fourier transformation, it is important to choose FOV larger than the object to avoid image overlapping (aliasing artifact). Therefore, the following condition should be satisfied:

$$x_{min} = -\frac{1}{\Delta k_x} \leq x \leq +\frac{1}{\Delta k_x} = x_{max} \tag{2.84}$$

and analogically for the y and z coordinates. This condition is known as the Nyquist-Shannon sampling criterion.

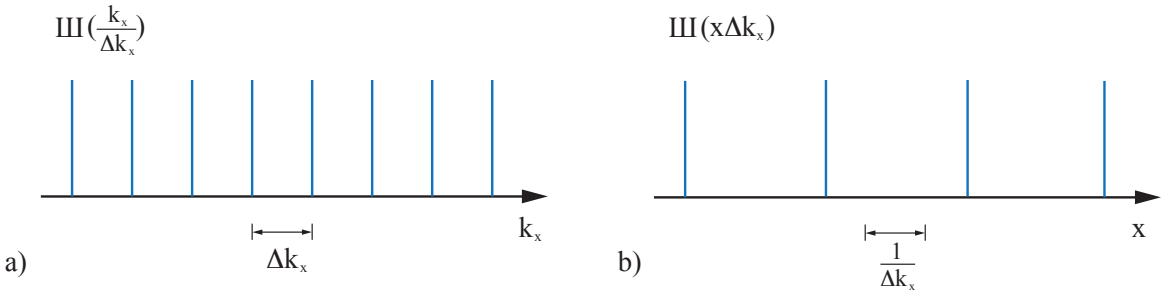

Figure 2.8: *One dimensional Shah function in the k-space (a). The Fourier transform of the Shah function in the spatial domain (b).*

2.2.4 Resolution

In the last paragraph, it was assumed that the sampling function Ш has no boundaries and covers the whole k-space. However, in practice only a finite volume of the k-space can be sampled. Spatial constraints can be defined by multiplying the discrete image sampled by the rectangular functions along each direction. The rectangular window and its Fourier transform are given by:

$$\Pi\left(\frac{k_x+\Delta k_x/2}{2k_x^{max}}\right) = \begin{cases} 0 & \text{if } |\frac{k_x+\Delta k_x/2}{2k_x^{max}}| > \frac{1}{2} \\ \frac{1}{2} & \text{if } |\frac{k_x+\Delta_x/2}{2k_x^{max}}| = \frac{1}{2} \\ 1 & \text{if } |\frac{k_x+\Delta k_x/2}{2k_x^{max}}| < \frac{1}{2} \end{cases} \tag{2.85}$$
$$\mathcal{F}\left[\Pi\left(\frac{k_x+\Delta k_x/2}{2k_x^{max}}\right)\right] = 2k_x^{max}\text{sinc}(k_x^{max}x)$$

where the maximal value acquired in the k-space along the k_x direction is:

$$k_x^{max} = \frac{N\Delta k}{2} \tag{2.86}$$

Then, the discrete sampled image $S_{d,c}$ constrained in all spatial directions is defined as:

$$\begin{aligned} S_{d,c}(k_x,k_y,k_z) = S(k_x,k_y,k_z)\cdot {}^3\text{Ш}\left(\frac{k_x}{\Delta k_x},\frac{k_y}{\Delta k_y},\frac{k_z}{\Delta k_z}\right)\frac{1}{\Delta k_x\Delta k_y\Delta k_z} \\ \cdot\Pi\left(\frac{k_x+\Delta k_x/2}{2k_x^{max}}\right)\cdot\Pi\left(\frac{k_y+\Delta k_y/2}{2k_y^{max}}\right)\cdot\Pi\left(\frac{k_z+\Delta k_z/2}{2k_z^{max}}\right) \end{aligned} \tag{2.87}$$

The Fourier transform of the equation 2.87 introduces a convolution of a periodically replicated discrete image with the *point spread function* (PSF):

$$\begin{aligned} {}^3\mathcal{F}[S_{d,c}(k_x,k_y,k_z)] \equiv \tilde{S}_{d,c}(x,y,z) = 8\ k_x^{max}k_y^{max}k_z^{max}\left\{\tilde{S}(x,y,z) * {}^3\text{Ш}(\Delta k_x x,\Delta k_y y,\Delta k_z z)\right\} \\ * \text{sinc}(k_x^{max}x) * \text{sinc}(k_y^{max}y) * \text{sinc}(k_z^{max}z) \end{aligned} \tag{2.88}$$

In this example, when the sampled k-space data has a form of a cuboid the PSF is represented by the three dimensional sinc function.

The spatial resolution is a smallest distance between two objects, at which they can be independently recognized from each other. Any point in the spatial domain will be widened by the PSF function. Thus, the useful measure of the resolution is a full width of the PSF at half its maximum (FWHM), which for the sinc function is equal to $1/2k_i^{max} = FOV_i/N_i$. This value corresponds directly to the distance between two voxels in the spatial domain and can be expressed as:

$$\Delta x = \frac{\mathrm{FOV}_x}{N_x} = \frac{1}{N\Delta k_x} = \frac{1}{|2k_x^{max}|} \tag{2.89}$$

analogically for the y and z dimensions. A sharp cut-off in the k-space for small acquisition matrices, i.e. convolution with the sinc function in the spatial domain may appear as a truncation artifact (Gibbs ringing) in a reconstructed image. The artifact is particularly visible on sharp edges. The raw data can be additionally filtered to suppress the ringing artifact e.g. using a Hamming window.

For the discrete sampled k-space data the three-dimensional *Discrete Fourier Transform* (DFT) is given by:

$$\tilde{S}_{d,c}(x,y,z) = \sum_{x=-\frac{N_x}{2}}^{\frac{N_x}{2}-1} \sum_{y=-\frac{N_y}{2}}^{\frac{N_y}{2}-1} \sum_{z=-\frac{N_z}{2}}^{\frac{N_z}{2}-1} S_{d,c}(k_x,k_y,k_z) e^{-2\pi i\left(\frac{xk_x}{N_x}+\frac{yk_y}{N_y}+\frac{zk_z}{N_z}\right)} \tag{2.90}$$

In practice, however, for the calculation of the DFT from a uniform sampled data the algorithm of *Fast Fourier Transform* (FFT) [Cooley and Tukey, 1965] is commonly used. The FFT allows for a rapid computation of the sampled data in $\mathcal{O}(Nlog(N))$ operations compared to the direct calculation from the definition (Eq. 2.90) where $\mathcal{O}(N^2)$ steps are required. The well-known radix-2 Cooley-Tukey FFT algorithm can compute the same result even faster, when the number of samples N is restricted to be a power of 2.

2.2.5 Two- and three-dimensional sequences

The k-space acquisition methods can be divided into two different groups: 2D and 3D sampling techniques. The 2D acquisition techniques use a selective RF pulse to excite a slice with a given thickness at any arbitrary spatial orientation. In this case, only the spins contained in the selected slice contribute to the MR signal. In 3D imaging techniques a whole object volume is excited using a non-selective RF pulse. Thus, all the spins in the excited volume contribute to the measurement signal.

2.2.5.1 Two dimensional sequences and the slice selection

The 2D imaging techniques use simultaneous RF pulse excitation and a magnetic field gradient to select a chosen slice from an imaged object volume (Fig. 2.9b). It can be assumed without

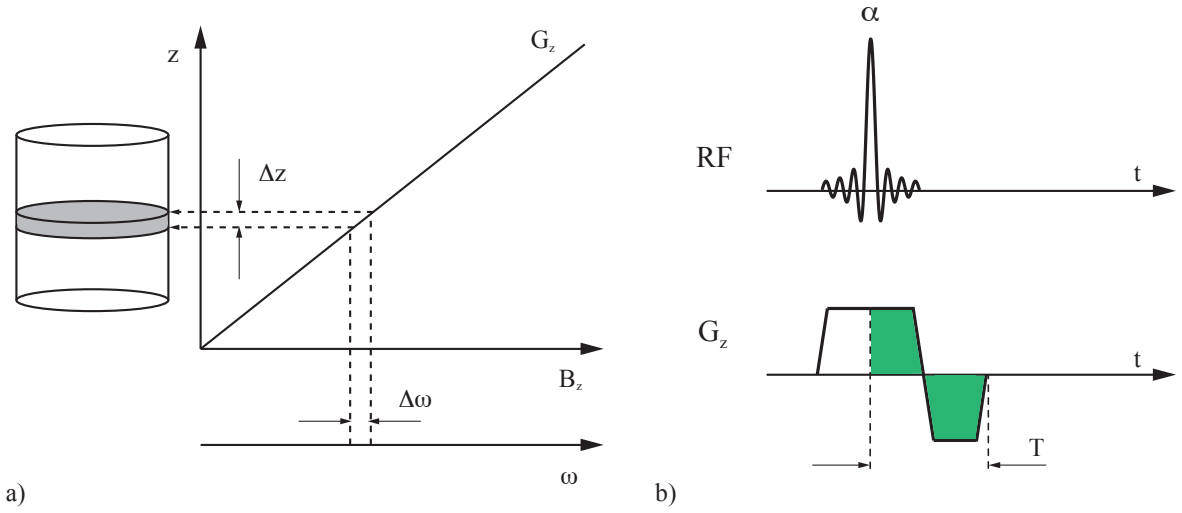

Figure 2.9: *The illustration (a) depicts the principle of the slice selective excitation. The frequency bandwidth $\Delta\omega$ of the RF pulse together with the slice selection gradient G_z defines the slice thickness Δz. In the diagram (b) RF pulse excitation and the slice selection gradient has been shown. In order to compensate for the spin dephasing during the RF pulse application, an additional gradient of inverted polarity is switched on immediately afterwards. The area of the dephasing gradient is equal to the half of the slice selection gradient area.*

loss of generality, that the excited slice lies in the xy-plane. Then, the slice-selective magnetic field gradient G_z is applied in the z-direction. Since the spin packets are located in the position dependent magnetic field $B_z(z)$, they also posses a position dependent precession frequency:

$$\omega(z) = \gamma B_z(z) = \gamma(B_0 + G_z) = \omega_0 + \gamma G_z z \tag{2.91}$$

An RF pulse contains frequency components in an interval $[\omega - \frac{\Delta\omega}{2}, \omega + \frac{\Delta\omega}{2}]$, for this reason only the spin packets for which the resonant frequency configured by gradient field G_z lies in the bandwidth $\Delta\omega$ will be excited (Fig. 2.9a). The profile and thickness of the selected slice are given by the frequency spectrum of the RF excitation pulse. It can be derived from the Bloch equations, that for the small flip angles the slice profile corresponds to the Fourier transform of the amplitude of the RF pulse envelope [Haacke et al., 1999]. The slice thickness is given by the relation:

$$\Delta z = \frac{\Delta\omega}{\gamma G_z} \tag{2.92}$$

Application of an infinitively long RF pulse in a form of a sinc function allows for producing a rectangle slice profile:

$$B_1(t) = B_1 \mathrm{sinc}(\frac{\pi t}{\tau_s}) \tag{2.93}$$

$$\Delta\omega = \frac{1}{\tau_s} \tag{2.94}$$

here t_s is a time at the first zero-crossing of the sinc-shaped pulse. Since the time of the RF excitation must be finite, the sinc-shaped pulse has to be truncated and an ideal rectangular slice profile cannot be achieved. For fast imaging sequences, where the excitation time is strongly reduced, Gaussian-shaped RF pulse forms are often used. In this case, the frequency bandwidth of the Gaussian slice profile is given by:

$$\Delta\omega = \frac{2\pi}{\tau_g} \tag{2.95}$$

where τ_g is the FWHM of the RF excitation pulse.

After the slice selection, the spatial information is retrieved by means of the frequency and phase encoding within the slice, using the gradient magnetic fields G_x and G_y, respectively. To reconstruct an image in the spatial domain the 2D FFT is calculated from the acquired data.

2.2.5.2 Three dimensional sequences

In 3D imaging techniques the MR signal is collected from the entire object, which is therefore, imaged as a whole entity and provides high signal-to-noise ratios. Spins of the object being imaged located in the sensitive areas of the receiver coil are excited with non-selective RF pulses to produce transverse magnetization. The excitation can be performed using RF pulses of a simple rectangular form. In contrast to the 2D techniques, k-space is also encoded along the third dimension. Since no slice selection is performed, there is no need for switching of the dephasing gradient. Moreover, application of the rectangular excitation pulses allows for achieving required flip angle in a shorter time than in the case of the sinc-shaped pulses. Thus, the acquisition at very short echo times is possible. After the data acquisition, a 3D FFT is performed to reconstruct the imaged object. The disadvantage of the 3D sequences is the susceptibility to pulsation and motion artifacts.

2.2.6 Pulse sequences

There are many different ways of approaching the task of sampling the k-space. In this work, only the traditional Fourier encoded techniques involving sampling on a Cartesian grid are discussed. The Cartesian sampling enables fast image reconstruction, and is commonly used in clinical imaging. Besides this, other sampling methods, which utilize e.g. radial or spiral trajectories were developed. There are two fundamental types of pulse sequences: the gradient echo and the spin echo. Other category of so-called hybrid sequences exploits both phenomena to generate echoes. The following section describes the basic methods behind the gradient, and spin echo sequences.

2.2.6.1 Spin echo sequence

The most common pulse sequence used in MRI is based on the detection of a spin echo. Historically, spin echo was the first sequence to be used. The mechanism of spin echo generation

was discussed in the section 2.1.9. A simplest form of this sequence is illustrated in the pulse sequence timing diagram (Fig. 2.10a). The sequence uses a 90° RF pulse to rotate the longitudinal magnetization into the xy-plane. During the excitation pulse, a slice selection gradient G_z is applied to define the image slice position and thickness. After the excitation pulse is applied, the magnetization flipped into the transverse plane starts to dephase. The excitation pulse is followed by the simultaneous application of the rephasing lobe of the slice selection gradient, the phase encoding gradient G_y, and the dephasing lobe of the readout gradient G_x. The amplitude of the phase encoding gradient varies between $-G_y$ and G_y in N_y steps. The subsequent application of a 180° refocusing pulse together with the slice selection gradient at the time $TE/2$ generates a maximal echo signal occurring at the time TE. The signal readout is accomplished by switching on a rephasing gradient in the frequency encoding direction. After the readout, the longitudinal magnetization has to recover to its equilibrium state before the excitation and the acquisition series are repeated. In the simplest form of spin echo imaging presented here, the repetition time (TR) is defined as a time interval between two successive 90° excitation pulses. With each repetition, thanks to a different phase encoding, a whole k-space line is filled. The 180° rephasing pulse compensates for the constant field heterogeneities leading to a T_2-weighted echo signal.

Figure 2.10b shows the way in which k-space is mapped during the spin echo acquisition. Concurrent application of the rephasing and the phase encoding gradients after the 90° excitation is depicted as a path ($1 \rightarrow 2$), from the center of the plane to a certain position on the k-plane. The 180° pulse inverts the effect of the gradients ($2 \rightarrow 3$). The readout gradient following the rephasing pulse initiate the sampling of the k-space line defined by the phase encoding gradient ($3 \rightarrow 4$).

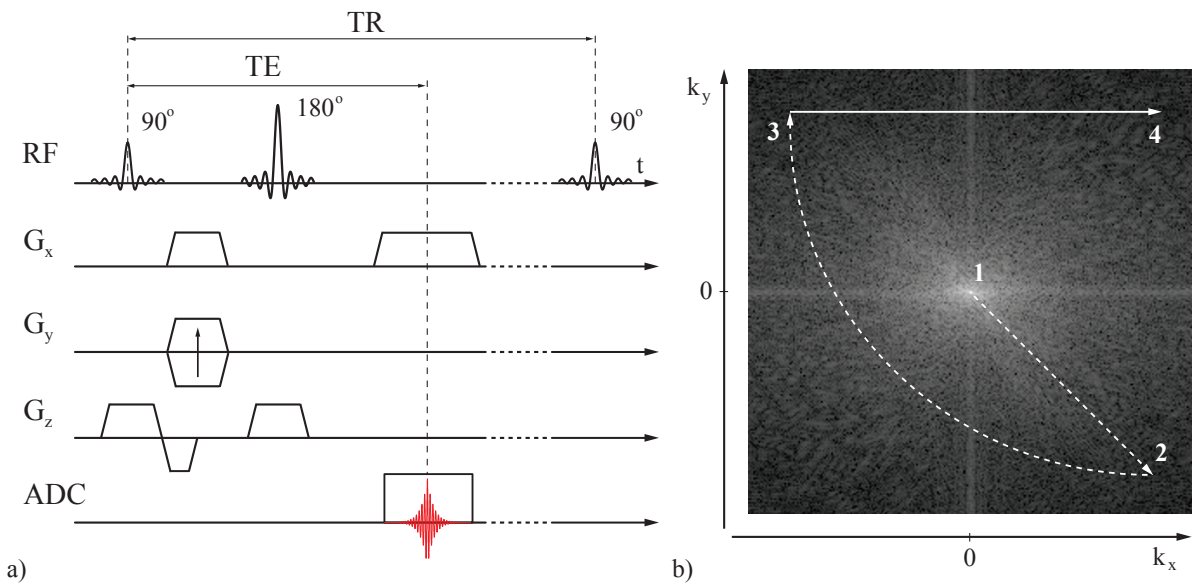

Figure 2.10: *Diagram of the spin echo pulse sequence (a) and its trajectory in the k-space (b).*

2.2.6.2 Gradient echo sequence

The gradient echo sequence differs from the spin echo sequence by the absence of a 180° RF rephasing pulse. The method to generate a gradient echo by using a pair of bipolar gradient pulses was discussed in the section 2.1.10. Figure 2.11a shows a timing diagram of the basic gradient echo sequence. The application of flip angles α lower than 90° decreases the amount of the net magnetization tipped into the transverse plane. This implies a faster recovery of the longitudinal magnetization. At the beginning of the sequence block, a slice selective excitation is accomplished by application of a slice selection gradient G_z and an RF pulse α. A phase encoding gradient G_y is applied simultaneously with the dephasing gradient in the frequency encoding direction. Subsequently, the rephasing frequency encoding gradient G_x is switched on during the data acquisition and an echo is generated. The echo time (TE) is defined as a time interval between the excitation pulse and the maximum of the echo signal.

The main advantage of the low flip angle RF excitations in the gradient echo technique is the possibility of using much shorter repetition times (TR) and reducing the image acquisition time. As a consequence of the short TR the longitudinal magnetization does not fully recover and after few initial pulses an equilibrium is established between the longitudinal magnetization recovery and its depletion due to the excitation pulses. The gradient echo based sequences are typically accomplished by examining the FID. Since the characteristic decay time constant associated with the FID is T_2^*, these sequences are prone to the magnetic susceptibility artifacts. Figure 2.11b shows the trajectory in the k-space during the gradient echo acquisition.

The most popular modification of the gradient echo sequence is the Fast Low Angle Shot (FLASH) sequence [Haase et al., 1986]. This sequence uses a semi-random spoiler gradient after each echo to destroy any remaining transverse magnetization by causing a spatially dependent phase shift. The FLASH sequence allows performing acquisition at extremely short echo times, which helps suppressing susceptibility artifacts.

2.2.7 Strategies of k-space sampling

As previously stated, the pulse sequences can be divided into few groups, involving 2D or 3D sampling schemes, based on gradient echo or spin echo acquisitions. Besides this classification, various strategies of k-space sampling on a rectangular grid can be implemented. In the next paragraphs, a short overview of those techniques is presented.

2.2.7.1 Single-shot and segment based acquisition

A huge progress in the MR technology allowed implementing fast pulse sequences, which utilize rapid and precise gradient switching to define the k-space trajectory. In single-shot techniques the entire k-space data is acquired after a single RF excitation pulse. The first single-shot pulse sequence called Echo-Planar Imaging (EPI) was proposed by Mansfield [1977]. In this imaging technique, the RF excitation is followed by a train of gradient echoes with different

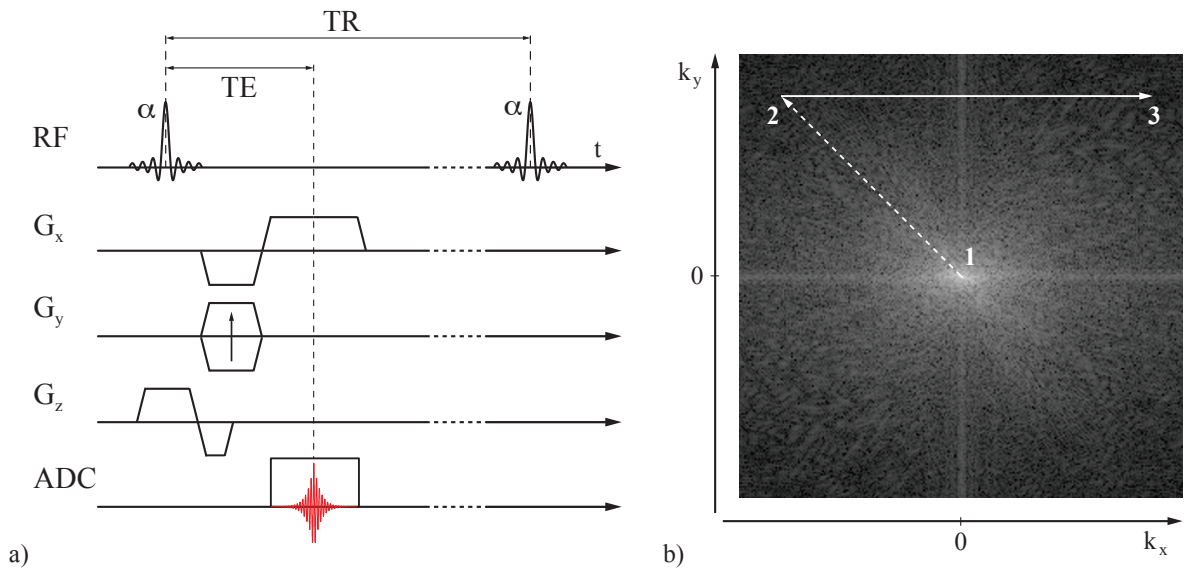

Figure 2.11: *Diagram of a gradient echo pulse sequence (a) and its trajectory in the k-space (b).*

spatial encoding. The frequency encoding gradients oscillate alternating the direction of the k-space readout. EPI is very demanding on the imaging hardware because of the high rate of the gradients switching. Another example is a spin echo based Rapid Acquisition Relaxation Enhanced (RARE) sequence [Hennig et al., 1986]. This sequence is characterized by a series of rapidly applied 180° rephasing pulses to generate multiple echoes. Each echo is produced for a different value of the phase encoding gradient. The signal in the single-shot sequences is sampled during the T_2 decay. As a consequence, these sequences are mostly used for 2D imaging and not for 3D, because of the limited time for the acquisition. The main advantage of the single-shot techniques is a short acquisition time of about $50 - 400$ ms per 2D slice comparing to the older techniques, where after the excitation pulse only one line of data is sampled. The faster scans help reducing motion-related artifacts. This type of sequences can be applied sequentially for multiple slice acquisitions, or for dynamic, time-resolved MR scans and functional imaging. It is, however not necessary to sample the whole of the k-space in a single shot. One can repeat the whole RF excitation sequence many times to cover each time different k-space area in so-called segments (Fig. 2.12a). The final image is reconstructed using a combination of the spatial information from all segments.

2.2.7.2 Centric and linear k-space sampling

The way in which the gradients encode the y or z phase directions is termed as the k-space sampling order. The k-space lines can be acquired in an arbitrary order. The standard method of data acquisition, one line in phase direction after the other, is called linear or sequential sampling. Using this ordering scheme the center line of the k-space providing most of the

contrast in the image, is sampled in the middle of the acquisition. In the centric ordering, the middle of k-space is acquired first (low frequency components), and then sampling is continued towards the peripheries of the k-space (high frequency components). For the $N \times N$ matrix the following 2D sampling schemes are possible:

- linear: $-N+1, \cdots -1, 0, 1 \ldots N-1, N$
- reversed linear: $N, N-1, \ldots 1, 0, -1 \cdots -N+1$
- centric: $0, 1, -1 \ldots N-1, -N+1, N$
- reversed centric: $N, -N+1, N-1 \cdots -1, 1, 0$

The choice of the sampling scheme can influence signal-to-noise ratio and susceptibility to image artifacts.

2.2.7.3 Partial Fourier Technique

One of the fundamental properties of the Fourier transformation is the symmetry in k-space so-called Hermitian symmetry:

$$S(\vec{k}) = S^*(\vec{k}) \tag{2.96}$$

The real and imaginary parts of its transform are even (symmetric) and odd (anti-symmetric), respectively:

$$\vec{k} \to -\vec{k}, \quad \mathrm{Re}[S(\vec{k})] = \mathrm{Re}[S(-\vec{k})] \quad \text{and} \quad \mathrm{Im}[S(\vec{k})] = -\,\mathrm{Im}[S(-\vec{k})] \tag{2.97}$$

In case of real valued functions the data on one half of the k-space can be used to recreate the data on the other half. This redundancy between the real valued data on both halves of the k-space allows reducing the data acquisition time by acquiring only a part of k-space data. There are variety of factors that can change the phase of the signal and cause the reconstructed object to be complex, such as unwanted phase shifts resulting from a motion, resonance frequency offsets due to the chemical shift or magnetic field inhomogeneities. Moreover, the center of the k-space contains high amplitude components. Thus, it is reasonable to fully sample the low frequency region to correct for the slowly varying phase shifts and increase the signal intensity. The partial Fourier fraction (PFF) parameter describes the ratio of the acquired number of k-space lines and the full k-space data size with the same spatial resolution. In case of PFF $= \frac{1}{2}$ the half-Fourier acquisition is performed. Practically used sampling strategies cover e.g. $\frac{3}{4}$, or $\frac{5}{8}$ of the k-space. The method of partial Fourier acquisition can be successfully applied in both gradient and spin echo based sequences. The Fast Spin Echo sequence with the partial Fourier acquisition is known as the HASTE sequence (half-Fourier acquisition single-shot turbo spin echo) [Semelka et al., 1996]. The acquisition scheme of the partial Fourier acquisition is shown in figure 2.12b.

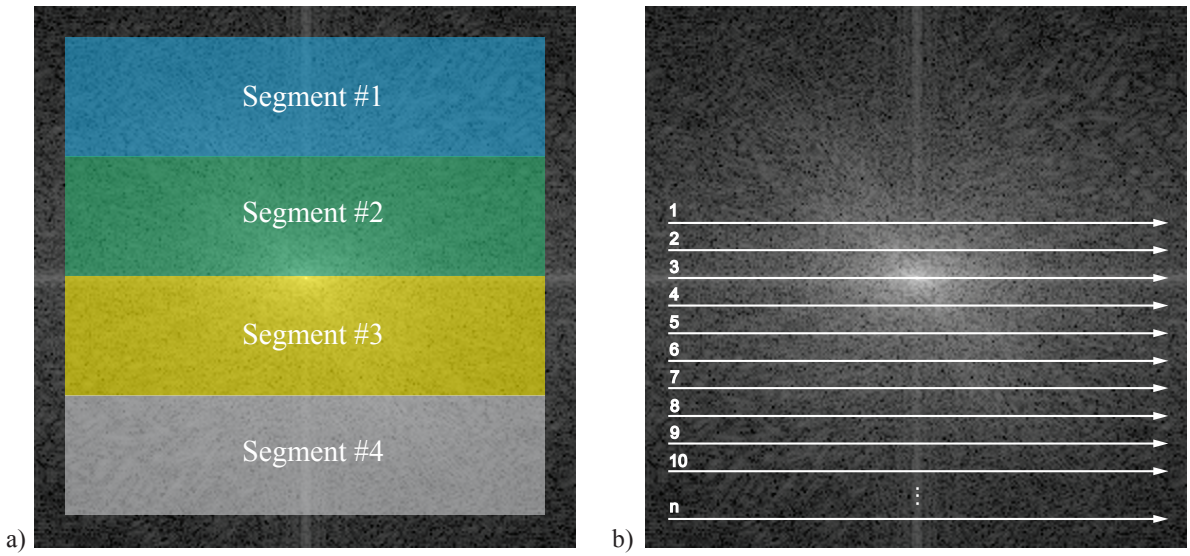

Figure 2.12: *Image (a) shows a segmented acquisition of the k-space. Image (b) presents the scheme of the partial Fourier acquisition in the k-space. In this example the acquisition in the phase direction begins slightly before the center of the k-space and follows to its peripheries.*

2.2.7.4 View Sharing Technique

For further improvement of the time efficiency and temporal resolution of the MR scans, strategies to share the spatial information among the consecutive images of a dynamic MR acquisition have been developed. View sharing is a reconstruction method that reuses some of the k-space data in order to reconstruct two or more different images. In its most popular implementation, the low frequency components of the k-space which contains most of the image energy are sampled more frequently than the high frequency regions of the k-space which is interpolated or shared between subsequent time frames. View sharing reduces the time needed to acquire the complete time-resolved MR data set. Currently, clinically available view sharing techniques comprise various 3D acquisition methods of sharing inner and outer k-space regions e.g. TRICKS (time-resolved interpolated contrast kinetics) [Korosec et al., 1996] or TWIST (time-resolved imaging with stochastic trajectories) [Vogt et al., 2007].

2.2.8 Image contrast

Image contrast in MRI is created by differences in the signal amplitude, or phase retrieved from different locations within the studied object. The differences in a measured signal amplitude after the RF excitation are dependent on the relative density of the protons ρ, longitudinal relaxation time T_1 and transverse relaxation times T_2 and T_2^*. Due to the exponential nature of the relaxation processes, variations of echo time TE and repetition time TR sequence parameters

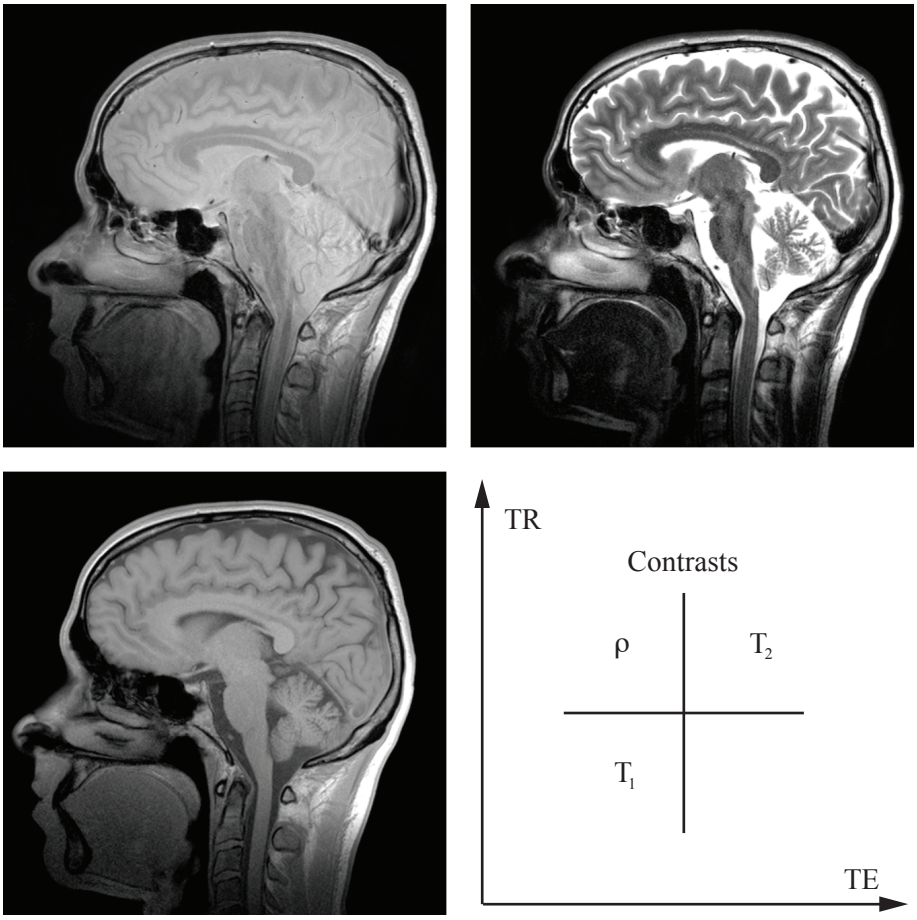

Figure 2.13: *Sagittal image of a volunteer's head acquired using three different contrast-weightings: proton density ρ (upper left), T_2 (upper right) and T_1 (lower left). The diagram (lower right) shows the dependence of the TE and TR parameters on the MR contrast.*

affect the characteristics of the image contrast (Fig. 2.13). The T_1-weighting will be obtained for short echo time ($TE \ll T_2^*$) and short repetition time. Since the chosen echo time is short, the influence of T_2 signal decay is minimized. On the contrary, the short interval between RF excitations i.e. short TR enhance differences in signal arising from differences in the T_1 of tissues. A combination of long echo times and long repetition times result in a T_2-weighted image. The long TE allows developing larger differences between the signal amplitudes of tissues, while the long TR minimizes the effect of longitudinal relaxation. The proton density weighting can be achieved using short echo times ($TE \ll T_2^*$), and long repetition times ($TR \gg T_1$). Then, the measured signal is proportional to the density of the resonant nuclei in a tissue. Moreover, mixed contrast configurations can be obtained e.g. T_2/T_1 contrast, using a balanced steady-state free-precession sequence (bSSFP), which is described in detail in section 3.4.1.

The image contrast can be influenced by the application of the magnetization preparation techniques. There are many different methods to achieve the T_1- or T_2-preparation. One of the most

popular and simple mechanisms for generating T_1 contrast is to use an inversion recovery (IR) sequence by the application of a 180° pulse to invert the longitudinal magnetization before the image acquisition. The method is described in the next subsection. Another type of magnetization preparation can be performed to produce a T_2-weighted image. Such a T_2-preparation sequence typically includes a first 90° pulse, multiple 180° pulses, and a second 90° pulse. Duration of the magnetization preparation corresponds to the degree of T_2-weighting.

Introduction of the external chemical substances so-called contrast agents into the anatomical structures being imaged can also be used to increase the signal intensity differences between distinct tissues. The MRI contrast agents change the relaxation times of tissues, which gives a higher or lower signal depending on the image weighting. The contrast media can be delivered intravenously, orally, or through an inhalation route. Positive contrast agents cause a reduction in the T_1 increasing signal intensity on T_1 weighted images. Most commonly used positive contrast agents contains gadolinium chelates. Paramagnetic oxygen can be also used as a positive contrast to enhance the signal from pulmonary tissue. Negative contrast agents consisting of suspended colloids of iron oxide nanoparticles (superparamagnetic iron oxide or ultra-small superparamagnetic iron oxide) appear dark on MR images. Spin-spin relaxation effects induced by these groups of contrast agents shorten T_2 and T_1 relaxation times.

2.2.8.1 Inversion recovery sequence

The inversion recovery (IR) is a magnetization preparation technique allows for generation of the T_1 contrast in MR images. The sequence starts with a 180° RF pulse, which inverts the longitudinal magnetization $M_z \rightarrow -M_z$. Due to the T_1 relaxation, longitudinal magnetization will return to its initial value according to the equation:

$$M_z(t) = M_0(1 - 2e^{\frac{-t}{T_1}}) \tag{2.98}$$

The inversion pulse is followed by the spin echo, or gradient echo based imaging sequence (Fig. 2.14a). The excitation pulse of the imaging sequence block flips the available longitudinal magnetization into the transverse plane. Different tissues are characterized by different T_1 relaxation times. The signal intensity of a given tissue in the image depends on the interval TI between the inversion pulse and the image acquisition block. The inversion process allows nulling a specific tissue characterized by certain T_1 relaxation time by choosing an appropriate value of $TI = TI_0$:

$$TI_0 = T_1 \ln\left(\frac{2}{1 + e^{-TR/T_1}}\right) \tag{2.99}$$

Consider two different tissues with relaxation times T_{1a} and $T_{1b} = 2T_{1a}$. The transverse magnetization available after the inversion pulse for those tissues as a function of time is shown in figure 2.14b. The TI can be chosen in that way, that the signal intensity from the tissue with a relaxation time T_{1b} will be totally nulled. The inversion recovery based sequences have found an application in a clinical practice e.g. Short Tau Inversion Recovery (STIR) sequence to suppress the fat tissue, and a similar technique called Fluid Attenuation Inversion Recovery (FLAIR) to suppress the blood, or the cerebrospinal fluid. Inversion recovery imaging offers a

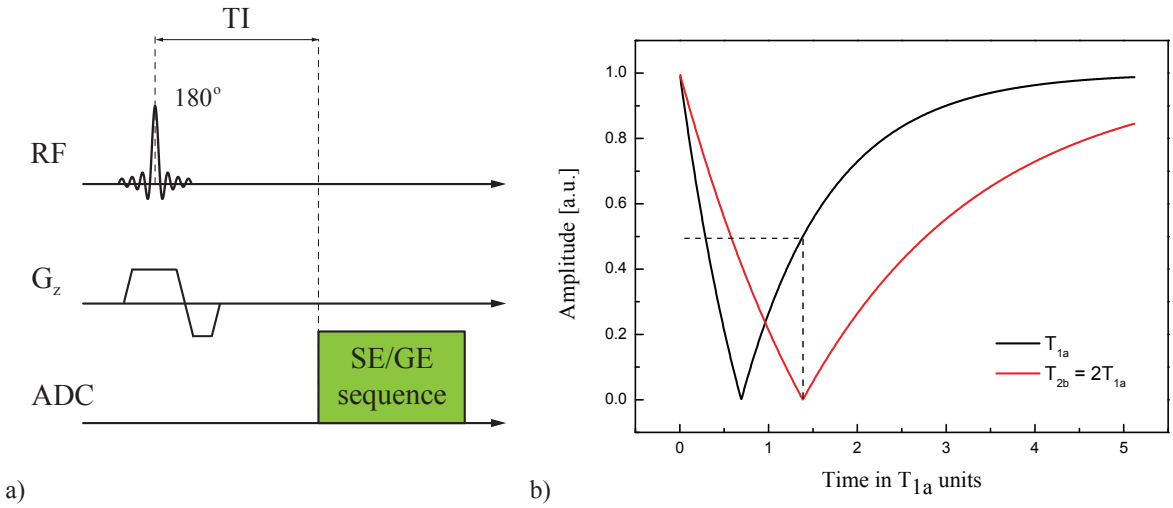

Figure 2.14: *Schematics of slice selective inversion recovery pulse sequence (a). The inversion pulse is followed by the imaging sequence block, after the time interval (TI). Figure (b) shows the amplitude of the transverse magnetization measured during the imaging sequence block as a function of time for two tissues with different relaxation times (T_{1a} and $T_{1b} = 2T_{1a}$).*

possibility to calculate spatially-resolved T_1 maps using a set of images acquired with different time intervals TI. The main disadvantage of these imaging methods is low time efficiency due to the introduction of the time interval between the inversion pulse and echo acquisition block.

2.2.9 Effect of the chemical shift in imaging

The chemical shift has its origin in the magnetic shielding of the nucleus produced by electrons. The hydrogen nuclei in molecules are surrounded by electron clouds. The electron distribution usually varies according to the local geometry e.g. binding partners, bond lengths, angles between bonds. Since electrons are also magnetic particles, when the external magnetic field $\vec{B}_0$ is applied, the electrons circulate and generate a small magnetic field $\vec{B}_{ind}$ opposing the applied field (Lenz's law). Thus, the effective magnetic field $\vec{B}_{nuc}$ actually felt by protons is slightly different and given by a formula:

$$\vec{B}_{nuc} = \vec{B}_0 - \sigma\vec{B}_0 = \vec{B}(1-\sigma) \tag{2.100}$$

where σ is the shielding factor (ca. 10^{-5} for protons in water). The electron shielding influences the Zeeman energy levels and resonance frequency, resulting in the following Larmor equation:

$$\omega_0 = \gamma B_0(1-\sigma) \tag{2.101}$$

In case of solids the shielding factor σ has a form of a three dimensional tensor. However, in liquids and gases the averaging of the shielding interaction due to rapid, random tumbling of molecules simplifies σ to a scalar quantity.

The chemical shift is designated by the symbol δ,given with respect to a reference frequency or reference sample, and defined by:

$$\delta \equiv \frac{\omega_S - \omega_R}{\omega_R} \cdot 10^6 \tag{2.102}$$

where ω_S is the resonant frequency of a sample and ω_R the resonant frequency of a reference. The chemical shift is measured in parts per million (ppm). The detected resonant frequencies of samples are usually referenced against TMS (tetramethylsilane) which is assigned the chemical shift of zero.

The chemical shift allows exploring molecular properties of substances and is of great importance for NMR spectroscopy. However, in MRI chemical shift is often a source of image artifacts. Even for a perfectly homogeneous external magnetic field, protons in water experience a different field from those in lipid-based molecules. Most protons in fat in the human body have a chemical shift of 3.35 ppm, which leads to a frequency shift of about 217 Hz at 1.5 T. Because the protons in fat are shifted in frequency relative to protons in water, the fat misregistration will be manifest along a frequency encoding direction:

$$\omega_f(x) = \gamma G_x x + |\omega_f(x) - \omega_w(x)| \tag{2.103}$$

where ω_w is the resonant frequency for water and for ω_f fat. This artifact will result as a bright or dark band at the edge of the imaged organs. A higher magnetic field strength increases the spatial misregistration, while a higher gradient strength minimizes this effect.

2.3 Anatomy of the human lung

The purpose of this section is to provide basic information regarding the anatomy of the thorax and the human respiratory system. In humans the anatomical features of the respiratory system include airways, lung parenchyma, vessels, and the respiratory muscles (Fig. 2.15). The respiratory system can be subdivided into an upper respiratory tract and a lower respiratory tract. The upper part of the respiratory tract comprises the nasal cavity, mouth, pharynx, and the larynx. The function of nasal cavities is warming and moistening of the inspired air, as well as filtering the air removing large particles. The larynx contains the vocal folds vibrating and producing sounds (speech) as the air passes between them. The lower respiratory tract starts below the larynx with the trachea and splits into the two main bronchi that enter the roots of the lung (hilum).

The lungs, which are the essential respiration organs of the respiratory system, are located in the chest. Each lung is conical in shape and placed upon the convex dome of the diaphragmatic surface referred to as the base of the lung. The costal surface of the lung is large, convex and related to the costal pleura, which separates it from the ribs, costal cartilages and the innermost intercostal muscles. The medial surface of the lungs is concave because of the presence of mediastinal structures. The lungs are separated from each other by the heart and great vessels in the middle mediastinum. They are attached to the heart and trachea by the structures in the

root of the lungs (in hilum), and to the pericardium by the pulmonary ligaments. Both lungs are separated into lobes by fissures. Each lobe is penetrated by vessels, lymphatic vessels and nerves. The right lung is larger and heavier than the left lung and consists of three lobes: superior (upper), middle, and inferior (lower) separated by horizontal and oblique fissures. The left lung is divided into superior and inferior lobes by a long deep oblique fissure. The anteroinferior part of the superior lobe has a small tongue-like projection called the lingula. The left lung is longer and narrower than the right lung, because the left dome of the diaphragm is lower. Moreover, the heart and the pericardium bulge more to the left. The lobes are further subdivided into the bronchopulmonary segments (10 right lung, 9 left lung) and the segments into hexagonal shaped lobules. The lungs are surrounded by the pleura, a double membrane consisting of an inner layer (visceral pleura), which surrounds each lung, and an outer layer (parietal pleura). The narrow space between the two membranes, the pleural cavity, is filled with a lubricant secreted by the pleura (15 to 25 mL in an average adult).

The airways consist of the bronchial tree and alveoli. The main bronchus accompanies the pulmonary artery into the wedge-shaped hilum of the lung, where it subdivides. The right main bronchus is wider, shorter, and more vertical than the left one. The diameter and length of the bronchi decrease as they dichotomously branch and extend deeper into the lung. Each branch enters a clearly defined sector of the lung. The terminal bronchioles represent the deepest point of the bronchial tree. They terminate after about 23 levels of branches in alveolar sacs. All these structures form a continuous passageway for air to move in and out of the lungs. Alveolar sacs are made up of clusters of alveoli. Figure 2.16 shows the alveoli forming grape like structures where the individual alveoli are tightly wrapped in capillaries. An alveolus has an average diameter of 0.2 - 0.3 mm. The lung contains between 300 to 500 million alveoli, and the total surface area of the alveoli of an adult is about 140 m^2 [Thews, 1997]. The alveolar epithelium is composed of cuboidal type II cells and squamous type I cells.

The pulmonary arteries distribute the deoxygenated blood and arise from the pulmonary trunk belonging to the pulmonary circulatory system. The right and left pulmonary arteries give off branches to the superior lobes before they enter the hilum. The arteries are branching to each lobe, bronchopulmonary segment and lung lobule. The bronchial arteries supply blood to the connective tissue of the bronchial tree and arise from the systemic circulatory system. The pulmonary veins carry oxygenated blood back to the left atrium of the heart. A main vein drains each bronchopulmonary segment. The bronchial veins drain only the part of the blood delivered by the bronchial arteries to the bronchial tree.

2.4 Physiology of the human lung

The following paragraphs describe the most important aspects of the respiratory functions. A deeper insight into the topic of the lung physiology can be found in the textbooks of Thews [1997], Ganong [2003] or Levitzky [2007]. A mathematical approach to describe the physiological processes taking place in the human respiratory system can be found in the textbook of Keener and Sneyd [1998].

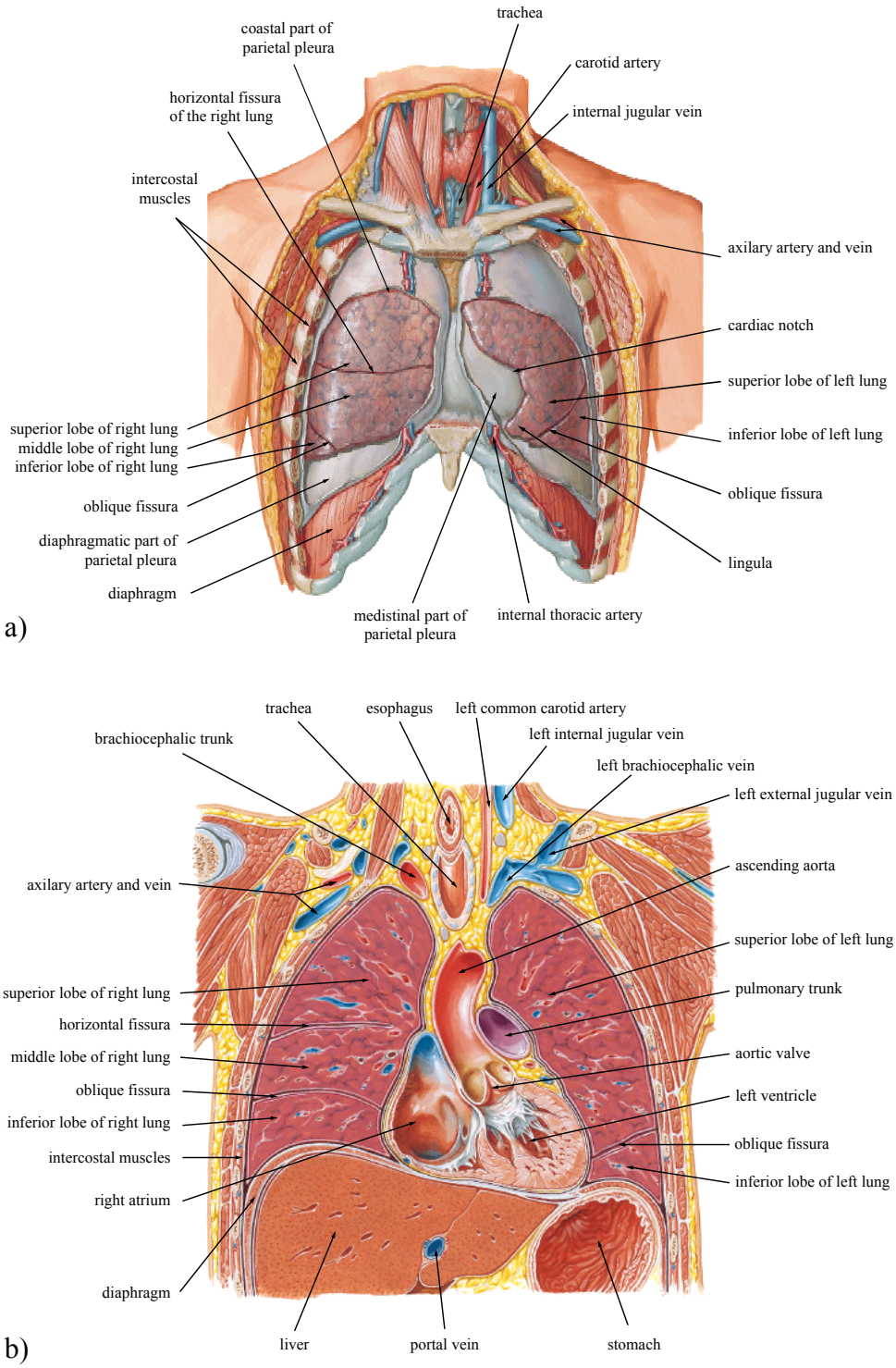

Figure 2.15: *Figure (a) shows the thorax and location of the main anatomical structures surrounding the lungs. A coronal slice through the human chest is shown in figure (b). Pictures were adapted from the "Atlas of Human Anatomy" [Netter et al., 2000].*

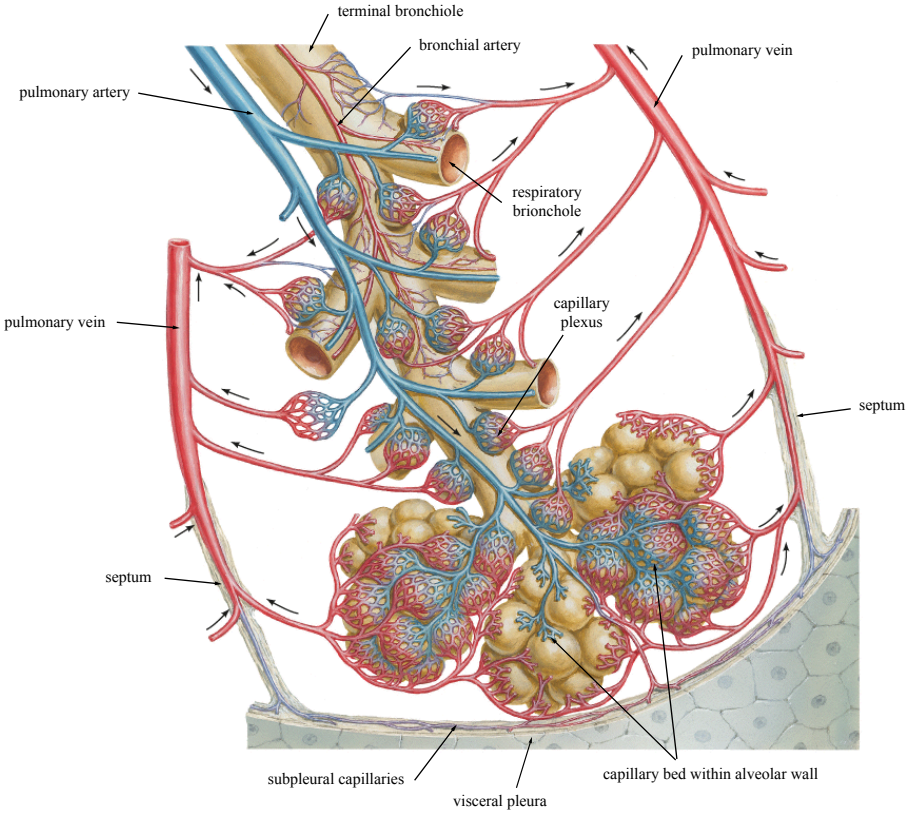

Figure 2.16: *Schematic illustration of the terminal bronchiole and its alveolar sac connected to the network of the capillary system. Picture was adapted from the "Atlas of Human Anatomy" [Netter et al., 2000].*

2.4.1 Mechanics of respiration

In order to move the air in and out of the lungs, a difference between the atmospheric pressure and the alveoli has to be established. The atmospheric pressure is referred to as 0 mm H_2O. The respiratory system contains a "pump" used to ventilate the lung. This "pump" is made up of the respiratory muscles, which increase or decrease the size of the elastic structures in the thoracic cavity and in the lungs. The presence of a thin layer of fluid between the visceral and the parietal pleura enables the lungs to slide easily along the thoracic wall. When respiratory muscles are relaxed, the interpleural pressure is subatmospheric. This negative pressure is caused by the mechanical interaction between the lungs and the thoracic wall. The lungs have a tendency to decrease their volume, which is determined by the inward elastic recoil property of the distended alveolar walls. On the opposite, the thoracic wall tends to extend because of its outward elastic recoil.

During inspiration, which is an active process, air is moved from the external environment through the airways into the alveoli. The interpleural pressure, which normally has a value of

about -5 mm H_2O at beginning of the inspiration, decreases to about -8 mm H_2O at the end of inspiration. At this point, before any airflow occurs, the pressure inside the alveoli is equal to the atmospheric pressure. Respiration is controlled in the respiratory command center in the brain. Nerves forward the signals to the inspiratory muscles. The muscles contributing to inspiration are: the diaphragm, the external intercostals, and the accessory inspiratory muscles. The large diaphragm muscle separating the chest cavity from the abdominal cavity is the primary inspiratory muscle. The diaphragmatic contraction during normal quiet breathing flattens its dome and elongates the thorax. In supine position (position of patients and volunteers in the whole-body MR-scanner) the diaphragm is responsible for more than two thirds of the volume increase in comparison to only about one half in the upright position. The function of the external intercostal, parasternal intercostal and scalene muscles is to enlarge the rib cage. Only the simultaneous work of the diaphragm and these muscles enables an adequate inspiration. The accessory muscles of inspiration contract during forced respiration, coughing or sneezing. The alveoli are extended passively through an increased distending pressure, which acts on the alveolar walls. Thus, with increasing alveolar volume the pressure inside the alveoli becomes slightly negative. The air flows into the lungs following the generated pressure gradient, and overcoming the resistance of the conducting airways. Air flows into the alveoli until the alveolar pressure is equal to the atmospheric pressure.

The expiration is a passive process. At the end of the inspiratory phase the brain ceases the inspiratory command, and the respiratory muscles start to relax. During quiet respiration no contraction of the muscles, which decrease the intrathoracic volume occurs. However, the forced expiration is supported by the muscles of the abdominal wall, which pushes the diaphragm upward, while the internal intercostal muscles push the rib cage downwards. During the expiration, the volume of the thorax reduces, increasing the interpleural pressure. This enables the lung parenchyma to recoil, decreasing the volume of alveoli and compressing the alveolar gas. Presence of elastin and collagen in the alveolar walls augment its elastic recoil properties. However, the elastic recoil is mainly caused by the surface tension forces, which occur at the gas-liquid interfaces. The physical stability of the alveoli is imposed by the presence of the pulmonary surfactant, and the structural independence of the alveoli. The surfactant decreases the surface tension eliminating the risk of the alveolar collapse. The air flows out of the lungs when the inverted pressure gradient is generated, as long as the alveolar pressure of 0 mm H_2O is achieved. The alveolar pressure must be sufficiently higher than the atmospheric to overcome the resistance of the conducting airways.

2.4.2 Lung volumes and lung capacities

The amount of gas in the lung is a dynamic value, depending on the phase of the respiratory cycle, as well as on the mechanics of the thoracic wall and lung motion. Normally, the amount of air inspired per minute is about 6 $L \cdot s^{-1}$ at a respiratory rate (RR) between 12 to 16 breaths per minute. The lung volume depends on many factors e.g. height, weight, body surface area, sex, age and health condition.

The standard lung volumes and capacities can be described as follows:

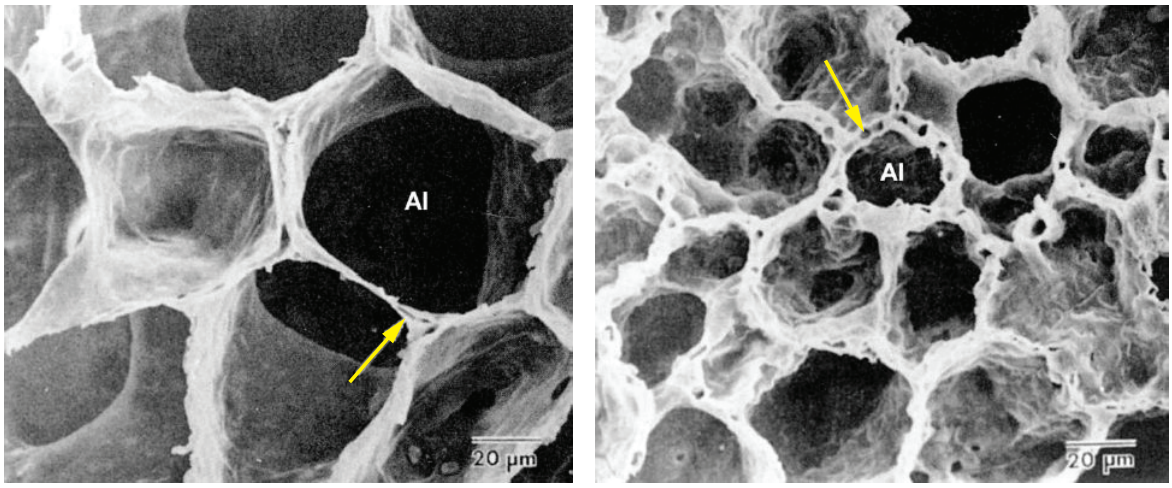

Figure 2.17: *Scanning electron microscope view of lung alveoli (magnified 750 times). Images show the change of the shape and size of alveoli in different phases of the respiratory cycles; in respiratory inspiration (left) and expiration (right). The capillaries are visible within flat alveoli walls (yellow arrows). Pictures were adapted from Albertine, K. H., Williams, M. C., and Hyde, D. M. (2000). Fig. 1.22, p. 17. in the Textbook of Respiratory Medicine, 3rd edition. (ed. J. F. Murray and J. A. Nadel). W. B. Saunders, Philadelphia.*

Tidal volume (VT) - is the volume of air inhaled, or exhaled during a normal quiet respiration, determined by the activity of the respiratory control centers located in the brain.

Residual volume (RV) - represents the volume of air left in the lungs after a maximal forced exhalation. This amount of gas stays in the lungs and depends on the maximal force generated by the expiratory muscles, as well as by the elastic recoil of the thoracic wall and lungs, which acts in opposed directions. The RV prevents the lungs from collapsing.

Expiratory reserve volume (ERV) - describes the volume of gas that can be exhaled from the lungs during a maximal forced expiration, which starts after the end of a tidal expiration.

Inspiratory reserve volume (IRV) - is the additional volume of air that can be inhaled into the lungs during a maximal forced inspiration, after the end of a tidal inspiration. The value of IRV depends on the strength of the inspiratory muscle contraction, as well as on the elastic recoil properties of the thoracic wall and the lungs.

Functional residual capacity (FRC) - is the volume of air present in the lungs at the end of tidal expiration. The FRC is achieved by the balance between the forces generated by the elastic recoil of the lungs and the thoracic wall is achieved. The forces are equal but oppositely directed. The FRC is the sum of ERV and RV.

Inspiratory capacity (IC) - describes the volume of air that can be inspired following a normal expiration. This value is dependent on the strength of inspiratory muscle contraction and the elastic recoil properties of the thoracic wall and the lungs. The IC is equal to the sum of VT and IRV.

Total lung capacity (TLC) - is the volume of air contained in the lung after a maximal inspiratory effort. The TLC consists of the IRV, VT, ERV and RV.

Vital capacity (VC) - represents the volume of air that can be exhaled after a maximal forced expiration. The VC is equal to the difference between TLC and RV.

Figure 2.18 shows the lung volumes and capacities for an average 70 kg adult male. In addition to the volumes and capacities listed above, one can define a lung dead space V_D, which is the amount of inhaled air that does not participate in the gas exchange process. The total dead space can be divided into the anatomical and alveolar dead scape. The anatomical dead space comprises the air in the conducting zones of the respiratory system, which do not have contact with the alveoli. The alveolar dead space is the volume of air introduced to the lung areas without blood flow in their pulmonary capillaries. Thus, the alveolar dead space is ventilated but not perfused. As a consequence the alveolar ventilation $\dot{V}_A = (VT - V_D) \cdot RR$, defined as the volume of gas reaching the alveoli per minute, is less than the total volume of gas entering the lungs per minute, the so-called minute ventilation $\dot{V}_E = VT \cdot RR$.

All these global values related to the ventilation can be measured using the spirometry (except RV), nitrogen-washout or helium dilution techniques, and body plethysmography. Many pulmonary pathologies can alter specific lung volumes, and for this reason the measurement of the described respiratory variables is clinically important.

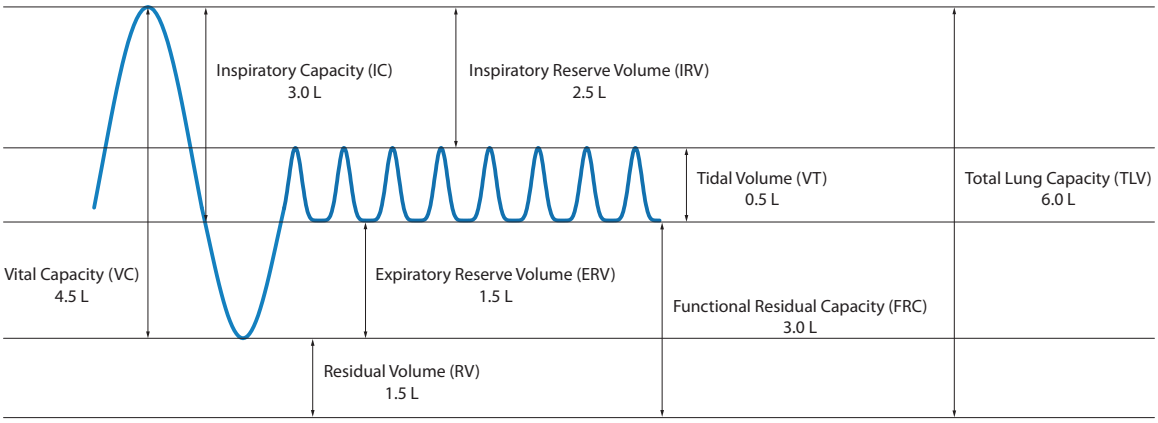

Figure 2.18: *The diagram shows standard lung volumes and capacities for a healthy 70 kg human male. The blue line represents the breathing curve.*

2.4.3 Pulmonary gas exchange and diffusion through the alveolar wall

The primary function of lungs is to provide continuous gas exchange between the inspired air and the blood in the pulmonary circulation. With each inspiration approximately 350 mL of fresh air (difference between the tidal volume and the dead space) is moved into the lungs and mixed

with 3 L of functional residual capacity (FRC). The composition of dry inspired air is 20.98% O_2, 0.04% CO_2, 78.06% N_2 and 0.92% of other gases [Ganong, 2003]. Expiration removes 350 mL air, which contains about 15% O_2 and 5% CO_2. According to the Dalton's law, in a gaseous mixture the pressure exerted by each individual gas is independent of the pressures of the other gases. The partial pressures of O_2 and CO_2 in the inhaled air are given by:

$$\begin{aligned} P_{O_2} &= f_{O_2} \cdot P_T = 159 \text{ mm Hg} \\ P_{CO_2} &= f_{CO_2} \cdot P_T = 0.3 \text{ mm Hg} \end{aligned} \tag{2.104}$$

where f_{O_2} is the fraction of oxygen and f_{CO_2} the fraction of carbon dioxide in the inspired air, P_T is the total air pressure at sea level and equal to 760 mm Hg. The inspired air is moisturized before it reaches the lungs. The partial pressure of the water vapor is equal to $P_{H_2O} = 47$ mm Hg. This additional pressure expands the inhaled gas, so that the partial pressure of O_2 reaching the lungs is equal to $P_{O_2} = 149$ mm Hg. Change of the partial pressure of the P_{CO_2} in the inspired air is negligible.

During continuous breathing, a steady-state of the partial pressures in the alveoli is established and determined by the alveolar ventilation, the O_2 consumption, and CO_2 production. On the level of alveoli a simple diffusion along concentration gradients is responsible for the gas exchange. Oxygen diffuses from the alveoli to the blood in the pulmonary capillaries, while carbon dioxide diffuses from the blood into the alveoli. Fresh oxygenated air replaces O_2 that entered the blood. The CO_2 content in the alveoli is diluted and then exhaled. Diffusion to the blood takes place across the alveolocapillary membrane (Fig. 2.16). The diffusion capacity is proportional to the total alveolocapillary surface, and inversely proportional to its thickness. The mean alveolar P_{O_2} is about 100 mm Hg, and the mean P_{O_2} of the blood entering the pulmonary capillaries is 40 mm Hg. The CO_2 transported in the blood is dissolved in plasma and bounded as carbaminohaemoglobin. The P_{CO_2} of venous blood is about 46 mm Hg and 40 mm Hg in the alveolar space and arterial blood, respectively.

2.4.4 Pulmonary blood flow and perfusion

The pulmonary circulation and the bronchial circulation provides blood to the lungs. The bronchial blood flow constitutes only a small fraction of the output of the left heart ventricle, its main role is to nourish the bronchi and pleura. The entire output of the right heart ventricle supplies the lung with deoxygenated venous blood. Therefore, the pulmonary blood flow is equal to the cardiac output, which is about 3.5 $\text{L} \cdot \text{min}^{-1} \cdot \text{m}^2$ of the body surface, at rest. The pulmonary artery branches rapidly, creating a large tree of approximately $280 \cdot 10^9$ pulmonary capillaries. Pulmonary vessels have much thinner walls than those of the systemic vessels. This is physiologically important, making the pulmonary vessels more distensible and compressible, enabling the pulmonary circulation to operate at a lower pressure than the systemic circulation. The blood pressure in the pulmonary artery is about 25/10 mm Hg, while the pressure in the left heart atrium is about 8 mm Hg in the diastolic phase. This generates a gradient pressure, and forces the blood to flow. The high pressure in the pulmonary circulation is unnecessary, because the apices of the lungs are located in the short distance above the right ventricle.

The blood volume in the lungs is about 250 - 300 mL, from which 60 - 75 mL resides in the functional pulmonary capillaries, where the gas exchange takes place. Pulmonary capillary pressure is about 10 mm Hg, comparing to the oncotic pressure of 25 mm Hg, and blocks the fluid inflow from the vessels to the alveoli. The average diameter of the pulmonary capillaries is 6 µm, and makes them the major site of vascular resistance in the lungs. As a result, the velocity of the blood coming from the pulmonary artery falls off rapidly when it reaches the capillaries. It takes about 0.75 s for a red cell to pass through the capillaries at rest, and about 4 - 5 s to travel through the whole pulmonary circulation system. This process of the blood delivery to the capillary bed is called perfusion $\dot{Q}$ and can be quantitatively expressed as an amount of blood passing through gram of the pulmonary parenchyma in one minute $[\frac{\mathrm{mL}}{\mathrm{min} \cdot \mathrm{g}}]$. Not all the capillaries are perfused, at resting cardiac output. A large number of capillaries, requires a higher perfusion pressure to reach the critical opening pressure and overcome the vascular resistance caused by the hydrostatic forces. Increase of the mean pulmonary pressure and the blood flow, permits to oppose the hydrostatic forces and open the capillaries. Moreover, the increased pressure cause distention of the vessels, decreasing their resistance to blood flow.

2.4.5 Regional distribution of pulmonary ventilation and perfusion

Regional distribution of ventilation

The ventilation per unit lung volume depends strongly on the body position. In the upright position, the alveoli at the base of the lung receive more ventilation than the alveoli at the apex. In the supine position, the posterior lung portion is better ventilated than the anterior. These regional differences are influenced by the gravitation. The interpleural surface pressure, in case of supine position, is less negative in the (gravity-dependent) posterior regions of the thorax, than in the anterior regions. This creates a pressure gradient along the direction defined by gravitation. The interpleural surface pressure influences the regional alveolar ventilation. The difference between the alveolar and interpleural pressure is lower in the posterior lung regions, than the anterior, thus the anterior portion of lung is less expanded. Consequently, the higher pressure difference in the anterior region increase the lung expansion. A difference in the ventilation is created, because the alveoli in the gravity-dependent lung regions have a higher change in volume during the respiration. Thus, are better ventilated than the alveoli in the non-gravity dependent regions.

Effect of gravitation on the distribution of perfusion

The pulmonary vasculature is prone to the effects of gravity and body position on the vascular resistance, mainly due to the low intravascular pressure, high distensibility, and thin-structured vascular walls. The gravitational force influences the perfusion process in various lung areas. In the upright position, the apex of the lungs is located above the heart, and the base below it. The gravity generates a gradient pressure between the upper and the lower portion of the pulmonary arteries, which results in a linear increase of the blood flow in the direction of the gravitational force. A decrease of the pressure in the upper portion of the lungs, may cause the pulmonary capillaries to collapse, creating a physiological dead space, if the alveolar pressure exceeds the

arterial pressure. In the middle portion of the lungs the arterial pressure is higher than the alveolar, but may be lower than the pressure of the pulmonary veins, causing them to collapse during the normal expiration. The effective driving pressure for the blood flow is lowered and equal to the difference between the arterial and alveolar pressures. Blood is pushed into the veins, which are compliant. As a result, the perfusion values in this region are decreased. In the lower portion of the lung the pulmonary artery pressure and the pulmonary vein pressure are higher than the alveolar pressure. The effective driving pressure is equal to the difference between the arterial and vein pressure. In this region the perfusion has the highest value. The same effect occurs in the supine position, where the anterior portion of the lungs is less perfused than in the posterior areas of the lungs.

2.4.6 The Euler-Liljestrand mechanism

The Euler-Liljestrand mechanism describes the connection between the pulmonary ventilation and perfusion [Von Euler and Liljestrand, 1946]. In case of a local alveolar hypoxia, i.e. decreased ventilation in a part of the lung, a local hypoxic vasoconstriction occurs in that area. Hypoxia acts directly on pulmonary smooth muscles and produces hypoxic pulmonary vasoconstriction. This is a beneficial adaptive mechanism, because the blood is shunted to the other lung regions, where the gas exchange can take place. The increased surface area available for gas diffusion corrects the global ventilation to perfusion ratio.

2.4.7 Ventilation to perfusion ratio

Continuous respiration and gas exchange in the alveoli maintains a constant concentration gradient between oxygen and carbon dioxide. In an average adult, alveolar ventilation is around 4 - 6 $\mathrm{L \cdot min^{-1}}$ and the blood flow has a similar range. Thus, the ratio between ventilation and perfusion ($\dot{V}/\dot{Q}$) for the whole lung at rest is in a range of 0.8 - 1.2. The value of the ($\dot{V}/\dot{Q}$) ratio is related to the venous and alveolar partial pressures of O_2 and CO_2.

In an ideal case, shown in figure 2.19b, when the alveoli are ventilated and perfused assuring proper values of the O_2 and CO_2 partial pressures, the $\dot{V}/\dot{Q}$ is in the normal range. A completely occluded area of the lung is unventilated, and the $\dot{V}/\dot{Q}$ ratio is zero (Fig. 2.19a). No air flow takes place, and as a result the air trapped in this area will balance its content with the gas dissolved in the blood flowing in pulmonary capillaries. After a steady-state is reached, no gas exchange occurs. This can lead to local hypoxic vasoconstriction, causing a redistribution of perfusion. A lung area blocked by a pulmonary embolus is shown in figure 2.19c. In this case the pulmonary arteries are collapsed, no blood flow occurs and the area is completely unperfused. The $\dot{V}/\dot{Q}$ ratio is infinite, because no oxygen diffuses from the alveoli to the blood in the pulmonary capillaries, this is an alveolar dead space.

A whole spectrum of $\dot{V}/\dot{Q}$ values is possible in partially perfused or ventilated areas. Moreover, there are regional differences in $\dot{V}/\dot{Q}$ across the lungs, due to the influence of gravitation on the distribution of perfusion and ventilation. The gradient of perfusion is higher, than the ventilation

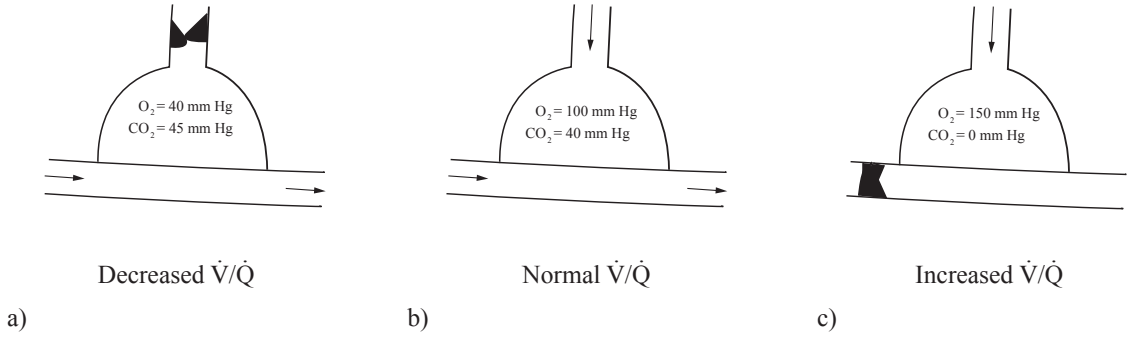

Figure 2.19: *Figure (a) shows an obstructed alveolus, where no ventilation takes place, and the $\dot{V}/\dot{Q}$ value is decreased. In a well ventilated and perfused alveolus in figure (b), the gas exchange between the alveolar air and the blood occurs, providing normal $\dot{V}/\dot{Q}$ ratio. An unperfused, but ventilated alveolus in figure (c) has increased value of the $\dot{V}/\dot{Q}$.*

gradient, resulting in lower $\dot{V}/\dot{Q}$ values in the gravity dependent regions. In many pulmonary diseases, the distribution of the $\dot{V}/\dot{Q}$ ratio is nonuniform. Therefore, methods to measure this relationship are clinically of great importance.

2.4.8 Additional lung functions

In addition to their function in respiration, lungs have several other important physiological roles. For instance, the lung has a number of metabolic functions. One of the additional functions of the lung includes the formation and release of chemical substances by the pulmonary cells for local use. The most familiar of these is the pulmonary surfactant, which is released at the alveolar surface. Surfactant plays an important role in reducing the alveolar elastic recoil and decrease the surface tension. Bronchial secretions contain immunoglobulins and other substances that increase the resistance to infections and protect the integrity of the mucosa. Alveolar macrophages, large mononuclear amoeboid cells that inhabit the alveolar surface help destroying inhaled particles. Different substances produced and stored by the lung cells may be released into the general circulation under various circumstances. Lungs have the ability to response to injury, the type II alveolar epithelial cells can proliferate, replace destroyed type I cells and reconstruct a continuous epithelial surface. The pulmonary circulation fulfills functions that are not directly related to the gas exchange. The large area of the pulmonary capillary bed helps filtering out small blood clots, or gas micro-bubbles from the venous blood stream. Moreover, the lungs can regulate the pH of blood by facilitating alterations in the partial pressure of carbon dioxide.

Chapter 3

Materials and methods

3.1 Characteristics of the MR scanner

All MR measurements presented in this work were performed in a 1.5 T whole-body MR scanner (MAGNETOM Avanto, Siemens Healthcare, Erlangen, Germany). The parameters of the gradient system are shown in table 3.1. In this work, the axes of the MR scanner are defined as follows: the z-axis defines the main magnetic field $\vec{B}_0$, the x-axis is the horizontal axis, and the y-axis the vertical axis of the MR scanner. The maximal field of view offered by the Avanto MR scanner is 50 cm, and the diameter of sphere volume of the homogeneous magnetic field is slightly larger. The chest examinations were performed using a body coil to transmit RF pulses, and a combination of a flexible 12-channel chest coil array and a 24-channel spine coil integrated into the table to receive the MR signal. Figure 3.1 shows a volunteer in supine position and configuration of coils used for the chest examination.

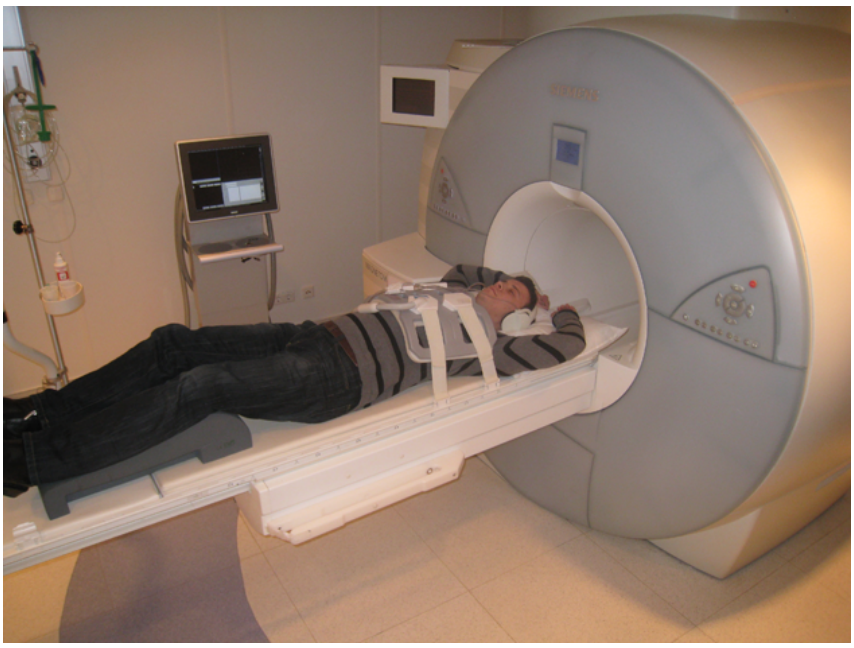

Figure 3.1: *Image shows a volunteer in the supine position in the MR scanner and configuration of coils used for thorax examinations. Anterior part of the chest is covered by a flexible coil array, the posterior part lies on a spin coil array, which is integrated into the table.*

Table 3.1: *Maximal amplitudes, slew rates, and rise times of the gradient system of the* 1.5 T *whole-body MR scanner (MAGNETOM Avanto, Siemens Healthcare, Erlangen, Germany).*

	x-axis	y-axis	z-axis
maximal amplitude	40 mT/m	40 mT/m	45 mT/m
maximal slew rate	180 T/m/s	180 T/m/s	220 T/m/s
minimal rise time	222 µs	222 µs	204 µs

3.2 Morphological MRI of the lung

The following section describes the challenges of the lung MRI, as well as basic pulse sequences currently used in the thoracic imaging.

Lung diseases: acute, chronic and malignancies are responsible for high morbidity and mortality worldwide, therefore, lung imaging is one of the most frequent and important radiological procedures. MRI provides an excellent soft tissue contrast and is an ideal tool to evaluate chest masses, or tumors of mediastinum [Landwehr et al., 1999; Shiotani et al., 2000]. Moreover, its role in imaging the heart and large vessels has been widely accepted [Finn et al., 2006; Fitzgerald et al., 2006]. Despite a great advance in a field of proton based MRI during the past decades, the largest, organ of the thorax, the lungs are usually investigated with the conventional X-ray and computed tomography (CT). The main advantages of these imaging modalities are high accessibility and robustness. However, X-ray and CT are criticized for the associated radiation exposure, especially in children, in pregnancy or in a patient who requires frequent follow-up examinations. The effective dose in chest CT is in the order of 8 mSv, which is around 400 times more than chest X-ray. Unfortunately, chest X-ray is only a projection technique providing lower sensitivity and limited morphological information.

Exposition to the ionizing radiation increases the risk of developing cancer [Diederich and Lenzen, 2000]. Thus, research of non-invasive and radiation-free techniques is of paramount importance. Chest MRI is a radiation-free alternative and has been explored since 1990s. A constant progress in MR technology e.g. improved quality of hardware, gradient and coil systems, or new pulse sequences has increased the value of this modality for the lung imaging.

Nevertheless, lung MRI is still a difficult and challenging task. There are several problems associated with lung MRI. Lungs have a unique foam like structure containing about 800 g of tissue distributed over a volume of $4 - 6$ L. This results in a low proton density in comparison to other parts of the body. The density of the lung parenchyma decreases with age [Van Dyk et al., 1982; Long et al., 2005]. The lung tissue is especially dense during the alveolar phase of the lung development. Predominance of air within the pulmonary tissue implying low proton density reduces the signal intensity. A large number of air-tissue interfaces in lung alveoli leads to local field inhomogeneities inducing high susceptibility differences on intra-voxel scales, which are responsible for rapid signal decay. This sophisticated lung structure results in extremely short effective transverse relaxation time e.g. at a 1.5 T magnetic field, T_2^* on the order of 1 ms

and T_2 of $30 - 80$ ms [Hatabu et al., 1999a,b]. On the other hand, the longitudinal relaxation time T_1 of $1100 - 1500$ ms is long [Stadler et al., 2005]. Due to the short T_2^*, the images obtained using a conventional MR pulse sequences show a "black hole" inside the thoracic cavity instead of the lungs. To overcome these restrictions, very short TE gradient-echo and spin-echo sequences were developed [Stock et al., 1999; Hatabu et al., 1999b; Deimling, 2000].

The second major problem of the lung imaging is the continuous motion of all anatomical structures induced by blood flow, cardiac and pulsation of vessels, but first of all by respiratory movement. The artifacts caused by the motion degrades the image quality and are usually more prominent in the basal and anterior regions of the thoracic structures. The respiratory motion can be overcome by use of breath-holds techniques. During a single inspiratory or expiratory breath-hold, images of the whole-lung volume can be acquired in about 20 s. However, the breath-hold technique may be demanding for the patients in poor condition. The limited acquisition time to one breath-hold results in lower spatial resolution. The acquisition can be split into few breath-holds using the segmented acquisition techniques (method described in section 2.2.7.1). Additionally to overcome the respiratory motion, a pneumatic belt or cushion placed at the upper abdomen or chest of the patient can be used. The pressure in the belt or cushion is monitored and changes during the respiration. Thus, the MR pulse sequence can be triggered in an appropriate respiratory phase. The images obtained in the end-expiration are characterized by much higher reproducibility. Moreover, due to the lung compression in the expiration the density of the parenchyma increases providing higher MR signal intensity.

An alternative technique, uses a navigator sequence to track the diaphragm movement during respiration with a continuous real-time image acquisition. A segmented pulse sequence can be triggered to acquire part of the k-space in every respiratory cycle. The navigator technique allows performing the lung imaging under free breathing conditions. Unfortunately, the standard navigator sequence has to be stopped during the acquisition of diagnostic images. Recently developed navigator techniques use the acquisition of DC signal (signal corresponding to the central k-space point) as a part of the imaging sequence [Brau and Brittain, 2006; Buehrer et al., 2008]. The variation of the DC signal arises from changes of the diaphragm position and the cardiac movement. The DC signal can be tracked and used for respiratory self-gating. A combination of this acquisition technique with 3D FLASH sequence allowed obtaining images of high spatial resolution and quality [Weick et al., 2009].

Blood flow in the lung is pulsatile and the artifacts associated with the cardiac pulsation can be controlled with either ECG monitoring or peripheral pulse oximetry. Technically the triggering is not problematic in healthy subjects, however, in patients with arrhythmias can present considerable difficulty. The main disadvantage of the triggering techniques is a prolonged acquisition time. Due to the limitations of acquisition time and problems with continuous motion of the thoracic structures, application of fast imaging sequence is required. Rapid imaging sequences like T_2-weighted HASTE, FLASH, balanced steady-state free-precession (bSSFP), or T_1-weighted 3D gradient echo such as volumetric interpolated breath-hold examination (VIBE) helps minimizing the influence of motion. To further decrease the acquisition time, parallel imaging techniques (section 3.4.2) like: generalized autocalibrating partially parallel acquisition (GRAPPA), or sensitivity encoding (SENSE) should be applied. As a result, the image acquisition can be speed

up two- or threefold. Recently, a comprehensive routine MRI protocol for the whole chest including lung parenchymal diseases at 1.5 T magnetic field has beed proposed [Puderbach et al., 2007b]. The protocol consists of fast and optimized imaging sequences: HASTE, VIBE, bSSFP, STIR, 3D FLASH, TREAT/TWIST, covering a wide range of clinical indications for lung imaging. High quality MRI has an important diagnostic value in a lot of pulmonary diseases such as bronchogenic carcinoma, mesothelioma, pulmonary arterial hypertension, acute pulmonary embolism, airway diseases such as cystic fibrosis, interstitial lung disease, and pneumonia. Thus, MRI of the lung may be a valuable alternative to X-ray and CT. Figure 3.2 shows example images obtained using the HASTE, bSSFP and VIBE sequences. Alternatively, non-cartesian k-space sampling using radial trajectory can be applied for lung imaging at 1.5 T [Lohberger et al., 2006]. A combination of this method with the parallel imaging technique and imaging at higher magnetic field strength (3 T) may further improve the visibility of the lung parenchyma.

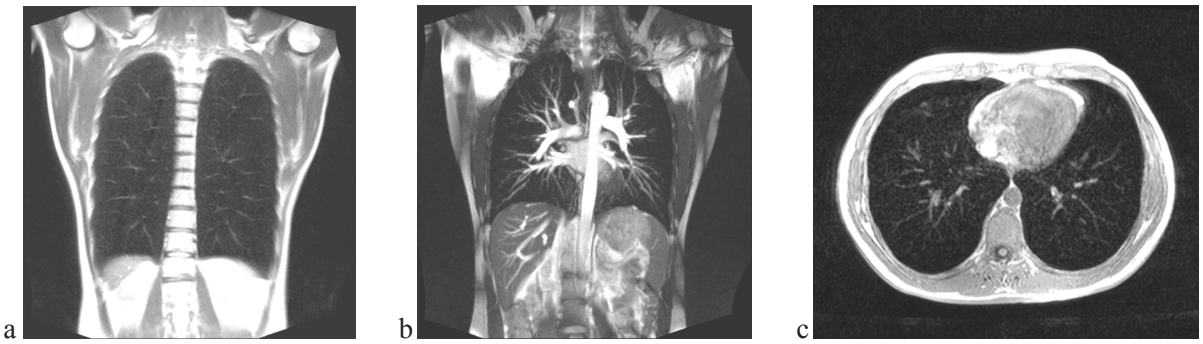

Figure 3.2: *Examples of morphological chest MRI of a healthy volunteer: coronal slice of the 2D HASTE acquisition (a), coronal slice of the 2D bSSFP acquisition with Maximum Intensity Projection to visualize pulmonary vessels (b), transverse slice obtained using the 3D VIBE acquisition (c).*

3.3 Functional lung MRI techniques

Assessment of the pulmonary perfusion and ventilation has an important clinical value as an indicator of lung function. Many pulmonary disorders are characterized by regional ventilation or perfusion abnormalities. The ability to qualitatively and quantitatively evaluate such alterations in pulmonary function can provide insight into how diseases affect the lung function. A great advantage of MRI over the CT is a number of possible techniques to acquire regional information about the lung function. Most of the current methods for evaluation of the lung function are dependent on the application of the intravenous contrast agents or inhalative gaseous tracers.

A review of selected functional lung MRI methods is given in this section. Detailed information about the recent developments in the field of morphological and functional lung imaging can be found in textbooks of Lipson and van Beek [2005], or Kauczor [2009].

3.3.1 Perfusion imaging

Perfusion is a general term often used as a synonym for pulmonary blood flow and describes the delivery of arterial blood to a capillary bed. Most important physiological aspects of the pulmonary perfusion were described in the previous chapter. The measurement of pulmonary blood flow using MRI is difficult, the proof of principle to measure this quantity was presented by von Schulthess et al. [1985]. All the previously discussed issues regarding the lung imaging have to be considered when designing methods to study the pulmonary perfusion. In general, two types of MR acquisitions to obtain information about the regional perfusion have been established. The first technique is known as Dynamic Contrast-Enhanced MRI (DCE-MRI) or bolus tracking, where time-resolved acquisition of multiple lung volumes follows the administration of an intravenous contrast-agent. The second technique called Arterial Spin Labeling (ASL) uses magnetically "tagged" blood as an endogenous contrast-agent.

3.3.1.1 Dynamic Contrast-Enhanced MRI

The basic principle of the Dynamic Contrast-Enhanced MRI (DCE-MRI) is a time-resolved data acquisition following an intravenous bolus injection of a paramagnetic contrast agent, such as gadolinium-diethylenetriaminepentaacetic acid (DTPA). The injected contrast agent circulates through the body and enters into the extravascular space. Application of rapid MR sequences enables to track the peak enhancement of the lung parenchyma, as the contrast passes through the pulmonary circulation (Fig. 3.3). Increase of the contrast agent concentration within a voxel, results in the signal enhancement in that voxel caused by a local decrease in the longitudinal relaxation time T_1. Regions of the perfusion deficit will be identified as areas of poor regional signal intensity enhancement. This technique uses T_1-weighted short TE and TR gradient echo sequences [Hatabu et al., 1996]. Both 2D and 3D pulse sequences can be used for the acquisition, depending on the required spatial and temporal resolution. Current clinical protocols use 3D FLASH and TREAT/TWIST imaging sequences [Puderbach et al., 2007b]. Several post-processing methods of DCE-MRI data are possible. A simple subtraction of the data after and before the contrast bolus arrival can be used to improve the visualization of the perfusion signal. More sophisticated, quantitative evaluation of pulmonary perfusion can be achieved using the indicator dilution principle [Levin et al., 2001; Nikolaou et al., 2004; Fink et al., 2004]. This method allows deriving quantitative values for blood volume, blood flow, and mean transit time from the time intensity curve, defined by the time-resolved series of DCE-MRI images. The major difficulty of quantitative DCE-MRI is the choice of suitable contrast agent dose, in order to ensure a linear relationship between the local contrast agent concentration and the MR signal intensity.

The main advantages of the DCE-MRI technique are: good spatial and temporal resolution and the possibility to demonstrate change of the patterns of perfusion over time within the lungs. However, the method has also some disadvantages. There is a limit in the total amount of contrast material, which can be introduced intravenously to the patient in a given period of time, limiting the number of possible acquisitions. Recently, several studies have shown that

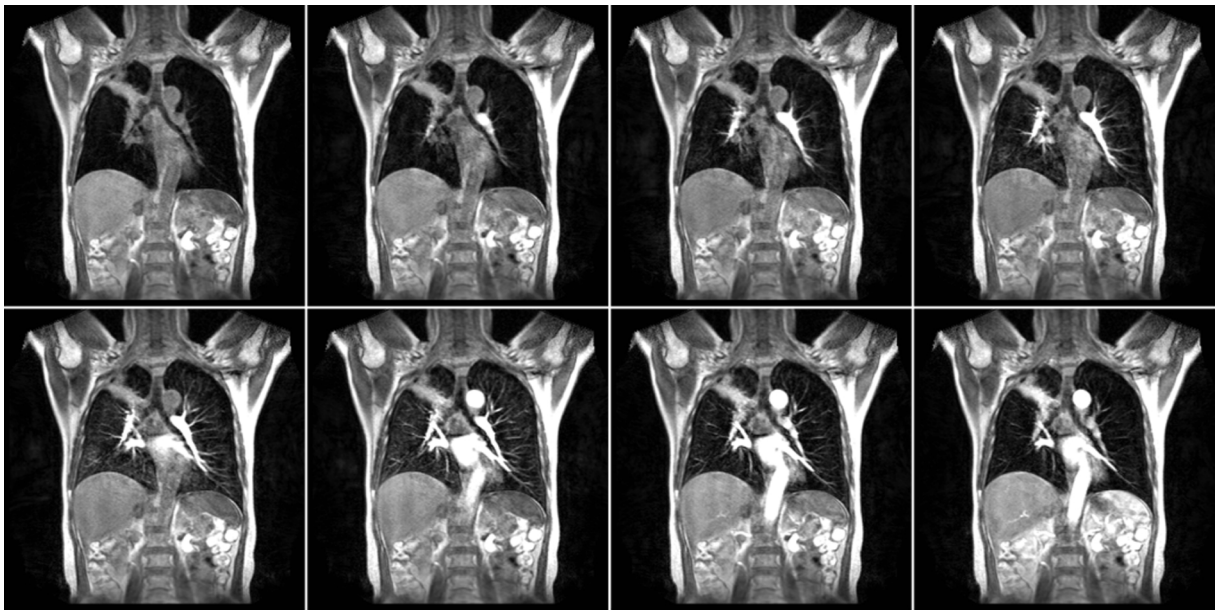

Figure 3.3: *Dynamic Contrast-Enhanced MRI data set of pulmonary perfusion in a patient with bronchial cancer showing eight consecutive images of a single coronal slice. The slice was chosen from a 3D volume acquired every 1.5 s using TWIST sequence. A gradual increase in signal intensity of the lung parenchyma is observed, as the contrast agent reaches the pulmonary circulation. (Images courtesy of C. Hintze, DKFZ, Heidelberg, Germany)*

certain patient groups have a risk of developing the nephrogenic systemic fibrosis (NSF), or severe allergic reactions following the administration of gadolinium based contrast agents [Grobner, 2006].

3.3.1.2 Arterial Spin Labeling

The second major approach for perfusion MRI is the use of Arterial Spin Labeling (ASL) technique, which has been used to quantify regional blood flow in many human organs. A few different imaging methods based on ASL have been developed to assess the pulmonary perfusion [Mai and Berr, 1999; Roberts et al., 1999]. The primary advantage of the ASL technique is the absence of an intravenous contrast agent. The signal intensity of the ASL perfusion image is proportional to the regional blood flow. The ASL techniques use RF excitation pulses to invert the magnetization of protons within the blood circulating in a body, and utilize them as an endogenous contrast agent. The arterial blood labeling can be performed in a continuous or pulsed mode, both techniques allows for quantification of perfusion [Buxton et al., 1998]. Most of the ASL based techniques require two different images: control and tag, to produce a perfusion map. The control image is acquired by application of a selective magnetization inversion pulse to the slice of interest. All spins within a single slice are inverted and after a certain amount of time a control image is acquired. During the chosen time interval TI between the inversion and image

acquisition, fully relaxed spins flows into the slice enhancing the signal intensity. The tag image is acquired by application of a global inversion pulse, as a result all spins within the imaged volume are inverted. After the same time interval TI, the tag image is obtained. The image acquisition is usually performed using HASTE sequence at magnetic field strength of 1.5 T. Study utilizing the bSSFP sequence at low field 0.2 T was also reported [Martirosian et al., 2006]. Subtraction of the tag and control images produces a perfusion image, which represents the arterial blood delivered to the imaged slice. This technique was used for absolute quantification of the regional pulmonary blood flow [Bolar et al., 2006].

The use of two images acquired often in separate breath-holds increases the acquisition time and may lead to misregistration artifacts. Thus, a retrospectively gated method was proposed to overcome this difficulty [Wiedemair et al., 2007]. Alternatively, two different approaches: double inversion recovery (DIR) and the spin echo entrapped perfusion image (SEEPAGE) have beed proposed. The most important feature of these techniques is the requirement of only one single acquisition to obtain the information about the regional perfusion [Pracht et al., 2006; Fischer et al., 2008]. Since no administration of the intravenous contrast agent is needed, the acquisition can be repeated many times. The disadvantage of the ASL techniques is the lack of perfusion dynamics information, which is offered by the DCE-MRI.

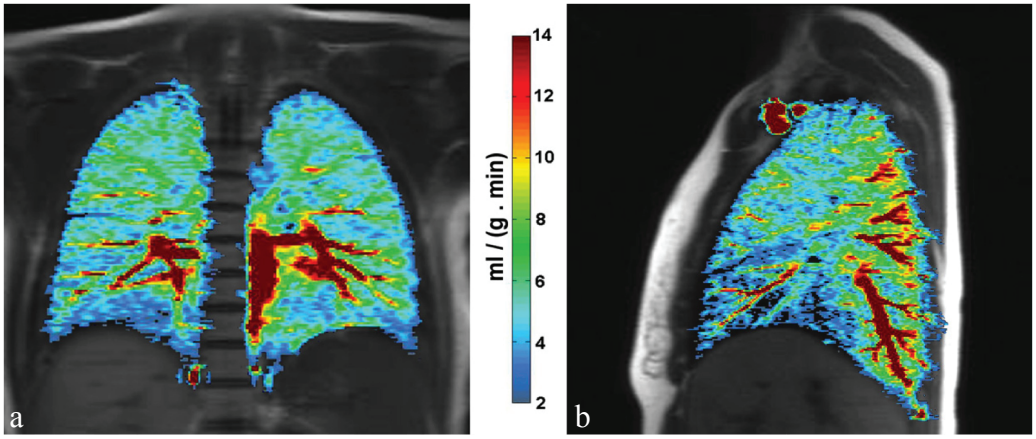

Figure 3.4: *Quantitative Arterial Spin Labeling imaging of the pulmonary perfusion showing coronal (a) and sagittal (b) images obtained from a healthy volunteer [Wiedemair et al., 2007].*

3.3.2 Ventilation imaging

Ventilation is a process providing to the oxygen delivery and exertion of the carbon dioxide by the lungs. Several different MRI based techniques have been developed for the measurement of regional ventilation. Hyperpolarized gas MRI with ^{3}He and ^{129}Xe offers the best quality of ventilation images at the cost of high technical demand. Other imaging techniques utilize paramagnetic contrast agents, which have the potential to enhance the MR signal from the lung parenchyma. The MR based techniques include MRI of aerosolized contrast agents such as gadolinium-chalets and Oxygen-Enhanced MRI as a measure of regional lung ventilation.

Alternatively, non-contrast-enhanced MRI techniques measuring the regional variation in the lung parenchyma density have been proposed.

3.3.2.1 Hyperpolarized Gas MRI

Application of hyperpolarized gaseous tracers in MRI has been explored since the middle of the 1990s. Hyperpolarized ^{3}He and ^{129}Xe MRI offers high quality images of lung ventilation with an excellent spatial and temporal resolution.

First images of hyperpolarized ^{3}He gas in human lungs were demonstrated by Middleton et al. [1995]; Ebert et al. [1996] and Bachert et al. [1996]. Since that time, polarization techniques and imaging methodology have developed, and currently provide supreme images of regional lung ventilation, as well as a wide range of functional information. This technique found potential in diagnostics of various human lung diseases including COPD [Kauczor et al., 1996; Swift et al., 2005; Stavngaard et al., 2005], asthma [Altes et al., 2001], cystic fibrosis [Donnelly et al., 1999; Mentore et al., 2005], or lung cancer [Gast et al., 2003]. ^{3}He gas is a radio-stable isotope of the inert gas helium with the spin 1/2 coupled with high gyromagnetic ratio and very low natural abundance (see Tab. 2.1). Helium is highly diffusive, thus, can be used to measure the apparent diffusion coefficient and to probe alveolar length scales in the lungs. This feature was used in studies of asthma and COPD patients [Wild et al., 2007; Wang et al., 2008].

Polarization of ^{3}He can be performed using two different techniques: spin exchange optical pumping (SEOP), or meta-stable spin exchange optical pumping (MEOP) (see section 2.1.3). The polarized gas can be stored for a longer time (days) [Wild et al., 2002]. The hyperpolarized ^{3}He is delivered to the subject for inhalation in a form of a mixture with a larger volume of nitrogen or pure. After the administration of the hyperpolarized ^{3}He to a subject, interaction with a paramagnetic oxygen reduces to a time of about 20 s which can be used for imaging. The imaging protocols use short sequences constrained by subject's breath-holding capacity and limited polarization time including: short spoiled gradient echo sequence (SPGR), bSSFP [Wild et al., 2006], non-Cartesian sequences [Wild et al., 2003], or pulsed gradient spin echo technique (PGSE) for ADC measurements [Mugler et al., 1998].

The first studies with hyperpolarized ^{129}Xe were performed in the last decade [Albert et al., 1994; Mugler et al., 1997]. Unlike ^{3}He, xenon has wide availability and increased natural abundance. Polarization of ^{129}Xe is obtained using the spin-exchange optical pumping technique. The polarization process of xenon is more complex than of helium, due to the smaller spin exchange cross-section and shorter T_1 relaxation time. However, recently polarization up to 50% of xenon at a high production rate has become possible [Ruset et al., 2006; Hersman et al., 2008]. The next difficulty associated with the xenon MRI is the fact that the gyromagnetic ratio of ^{129}Xe is three times smaller than ^{3}He and therefore, the NMR sensitivity is lower. Xenon is characterized by a high solubility in water and exhibits a large chemical shift spectrum.

Hyperpolarized xenon can be delivered directly through the respiratory system in the form of inhlated gas. Alternatively, it can be incorporated in an appropriate carrier agent and injected

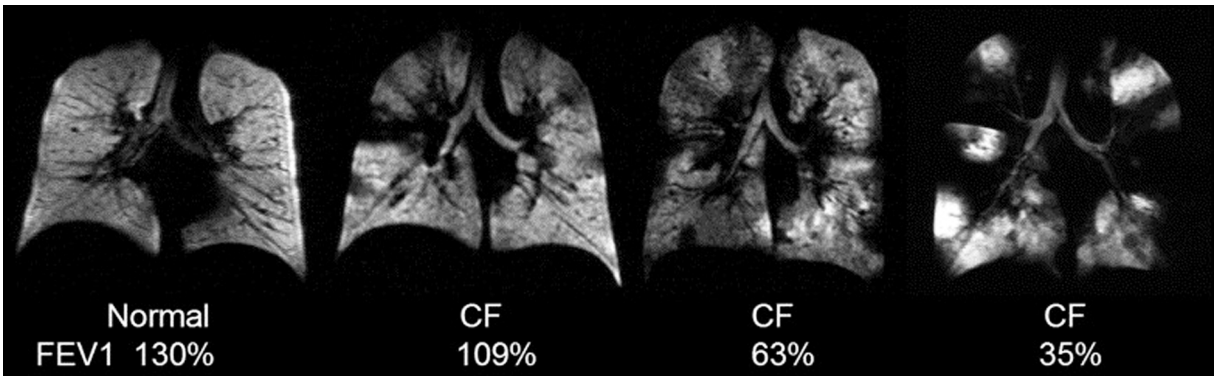

Figure 3.5: *Hyperpolarized* ^{3}He *MRI of the lung of a healthy volunteer (left) associated with high value of forced expiration volume in one second (FEV1), and cystic fibrosis patients with lower FEV1 values [Mentore et al., 2005].*

intravenously. Inhaled ^{129}Xe follows the same pathway as oxygen. This fact can be used for study of the alveolar/capillary membrane, and provides additional information regarding the diffusion capacity of the lung [Ruppert et al., 2004; Patz et al., 2007]. High quality images of obtained using the hyperpolarized ^{129}Xe in a healthy volunteer are shown in figure 3.6. One of the main drawbacks of ^{129}Xe are its anesthetic properties, thus the concentration of the xenon in the inhaled gas mixture has to be kept on a safe level [Latchaw et al., 1987].

Despite a significant scientific potential, hyperpolarized lung MRI techniques are difficult to apply in the clinical routine because of increased cost of additional equipment, e.g. gas polarizers, more complicated imaging protocol and measurement setup.

3.3.2.2 Oxygen-Enhanced MRI

Utilization of the inhaled molecular oxygen as a contrast agent for proton MRI of the lung was first suggested by Edelman et al. [1996]. Molecular oxygen has two unpaired electrons, which results in a weak paramagnetic properties (magnetic moment of 2.8 Bohr magnetons).
The contrast mechanism of molecular oxygen is similar to that of gadolinium based contrast agents. The longitudinal relaxation time T_1 in the lung tissue is shortened depending on the oxygen concentration in the inhaled air. After inhalation of oxygen, most of the oxygen molecules are bound to hemoglobin in the pulmonary capillary bed, smaller fraction can be enclosed within other tissues e.g. blood vessels, alveolar cells, connective tissue. The hemoglobin bound oxygen is incorporated inside the erythrocytes and for this reason the tissue water protons do not participate in a spin-lattice interaction, which causes T_1 relaxation [Brooks and Di Chiro, 1987]. It was found that the partial oxygen pressure is linearly correlated with the lung parenchyma relaxivity [Ohno et al., 2001]. The difference in the lung parenchyma signal intensity between images acquired when the pure oxygen and room air was inhaled can be visualized directly by a simple image subtraction, or relative difference after pixel-wise normalization to the room air

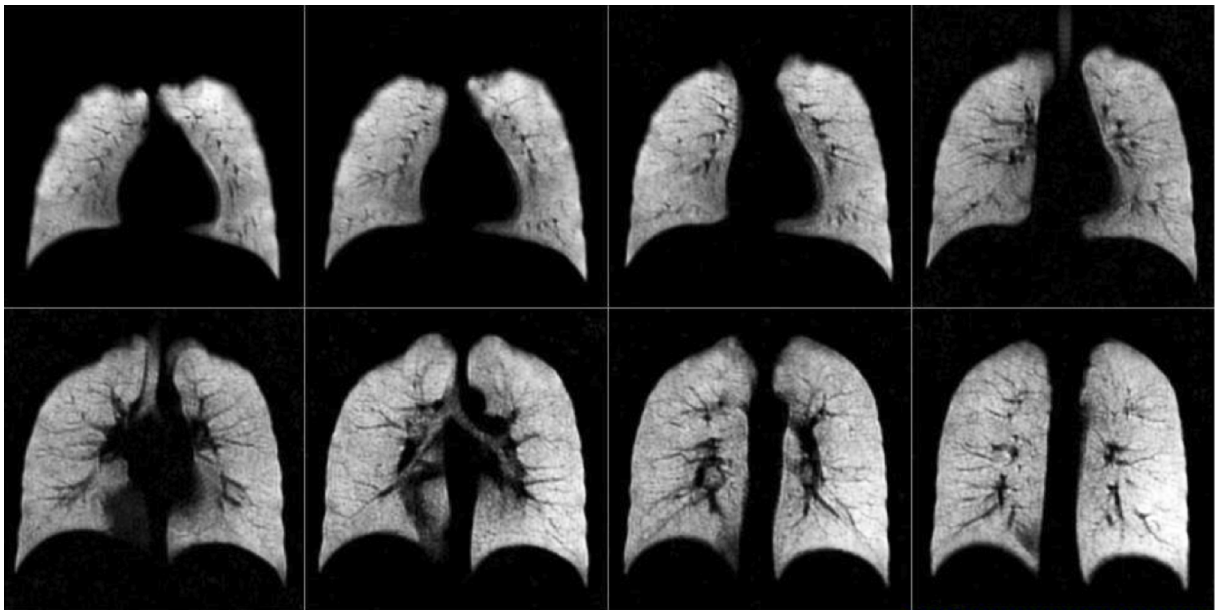

Figure 3.6: *Hyperpolarized* ^{129}Xe *MRI of the lung obtained in a healthy volunteer using a 2D GRE pulse sequence. The high quality images show homogeneous distribution of signal intensity within the pulmonary parenchyma. (Images courtesy of J. Mugler, UVA, Charlottesville, Virginia, USA)*

signal. Figure 3.7 shows subtraction images acquired using the Oxygen-Enhanced MRI. Alternatively, the acquisition can be performed for different concentrations of oxygen to determine the so-called oxygen transfer function, which describes the change of T_1 in the lung parenchyma depending on the local oxygen concentration [Jakob et al., 2004].

In addition to the T_1-based Oxygen-Enhanced MRI, it is possible to measure change in the effective transverse relaxation time T_2^* [Pracht et al., 2005]. However, this approach is very difficult since the measured change in the relaxation time is minimal and the T_2^* relaxation time of the lung tissue is extremely short.

Information provided by the Oxygen-Enhanced MRI should be regarded as a combination of ventilation, diffusion, and perfusion. Only in lung areas sufficiently ventilated with oxygen, a reduction of T_1 relaxation time can be achieved. Furthermore, diffusion, i.e. transition of the oxygen from the alveoli through the alveolar wall into the lung capillaries, must take place. Moreover, since most of the inhaled oxygen is solved in the capillary blood, lung perfusion is required to observe the T_1 change. The impact of the inhalation of the pure oxygen on the pulmonary perfusion was studied by Ley et al. [2007].

The pulse sequences used in Oxygen-Enhanced MRI usually utilize an inversion recovery technique to provide T_1 weighting. Application of fast imaging sequences e.g. RARE, HASTE, bSSFP, snapshot-FLASH reduces the effect of cardiac and respiratory motion artifacts [Edelman et al., 1996; Chen et al., 1998; Ohno et al., 2001; Mueller et al., 2001; Jakob et al., 2001; Mai et al., 2003]. Influence of the blood inflow and cardiac pulsation on the signal intensity and

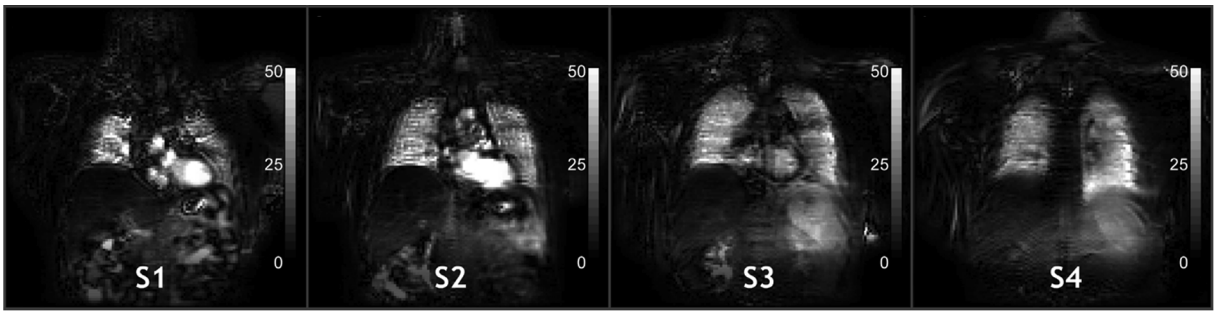

Figure 3.7: *Figure shows four images acquired from different coronal slices using the Oxygen-Enhanced MRI technique. The images were produced by subtraction of the data acquired during oxygen, and room air ventilation. (Images courtesy of F. Molinari, Catholic University of Rome, Rome, Italy)*

image quality can be further reduced by using ECG triggering. Since signal acquisition is performed during different breath-hold periods, application of combined respiratory and ECG triggering is beneficial [Molinari et al., 2007]. Alternatively, image registration can be used to compensate for thorax motion [Naish et al., 2005].

Oxygen is industrially available and safe to use. Therefore, the Oxygen-Enhanced MRI technique is easy to implement and inexpensive. The drawback of this technique is the long acquisition time required to cover the whole chest volume in a reasonable time.

3.3.2.3 Aerolized gadolinium-based contrast agents

The feasibility of ventilation MRI using aerosolized gadopentetate-dimeglumine as a contrast agent was proposed by [Montgomery et al., 1987; Berthezene et al., 1992]. The method utilized T_1-weighted sequences to observe the signal enhancement of extravascular water in the lungs. Most of these studies were performed in animals, while the first application in humans was described by [Haage et al., 2003, 2005]. However, this approach is not yet available in clinical settings, because the application of gadolinium-chelates has not been approved for use in humans in the form of an inhaled aerosol. A long inhalation time (more than 10 minutes) to obtain sufficient signal enhancement is an additional limitation of this technique.

3.3.2.4 Non-contrast-enhanced lung imaging

The MR signal intensity of the lung parenchyma obtained by using the conventional proton based MRI is very low. However, it was observed that signal intensity changes significantly with lung volume [Bankier et al., 2004]. This fact can be employed to assess the ventilation information directly from proton based images. Several methods to obtain this information were recently proposed [Rupprecht et al., 2003; Topf et al., 2004, 2005; Zapke et al., 2006; Marcus et al., 2007]. Most of these methods use HASTE or bSSFP dynamic lung image acquisitions at a low

magnetic field strength of 0.2 T due to the reduced susceptibility effects in the lung parenchyma. Subtraction of the images obtained in the respiratory expiration, and inspiration, provides the information about the regional parenchyma density variation. As respiration causes a significant deformation of the lung tissue, in the work of Zapke et al. [2006] a non-rigid registration algorithm was applied to correct for the respiratory movement.

Information about the regional ventilation can also be retrieved from monitoring of the lung parenchyma displacement. Different imaging method using SPAMM tagging [Chen et al., 2001; Napadow et al., 2001; Voorhees et al., 2005], or direct tracking of the lung structures [Gee et al., 2003; Sundaram and Gee, 2005] have been proposed.

A novel approach presented in this work uses sets of 2D dynamic lung images acquired with high temporal resolution to spectrally retrieve the regional ventilation, as well as perfusion information. The method was implemented at low magnetic field strength of 0.35 T [Deimling et al., 2008], and higher of 1.5 T [Bauman et al., 2009]. This technique uses elastic non-rigid image registration to compensate for the respiratory motion.

3.3.3 Nuclear medicine techniques for functional lung imaging

Nuclear medicine techniques are routinely used in a clinical setting to visualize pulmonary perfusion and ventilation. Although these methods are noninvasive, and considered as the gold standard, they are limited by poor spatial and temporal resolution. Furthermore, the nuclear medicine techniques carry a risk associated with an exposure to radiation. Scintigraphy of ventilation can be carried out by utilization of radioactive gases, such as: ^{127}Xe, ^{133}Xe, ^{81,m}Kr, or ultra fine radio-labeled aerosols: ^{99,m}Tc, ^{99,m}Tc-Technegas and ^{99,m}Tc-DTPA [White et al., 1991; Senden et al., 1997]. In addition to ventilation examinations, also lung perfusion can be studied. The most widely used radiotracer to study the pulmonary blood flow is ^{99,m}Tc macro aggregated albumin. Single photon emission computed tomography (SPECT) offers cross-sectional images of improved contrast resolution being superior to planar images provided by the nuclear scintigraphy [Petersson et al., 2007; Roach et al., 2008]. More sophisticated and technically very demanding nuclear medicine methods for functional lung imaging employ positron emission tomography (PET), which utilizes short half-live isotopes ^{13}N, ^{15}O, ^{19}Ne, or ^{11}C [Vidal Melo et al., 2003; Richard et al., 2005].

3.4 Methods for time-resolved MRI of the lung

This section provides a description of the k-space sampling methods used to produce time-resolved MR images of the lung. Image acquisition was performed using a 2D balanced steady-state free-precession (bSSFP) sequence combined with the parallel imaging technique of generalized autocalibrating partially parallel acquisitions (GRAPPA).

3.4.1 Balanced steady-state free-precession (bSSFP) sequence

The technique of balanced steady-state free-precession (bSSFP) pulse sequences is based on gradient echo sequences with short repetition time as described in section 2.2.6.2, and was first proposed in a similar form by Oppelt et al. [1986]. In contrast to the spoiled gradient echo techniques, where only a steady-state of the longitudinal magnetization is obtained, the bSSFP sequences include transverse coherences from overlapping multi-order spin echoes and stimulated echoes. This is accomplished, in case of the bSSFP sequence, by refocusing all imaging gradients. The following condition for the m_0 and m_1 gradient moments in a time interval between n-th and $(n+1)$-th RF excitation must be fulfilled:

$$\begin{aligned} m_{0,i} &= \int_{nTR}^{(n+1)TR} G_i(\tau)d\tau = 0 \quad \text{for} \quad i = \{x, y, z\} \\ m_{1,i} &= \int_{nTR}^{(n+1)TR} G_i(\tau)\tau d\tau = 0 \quad \text{for} \quad i = \{x, z\} \end{aligned} \tag{3.1}$$

Figure 3.8 shows a pulse sequence diagram of bSSFP sequence and its trajectory in the k-space.

A propagation of the Bloch equations was used to simulate the evolution of the magnetization for the bSSFP sequence similar to the methods presented by Hargreaves et al. [2001] and Leupold [2005]. The initial magnetization vector is defined as:

$$\vec{M}_0 = [0, 0, M_0]^T \tag{3.2}$$

The rotation matrix R represents the nutation of spin isochromats:

$$R(\alpha, \phi) = \begin{bmatrix} \cos^2(\phi) + \cos(\alpha)\sin^2(\phi) & \sin^2(\frac{\alpha}{2})\sin(2\phi) & -\sin(\alpha)\sin(\phi) \\ \sin^2(\frac{\alpha}{2})\sin(2\phi) & \sin^2(\phi) + \cos(\alpha)\cos^2(\phi) & \sin(\alpha)\sin(\phi) \\ \sin(\alpha)\sin(\phi) & -\sin(\alpha)\sin(\phi) & \cos(\alpha) \end{bmatrix} \tag{3.3}$$

where α - flip angle, ϕ - phase angle of the RF excitation pulse, which defines the direction of the $\vec{B}_1$ magnetic field emission (Fig. 3.9). The influence of the longitudinal and transverse relaxation, $E_1(\tau) = \exp(-\tau/T_1)$ and $E_2(\tau) = \exp(-\tau/T_2)$, respectively, as well as a dephasing angle $\theta(\tau) = 2\pi\Delta f\tau$ (where $\Delta f = \gamma\Delta B$ and ΔB - the field inhomogeneities) between excitation pulses over the time τ is represented by a rotation matrix $C(\tau)$:

$$C(\tau) = \begin{bmatrix} E_2(\tau)\cos(\theta(\tau)) & E_2(\tau)\sin(\theta(\tau)) & 0 \\ -E_2(\tau)\sin(\theta(\tau)) & E_2(\tau)\cos(\theta(\tau)) & 0 \\ 0 & 0 & E_1(\tau) \end{bmatrix} \tag{3.4}$$

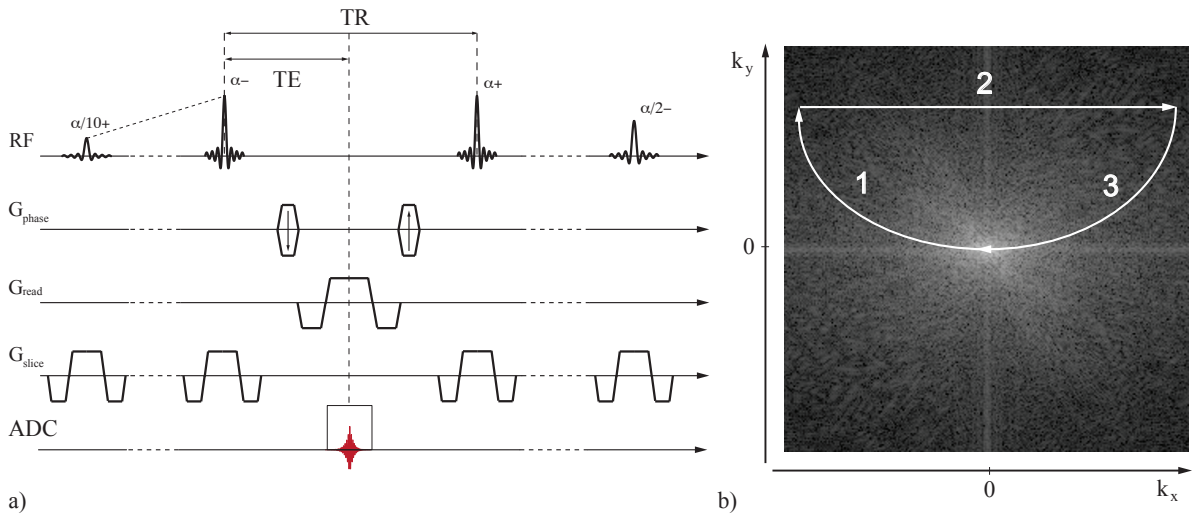

Figure 3.8: *Diagram of a bSSFP pulse sequence (a) and its trajectory in the k-space (b). After an RF excitation, the phase and frequency encoding gradients are switched on. This is depicted as the path (1) from the center of the k-space to its peripheries. During a signal acquisition, the trajectory follows the path (2). Finally, the phase and frequency encoding gradients are switched on to fulfill the Eq. 3.1, and the trajectory returns to the k-space center (3).*

and a vector $D(\tau)$:

$$\vec{D}(\tau) = [I - C(\tau)]\,\vec{M}_0 \tag{3.5}$$

where $I = \mathrm{diag}(1, 1, 1)$ is the identity matrix. The resulting magnetization vector $\vec{M}$ after the i-th RF excitation is given by:

$$\vec{M}_i(0) = R(\alpha, \phi)\vec{M}_{i-1}(TR - TE) \tag{3.6}$$

at the echo time:

$$\vec{M}_i(TE) = \vec{D}(TE)\vec{M}_i(0) + [I - \vec{D}(TE)]\vec{M}_0 \tag{3.7}$$

and before the next RF excitation:

$$\vec{M}_i(TR - TE) = \vec{D}(TR - TE)\vec{M}_i(TE) + [I - \vec{D}(TR - TE)]\vec{M}_0 \tag{3.8}$$

After a certain number of RF pulse excitations, the magnetization vector achieves the so-called steady-state. In this case, the following condition must be fulfilled:

$$\vec{M}_i(0) = \vec{M}_{i-1}(0) \tag{3.9}$$

The components of the magnetization vector in steady-state can be determined by solving the

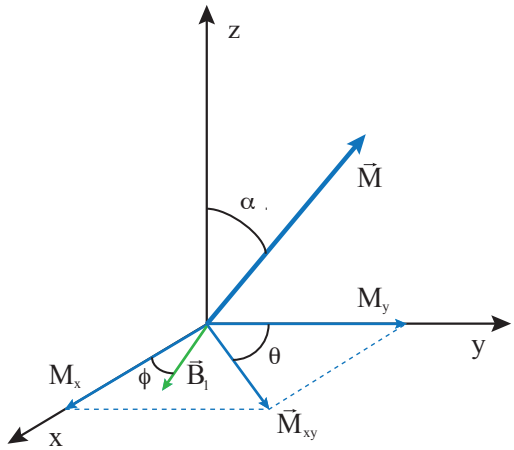

Figure 3.9: *Coordinate system showing the magnetization vector $\vec{M}$, transverse magnetization $\vec{M}_{xy}$, its components M_x, M_y, flip angle α, dephasing angle θ, and phase angle of the RF excitation pulse ϕ.*

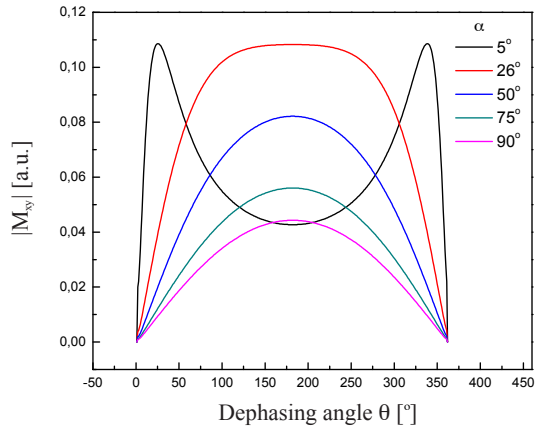

Figure 3.10: *Dependence of the flip angle α on the Frequency Response Function for $T_1 =$ 1100 ms and $T_2 = 50$ ms.*

system of equations defined by Eqs. 3.6, 3.7, 3.9, and are given by:

$$\begin{aligned} M_x(0) &= M_0[1 - E_1(TR)]\frac{E_2(TR)\sin(\alpha)\sin(\theta)}{d} \\ M_y(0) &= M_0[1 - E_1(TR)]\frac{\sin(\alpha)[1 - E_2(TR)\cos(\theta)]}{d} \\ M_z(0) &= M_0[1 - E_1(TR)]\frac{\{E_2(TR)[E_2(TR) - \cos(\theta)] + [1 - E_2(TR)\cos(\theta)]\cos(\alpha)\}}{d} \end{aligned} \tag{3.10}$$

where:

$$d = (1 - E_1(TR)\cos(\alpha))(1 - E_2(TR))\cos(\theta)) - E_2(TR)(E_1(TR) - \cos(\alpha))(E_2(TR) - \cos(\theta)) \tag{3.11}$$

and $\theta = 2\pi\Delta f TR$ is the phase accumulated during a single repetition time TR.

The bSSFP sequence used in this work offers high signal intensity for short repetition times and high flip angles, but is very sensitive to $\vec{B}_0$ field inhomogeneities and susceptibility differences. It therefore requires a static magnetic field of high homogeneity. The dependence of the dephasing angle θ on the transverse magnetization $|M_{xy}(\theta)|$ is shown for the Frequency Response Function (FRF). The maxima and minima of the FRF occur with 180° periods at frequency offsets:

$$\Delta f = \frac{(1 + 2n)}{2 \cdot TR} \quad \text{for} \quad n = \{0, 1, 2, \dots\} \quad \text{where:} \quad f = \frac{\theta}{360° \cdot TR} \tag{3.12}$$

The minima of the FRF are responsible for banding artifacts and cause a narrow signal intensity drop. Figure 3.10 shows the FRF in steady-state and the influence of the flip angle α on its shape.

For the bSSFP sequence with $\theta = 180°$, and for $TR \ll T_1, T_2$ the signal intensity can be approximated as:

$$M_y(0) \simeq \frac{M_0 \sin(\alpha)}{1 + \cos(\alpha) + (1 - \cos(\alpha))(T_1/T_2)} \qquad (3.13)$$
$$M_x(0) \simeq 0$$

Maximal signal intensity is obtained for the flip angle:

$$\alpha_{opt} = \frac{T_1/T_2 - 1}{T_1/T_2 + 1} \qquad (3.14)$$

Thus, the maximal signal intensity for α_{opt} is:

$$M_y(0) \simeq \sqrt{\frac{T_2}{T_1}} \frac{M_0}{2} \qquad (3.15)$$

providing the contrast weighted by a mixture of T_1 and T_2 relaxation times.

In practice, the FRF can be shifted in such a way that its maximum appears for the dephasing angle $\theta = 0°$ (on-resonance condition) and the optimal flip angle α_{opt}, which is obtained incrementing the phase ϕ by 180° for every RF pulse excitation.

In the bSSFP sequence used in this work, an initial train of 10 preparation pulses with linearly increasing flip angles from $\alpha/10$ to α was used to achieve a smoother stabilization of the magnetization vector [Deshpande et al., 2003] (Fig. 3.11). The order of the phase encoding was centric. An $\alpha/2$ RF pulse was used to restore the residual magnetization into the longitudinal magnetization. Since the train of RF pulses is very short for a single image acquisition, all the data are measured in the transient response of the magnetization. To further restore the longitudinal magnetization, a time interval was introduced between each single image acquisition (Fig. 3.12).

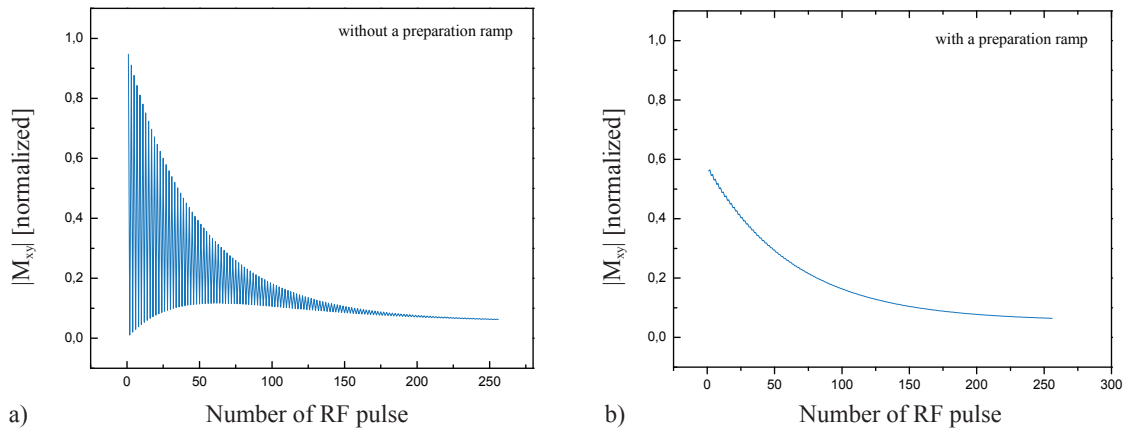

Figure 3.11: *Diagram (a) shows oscillations of the magnitude of the transverse magnetization for a bSSFP sequence without a preparation ramp. In the diagram (b) a smooth stabilization of the magnetization is achieved using a train of RF pulses with linearly increasing flip angles from $\alpha/10$ to α. Notice that the steady-state of the magnetization is achieved after a large number of RF excitation.*

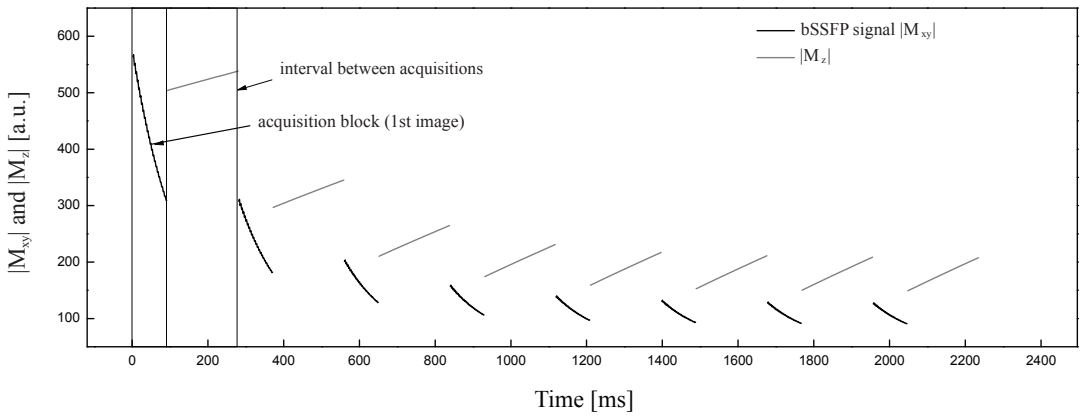

Figure 3.12: *Time course of simulated transverse magnetization $|M_{xy}|$ for a set of eight images. Every image is acquired using 48 RF excitation pulses with $\alpha = 75°$, $TR = 1.9$ ms, $TE = 0.8$ ms, and the delay between acquisitions $TW = 188$ ms. The relaxation times were set to: $T_1 = 1100$ ms and $T_2 = 50$ ms. Since the steady-state is not achieved during the single image acquisition, the available signal intensity decays by acquisition time for images in the time-resolved data set. The longitudinal magnetization $|M_z|$ recovers during the intervals inserted between each image acquisition.*

3.4.2 Parallel imaging techniques

Parallel MR imaging techniques (pMRI) exploit the difference in sensitivities between individual coil elements in a receive array to inherit additional information, which is used to partially replace time-consuming spatial encoding. The number of phase encoding steps can be reduced by a reduction factor R which, however, lowers the signal-to-noise ratio (SNR) by a factor of $\sqrt{R}$. The application of pMRI results in an accelerated image acquisition, while maintaining full spatial resolution and image contrast. It can be used to improve temporal resolution of dynamic acquisitions or minimize the influence of motion on image quality. In current clinical routine, reduction factors of 2 to 3 are often applied for the 2D imaging sequences to accelerate measurements. For 3D imaging sequences, a reduction factor of 5 to 8 can be used, because the acceleration is performed in two phase-encoding directions. The maximally possible reduction factor depends on the number of independent receiver channels.

pMRI algorithms can be dived into two main groups. The first group of algorithms performs the reconstruction in the image domain: sensitivity encoding (SENSE) [Pruessmann et al., 1999], partially parallel imaging with localized sensitivity (PILS) [Griswold et al., 2000], while the second group reconstructs images in the k-space: simultaneous acquisition of spatial harmonics (SMASH) [Sodickson and Manning, 1997], generalized autocalibrating partially parallel acquisitions (GRAPPA) [Griswold et al., 2002]. All mentioned pMRI techniques derive the coil sensitivity information to eliminate the undersampling effect by means of a prescan, or a few additional k-space lines acquired prior to an image acquisition. A technical overview of all modern pMRI reconstruction methods is given in the review by Blaimer et al. [2004].

3.5 Non-rigid image registration

Image registration is the process of finding a spatial transformation that maps one image into another by optimizing a certain criterion. Many registration techniques have been developed for medical imaging in order to recover geometric distortions and misalignments between image data sets. There are two main categories of registration techniques. The first category relies on the assumption that images were acquired using the same modality, thus present a very similar intensity range. These mono-modal registration algorithms perform geometric transformations, which minimize the sum of differences, or squared differences between intensity values of images being processed. The second category of registration algorithms copies with images, which have different intensity maps, for instance, images acquired using various modalities e.g. fusion of MRI or PET images, or matching of MRI images acquired with different contrasts. In this case, signal intensities within the images can no longer be compared by their difference. These multi-modal registration methods use statistical similarity measures, such as cross-correlation, the correlation ratio [Roche et al., 1998] or mutual information [Wells III et al., 1996].

Furthermore, the registration algorithms can be classified according to the geometric transformation models they use. The first class of algorithms utilizes linear transformations, which include translation, rotation, scaling, shearing, and other affine transforms. Linear transformations can model global geometric differences between images. The second class of methods uses elastic, or non-rigid transformations, and therefore, allows for local warp of the target image for alignment with the reference image. The non-rigid transformations include e.g. thin-plate or surface splines, physical models of viscous fluids, and large deformation models (diffeomorphisms). A detailed description of current image registration algorithms can be found in the textbook of Ardeshir Goshtasby [2005].

The shape of the lungs changes significantly during the respiratory cycle and involves elastic deformations. In order to analyze corresponding regions of interest (ROIs) on MR lung images acquired during free breathing, the application of an image registration algorithm is mandatory to correct for the motion of the lung margins and pulmonary structures. In this work, a non-rigid image registration algorithm proposed by Chefd'hotel et al. [2001, 2002] has been applied to compensate for the respiratory motion. Motion-correction is achieved by aligning, via pairwise non-rigid registration, a reference image to the remaining images in the time series. For each pair of images, the algorithm maximizes the statistical similarity criterion (local cross-correlation) between the reference and the (uncorrected) target image. Calculation of the corresponding gradients is used to drive a flow of diffeomorphism, and allows for large deformations. The flow is introduced through a template propagation method, by composition of small displacements with a regularization step performed by low-pass filtering (gaussian filter). Application of the fast recursive filtering techniques increases robustness and computational efficiency of the method. The reference image was chosen halfway through the inspiration or expiration phase. The registration algorithm applies only a geometric transformation to the data, preserving local signal intensities within images, which allows for further analysis of local signal change across a time-resolved MR set.

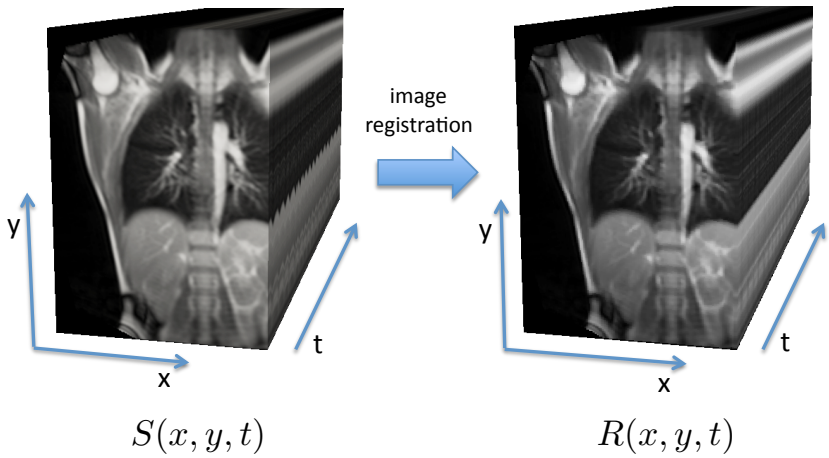

Figure 3.13: *Registration of time-resolved MR data sets acquired using the 2D+t SSFP sequence.*

In order to register time-resolved sets of 2D bSSFP images, the two-dimensional version of the algorithm was used. However, the algorithm can be generalized and applied for 1D signal, 3D volume matching, or any scalar signals defined on a bounded domain $\Omega \subset \mathbb{R}^n$. Figure 3.13 shows the idea of image registration for time-resolved data sets. A 2D+t set $S(x, y, t)$ is transformed using the registration algorithm and a new 2D+t set $R(x, y, t)$ is produced. The mathematical description of the registration algorithm is given in the next sections.

3.5.1 General formulation of a registration problem

Consider the reference and the template images, respectively represented by two functions:

$$f : \Omega \subset \mathbb{R}^2 \to [0, 1] \quad \text{and} \quad g : \Omega \subset \mathbb{R}^2 \to [0, 1] \tag{3.16}$$

The deformation is modeled by a mapping $u : \Omega \subset \mathbb{R}^2 \to \Omega$. It is assumed that u belongs to a Hilbert space $\mathcal{H}$.

The registration problem is defined as the minimization of a cost functional:

$$\mathcal{I}[u] = \mathcal{S}[u] + \alpha \mathcal{R}[u] \tag{3.17}$$

where $\mathcal{S}$ is a measure of similarity of images f and g for a given displacement u, $\mathcal{R}$ is a regularizing term imposing smoothness of the transformation. The parameter α controls the influence of $\mathcal{S}$ and $\mathcal{R}$. Using the classical variational calculus, the Gâteaux variation of the $\mathcal{I}$ functional is defined as:

$$d\mathcal{I}[u, h] = \lim_{\epsilon \to 0} \frac{\mathcal{I}[u + \epsilon h] - \mathcal{I}[u]}{\epsilon} = \left. \frac{\partial \mathcal{I}[u + \epsilon h]}{\partial \epsilon} \right|_{\epsilon = 0} \tag{3.18}$$

where $h \in \mathcal{H}$. It can be shown that if $\mathcal{I}$ has a local extremum u in $\mathcal{H}$, its first variation at u must vanish:

$$\forall\ h \in \mathcal{H},\ d\mathcal{I}[u, h] = 0 \tag{3.19}$$

The above equation can be formulated using the definition of the gradient of functional $\mathcal{I}$:

$$d\mathcal{I}[u,h] = \langle \nabla_u \mathcal{I}, h \rangle_{\mathcal{H}} \tag{3.20}$$

The previous condition can be expressed in the form of Euler-Lagrange equation:

$$\nabla_u \mathcal{I} = 0 \tag{3.21}$$

The solution of the problem is based on a gradient descent strategy. The classical gradient flow is expressed as:

$$\begin{cases} \frac{du}{dt} & = -\nabla_u \mathcal{I} \\ u(0,\,\cdot\,) & = u_0 \end{cases} \tag{3.22}$$

where u_0 is the initial field following the infinitesimal gradient of the functional $\mathcal{I}$.

3.5.2 Statistical similarity criterion

In the algorithm proposed by Chefd'hotel the unknown is considered to be the transformation ϕ, unlike the displacement field u as in the classical gradient flow equation 3.22. The diffeomorphism ϕ can simply be decomposed as $\phi = I + u$, where u is the displacement field and $I = \mathrm{diag}(1, 1, \ldots, 1)$ is the identity matrix of $n \times n$ size. The diffeomorphism acts on a template image g by composition to form a new image $g \circ \phi$.

If the intensity values of the images being registered are not expected to be identical but a linear relationship between them can be assumed, it is possible to register these images using the cross-correlation similarity measure. The similarity criterion is based upon an estimate of the joint probability of the grey levels of f and $g \circ \phi$, which are modeled by two random variables X and Y_ϕ. The cross-correlation of X and Y_ϕ is defined from the corresponding joint probability denoted $p_\phi(i,j)$, and estimated by the Parzen window method [Parzen, 1962]. The function $p_\phi(i,j) : [0,1] \times [0,1] \to \mathbb{R}$ is defined by:

$$p_\phi(i,j) = \frac{1}{|\Omega|} \int_\Omega G_\beta(f(x) - i, (g \circ \phi)(x) - j) dx \tag{3.23}$$

where G_β is a Gaussian window with variance $\beta > 0$. One can construct a space dependent version of this estimator, valid for a region around each point x_0 and given by:

$$p_\phi(i,j,x_0) = \frac{1}{\mathcal{G}(x_0)} \int_\Omega G_\beta(f(x) - i, (g \circ \phi)(x) - j) G_\gamma(x - x_0) dx \tag{3.24}$$

where $\mathcal{G}(x_0) = \int_\Omega G_\gamma(x - x_0) dx$ and γ is the variance of the Gaussian weighting function G_γ.

Two classes of the similarity measure $\mathcal{S}(\phi)$ expressed in terms of p_ϕ can be constructed, a global one using Eq. 3.23 and a local one using Eq. 3.24. The infinitesimal gradient of the local similarity criterion has a generic form:

$$\nabla \mathcal{S}(\phi) = (G_\gamma * L^l_{CC,\phi})\,(f, g \circ \phi)\,\nabla(g \circ \phi) \tag{3.25}$$

where L^l_{CC} is a local intensity comparison function. One has to compute the first variation of the cross-correlation function based on its explicit form, which is given by:

$$CC^l(\phi, x_0) = \frac{v^2_{i,j}(\phi, x_0)}{v_i(x_0)v_j(\phi, x_0)} \tag{3.26}$$

where the mean and variance of the X variable is defined by:

$$\mu_i(x_0) \equiv \int_{\mathbb{R}} i \; p_\phi(i, x_0) di \tag{3.27}$$

$$v_i(x_0) \equiv \int_{\mathbb{R}} i^2 p_\phi(i, x_0) di - \mu_i^2(x_0) \tag{3.28}$$

The mean and variance of Y_ϕ additionally depend on the mapping ϕ:

$$\mu_j(\phi, x_0) \equiv \int_{\mathbb{R}} j \; p_\phi(j, x_0) dj \tag{3.29}$$

$$v_j(\phi, x_0) \equiv \int_{\mathbb{R}} j^2 p_\phi(j, x_0) di - \mu_j^2(\phi, x_0) \tag{3.30}$$

and their covariance is expressed by:

$$v_{i,j}(\phi, x_0) \equiv \int_{\mathbb{R}} ij \; p_\phi(i, x_0) p_\phi(j, x_0) \; di \; dj - \mu_i(x_0)\mu_j(\phi, x_0) \tag{3.31}$$

After computation of the first variation of the function $CC^l(\phi, x_0)$, its explicit form is given by:

$$L^l_{CC,\phi}(i, j, x_0) = -\frac{2}{\mathcal{G}_\gamma(x_0)} \left(\frac{v_{i,j}(\phi, x_0)}{v_j(\phi, x_0)} \left(\frac{i - \mu_i(x_0)}{v_i(x_0)} \right) - CC^l(\phi, x_0) \left(\frac{j - \mu_j(\phi, x_0)}{v_j(\phi, x_0)} \right) \right) \tag{3.32}$$

For more information about calculation of the similarity criteria, readers are advised to read the work of Hermosillo [2002].

3.5.3 Diffeomorphic matching

The matching problem is solved by constructing a one-parameter family of diffeomorphisms $\phi(t)(0 \leq t \leq \infty)$ and taking $\phi(\infty)$ as the solution. This family of diffeomorphisms is constructed as the solution to the initial value problem, given by:

$$\begin{cases} \frac{\partial \phi}{\partial t} & = & D\phi \cdot v, \qquad \phi(0) = I \\ v(t) & = & \mathcal{R}(\nabla \mathcal{S}(\phi)) \end{cases} \tag{3.33}$$

where D denotes Jacobian, v is the time-dependent vector field and its regularity is ensured by direct application of a regularization operator $\mathcal{R}$ to $\nabla \mathcal{S}(\phi)$. In order to maximize a similarity criterion one can build a sequence of transformations following its gradient direction, consistent with the continuous flow in Eq. 3.33. The algorithm starts from $\phi_0 = I$ and the first step yields:

$$\phi_1 = \phi_0 + \epsilon \mathcal{R}(\nabla \mathcal{S}(\phi_0)) = I + \epsilon \mathcal{R}(\nabla \mathcal{S}(I)) \tag{3.34}$$

However, the template g can be immediately propagated into $g_1 = g \circ (I + \epsilon\mathcal{R}(\nabla\mathcal{S}(I))$ instead of building the sequence ϕ_k. The matching problem between f and g_1 starts with $\phi = I$. If g_k is the propagated template after k iterations, ϕ_k is defined as the transformation satisfying:

$$\forall k,\ g_k = g \circ \phi_k \tag{3.35}$$

In summary, the previous reduces to the following algorithm:

$$\begin{aligned} &1.\ v_k \leftarrow (G_\gamma * L^l_{CC,\phi})\,(f, g \circ \phi)\,\nabla(g \circ \phi) \\ &2.\ v_k \leftarrow \mathcal{R}(v_k) \\ &3.\ \phi_{k+1} \leftarrow \phi_k \circ (I + \epsilon_k v_k) \end{aligned} \tag{3.36}$$

The algorithm starts with calculation of a displacement field v_k, from the gradient of the local cross-correlation criterion. In the second step, a regularization operator is applied on the displacement field. Finally, a new diffeomorphism ϕ_{k+1} is calculated. The regularization operator $\mathcal{R}$ is defined as:

$$\mathcal{R}(v) = \kappa * v \tag{3.37}$$

where κ is a Gaussian window with width $\sigma > 0$. Thus, the rigidity constraint of the deformation field depends on the standard deviation σ of the Gaussian filter. The choice of the Gaussian regularization is based upon the fact that tissues in the body are very heterogeneous and cannot be globally approximated by an elastic model. The chosen regularization model has a simple parametrization and can be implemented very efficiently using recursive filters. Further information regarding the construction of the regularization operator can be found in work of Chefd'hotel et al. [2002].

The numerical implementation of the image registration algorithm operates on the pixel level of data, however, it is embedded in a multi-resolution strategy to increase speed and prevent trapping in local extrema. First, a coarse version of the displacement field from a lower resolution representation of the data is calculated. This result is upsampled and used as a starting point to refine the displacement field at a higher resolution. This process is repeated until the original image resolution is reached. For each resolution level, a maximal number of iterations is defined. If the algorithm reaches a local minimum, iterations are automatically stopped. A bilinear interpolator is used to estimate pixel intensities outside the grid points, which helps reaching a sub-voxel accuracy in ideal cases. A schematics of this process is shown in figure 3.14.

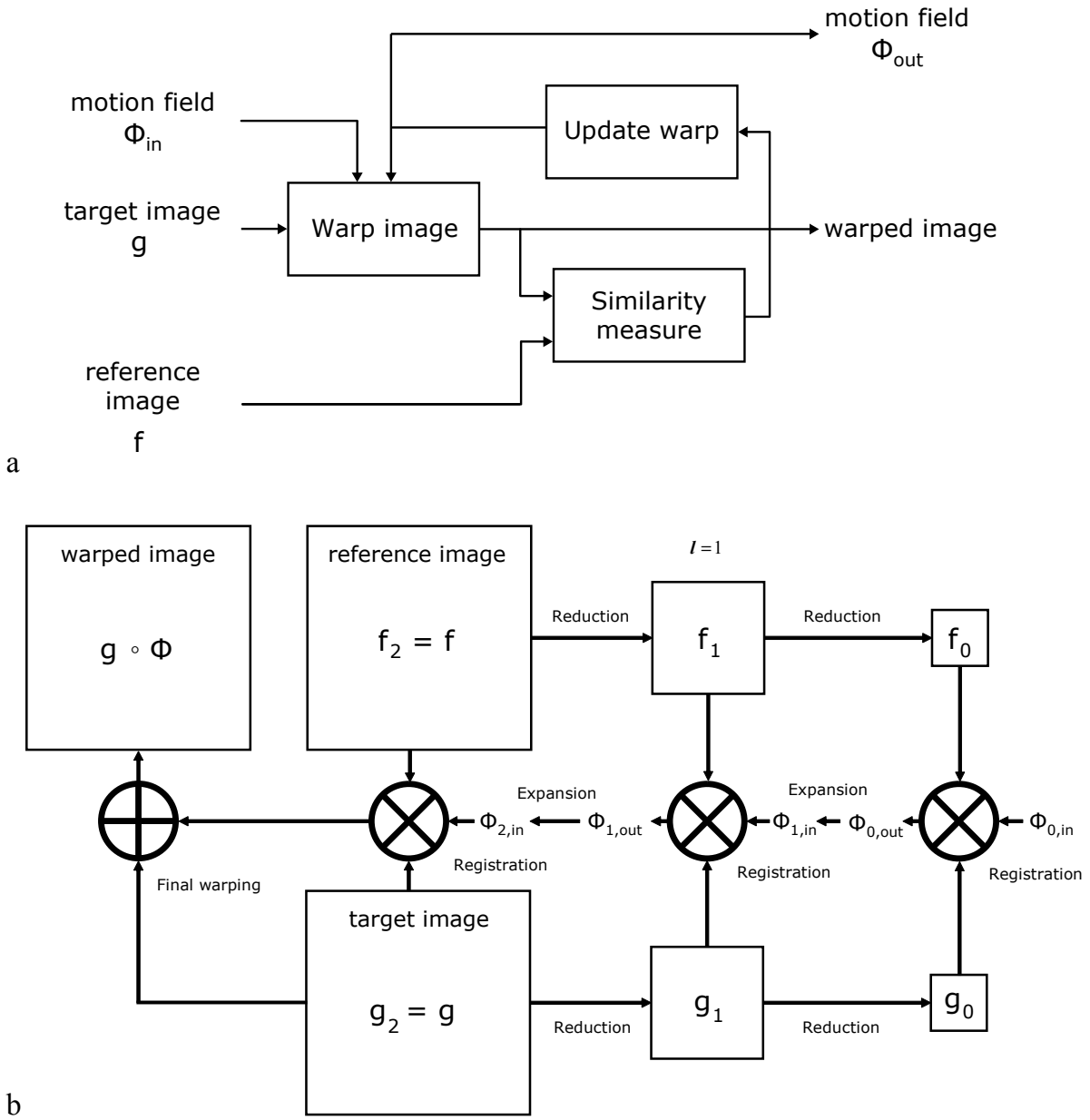

Figure 3.14: *In figure (a) the schematics of a non-rigid image registration between a target and its reference has been shown. Figure (b) presents the registration algorithm applied in a coarse-to-fine fashion to a pyramid of reduced images (reduced both in size and resolution). Once the algorithm converges at a given resolution, the recovered motion field is expanded via bilinear interpolation and used as an initial motion field at the next level in the pyramid.*

Chapter 4

Results

4.1 Optimization of the bSSFP sequence

In order to increase the signal intensity of the lung parenchyma and reduce motion artifacts in MR images, the bSSFP sequence (see section 3.4.1) was optimized using the combination of asymmetric echo sampling for submillisecond TE and parallel imaging MRI (pMRI). The MR acquisition scheme shown in figure 3.12 was executed for various parameters: TE ($0.7-1.6$ ms), TR ($1.9-3.7$ ms), TW ($50-350$ ms), flip angle α ($5-100°$), bandwidth BW ($698-1502$ Hz / px), slice thickness ST ($4-30$ mm), centric and linear k-space sampling. Fixed parameters set during the sequence optimization were: $FOV = 450^2$ mm^2, $matrix = 128 \times 128$, right to left phase encoding. pMRI technique GRAPPA with an acceleration factor = 3 for coronal slices and factor = 2 for sagittal slices, along with acquisition of 24 auto-calibration signal lines was applied prior to each image scan. The data used for the sequence optimization were acquired in a healthy volunteer. To determine optimal bSSFP sequence parameters, simulations of the evolution of the magnetization vector using Bloch equations were performed. For the acquisition with GRAPPA factor = 3 the number of the sampled k-space lines in the phase encoding direction was reduced to 48 per image.

A strong dependence between signal intensity within the lung parenchyma and TE for the magnetic field of 1.5 T is shown in Fig 4.1a. Short values of TE increase the signal intensity, as well as difference in signal intensity between expiratory and inspiratory phases. The application of short TR increases the frequency offsets at which the banding artifacts occur (Eq. 3.12), and makes the requirement for field homogeneity within the FOV less important. Figure 4.1b presents the frequency response function for the transient and steady-state of the magnetization vector. Asymmetric echo sampling (factor $s = 0.4$) was used to keep the TE and TR as short as possible. The acquisition time TA of a single image was decreased significantly to reduce the influence of the motion artifacts.

The next step in the sequence optimization was to determine the optimal flip angle. A series of simulations was performed by propagation of the magnetization vector for sequence parameters of $TE/TR = 0.8/1.9$ ms, $TW = 188$ ms, and for different tissues characterized by relaxation times given in table 4.1.

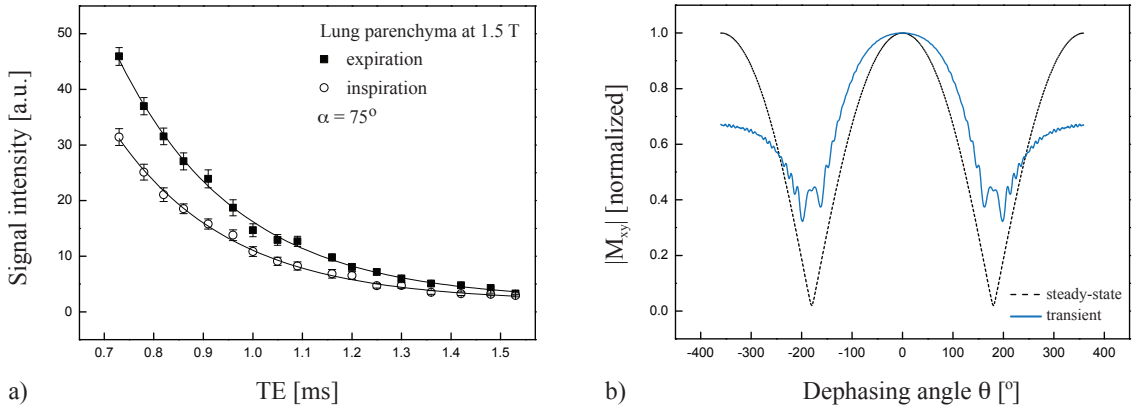

Figure 4.1: *Diagram (a) shows the influence of the TE on the signal intensity in the lung parenchyma for images acquired using the bSSFP sequence in expiration and inspiration at* 1.5 T. *The frequency response function (b) in transient and steady-state was simulated for the bSSFP sequence ($TE/TR/TW =$ 0.8/1.9/188 ms, number of RF pulses = 48) to show the minima of the transverse magnetization occurring for dephasing angle $\theta = 180°$.*

Table 4.1: *Relaxation times T_1 and T_2 of various tissues at the magnetic field of* 1.5 T *[Stanisz et al., 2005; Stadler et al., 2005]*

	T_1 [ms]	T_2 [ms]
Lung parenchyma	1266 ± 142	51 ± 4
Blood	1441 ± 120	290 ± 30
Fat	343 ± 37	58 ± 4
Liver	576 ± 30	46 ± 6

Figure 4.2 shows results of these simulations. In case of the transient behavior of the magnetization and application of very short TR, the optimal flip angle for the lung parenchyma was much higher than the value of 52° calculated directly from the Eq. 3.14. Comparison between values measured and simulated in the lung parenchyma for different flip angles are shown in figure 4.3a. The maximal allowed flip angle of 75° was considered to be optimal, because of the limitations of the specific absorption rate (SAR) for chest measurements in humans. The specific energy dose for a measurement of one MR data set corresponding to a time of 60 seconds, was on average 102 J/kg, while the SAR was 2.8 W/kg.

Introduction of intervals TW between each image acquisition improved significantly the signal intensity in the lung tissue (Fig. 4.3b). Increase of the TW allowed restoring partially the longitudinal magnetization between single image acquisitions, and as a result provided higher signal intensity in the lung parenchyma per image. For the acquisition rate of 3.33 images/second and $TA = 112$ ms, the TW was set to 188 ms. Signal gain of $26.4 \pm 3.1\%$ in the lung parenchyma was achieved for acquisitions with the centric k-space sampling scheme comparing to the linear sampling scheme (for parameters of $TE/TR/TW = 0.8/1.9/188$ ms, $\alpha = 75°$).

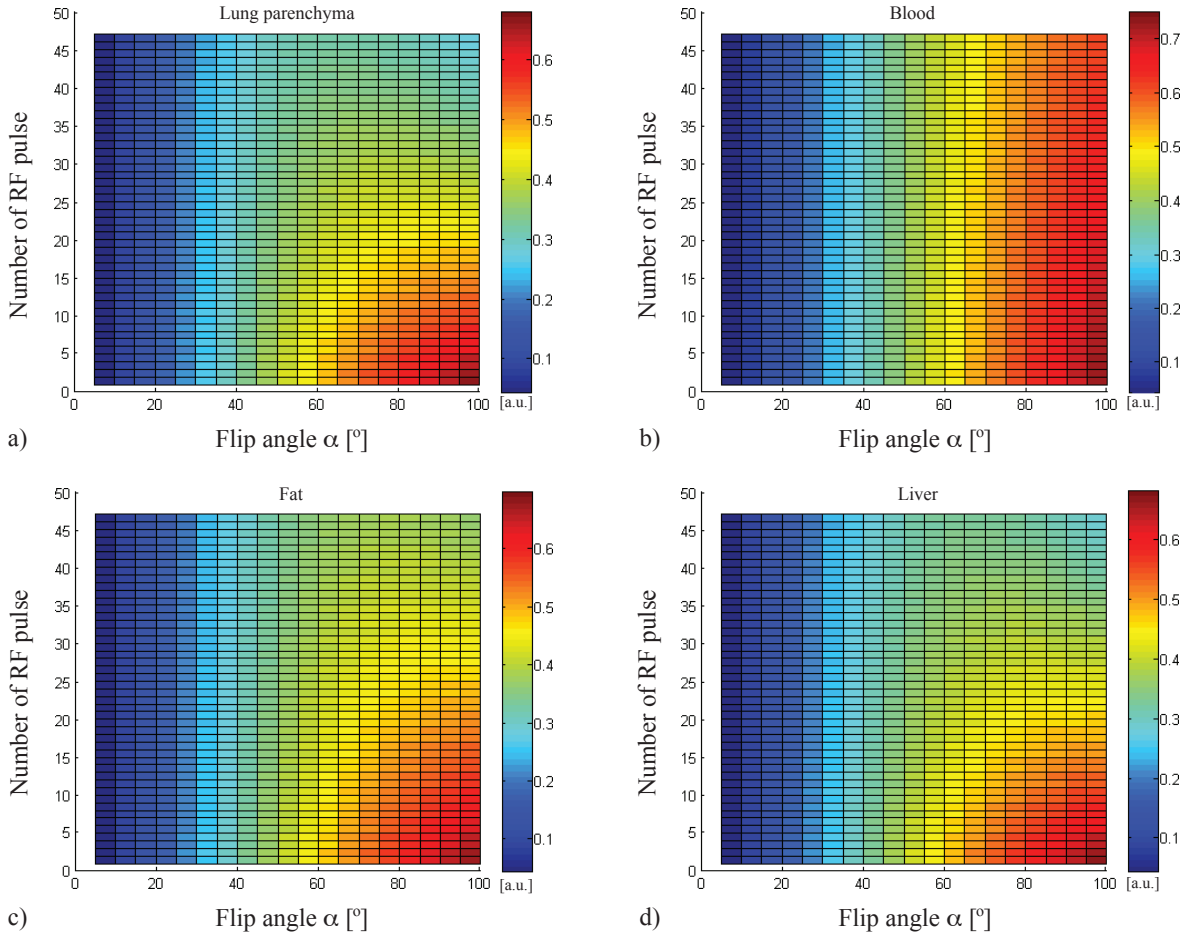

Figure 4.2: *Simulations of the propagation of the magnetization vector for different flip angles, fixed parameters of* $TE/TR/TW = 0.8/1.9/188$ ms, *and 48 RF pulses.*

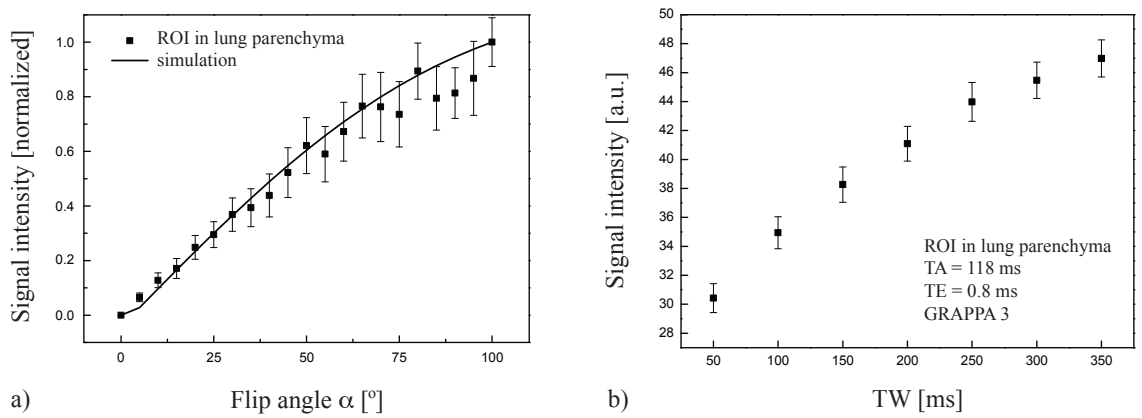

Figure 4.3: *Signal intensity measured and simulated in the lung parenchyma for the bSSFP sequence as a function of the flip angle* α *(a). Dependence between the signal intensity and the time interval* TW *(b).*

The SNR dependence on the bandwidth BW assuming that $T_1 \gg TR$ can be expressed as:

$$\text{SNR} \propto \frac{\rho e^{-TE/T_2^*}}{\sqrt{BW}} = \frac{\rho e^{-(\tau+s/BW)/T_2^*}}{\sqrt{BW}} \quad \text{where} \quad TW = \tau + \frac{s}{BW} \tag{4.1}$$

and ρ - proton density, τ - time between the middle of RF pulse and acquisition window, s - asymmetric echo sampling factor. This relationship was measured for the lung parenchyma and is shown in figure 4.4a. The minimal BW of 1302 Hz/px was required to achieve short TE of 0.8 ms.

Figure 4.4b shows dependence between the signal intensity divided by standard deviation measured in the lung parenchyma and the slice thickness ST. The optimal value of $ST = 15$ mm was estimated. Larger values of ST reduce the quality of images, due to the partial volume effects and increase the effect of intravoxel dephasing.

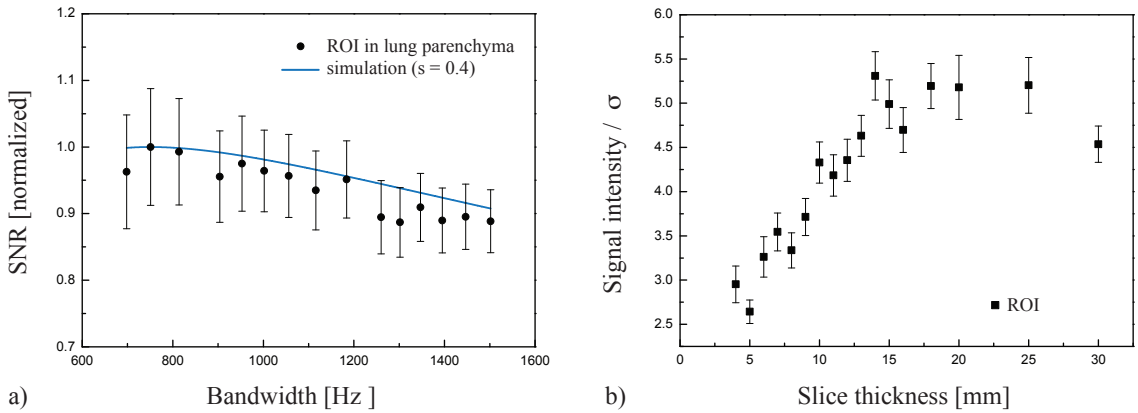

Figure 4.4: *The SNR measured and simulated in the lung parenchyma for the bSSFP sequence as a function of BW (a). Relationship between the signal intensity divided by a standard deviation of the signal intensity in the lung parenchyma, and the slice thickness ST is shown in the diagram (b).*

4.1.1 Protocol for the time-resolved bSSFP acquisition

The parameters of the 2D bSSFP sequence used to produce time-resolved data sets of the lung were as follows: repetition time $TR = 1.9$ ms, echo time $TE = 0.8$ ms (asymmetric echo sampling factor 0.75), acquisition time $TA = 112$ ms, acquisition rate between 3 and 4 images/s, $\alpha = 75°$, slice thickness ST between $10 - 15$ mm, bandwidth $BW = 1302$ Hz / px, *matrix* $= 128 \times 128$ resized using bicubic interpolation to 256×256, centric k-space sampling. The acquisitions were accelerated using pMRI with GRAPPA factor 3 and phase $FOV = 100\%$ in case of coronal acquisitions, and with GRAPPA 2 for sagittal acquisitions with reduced phase FOV of $60 - 70\%$. The FOV was adjusted individually to the patient in range $375^2 - 450^2$ mm^2. During measurements, neither respiratory nor ECG-triggering was used. Volunteers and patients were asked to move their arms behind their neck, which allowed decreasing the FOV and preventing aliasing artifacts.

4.2 Spectral analysis of the time-resolved bSSFP data

It was shown that using fast acquisition with the balanced SSFP sequence at a low magnetic field of 0.2 T combined with a non-rigid image registration, it is possible to observe regional changes of parenchyma density and visualize local alterations of the lung tissue [Zapke et al., 2006]. An alternative method was developed at a low magnetic field of 0.35 T by the application of Fourier decomposition to spectrally separate and retrieve perfusion- and ventilation-related information during a single SSFP acquisition series [Deimling et al., 2008]. In this work, the method of Fourier decomposition was implemented on a 1.5 T whole-body MR system [Bauman et al., 2009], and furthermore, extended by the application of a wavelet analysis to produce perfusion- and ventilation-weighted images [Bauman et al., 2010a].

4.2.1 Fourier decomposition (FD)

Two main physiological processes contribute to the signal change within the ungated MR image series of the lung parenchyma: cardiac and respiratory cycle. Mechanics of the respiratory cycle involves the diaphragm, external intercostal muscles, and abdominal muscles. During the inspiratory contraction of the diaphragm, the volume of the lung grows and the internal pressure decreases. The thoracic volume rises as the diaphragm changes its position in the apical-basal direction. Air flows into the lung following its pressure gradient. Alveoli increase their size, decreasing the local parenchyma density. Expiration is caused by diaphragm relaxation, contraction of the external intercostal muscles, and elastic recoil of pulmonary alveoli. The parenchyma density increases as air leaves the pulmonary structures. Mechanics of respiration was described in the section 2.4.1.

The hypothesis that equal relative changes in lung volume cause equal relative changes in MR signal intensity was described by Bankier et al. [2004] and correlated with pulmonary function tests. The proton density of the lung parenchyma is determined by phase of the respiratory cycle and scaled linearly with the lung volume. The shape of the respiratory curve can be described by the Lujan et al. [1999] formula:

$$z(t) = z_0 - A\cos^{2l}\left(\frac{\pi t}{\tau} - \phi\right) \tag{4.2}$$

where $z(t)$ is the position of the diaphragm in the apical-basal direction, z_0 - constant value, τ and ϕ - period and phase of the respiratory cycle, respectively, l - parameter influencing flatness and steepness of the curve, and A - amplitude of the respiratory cycle. By modifying the Eq. 4.2 the change of diaphragm position can be represented as signal intensity change $s(t)$ of lung parenchyma using the linear dependence between both variables. Moreover, signal variations modulated with the cardiac frequency were taken into account:

$$s(t) = s_0 - A_R\cos^{2l}\left(\frac{\pi t}{\tau_R} - \phi_R\right) + A_C\cos^{2m}\left(\frac{\pi t}{\tau_C} - \phi_C\right) \tag{4.3}$$

where s_0 - constant value, τ_R and ϕ_R - period and phase of the respiratory cycle, respectively, τ_C and ϕ_C - period and phase of the cardiac cycle, respectively, l, m - parameters influencing

the shape of the curve, A_R and A_C - amplitudes of both physiological cycles. The simulated respiratory and cardiac time courses are shown in Fig. 4.5a.

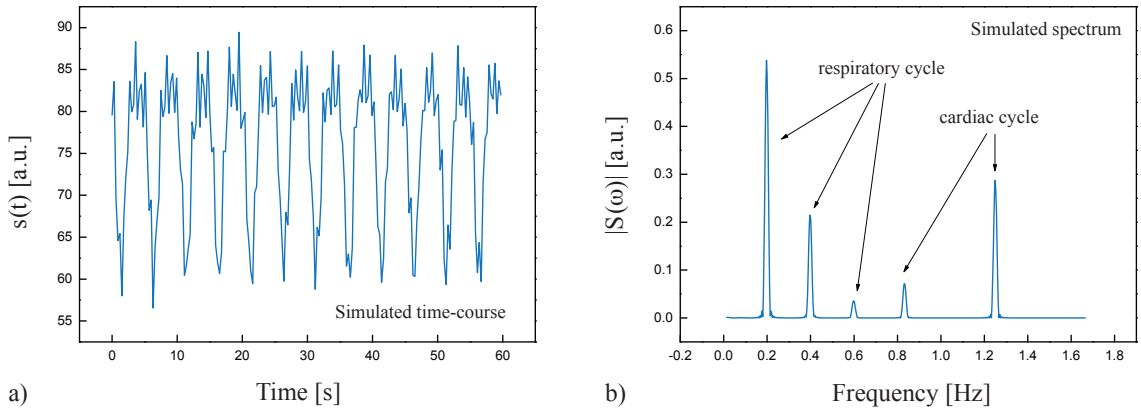

Figure 4.5: *Diagram (a) shows respiratory and cardiac time-courses simulated using modified Lujan formula for parameters:* $A_R = 12$, $A_C = 6$, $l = 3$, $m = 2$, $\tau_r = 5.0$ s, $\tau_c = 0.8$ s. *In diagram (b) Fourier analysis of the time-course shows spectral lines and harmonics, the first peak represents signal from respiratory cycle at* 0.2 Hz, *the second and the third its harmonics at* 0.4 Hz *and* 0.6 Hz, *the fifth peak represents cardiac cycle for* 1.25 Hz, *and the fourth its aliased harmonic at* 0.833 Hz.

In order to perform a spectral separation of the signal change caused by respiratory and cardiac cycles, a minimal imaging rate of at least double frequency of the highest frequency signal component is required according to the Nyquist criterion. Due to the limitation of the minimal acquisition time of an image, this condition is not preserved for the part of the Eq. 4.3 describing the cardiac cycle. After the Fourier transform of the simulated signal course few spectral lines appear (see Fig. 4.5b). Two main lines contain the signal from lung parenchyma and pulsatile pulmonary blood. Since the $s(t)$ curve does not have a sinusoidal time course, harmonics with different Fourier coefficients are observed. The maximal imaging rate is limited, thus the harmonics of the blood signal line may be aliased into the spectrum. In fact, respiratory and cardiac periods can change during the data sampling, as well as the amplitude A_R and A_C. These instabilities may affect shapes of the spectral lines.

Alignment of the lung structures along the time axis using the non-rigid image registration enabled to perform Fourier analysis on the acquired time-resolved data $R_j(x, y, t)$, $j \in 1, \ldots, k$ containing k different slices, and to spectrally separate of respiratory and cardiac signal changes.

After the registration process, signal was filtered using the Hann window to remove the Gibbs ringing:

$$\forall\{x, y\} \quad R_j^f(x, y, t) = R_j(x, y, t) \cdot u(t) \tag{4.4}$$

where $\{x,\ y\}$ denotes the position within a single image, $t = 1 \ldots N$ is the time position of an image in the data set, N is the number of images, and $u(t)$ is the Hann window of length N

defined by:

$$u(t) = \sin^2\left(\frac{\pi t}{N-1}\right) \tag{4.5}$$

The Fast Fourier Transform (FFT) was applied pixel-wise in the time domain of each filtered data set:

$$\forall\{x,y\} \quad \mathcal{F}[R_j^f(x,y,t)] = M_j(x,y,\omega) \tag{4.6}$$

where $\omega = 1 \ldots n$ is the frequency of the spectral image, and N is the number of spectral images. Every frame ranging from $\omega = 1 \ldots N/2$ of the transformed data set represented spectral image with spectral resolution of:

$$\Delta\omega = \frac{1}{n(TA+TW)} \tag{4.7}$$

where TA is the acquisition time, and TW the interval between every image acquisition. The maximal measurable frequency (the spectral bandwidth) for a given sample rate is:

$$\omega_B = \frac{1}{2(TA+TW)} \tag{4.8}$$

For the $TA + TW = 0.3$ s and $N = 192$ images acquired per slice, the spectral resolution $\Delta\omega = 0.017$ Hz and the spectral bandwidth $\omega_B = 1.667$ Hz.

In the next step, the squared magnitude of the data was calculated:

$$\forall\{x,y\} \quad |M_j(x,y,\omega)|^2 = M_j(x,y,\omega) \cdot \bar{M}_j(x,y,\omega) \tag{4.9}$$

To identify frequency frames associated with respiratory and cardiac cycles, ω_v and ω_p respectively, signal intensity was summed over the spatial dimensions for every image in the whole data set:

$$s_j(t) = \sum_{x,y} R_j^f(x,y,t) \tag{4.10}$$

Calculation of the FFT of $s_j(t)$ yields a frequency spectrum:

$$\mathcal{F}[s_j(t)] = S_j(\omega) \tag{4.11}$$

Two peaks corresponding to ω_v and ω_p were located in the squared magnitude frequency spectrum $|S_j(\omega)|^2$ by looking for downward zero-crossing in the smoother first derivate that exceeded defined slope threshold and peak amplitude. The Fourier transform of signal $s_j(t)$ is time averaged, which means that it contains only globally averaged information and has the potential to obscure transient or local-specific features within the signal. This limitation can be partly overcome by introduction of a sliding time window of fixed length to localize the time analysis. The short-time Fourier transform (STFT) provides a degree of temporal resolution, and can be

used to create a spectrogram (energy density function) allowing to observe the stability of the respiration and heart rate during the data acquisition:

$$\mathrm{STFT}[s_j(t)] \equiv S_j(\tau,\omega) = \sum_{n=-\infty}^{\infty} s_j(t)v(t-\tau)e^{-i\omega t}dt \tag{4.12}$$

where $v(t)$ is the Kaiser window of defined length centered around zero and expressed as:

$$v(t) = \frac{I_0\left(\pi\alpha\sqrt{1-(\frac{2t}{n-1}-1)^2}\right)}{I_0(\pi\alpha)} \tag{4.13}$$

where I_0 is the zeroth order modified Bessel function of the first kind, α is an arbitrary real number that determines the shape of the window. The squared magnitude of the STFT yields the spectrogram, which shows how the spectral density varies in time:

$$\mathrm{spectrogram}\{s_j(t)\} \equiv |S_j(\tau,\omega)|^2 \tag{4.14}$$

Figure 4.6 shows example spectrograms of the simulated signal time-courses.

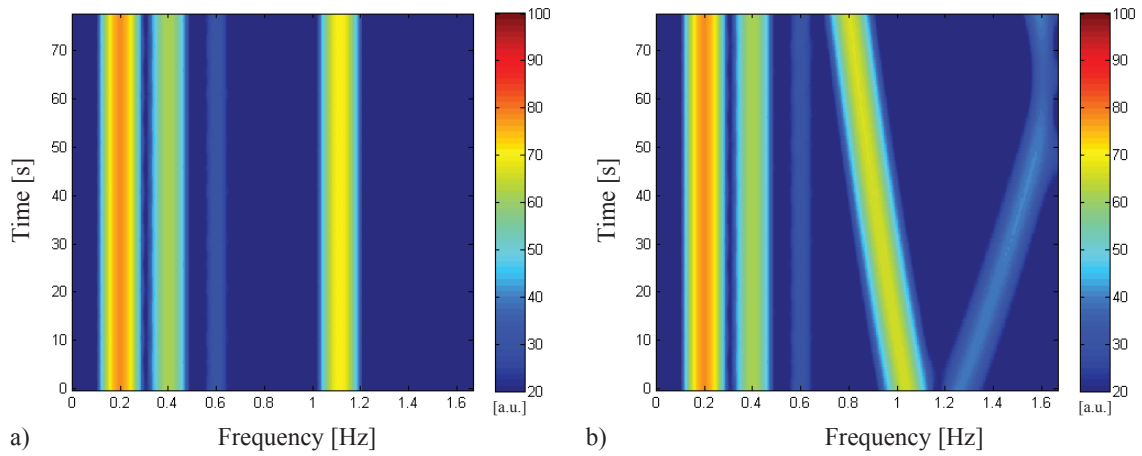

Figure 4.6: *The spectrogram (a) was created using the short-time Fourier transform from a simulated signal time-course for parameters: number of samples* $N = 256$, $A_R = 12$, $A_C = 6$, $\tau_r = 5$ s, $\tau_c = 0.9$ s, $l = 3$, $m = 2$, *length of the Kaiser window* $v = 64$ *and* $\alpha = 6$. *The respiratory and cardiac frequencies were stable. The spectrogram (b) was simulated for the* τ_c *changing linearly from* 0.9 s *to* 1.1 s. *Notice that the first and the second harmonic of the cardiac frequency change their location on the time-frequency plane.*

Integration of the appropriate frequency ranges (depending on the wideness of the spectral peaks) allowed producing ventilation- and perfusion-weighted images. Ventilation-weighted images provide information about regional signal intensity change, which is proportional to the regional density change of the pulmonary tissue caused by respiration. Thus, different pathological malformations of the pulmonary parenchyma can be observed as disturbed regional signal change (A_R). Information contained in perfusion-weighted images is related to the signal change in the pulmonary parenchyma between the systolic and diastolic phase of the heart cycle (A_C).

Ventilation-weighted image $V_j(x,y)$ and perfusion-weighted image $P_j(x,y)$ were generated from the squared magnitude $|M_j(x,y,\omega)|^2$ by pixel-wise integration of different frequency ranges:

$$V_j(x,y) = \sum_{i=-l}^{l} |M_j(x,y,\omega_v + i)|^2 \cdot G_\beta(i) \tag{4.15}$$

$$P_j(x,y) = \sum_{i=-l}^{l} |M_j(x,y,\omega_p + i)|^2 \cdot G_\beta(i) \tag{4.16}$$

where G_β is a Gaussian window of variance β.

In addition to images $V_j(x,y)$ and $P_j(x,y)$ showing the absolute local signal change, images representing signal change relative to the local mean signal can be produced dividing them by the DC component (zero-frequency image):

$$V_j^b(x,y) = \frac{V_j(x,y)}{|M(x,y,0)|} \tag{4.17}$$

$$P_j^b(x,y) = \frac{P_j(x,y)}{|M(x,y,0)|} \tag{4.18}$$

Improved visualization of the images was obtained by presenting them in the log-grayscale lookup table. The algorithm of the computation of the ventilation- and perfusion-weighted lung images images is shown in figure 4.7.

The signal change in the time-resolved data caused by the respiratory and cardiac cycles can be presented in form of an animation. The appropriate frequency range $[\omega_a, \omega_b]$ of the data transformed using the FFT has to be filtered out:

$$\forall\{x,y\} \quad M_j^a(x,y,\omega) = \begin{cases} M_j(x,y,\omega) \cdot G_\beta\left(\frac{|\omega_b - \omega_a|}{2}\right) & \text{if } \omega \in [\omega_a, \omega_b] \\ 0 & \text{otherwise} \end{cases} \tag{4.19}$$

As the next step, the data is transformed back into the time domain using the inverse Fourier transform yielding an animation:

$$\forall\{x,y\} \quad A_j(x,y,t) = \Re\{\mathcal{F}^{-1}[M_j^a(x,y,\omega)]\} \tag{4.20}$$

With a sufficient imaging rate an animation can show the dynamics of the signal change caused by blood pulsation A_C and tissue contraction in the lung A_R.

4.2.2 Wavelet analysis (WA)

A different method of the data postprocessing is based on the wavelet transform analysis. This is an alternative way to provide a time-frequency representation of the signal, which can be used to retrieve signal related to ventilation and perfusion. A local spectral and temporal information from a signal can be resolved more effectively than using the STFT by using a window of variable width. This means that the STFT gives a constant resolution of all frequencies, while the wavelet

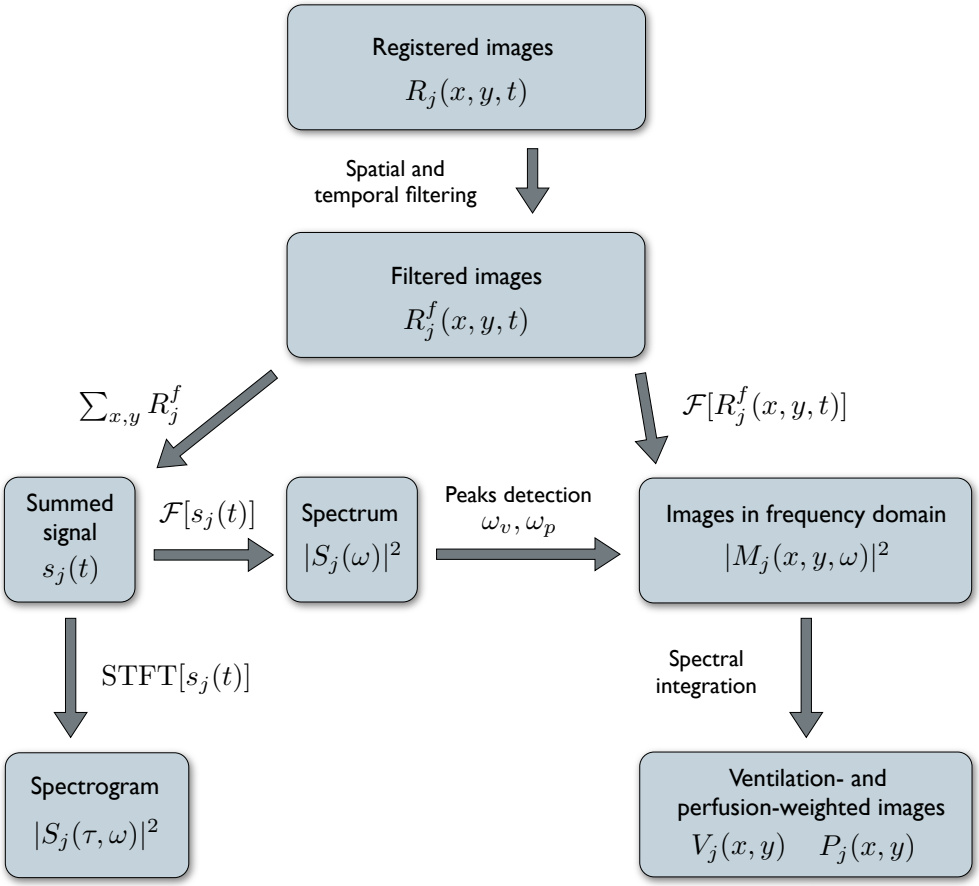

Figure 4.7: *The FD algorithm used to produce ventilation- and perfusion-weighted lung images. Each step of the algorithm is explained in the text.*

transform uses multi-resolution technique by which different frequencies are analyzed with different resolutions. Wavelet transform analysis has been applied to a wide variety of biomedical signals including electroencephalogram (EEG), electrocardiogram (ECG) or respiratory patterns [Unser and Akram, 1996; Akay, 2001]. The wavelet transform allows for a robust analysis of physiological signals, which most often show a non-stationary behavior [Weiss, 1999].

4.2.2.1 The Continuous Wavelet Transform and Scalograms

There are two distinct classes the wavelet transforms: Continuous Wavelet Transform (CWT) and the Discrete Wavelet Transform (DWT). The CWT of a signal $s(t)$ is provided by equation (definitions of formulas by Addison et al. [2009]):

$$T(a,b) = \int_{-\infty}^{\infty} s(t)\psi_{a,b}^*(t)dt \tag{4.21}$$

where $\psi^*_{a,b}(t)$ is the complex conjugate of the function $\psi_{a,b}(t)$ defined by:

$$\psi_{a,b}(t) = \frac{1}{\sqrt{a}}\psi\left(\frac{t-b}{a}\right) \tag{4.22}$$

All the wavelet functions used in the wavelet transform are derived from the mother wavelet $\psi(t)$ $(a = 1, b = 0)$ through scaling (dilation or compression) and translation (shifting). The scale parameter a corresponds to frequency information. Large scales dilate the signal providing detailed information contained in the signal, while small scales compress the signal and give global information about the signal. The translation parameter b relates to the location of the wavelet function as it is shifted through the signal, corresponding to the time information in the wavelet transform. The shifted and scaled wavelet is called a baby wavelet. The CWT allows for a high localization in time of high-frequency signal features using a variable window width, and is not limited to using sinusoidal analyzing functions.

The mother wavelet has a finite energy:

$$E = \int_{-\infty}^{\infty} |\psi(t)|^2 dt < \infty \tag{4.23}$$

An acceptable basis function must have a zero mean:

$$\int_{-\infty}^{\infty} \psi(t) dt = 0 \tag{4.24}$$

If the Fourier transform of $\psi(t)$ is given by:

$$\hat{\psi}(f) = \mathcal{F}[\psi(t)] \tag{4.25}$$

then the following condition should be satisfied:

$$C = \int_{0}^{\infty} |\hat{\psi}(f)|^2 df < \infty \tag{4.26}$$

here C is known as the admissibility constant.

The signal energy at the specific scale and location can be presented as a scalogram, given by the two-dimensional wavelet energy density function, and defined by:

$$E(a,b) = \frac{|T(a,b)|^2}{C} \tag{4.27}$$

The scalogram can be integrated across b to recover the relative contribution to the total energy contained within the signal at a specific scale a, yielding a scale-dependent spectrum:

$$E(a) = \frac{1}{C}\int_{-\infty}^{\infty} |T(a,b)|^2 db \tag{4.28}$$

In case of the signal $s(t)$ (Eq. 4.10) one can identify in $E(a)$ peaks corresponding to the respiratory and cardiac cycles. The scale-dependent spectrum and spectrogram can be converted

to the frequency domain. Since the spectral components are inversely proportional to the scale $f \propto 1/a$, the frequency associated with a wavelet is given by:

$$f = \frac{f_c}{a} \tag{4.29}$$

where f_c is a characteristic frequency of the mother wavelet at scale $a = 1$ and location $b = 0$. The original signal can be reconstructed using an inverse CWT:

$$s(t) = \frac{1}{C} \int_{-\infty}^{\infty} \int_{0}^{\infty} \frac{1}{a^2} T(a,b) \psi_{a,b}(t) da db \tag{4.30}$$

The scalogram was calculated from the summed signal $s_j(t)$ (Eq. 4.10) using the CWT and the 'morlet' wavelet given by:

$$\psi(t) = C \exp\left(-\frac{x^2}{2}\right) \cos(5t) \tag{4.31}$$

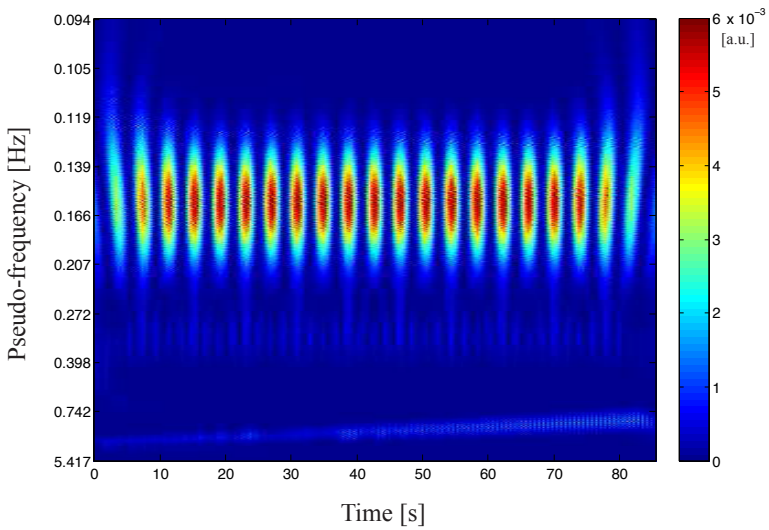

Figure 4.8: *Scalogram of simulated respiratory and cardiac time-courses created using the 'morlet' wavelet function ($N = 256$, $A_R = 12$, $A_C = 6$, $\tau_r = 7$ s, $\tau_c = 0.7 - 1.0$ s, $l = 3$, $m = 2$). The scale domain was transformed into the pseudo-frequency domain.*

4.2.2.2 The Discrete Wavelet Transform

The Discrete Wavelet Transform (DWT) is an implementation of the wavelet transform, which uses a discrete set of the wavelet scales and translations. The input signal is an initial wavelet approximation $s(t) \equiv A_0$. The transform is determined on a discretized grid of scales a and locations b. The DWT employs two sets of functions, called wavelet functions and scaling functions, which are associated with high-pass and low-pass filters, respectively. A doubly indexed set of baby wavelets are defined as follows (definitions of formulas by Addison et al. [2009]):

$$\psi_{m,n}(t) = \frac{1}{\sqrt{a_0^m}} \psi\left(\frac{t - n b_0 a_0^m}{a_0^m}\right) \tag{4.32}$$

where m controls the wavelet dilation and n translation. By choosing the scales to be powers of 2 and the time to be an integer of multiple of the scales, i.e. substituting $a_0 = 2$ and $b_0 = 1$, the dyadic grid wavelet given by:

$$\psi_{m,n}(t) = 2^{\frac{-m}{2}}\psi(2^{-m}t - n) \tag{4.33}$$

The baby wavelets form an orthogonal basis and have unitary energy, which is expressed as:

$$\int_{-\infty}^{\infty} \psi_{m,n}(t)\psi_{m',n'}(t)dt = \delta(m' - m)\delta(n' - n) \tag{4.34}$$

Thus, the information stored in a wavelet coefficients is not redundant and allows for a complete reconstruction of the original signal.

The scaling functions has the same form as the wavelet functions, given by:

$$\phi_{m,n}(t) = 2^{\frac{-m}{2}}\phi(2^{-m}t - n) \tag{4.35}$$

They are orthogonal to translations of itself but not to dilations of itself, and have unitary energy:

$$\int_{-\infty}^{\infty} \phi_{0,n}(t)\phi_{0,n}(t - n)dt = \delta(n) \tag{4.36}$$

Both, the wavelet and scaling functions span the same space $-\infty < m < \infty$ and $-\infty < n < \infty$.

The DWT of a signal $s(t)$ on a dyadic grid can be written as:

$$d_{m,n} = \int_{-\infty}^{\infty} s(t)\psi_{m,n}(t)dt \tag{4.37}$$

where $d_{m,n}$ is the detail coefficient for given scale and location.
The scaling function can be convolved with the signal to produce so-called approximation coefficients:

$$a_{m,n} = \int_{-\infty}^{\infty} s(t)\phi_{m,n}(t)dt \tag{4.38}$$

A continuous approximation of the signal at given scale m can be produced as a sum of scaling functions and approximation coefficients as follows:

$$A_m(t) = \sum_{n=-\infty}^{\infty} a_{m,n}\phi_{m,n}(t) \tag{4.39}$$

A signal detail at scale m is defined as:

$$D_m(t) = \sum_{n=-\infty}^{\infty} d_{m,n}\psi_{m,n}(t) \tag{4.40}$$

The original signal can be recovered using a series expansion with both the approximation and the detail coefficients, which is given by the multi-resolution representation [Mallat, 1989]:

$$s(t) = A_{m'} + \sum_{m=-\infty}^{m'} D_m(t) = \sum_{n=-\infty}^{\infty} a_{m',n}\phi_{m',n}(t) + \sum_{m=-\infty}^{m'} \sum_{n=-\infty}^{\infty} d_{m,n}\psi_{m,n}(t) \tag{4.41}$$

where m' denotes an arbitrary scale at which the signal was approximated. From Eq. 4.41 it can be shown that adding the signal detail to the approximation at an arbitrary scale m yields the signal at a smaller scale $m-1$ and at an increased resolution:

$$A_{m-1}(t) = A_m(t) + D_m(t) \tag{4.42}$$

The process of producing sets of approximation and detail coefficients at scale m from the approximation coefficients at scale $m-1$ is called analysis, while the reverse process is called synthesis.

A formula connecting the scale function to itself at two different time scales, so-called the two scale equation, is given by:

$$\phi(t) = \sum_{k=-\infty}^{\infty} H(k)\sqrt{2}\phi(2t-k) \tag{4.43}$$

where $H(k)$ are discrete filter coefficients. The two scale equation for the wavelet function employing another discrete filter $G(k)$ is defined as:

$$\psi(t) = \sum_{k=-\infty}^{\infty} G(k)\sqrt{2}\phi(2t-k) \tag{4.44}$$

It can be shown that the operations of analysis and synthesis can be performed using high-pass, or low-pass filters. Since the wavelet and the scaling functions are orthogonal at each scaling index level, the coefficients can be calculated as follows:

$$\begin{aligned}
a_{m,n} &= \sum_{k=-\infty}^{\infty} a_{m-1,k} \int_{-\infty}^{\infty} \phi_{m,k}(t)\phi_{m-1,n}(t)dt \\
&= \sum_{k=-\infty}^{\infty} a_{m-1,k} \int_{-\infty}^{\infty} \sqrt{2^m}\phi(2^m t-k)\sqrt{2^{m-1}}\phi(2^{m-1}t-n)dt \quad \text{(substitute } \; s = 2^{m-1}t-n) \\
&= \sum_{k=-\infty}^{\infty} a_{m-1,k} \int_{-\infty}^{\infty} \sqrt{2}\phi(2s+2n-k)\phi(s)ds \quad \text{(using the Eq. 4.43 for } \phi(s)) \\
&= \sum_{k=-\infty}^{\infty} a_{m-1,k} \int_{-\infty}^{\infty} \sqrt{2}\phi(2s+2n-k) \sum_{j=-\infty}^{\infty} H(j)\sqrt{2}\phi(2s-j)ds \\
&= \sum_{k=-\infty}^{\infty} a_{m-1,k} \sum_{j=-\infty}^{\infty} H(j) \int_{-\infty}^{\infty} \phi(2s+2n-k)\phi(2s-j)2ds
\end{aligned} \tag{4.45}$$

The last integral in Eq. 4.45 is 0 unless $j = k-2n$. This results in:

$$a_{m,n} = \sum_{k=-\infty}^{\infty} H(k-2n)a_{m-1,k} \tag{4.46}$$

Similar computation can be performed for the detail coefficients yielding:

$$d_{m,n} = \sum_{k=-\infty}^{\infty} G(k-2n)a_{m-1,k} \tag{4.47}$$

Equations 4.46 and 4.47 represent the multi-resolution decomposition algorithm of the fast wavelet transform, which allows calculating the wavelet coefficients more efficiently than computing them directly from the convolution (Eq. 4.37). Iteration of Eqs. 4.46 and 4.47 performs high-pass and low-pass filtering of the signal, respectively. The filter outputs are subsampled by 2. Figure 4.10 shows the iterative signal analysis algorithm. The discrete filter coefficients H and G determine the wavelet used.

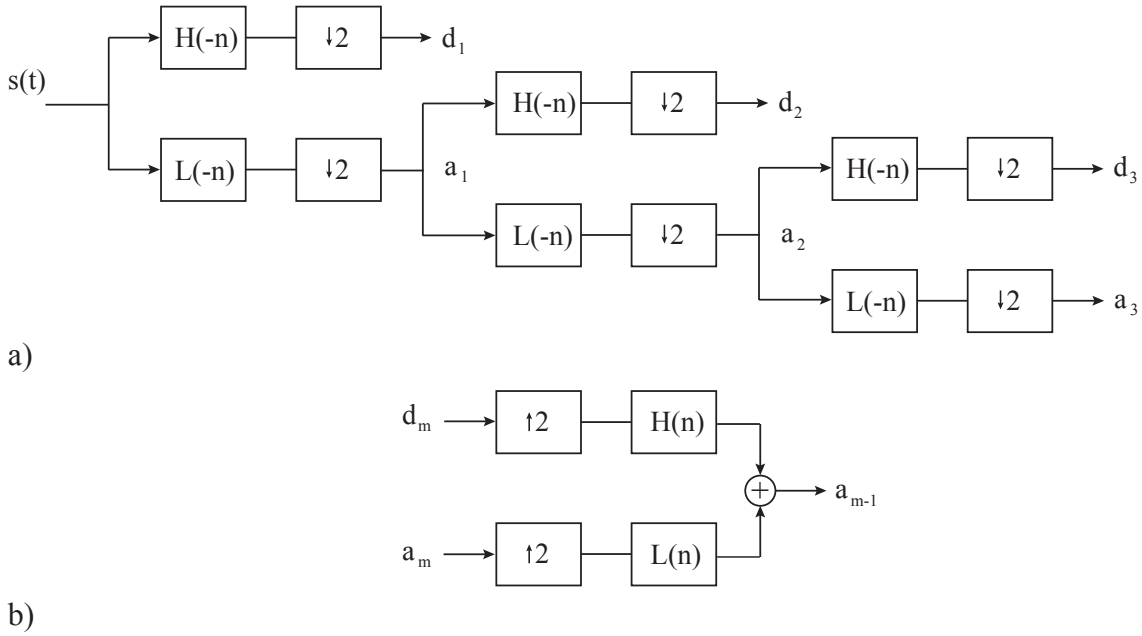

Figure 4.9: *Diagram (a) shows three-level analysis of a signal using an iterative algorithm. The coefficients $a_{m,k}$ and $d_{m,k}$ are calculated by iterating, or cascading the single stage filter bank in order to obtain a multiple stage filter bank. One stage synthesis of the signal is shown in the diagram (b).*

The reconstruction algorithm of the fast wavelet transform consists of upsampling by 2 and filtering:

$$a_{m-1,n} = \sum_{k=-\infty}^{\infty} H(n-2k)a_{m,n} + \sum_{k=-\infty}^{\infty} G(n-2k)d_{m,n} \tag{4.48}$$

The synthesis filters are identical with the decomposition filters except for the reverse time course.

If the analyzed signal $s(t)$ has a finite length of $N = 2^M$, the range of scales that can be used is limited to $0 < m < M$. Thus, the input signal can be as the signal at scale M plus a combination of detailed signals as follows:

$$\sum_{n=0}^{2^{M-m}-1} a_{0,n}\phi_{0,n}(t) = a_{M,n}\phi_{M,n}(t) + \sum_{m=1}^{M}\sum_{n=0}^{2^{M-m}-1} d_{m,n}\psi_{m,n}(t) \tag{4.49}$$

$$s(t) = A_M(t) + \sum_{m=1}^{M} D_m(t) \tag{4.50}$$

4.2.2.3 Wavelet analysis of respiratory and cardiac cycles

To analyze and synthesize signals of respiratory and cardiac cycles, an implementation from The Wavelet Toolbox of the MATLAB environment (The Mathworks, Inc., Natick, MA, USA) of the Daubechies 'db4' wavelet was used [Daubechies, 1988]. The scaling function coefficients H of the 'db4' wavelet are defined as follows:

$$h_0 = \frac{1+\sqrt{3}}{4\sqrt{2}},\ h_1 = \frac{3+\sqrt{3}}{4\sqrt{2}},\ h_2 = \frac{3-\sqrt{3}}{4\sqrt{2}}, h_3 = \frac{1-\sqrt{3}}{4\sqrt{2}} \tag{4.51}$$

and the wavelet function coefficients G are:

$$g_0 = h_3,\ g_1 = -h_2,\ g_2 = h_1,\ g_3 = -h_0 \tag{4.52}$$

The signal $R_j(x, y, t)$ was decomposed at levels $m = 1 \ldots 4$ with the 1D DWT into sets of approximation and detail coefficients for every pixel location $\{x, y\}$. Denoising of the signal was performed using the compromising method between the hard- and soft-thresholding [Donoho and Johnstone, 1994; Song and Zhao, 2001]. The thresh-holding operator is defined as:

$$\hat{d}_{m,n} = \begin{cases} d_{m,n} & \text{sign}(d_{m,n})(|d_{m,n}| - \alpha\lambda) \geq \lambda \\ 0 & |d_{m,n}| < \lambda \end{cases} \tag{4.53}$$

where $\lambda = \sigma\sqrt{2\log N}$ and $\alpha \in [0, 1]$.

Using the multi-resolution approach, the approximation and detail signals, A_m and D_m, respectively, were calculated for each decomposition level. In the next step, the standard deviation of the approximation and detail signals was determined pixel-wise to calculate the ventilation- and perfusion-weighted images:

$$\forall\ \{x, y\} \text{ for } \{m, m'\} \in \{1 \ldots 4\} : V(x, y) = \sigma(A_m)(x, y),\ P(x, y) = \sigma(D'_m)(x, y) \tag{4.54}$$

Changes of the signal intensity with regard to respiratory and cardiac cycles, are proportional to the standard deviation of the approximation and detail signal, respectively. The algorithm for computation of the ventilation- and perfusion-weighted images is shown in figure 4.10.

4.3 Software for postprocessing of the time-resolved bSSFP images of the lung

After the data acquisition, the images were transferred from the MR scanner to the computer workstation in form of DICOM (Digital Imaging and Communications in Medicine) images. In order to automatize the postprocessing of the acquired time-resolved data sets, two different software applications were required. The first application *fMRLung* (Siemens Corporate Research, Princeton, NY, USA) was used to perform the non-rigid image registration. Processing time for registration of a single data set containing 192 images of 256×256 pixels was approximately $35-40$ s (Intel Core 2 Quad CPU 2.83GHz, 8GB RAM). The registered images were saved

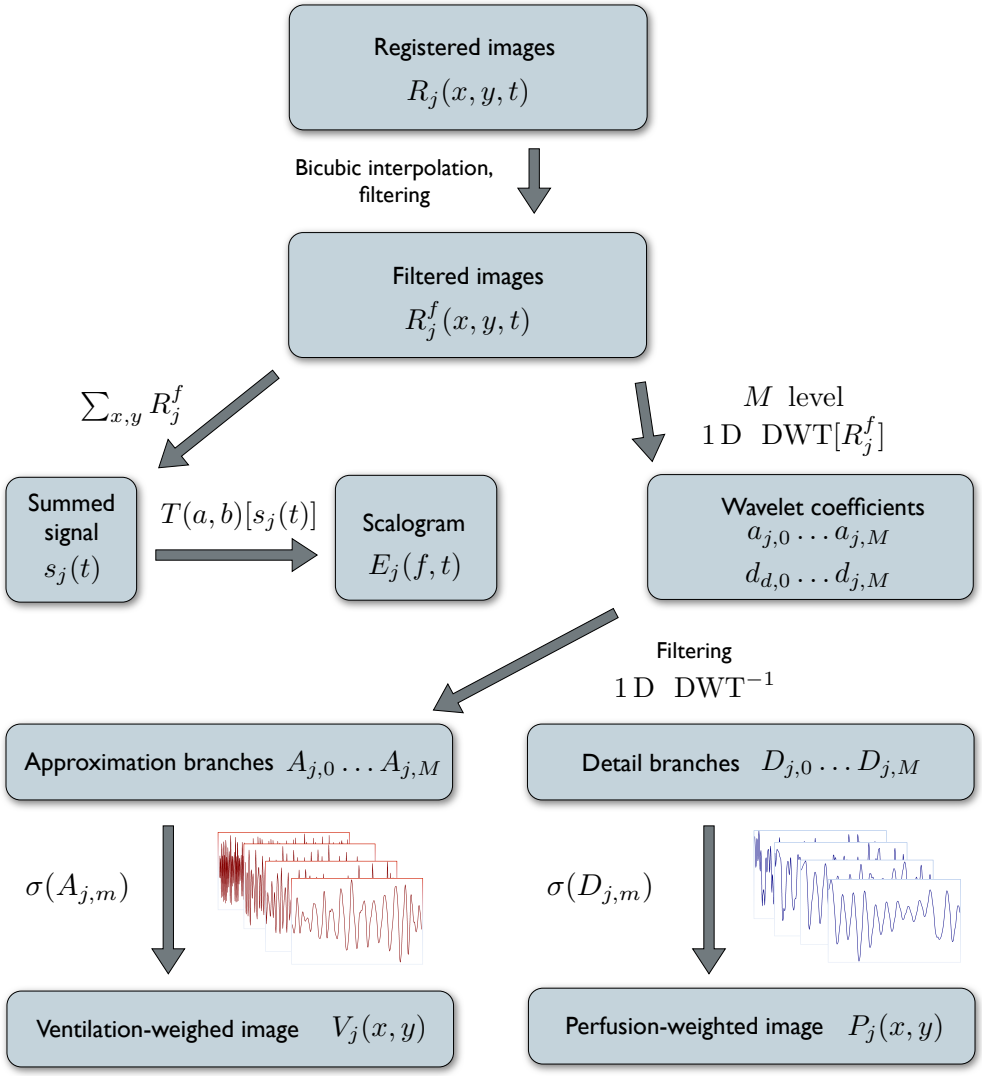

Figure 4.10: *The WD algorithm used to produce ventilation- and perfusion-weighted lung images. Each step of the algorithm is explained in the text.*

on the hard disk, and loaded by the second application *FD-MRI Postprocessing Software* programmed in the MATLAB 2009a environment (The Mathworks, Inc., Natick, MA, USA), which allows performing the spectral analysis by means of the Fourier decomposition (Fig. 4.11).

The application is able to handle with multiple-slice acquisitions. It calculates frequency spectrum, localizes respiratory and cardiac peaks, and transform the whole data into the frequency space separately for every slice. The appropriate frequency ranges are integrated to produce ventilation- and perfusion-weighted lung images. The images can be stored either in DICOM or PNG (Portable Network Graphics) formats. The application allows for various visualization of the images by filtering in the spatial and frequency domains. A simplified postprocessing workflow of time-resolved bSSFP data sets is shown in figure 4.12.

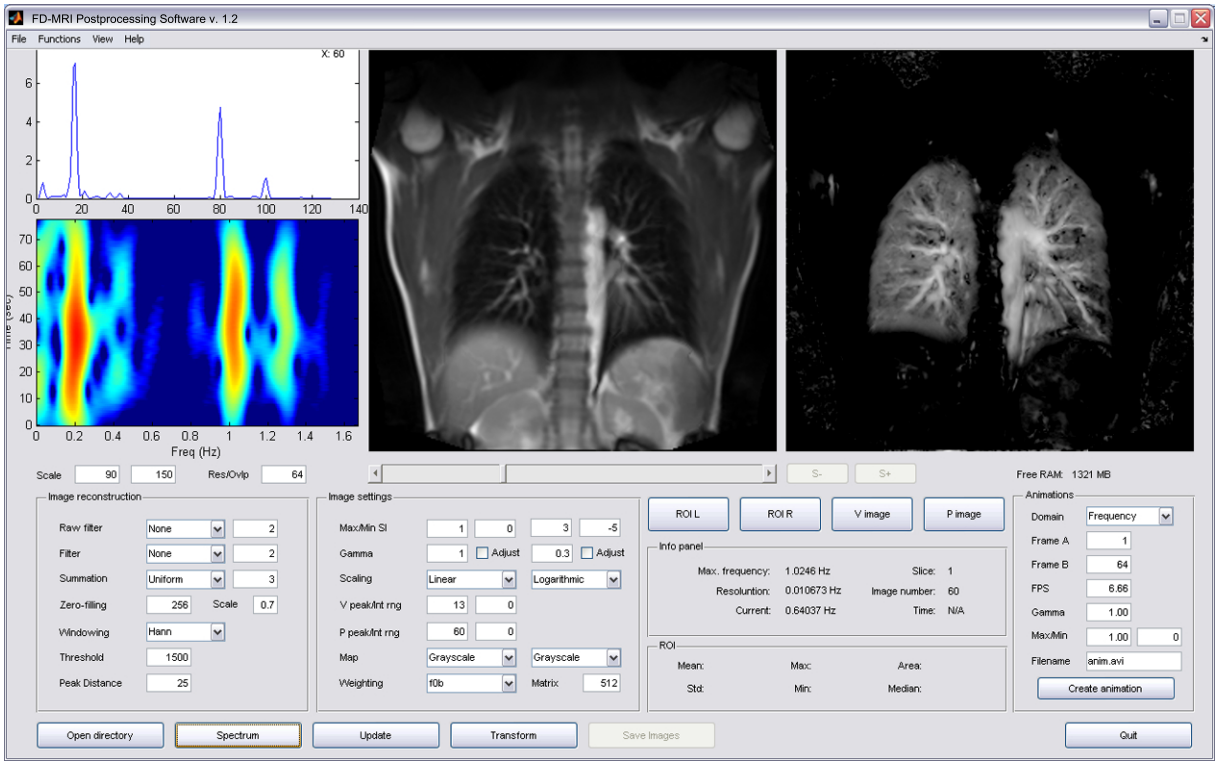

Figure 4.11: *The captured window shows the application for spectral analysis of the time-resolved data.*

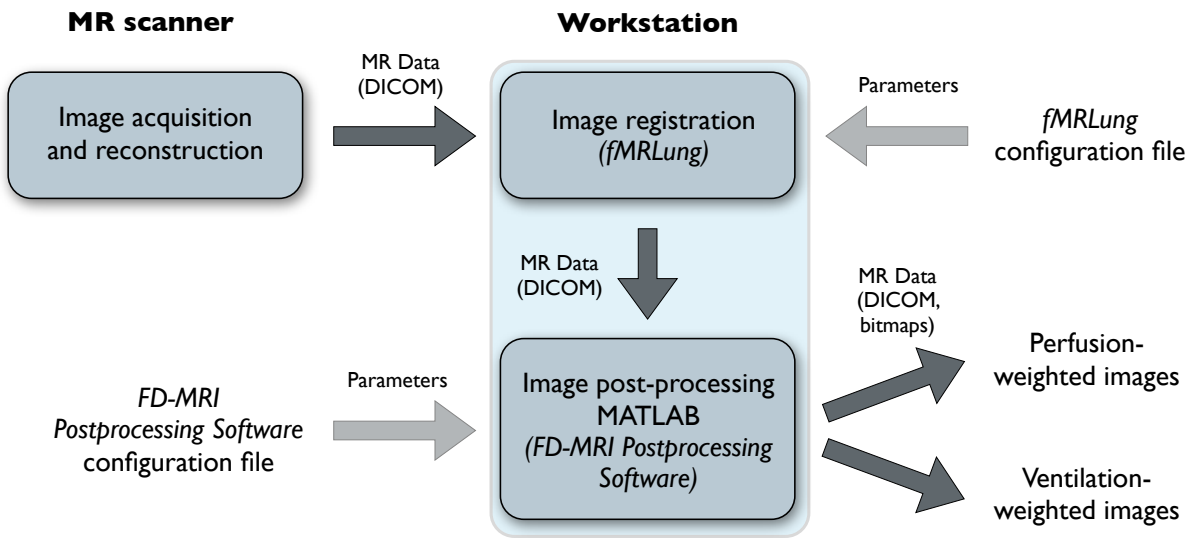

Figure 4.12: *An overview of the workflow used for postprocessing of the acquired time-resolved data and computation of the ventilation- and perfusion-weighted image arrays.*

4.4 Optimization of the image registration procedure

The non-rigid image registration algorithm presented in section 3.5 is automatic, and does not require the extraction of anatomical landmarks. An appropriate parametrization of the regularization operator allows maximizing the similarity of images. This is performed by optimizing the width σ of the Gaussian regularization operator (see Eq. 3.5.3). The peak signal-to-noise ratio (PSNR) was used as a measure of quality of the image registration. The mean squared error (MSE) is computed prior to calculation of the PSNR and defined as:

$$MSE(I,J) = \frac{1}{k \cdot m} \sum_{i=1}^{k} \sum_{j=1}^{m} (I(i,j) - J(i,j))^2 \tag{4.55}$$

where n and m are the pixel dimensions of the reference image I and the registered image J. The PSNR is given by:

$$PSNR(I,J) = 10 \cdot \log_{10} \left(\frac{b^2 - 1}{MSE(I,J)} \right) \tag{4.56}$$

here b is the maximum possible pixel value of the image and in case of 8-bit pixel samples is equal to 255.

The time-resolved data set containing $N = 198$ images acquired in free-breathing was registered using different values of σ. The mean PSNR and its standard deviation was calculated for a reference image, and all the registered images in the time-resolved data set:

$$\begin{aligned} \mu(PSNR) &= \frac{10}{N-1} \cdot \sum_{l=1}^{N-1} \log_{10} \left(\frac{b^2 - 1}{MSE(I,J_l)} \right) \\ \sigma(PSNR) &= \sqrt{\frac{1}{N-1} \sum_{l=1}^{N-1} (PSNR(I,J_l) - \mu(PSNR))^2} \end{aligned} \tag{4.57}$$

Figure 4.13 shows dependence between width of the regularization window σ and $\mu(PSNR)$ for the registered data set. The optimal value of σ was 0.5.

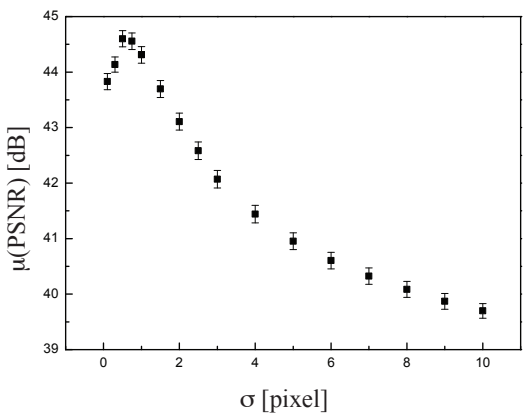

Figure 4.13: *Influence of the width of the Gaussian regularization window σ on the $\mu(PSNR)$ in the registered time-resolved thorax images.*

Perfusion- and ventilation-weighted images obtained using the Fourier decomposition method from unregistered and registered using different values of σ data sets are shown in figure 4.14. An example of a deformation vector field applied to a template image and calculated using the non-rigid registration algorithm is shown in figure 4.15.

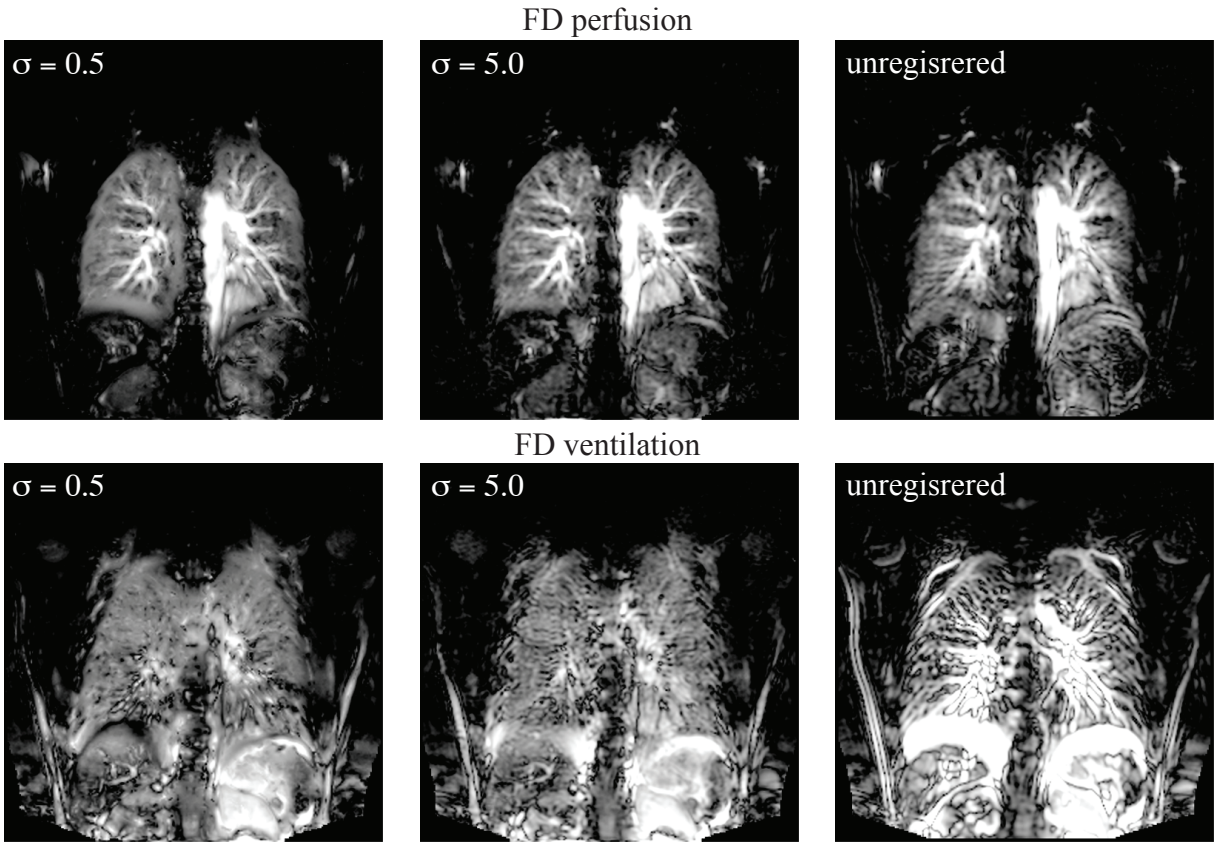

Figure 4.14: *Example of FD perfusion- and ventilation-weighted images obtained from the registered ($\sigma = 0.5$, $\sigma = 5.0$) and unregistered time-resolved data sets. The data was acquired in a healthy volunteer.*

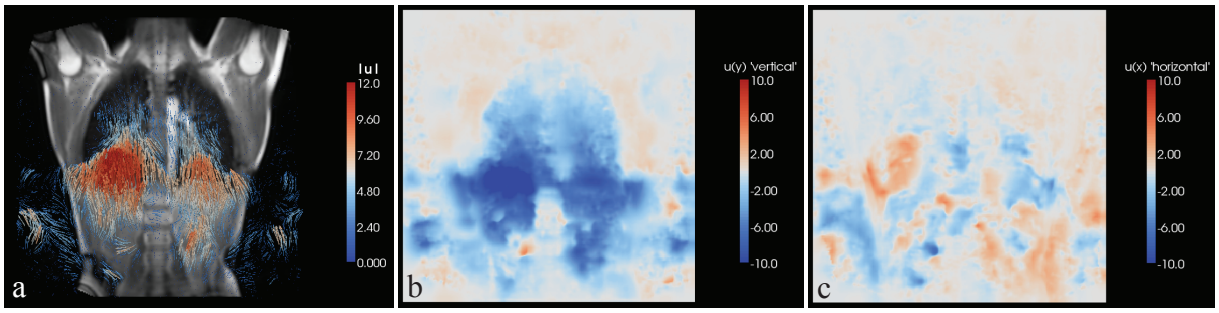

Figure 4.15: *Deformation vector field (a) was calculated using a reference image (acquired in a expiratory phase) and template image (acquired in a inspiratory phase). High deformation amplitudes are visible in the diaphragmatic regions. Images (b) and (c) show the vertical and the horizontal components of the deformation vector field. The majority of the movement takes place in the apical-basal direction.*

4.5 Examples of the perfusion- and ventilation-weighted images

In this section examples of perfusion- and ventilation-weighted images obtained using the Fourier decomposition (FD) (Fig. 4.16) and wavelet analysis (WA) (Fig. 4.17) postprocessing techniques have been shown. FD method was also used to generate dynamic animations of pulmonary perfusion (Fig. 4.18). Both spectral analysis methods were applied in a registered bSSFP data set acquired in a healthy volunteer.

4.5.1 FD-MRI

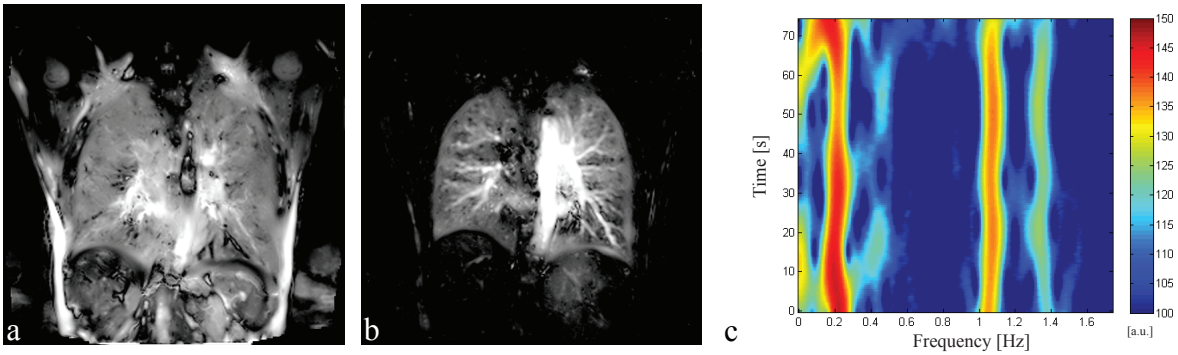

Figure 4.16: *Example FD ventilation-weighted (a) and perfusion-weighted (b) coronal images. Stability of the respiratory and cardiac frequencies during the bSSFP data acquisition can be analyzed with a spectrogram (c) using the STFT.*

4.5.2 WA-MRI

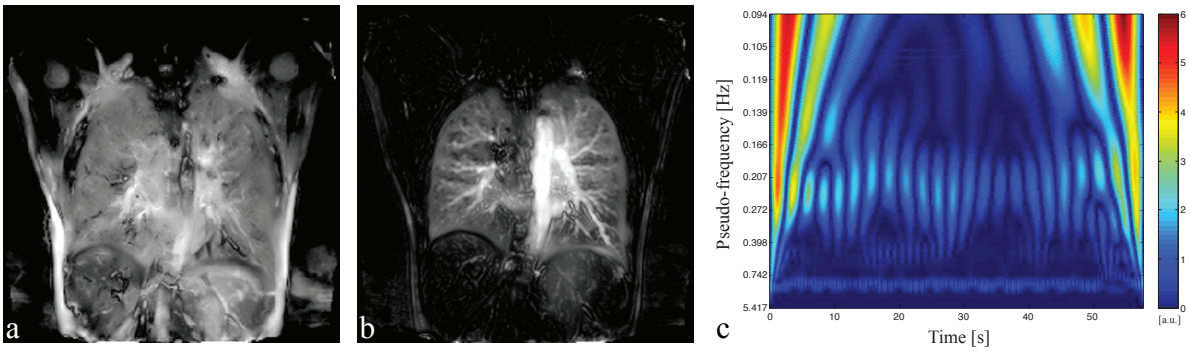

Figure 4.17: *Example WA ventilation-weighted (a) and perfusion-weighted (b) coronal images. Patterns of the respiratory and cardiac cycles are recognizable on a pseudo-frequency - time plane shown in a scalogram. The scalogram was calculated using the 'morlet' wavelet.*

4.5.3 Dynamic perfusion FD-MRI

The time-resolved bSSFP data set acquired in the same volunteer was postprocessed to create an animation showing dynamics of the pulmonary blood flow. Figure 4.18 shows six images obtained during a single cardiac cycle. After the FFT of the data set along the temporal dimension was performed, all frequency components other than the cardiac frequency were filtered out, and the remaining frequency components transformed using the inverse FFT back into the time domain yielding a time-resolved measurement of pulmonary blood flow (see section 4.2.1). The data was acquired with the rate of 6.66 images/second (TA = 122 ms, TW = 28 ms) in the same coronal slice position as the FD-MRI images shown in figure 4.29. The signal intensity of the consecutive image frames decreases as the blood flows into pulmonary arteries during the systole, and increases during the diastole.

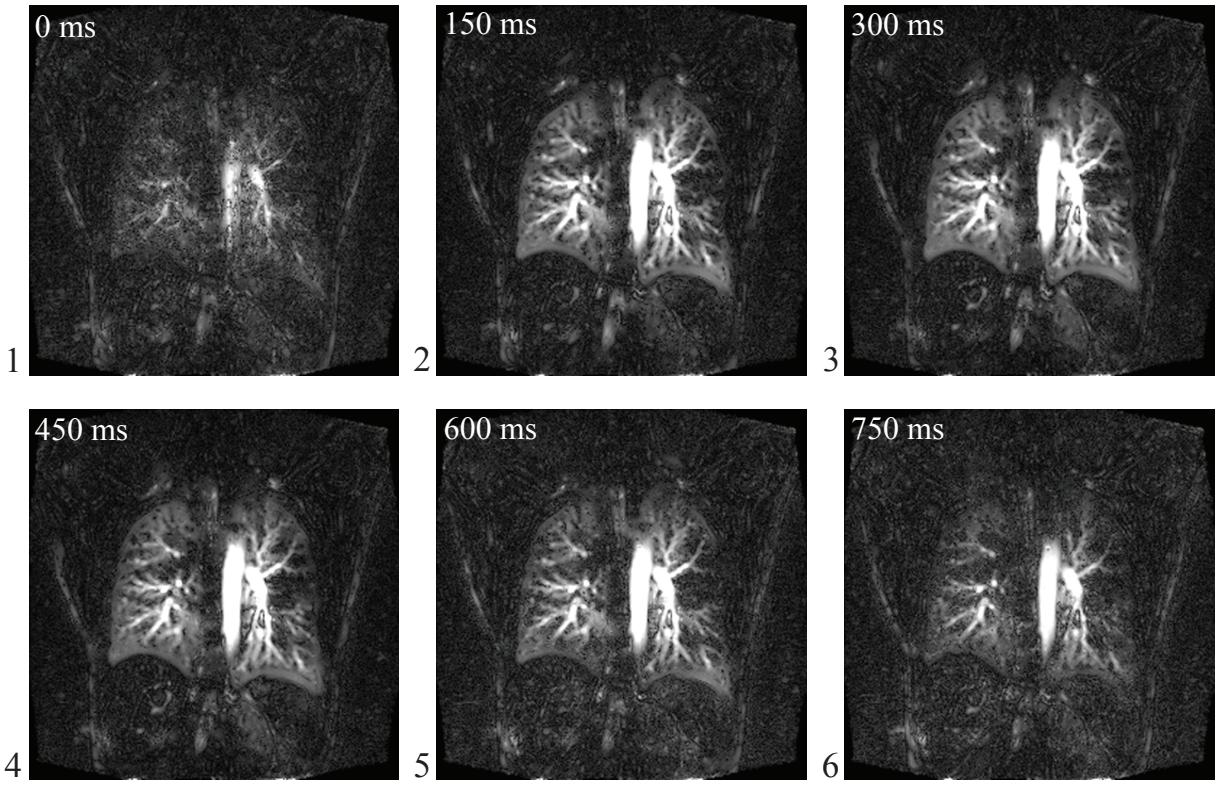

Figure 4.18: *Time-resolved pulmonary perfusion imaging using FD-MRI. Figure shows six images obtained during a single cardiac cycle.*

4.6 Reproducibility study of FD-MRI in a population of healthy volunteers

The goal of the study performed in a population of healthy volunteers was to verify the technical and medical reproducibility of Fourier decomposition MRI (FD-MRI). The study was approved by the ethic review board. Written informed consent was obtained from each subject prior to the examination. The study population comprised seventeen healthy nonsmoking volunteers (11 men, 6 women) with mean age of 36.5 ± 14.1 years (age range: 19 - 64 years).

4.6.1 MR protocol

The MR examinations were performed in a 1.5 T whole-body MR-scanner (MAGNETOM Avanto, Siemens Healthcare, Erlangen, Germany) using a combination of coils presented in section 3.1. All subjects were studied in head first supine position in the MR scanner with arms above the head. Prior to functional lung imaging, morphological scans were performed. The protocol started with a three-plane orthogonal localizers, HASTE sequence in coronal and transverse orientation in inspiration and 3D VIBE sequence in inspiration. Morphological imaging sequences served further for the slice positioning in all the subsequent scans. For FD-MRI the 2D bSSFP sequence (see section 4.1.1) was used. A set of five coronal slices numbered from posterior (S1) to anterior (S5) was acquired using time-resolved multi-slice scans to cover the volume of the chest (Fig. 4.19). The complete MR protocol comprising morphological and functional scans took no more than 20 minutes. The identical examination protocol was repeated after 24 hours in every subject.

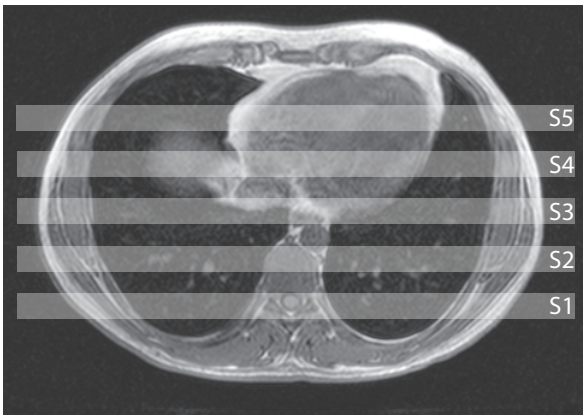

Figure 4.19: *A chest image in transverse orientation obtained using VIBE sequence in a healthy volunteer. The morphological scan was used for positioning of five coronal slices S1 (posterior) - S5 (anterior), which were further acquired with bSSFP sequence.*

4.6.2 Image postprocessing and analysis

All time-resolved bSSFP data sets acquired during the study were stored and registered to compensate for the respiratory motion. Perfusion and ventilation images were calculated for every acquired slice in all volunteers using the Fourier decomposition postprocessing method

(see section 4.2.1). Figures 4.20 and 4.21 show comparison between arrays of perfusion- and ventilation-weighted images obtained in a volunteer on the first and the second day of the study.

Analysis of the images was performed using *FD-MRI Postprocessing Software* application (see section 4.3). For the registered unprocessed bSSFP images, two regions of interest (ROI) in the left and two in the right lung were placed manually on the first image within every slice and propagated though the whole data set. Mean signal intensity $\mu_{i,j}(SI)$ was calculated in each ROI ($j = 1 \dots r$) for all images in a data set ($i = 1 \dots N$), and for every acquired slice ($k = 1 \dots 5$). An averaged mean signal intensity estimated for every propagated ROI is given by:

$$\mu_k(SI) = \sum_{j=1}^{r} \sum_{i=1}^{N} \frac{\mu_{k,j,i}(SI)}{rN} \tag{4.58}$$

A standard deviation of mean signal intensities calculated for each single ROI:

$$\sigma_k(SI) = \sum_{j=1}^{r} \frac{\sqrt{\sum_{i=1}^{N} (\mu_{k,j,i}(SI) - \mu_{k,j}(SI))^2 / N}}{r} \tag{4.59}$$

To estimate SNR, a standard deviation of the signal intensity was measured in two ROIs outside the body area. Positions of these ROI were projected through all registered unprocessed images:

$$\sigma_k(noise) = \sum_{j=1}^{r} \sum_{i=1}^{N} \frac{\sigma_{k,j,i}(noise)}{rN} \tag{4.60}$$

where $\sigma_{j,i}(noise)$ is standard deviation measured in a single ROI. The SNR was estimated as:

$$SNR_k = \frac{\mu_k(SI)}{\sigma_k(noise)} \tag{4.61}$$

To calculate the mean signal intensity change in the lung parenchyma with regard to the respiratory $\mu_k(A_R)$ and perfusion $\mu_k(A_C)$, the same ROIs as used for analysis of the unprocessed images were placed on the postprocessed perfusion and ventilation images. The values of $\mu_k(SI)$, $\mu_k(A_R)$ and $\mu_k(A_C)$ were used to determine the reproducibility of signal intensity among volunteers, and to estimate the expected mean slope of the signal intensity in the anterior posterior direction.

4.6.3 Statistical analysis

Statistical significance of similarities between means and variances of paired data was assessed using the paired t-test, or the non-parametric Wilcoxon signed rank paired test. The Jarque-Bera test was used to check whether the data was normally distributed. A P value of 0.05 was considered as statistically significant. Statistical analysis was performed with OriginPro 8.0 (OriginLab Corporation, Northampton, USA) and GraphPad Prism 5.01 (GraphPad Software, San Diego, California, USA).

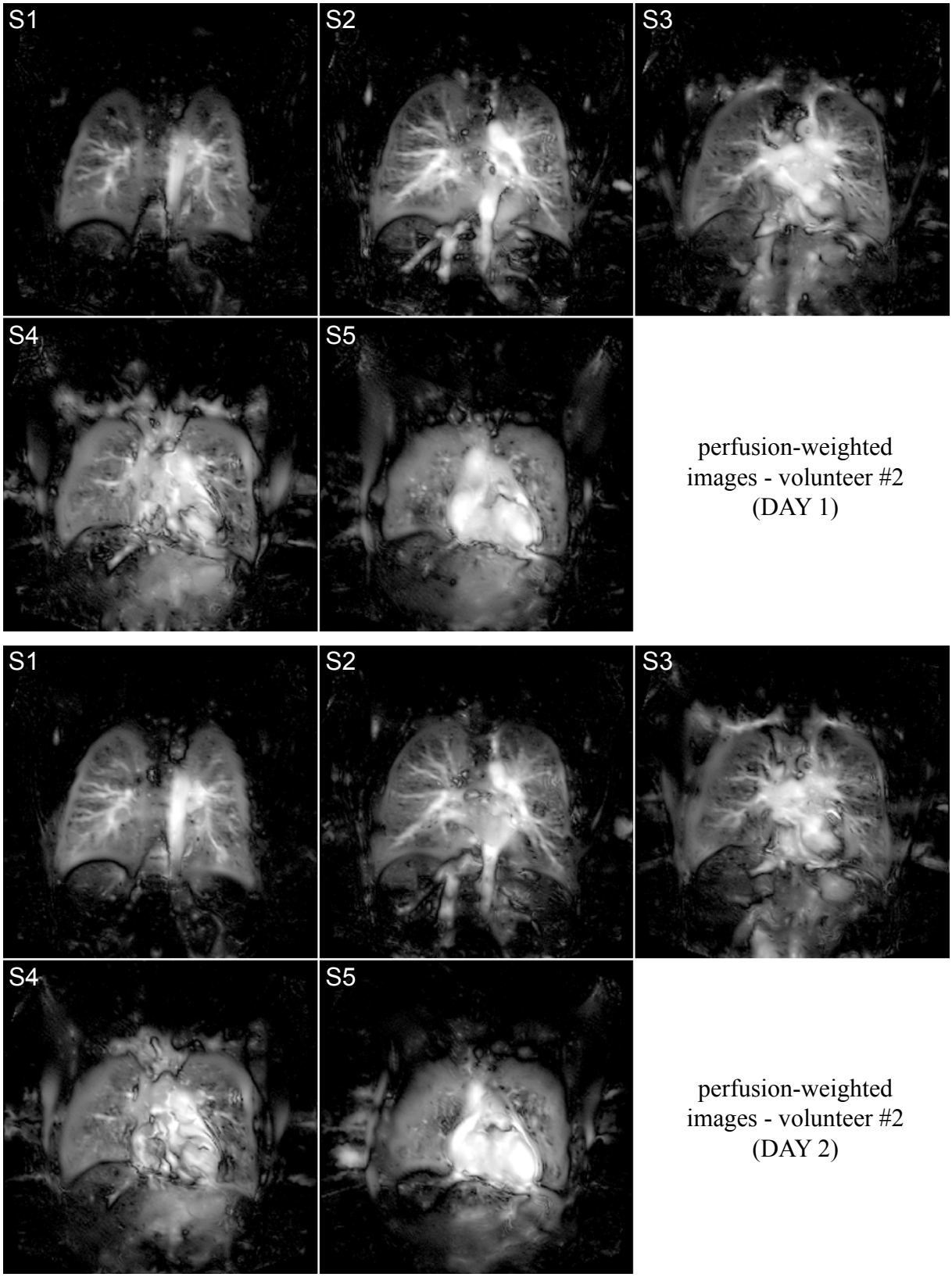

Figure 4.20: *Comparison between perfusion images obtained in five coronal slices using FD-MRI in a healthy volunteer. The images in the upper array were acquired on the first day, and in the lower array on the second day of the study.*

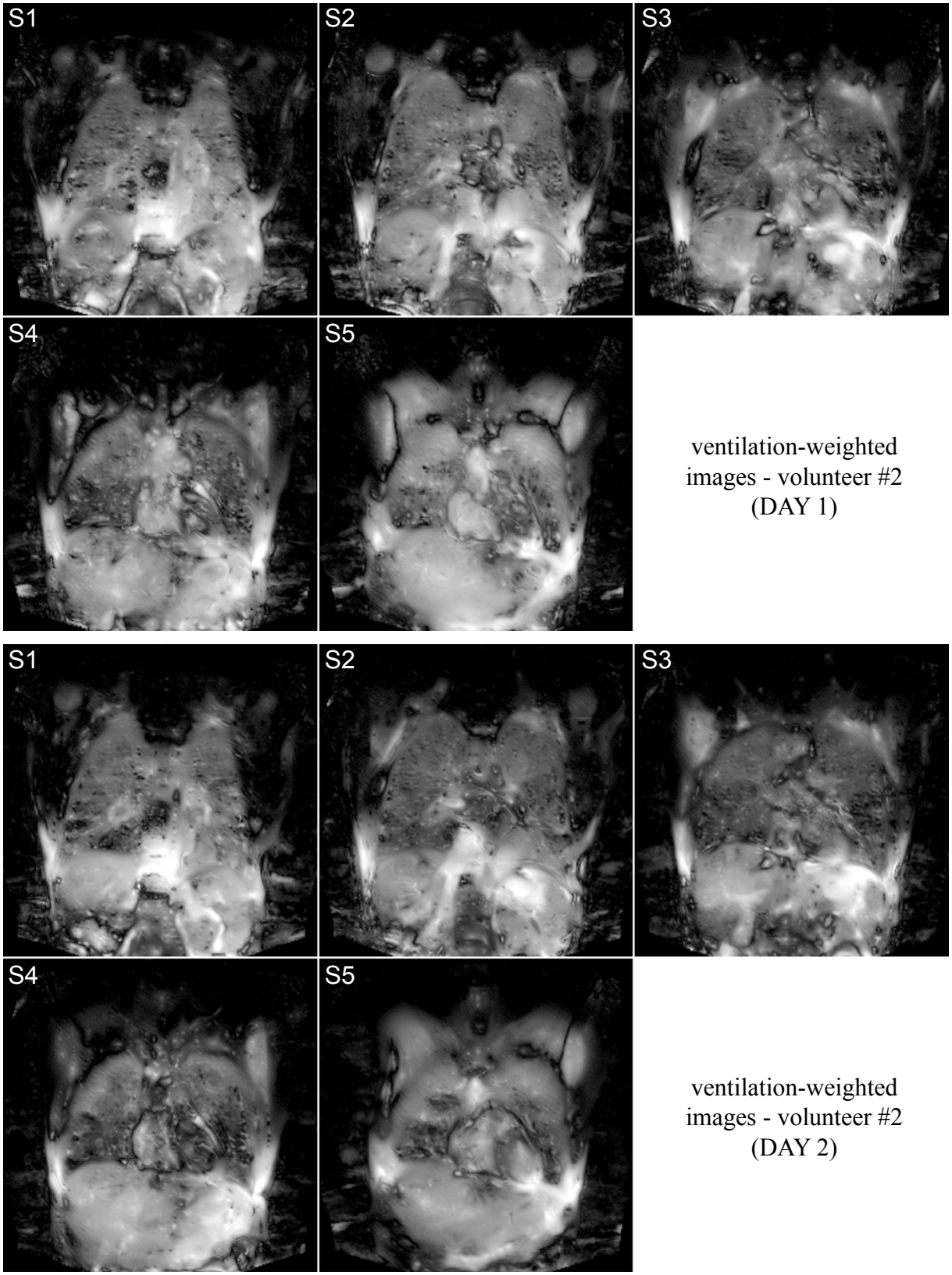

Figure 4.21: *Comparison between ventilation images obtained in five coronal slices using FD-MRI in a healthy volunteer. The images in the upper array were acquired on the first day, and in the lower array on the second day of the study.*

4.6.4 Technical reproducibility

The Wilcoxon signed pair rank test of $\mu(SI)$, $\mu(A_R)$, and $\mu(A_C)$ measured within all slices and all volunteers confirmed null hypothesis, which assumed no significant difference between values of measurements performed on the first and second day of the study ($\alpha = 0.01$). The values of $\mu(SI)$, $\mu(A_R)$, and $\mu(A_C)$ were log-normally distributed ($\alpha = 0.01$) and the function used to fit the data is given by:

$$y(x) = \begin{cases} \frac{a}{x} \exp\left(-\frac{\ln(x/x_0)}{2b}\right)^2 & \text{for} \quad x > 0 \\ 0 & \text{for} \quad x \leq 0 \end{cases} \tag{4.62}$$

where a, b, and x_0 are free parameters.

Figure 4.22 presents correlations of $\mu(SI)$, $\mu(A_R)$, and $\mu(A_C)$ values measured on the first and second day, as well as histograms with fitted log-normal functions. Parameters of log-normal distributions and the Spearman's rank correlation coefficients ρ for all these measurements are shown in table 4.2.

Table 4.2: *Parameters of log-normal distributions fitted to all values of $\mu(SI)$, $\mu(A_R)$, and $\mu(A_C)$ measured for each slice, along with the Spearman's rank correlation coefficient ρ between values measured on the first and second day of the study.*

	x_0	a	b	ρ ($P < 0.001$)
$\mu(SI)$	51.67 ± 0.77	1255.36 ± 67.77	0.24 ± 0.02	0.979
$\mu(A_R)$	5.61 ± 0.24	106.73 ± 4.79	0.68 ± 0.04	0.877
$\mu(A_C)$	4.29 ± 0.11	110.33 ± 5.94	0.37 ± 0.02	0.952

Signal intensity change in pulmonary parenchyma caused by respiration in registered unprocessed images was on average 10.6 ± 5.7 % of SI and by perfusion 8.4 ± 1.9 % of SI. Gravitational force influenced the parenchyma density and perfusion along the anterior-posterior direction in all volunteers placed in the MR scanner in the supine position. Mean slopes calculated for $\mu(SI)$, $\mu(A_R)$, and $\mu(A_C)$ in the anterior-posterior direction are shown in table 4.3.

Table 4.3: *Slopes of mean signal intensity, signal changes caused by respiratory and cardiac cycles in anterior-posterior direction.*

	Slope (anterior-posterior) [%/cm]
$\mu(SI)$	5.1 ± 0.6
$\mu(A_R)$	7.0 ± 0.9
$\mu(A_C)$	11.5 ± 1.2

The average SNR in the lung parenchyma in registered images for all subjects was 26.9 ± 5.3. The SNR in the most dorsal slice was 31.6 ± 9.7 and in the most ventral 22.8 ± 4.2.

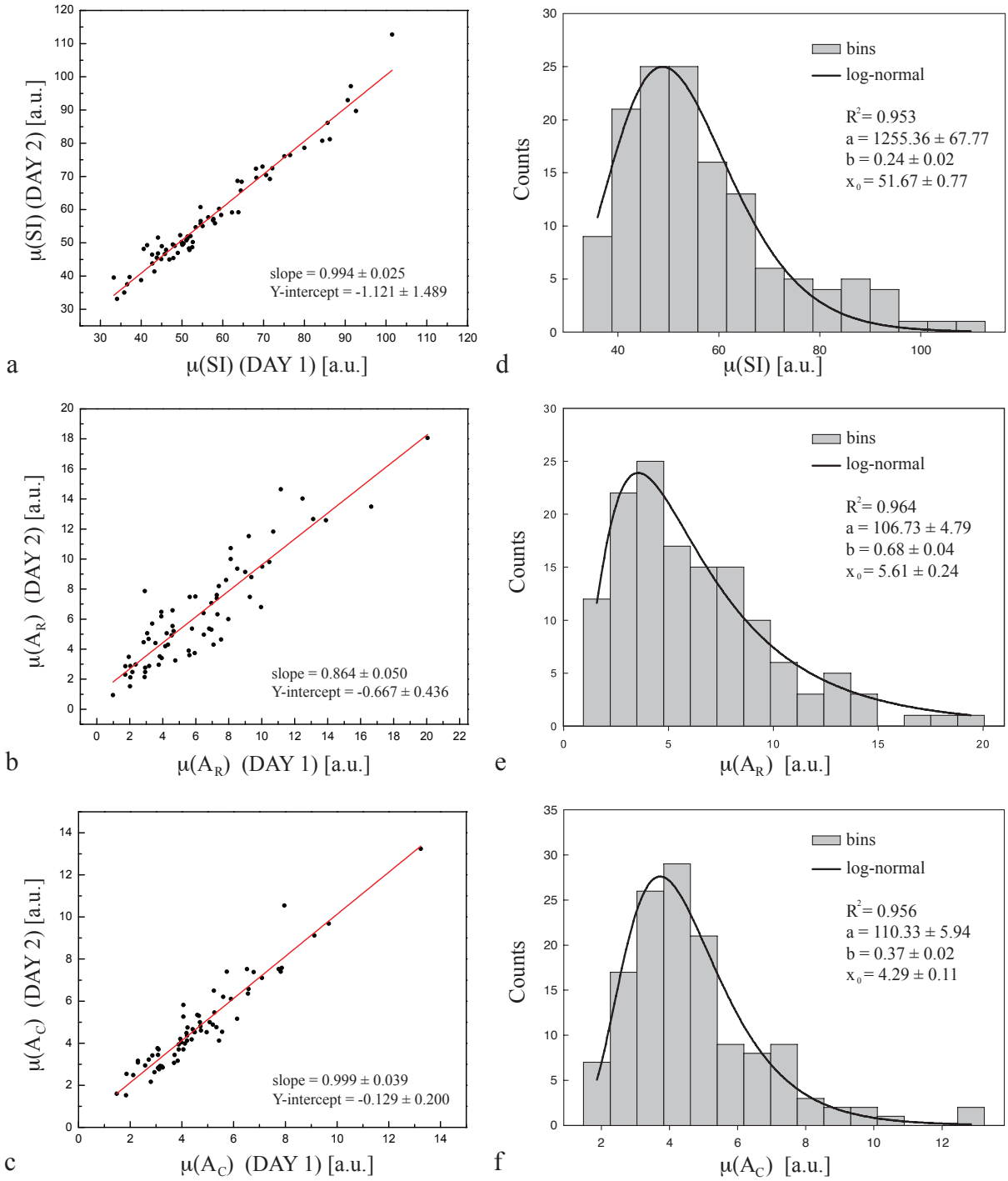

Figure 4.22: *The left column shows the correlation between values of $\mu(SI)$ (a), $\mu(A_R)$ (b) and $\mu(A_C)$ (c) measured for each slice in every volunteer. The right column presents histograms and log-normal distributions of all values of $\mu(SI)$, $\mu(A_R)$, and $\mu(A_C)$.*

4.6.5 Variability of respiratory and cardiac frequencies

One of the interesting aspects of the study was related to the respiratory and cardiac frequency variability, as well as to the minimal and maximal ranges of both frequencies in the population of volunteers (Fig. 4.23). The short-time Fourier transform (STFT) (see Eq. 4.12) was used to determine the frequency changes over time during the measurements. Due to the nature of signal intensity variations in the lung parenchyma (see Eq. 4.54) higher harmonic frequencies appear in a spectrum and spectrogram. Possible overlapping of frequency peaks in a spectrum, especially a back-folded second harmonic of the cardiac cycle can negatively influence the quality of perfusion and ventilation images. Amplitudes of the third and higher harmonics lies below the noise level thus they will not be taken into account.

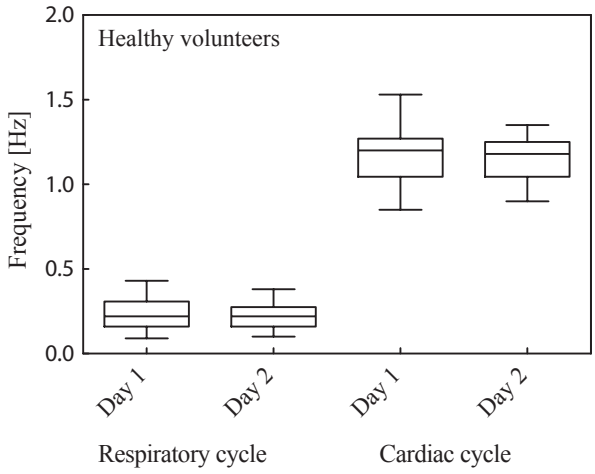

Figure 4.23: *Diagram shows respiratory and cardiac frequencies measured from frequency spectra in healthy volunteers on the first and second day of the study.*

Distribution of the first and the second harmonic frequency of the respiratory cycle ω_{R1} and ω_{R2}, as well as the first and the second harmonic frequencies of cardiac cycle, ω_{R1} and ω_{R2} measured in each slice were normally distributed (Jarque-Bera test, $\alpha = 0.01$). Two sample t-tests showed no significant difference for the distribution of ω_{R1} and ω_{C1} on the first and the second day of the study ($\alpha = 0.01$). The respiratory and cardiac frequency on the first day were $\omega_{R1} = 0.23 \pm 0.09$ Hz and $\omega_{C1} = 1.18 \pm 0.15$ Hz, on the second day $\omega_{R1} = 0.22 \pm 0.07$ Hz and $\omega_{C1} = 1.15 \pm 0.12$ Hz.

Gaussian distributions of the first and the second harmonic frequency of the respiratory cycle $G_{\omega_{R1}}$ and $G_{\omega_{R2}}$, as well as the first and the second harmonic frequencies of cardiac cycle, $G_{\omega_{C1}}$ and $G_{\omega_{C2}}$ were estimated to determine probabilities of frequency overlapping. Figure 4.24 shows histograms of all analyzed frequencies and estimated Gaussian distributions. Since there was no significant correlation between pairs of respiratory and cardiac frequencies measured in every volunteer (Pearson correlation coefficient $r = -0.198$, $P = 0.1$), thus, $P(\omega_{Ri})$ and $P(\omega_{Cj})$ for $i, j \in \{1, 2\}$ can be considered as independent events. The probability that two independent events occur is given by:

$$P(\omega_{Ri} \cdot \omega_{Cj}) = P(\omega_{Ri}) \cdot P(\omega_{Cj}) \quad \text{for} \quad i, j \in \{1, 2\} \tag{4.63}$$

Integration of the product of probability distributions over the whole frequency spectrum yields

probabilities of frequency overlapping. Assuming that the peak width $\Delta\omega = 0.05$ Hz and the spectral bandwidth $\omega_B = 1.667$ Hz:

$$P(\omega_{Ri} = \omega_{Cj}) = \sum_{\omega=1}^{\omega_B} G_{Ri}(\omega) \cdot G_{Cj}(\omega)\Delta\omega \quad \text{for} \quad i, j \in \{1, 2\} \tag{4.64}$$

Table 4.4 shows the mean values and the standard deviations of frequency distributions, as well as the probabilities of overlapping for the first and the second harmonic frequencies of the respiratory and cardiac cycles.

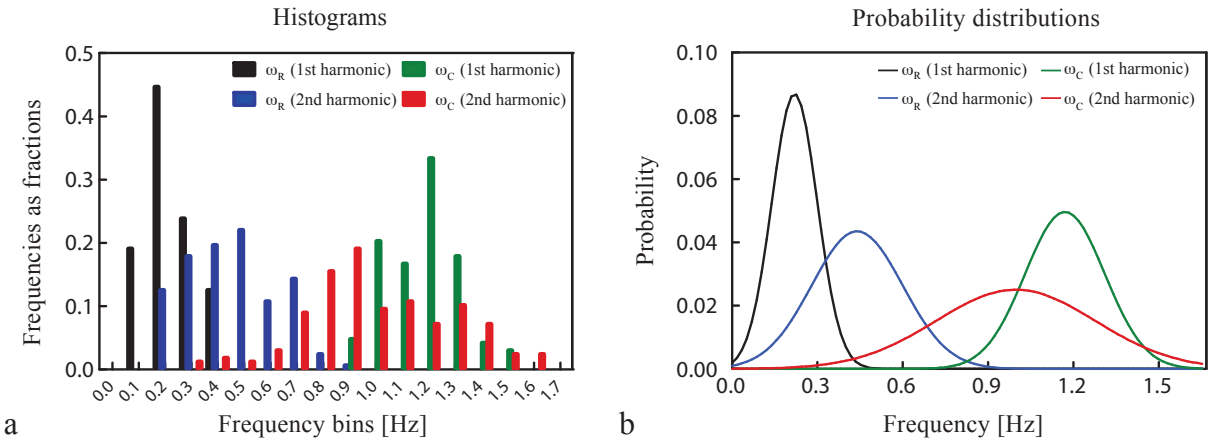

Figure 4.24: *Distributions of the first and the second harmonic frequencies of the respiratory and cardiac cycles measured for all slices in every volunteer shown in the histograms (a). Diagram (b) presents Gaussian probability distributions estimated from the histograms. Note that the distribution of the second harmonic frequency of cardiac cycle is aliased in the frequency spectrum.*

Table 4.4: *Means and standard deviations of the respiratory and cardiac frequency distributions along with the probabilities for overlapping of peak frequencies.*

	μ [Hz]	σ [Hz]	ω_{R1}	ω_{R2}	ω_{C1}	ω_{C2}
ω_{R1}	0.22	0.08	1	0	$< 10^{-8}$	0.004
ω_{R2}	0.44	0.16	0	1	$< 10^{-3}$	0.025
ω_{C1}	1.17	0.14	$< 10^{-8}$	$< 10^{-3}$	1	0.095
ω_{C2}	0.99	0.28	0.004	0.025	0.095	1

4.7 Comparison between FD-MRI and DCE-MRI in cystic fibrosis patients

Cystic fibrosis (CF) is the most frequent autosomal recessive disorder responsible for premature death in the Caucasian population. The genetic defect causes aberrations of volume and composition of airway surface fluid, which leads to chronic lung infections, airway obstructions as well as alteration of pulmonary perfusion and ventilation [Gibson et al., 2003]. Recent studies have shown high diagnostic value of ^{1}H MRI [Puderbach et al., 2007a], Dynamic Contrast-Enhanced MRI [Eichinger et al., 2006], as well as hyperpolarized ^{3}He MRI [Mentore et al., 2005] in detecting lung structural changes in CF patients.

The goal of this study was to compare two methods of assessment of the pulmonary perfusion: Fourier decomposition MRI (FD-MRI) and Dynamic Contrast-Enhanced MRI (DCE-MRI) in patients with CF [Bauman et al., 2010b].

4.7.1 MR protocol

Eight CF patients (mean age 7.3 years, range: 1 - 23 years) were examined on a 1.5 T whole-body MR-scanner (MAGNETOM Avanto, Siemens Healthcare, Erlangen, Germany) using a combination of coils presented in section 3.1.

Prior the the functional lung imaging morphological scans were performed. The protocol contained a three-plane orthogonal localizers and HASTE sequence in coronal and transverse orientation. Additionally, the non-cooperative patients (children) were scanned using a free-breathing 2D SSFP sequence in coronal and transverse orientation, while the cooperative patients (adults) were scanned using a VIBE sequence in transverse orientation. In the FD-MRI sequence the slice thickness (ST) was reduced to 10 mm, due to the fact that the signal intensity of the lung parenchyma in children is much higher than in adults, while the volume of the thorax is smaller. The FOV was adjusted for every patient, however, it should be noted that significant decrease in the FOV, reduces the minimal achievable TE, which implies a lower signal intensity in the lung parenchyma. Interval TW between acquisition of subsequent images of the time-resolved data sets was decreased to 120 ms for patients with cardiac frequency higher than 1.66 Hz. Other sequence parameters were identical with the protocol described in the section 4.1.1. For DCE-MRI, a 3D+t FLASH sequence ($TR/TE = 1.8/0.2$ ms, $\alpha = 20°$, $ST = 5$ mm) was performed after the FD-MRI acquisition. The contrast agent in form of gadopentetate dimeglumine (Magnevist, Bayer Vital, Germany) was administered in dose of 0.1 mmol/kg body weight at rate of $2 - 5$ mL/s. The image acquisition started simultaneously with the contrast agent injection. As a result 3D+t time-resolved data sets were generated as the contrast agent was passing through the pulmonary circulation enhancing signal intensity in perfused regions with a temporal resolution of 1.5 s/volume. Children below the age of 6 years were sedated with oral chloralhydrate 10% (100 mg/kg body weight) and monitored during the MR examination by pulsoxymetry and a pediatrician.

4.7.2 Radiological and statistical analysis

FD and DCE images were produced for every acquired slice. DCE images were produced by adding two neighboring DCE images obtained in slice positions corresponding to slice positions of FD images, due to the fact that the slice thickness of the DCE images were two times smaller than of the FD images. Images produced for the corresponding slice positions were visually independently assessed for perfusion defects using a field based dedicated scoring system. Each lung on the perfusion images was divided into three equal fields by marking manually two points (one in the apices of the lung and the second in the base of the lung) and plotting two parallel lines in 1/3 and 2/3 of the distance between them.

The scores for each field were defined as follows:

- 2 (perfusion defect in more than 50% of the lung field)
- 1 (perfusion defect in less than 50% of the lung field)
- 0 (no perfusion defect)

Score distribution per slice in all patients and in all images is shown in table 4.5.

Table 4.5: *Distribution of scores for FD-MRI and DCE-MRI techniques.*

	FD perfusion	DCE perfusion
Number of slices	24	24
Mean score per slice	5.22	5.30
Std. deviation of scores per slice	2.23	2.58
Sum of scores	120	122

Spearman rank test correlation between scores distributed in all patients for both imaging methods in all corresponding lung fields was $\rho_{all} = 0.82$ ($P < 0.05$). Correlations for scores distributed in corresponding lung fields are shown in table 4.6. The strongest correlation was achieved in the right lung and in the upper fields of the lung. The paracardiac region showed the weakest correlation.

Table 4.6: *Spearman rank test correlation between FD and DCE perfusion images in corresponding lung fields (RU - upper right lung, RM - middle right lung, RL - lower right lung, LU - upper left lung, LM - middle left lung, LL - lower left lung).*

	RU	RM	RL	LU	LM	LL
correlation ρ	0.94	0.79	0.86	0.88	0.59	0.59

To calculate SNR in the lung tissue, lung areas were segmented in all registered time-resolved data sets. The average SNR in the lung parenchyma within all patients and all slices was:

50.99 ± 21.52 (maximal 110.28 ± 6.04, minimal 18.01 ± 0.92). The respiratory and cardiac frequencies in all CF patients are shown in figure 4.25. The average respiratory and cardiac frequency were $\omega_{R1} = 0.48 \pm 0.13$ Hz (maximal 0.73 ± 0.07 Hz, minimal 0.36 ± 0.11 Hz) and $\omega_{C1} = 1.37 \pm 0.22$ Hz (maximal 1.74 ± 0.10 Hz, minimal 1.08 ± 0.15 Hz), respectively.

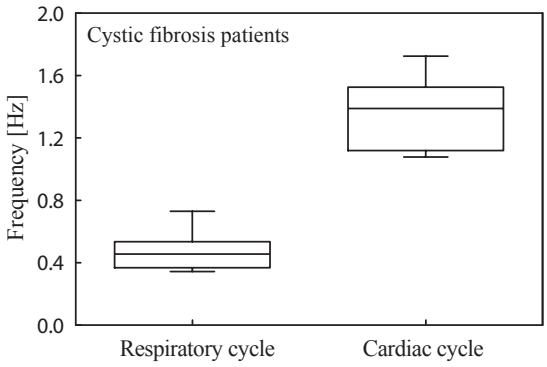

Figure 4.25: *Diagram shows respiratory and cardiac frequencies measured from frequency spectra in the cystic fibrosis patients.*

A visual comparison between FD-MRI and DCE-MRI perfusion images, as well as the score sum per slice are shown in figures 4.26 and 4.27.

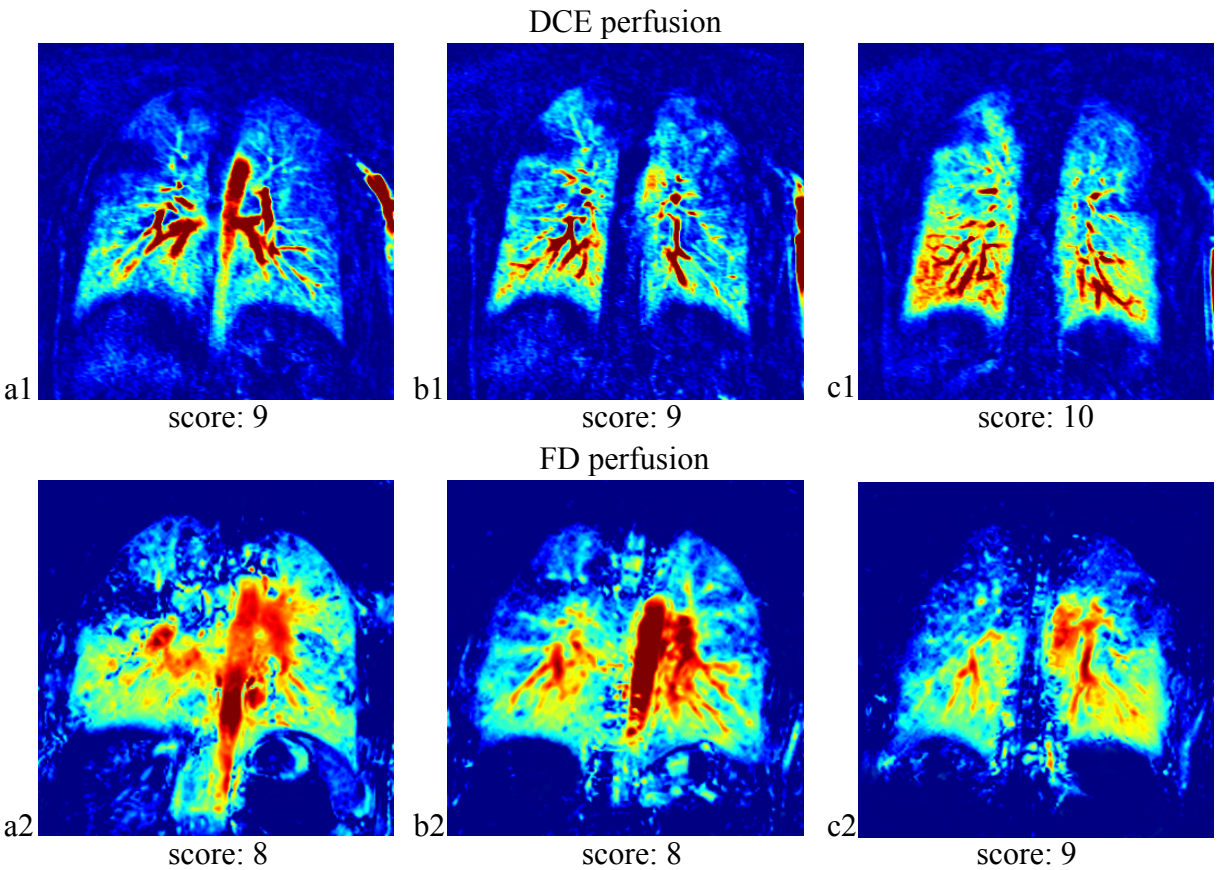

Figure 4.26: *Comparison between lung perfusion images obtained using DCE-MRI (upper row) and FD-MRI (lower row) for three corresponding coronal slice positions in a 23 years old female CF patient. The score sum per slice is given under each image.*

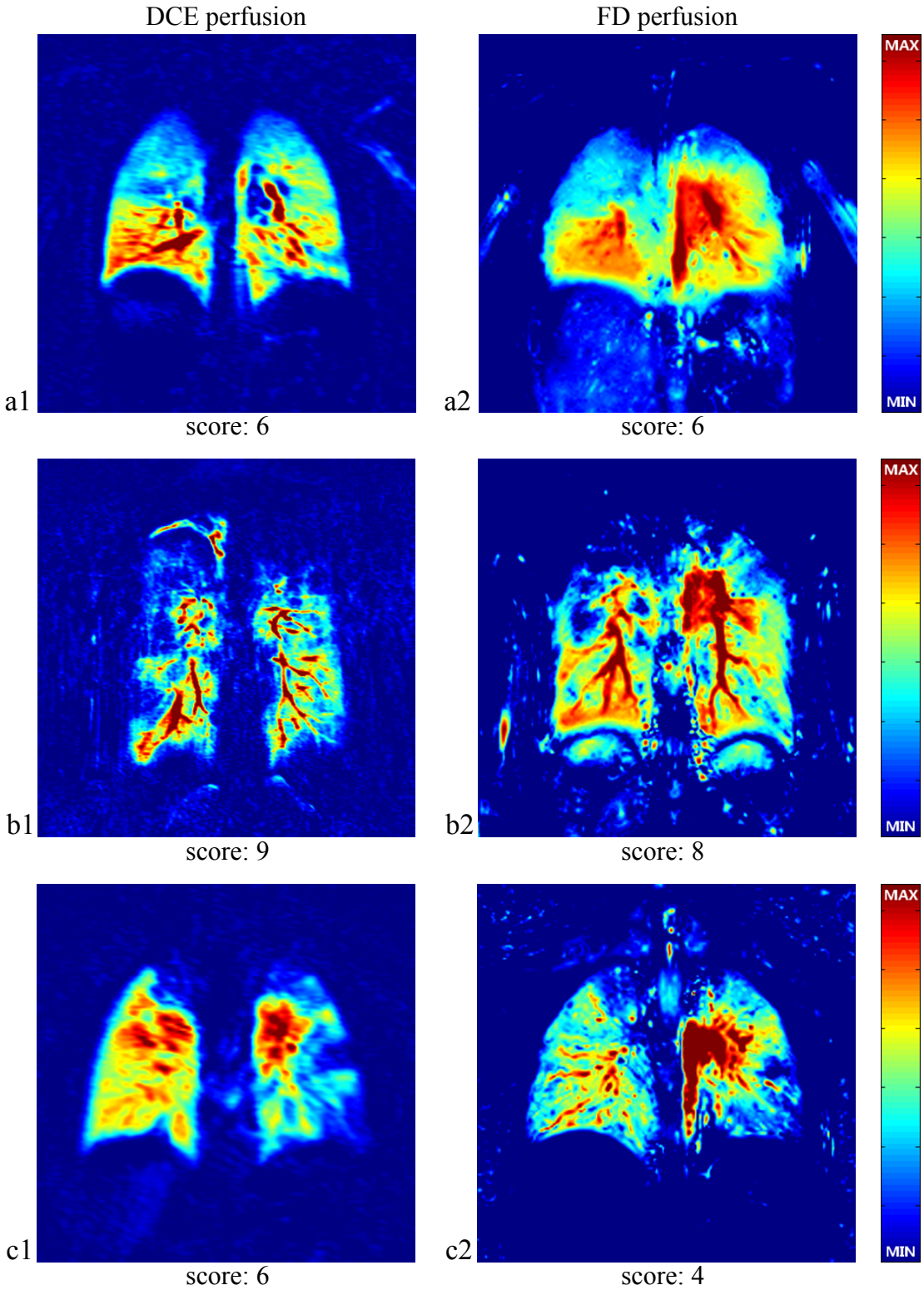

Figure 4.27: *Comparison between lung perfusion images obtained using DCE-MRI (left column) and FD-MRI (right column) for corresponding coronal slice positions in three CF patients: 4 years old male (a1, a2), 19 years old female (b1, b2), 3 years old female (c1, c2). The score sum per slice is given under each image.*

Figure 4.28 shows feasibility of FD-MRI in infants (younger than 1 year) where administration of the intravenous contrast agent is not recommended. A single bSSFP image from the time-resolved data set shows very high signal intensity in the lung parenchyma in comparison to older patients, which results in high amplitude of signal change in perfusion-weighted and ventilation-weighted images. The patient was lying on his left side during the MR examination. The signal intensity in all images in the left lung was higher than in the right lung, as a consequence of the gravitational effect on the distribution of pulmonary blood.

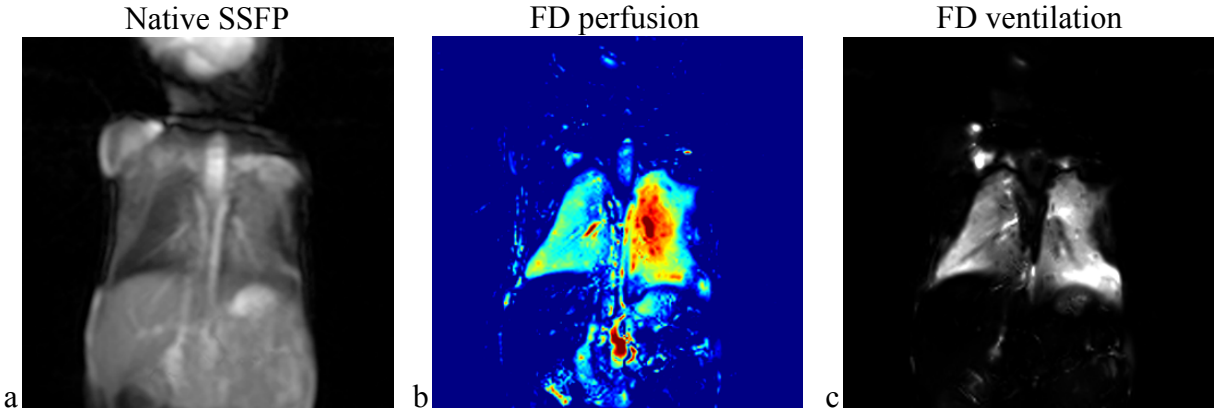

Figure 4.28: *Data obtained in a 3 weeks old male CF patient: a native bSSFP image (a), perfusion-weighted (b) and ventilation-weighted (c) images.*

4.8 Clinical examples

This section presents clinical examples, where FD-MRI acquisition was performed in combination with morphological chest MRI, CT scans, and DCE-MRI. This allowed for multimodal comparison of lung pathologies. The FD-MRI sequence (see the imaging protocol in section 4.1.1) was included into the standard thorax MR examination protocol and executed before an administration of an intravenous contrast agent.

4.8.1 Cystic parenchymal defect of the lung

Images from a 19 years old male patient with a cystic parenchymal defect in the right lower lobe preceded by an inflammation of the lung tissue are presented in figure 4.29. The CT scan shows lack of a lung tissue in the lower lobe of the right lung. The same information is provided by the ventilation-weighted image in a corresponding lung area.

Lack of contracting tissue in the affected lung region yields no detectable signal change at the respiratory frequency. Moreover, this lung area showed lack of signal on the perfusion-weighted image, due to the lack of the pulmonary blood flow. For comparison, a DCE-MRI scan was available for this patient.

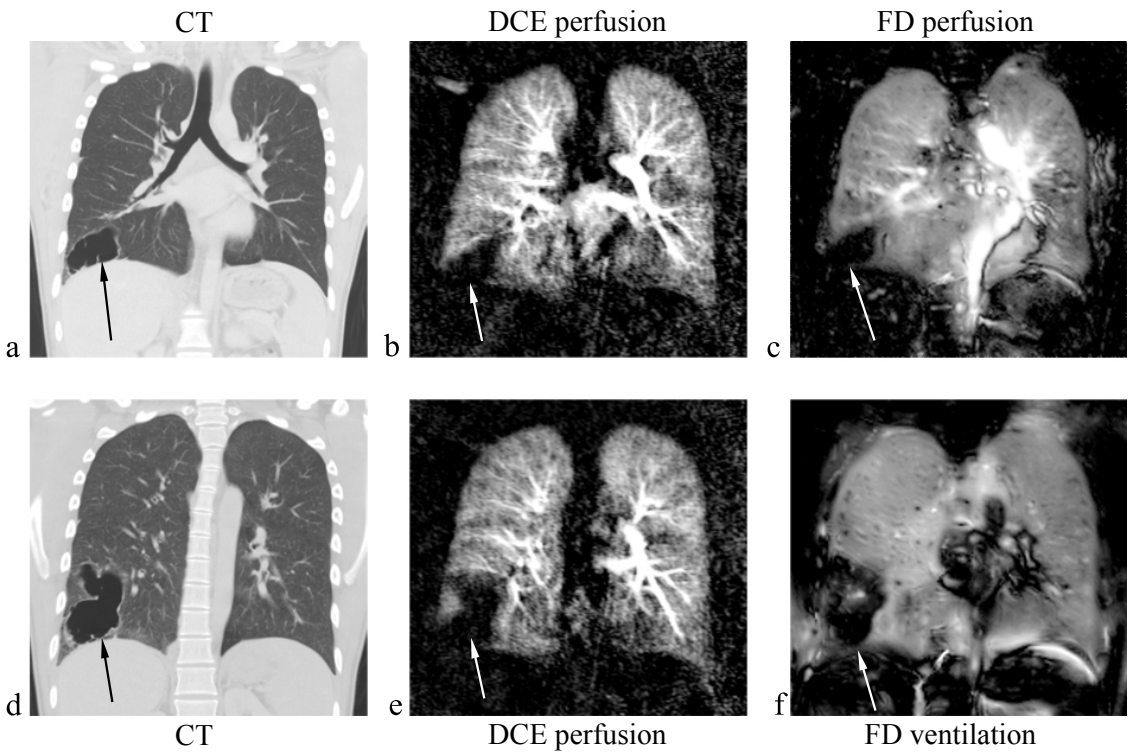

Figure 4.29: *Morphological CT in coronal view (a, d) of a* 19 *year old male patient with cystic parenchymal defect in the lobe of the right lung (arrows) shows a tissue density alteration. A perfusion defect in DCE-MRI perfusion image (b, e) is clearly visible on the FD perfusion-weighted image (c) and FD ventilation-weighted image (f).*

4.8.2 Pulmonary embolism

Figure 4.30 and 4.31 show results of follow-up using morphological MRI, FD-MRI and DCE-MRI in a 27 years old female patient with pulmonary embolism. Coronal SSFP image from the first examination showed a thrombus in the right lower artery in the lower lobe of the right lung blocking the pulmonary blood flow to this part of the lung. In this case, only the systemic circulation provides oxygenated blood to the affected lung region. Sagittal ventilation-weighted image showed no pathological alteration of the parenchyma density change. High signal intensity changes A_R and A_C can be noticed in the posterior parts of the lung, as a result of the influence of the gravity on the distribution of pulmonary blood and parenchyma (see section 2.4.5). The alveoli in the gravity-dependent regions have higher change of volume during respiration, and for this reason cause higher signal intensity change in the time-resolved MR data.

Large perfusion defects are visible in the perfusion-weighted images. In these regions also the systemic blood flow was not observed, since amplitude of the signal intensity change due to the blood flow through the bronchial arteries was not detectable.

The pulmonary embolism was treated with an anti-coagulant agent (phenprocoumon). During the therapy the MR examination was repeated. Native SSFP image obtained during the second examination showed no thrombus in the pulmonary artery.

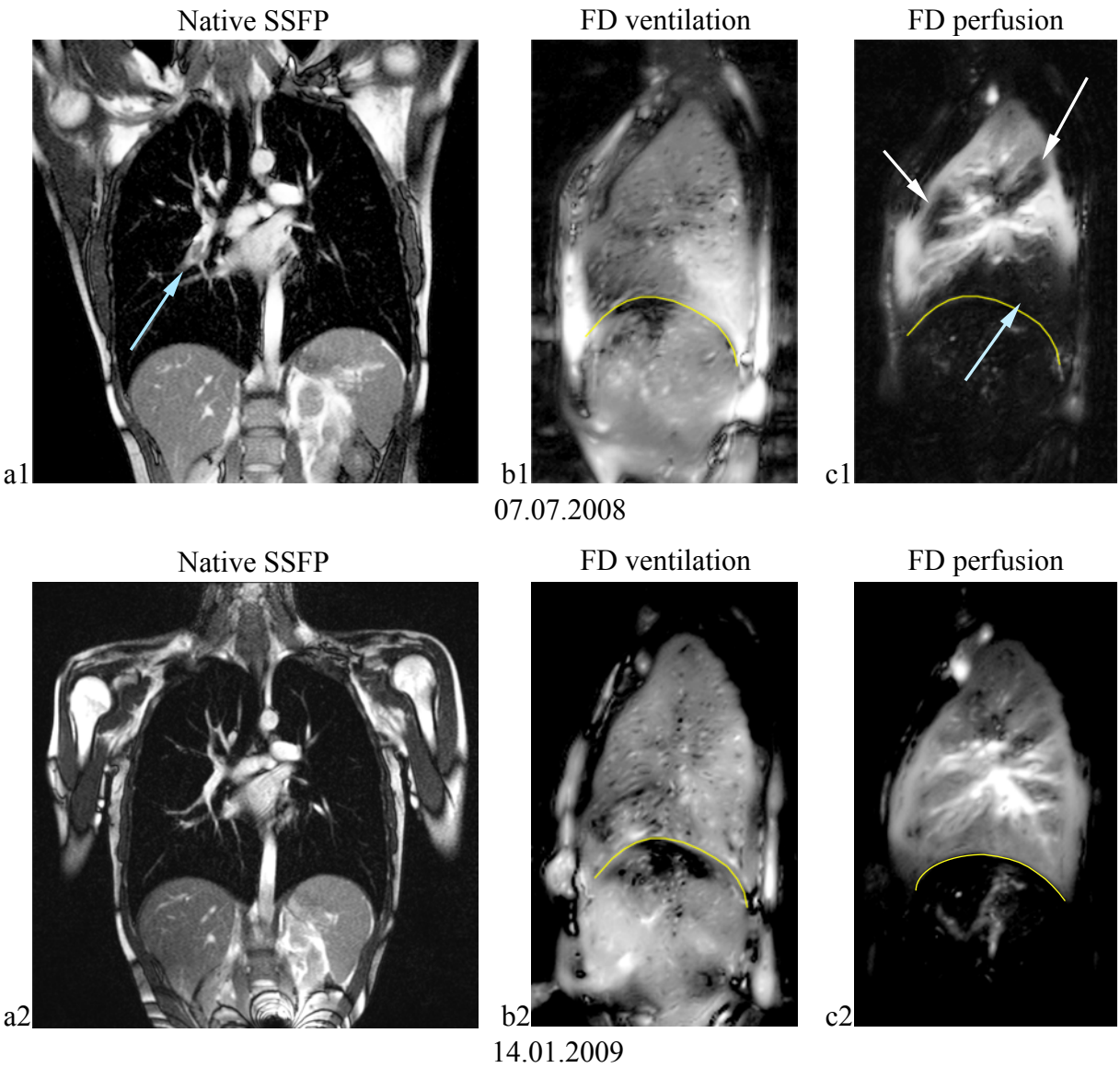

Figure 4.30: *Image (a1) shows a thrombus in lower lobe of the right lung (blue arrow) obtained from a 27 year old female patient with pulmonary embolism using native SSFP sequence. Sagittal FD ventilation images (b1, b2) shows no density change alteration. Sagittal FD perfusion image (c1) shows large defects in the upper and lower lobe of the right lung (arrows). Images from the second examination shows that the thrombus has dissolved (a2) and pulmonary perfusion improved (c2). For orientation the diaphragmatic position was marked by a yellow line in sagittal images.*

The pulmonary perfusion significantly improved in the previously affected regions. Comparison between coronal FD-MRI and DCE-MRI perfusion images acquired in the same patient during three follow-up examinations are shown in figure 4.31.

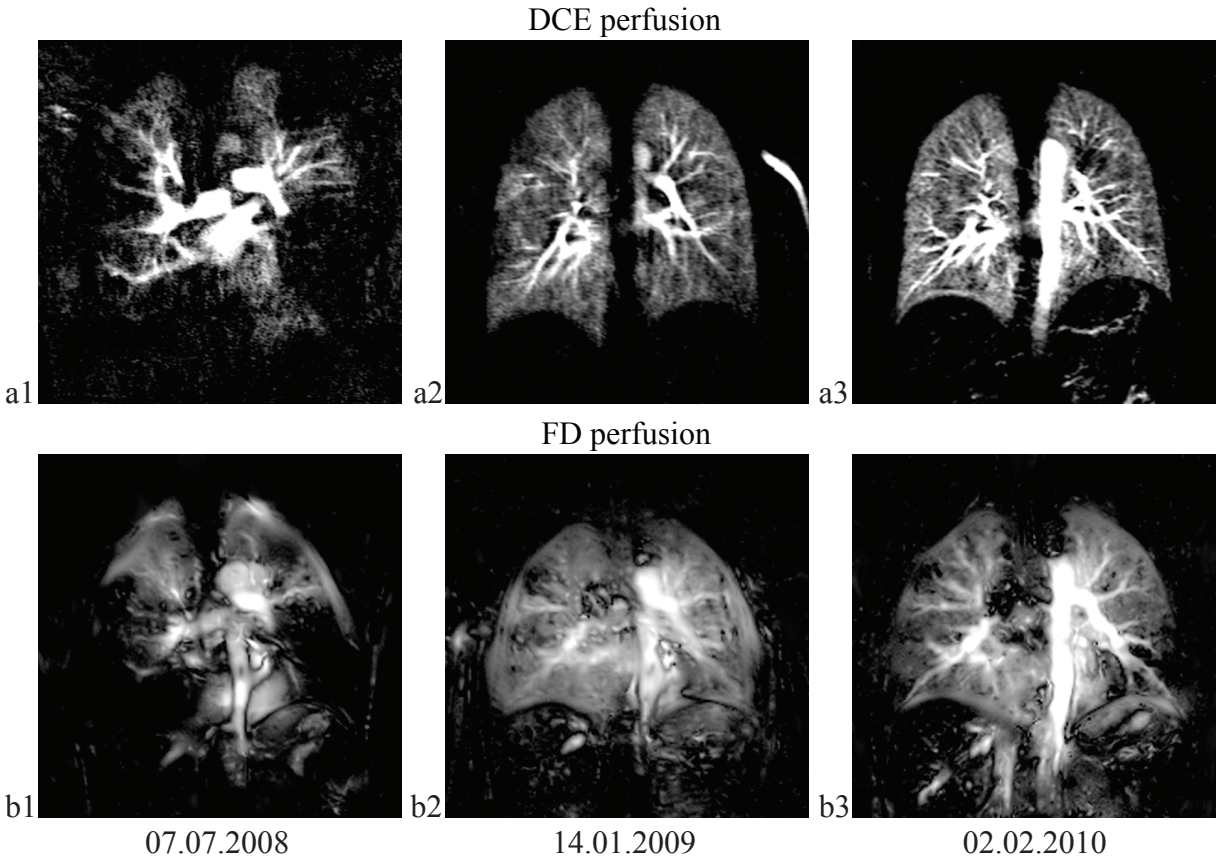

Figure 4.31: *Coronal images of pulmonary perfusion obtained using DCE-MRI (upper row) and FD-MRI (lower row) during three follow-up examinations. Notice the improvement of the pulmonary perfusion after the anticoagulant therapy in images created using both methods.*

4.8.3 Pneumonia / air-trapping

Figure 4.32 presents images acquired in a 32 year old female patient with treated pneumonia. The coronal CT scan performed during the first examination (18.06.2009) shows lung tissue inflammation in the upper lobe of the right lung and air-trapping in the middle lobe of the right lung caused by mucus plugging. Unfortunately, no MR data was acquired at this time point.

In the coronal and sagittal CT images obtained during the second examination (10.09.2009) no active pneumonia is visible. However, air-trapping in the middle lobe of the right lung remained unchanged. The CT scan was followed by a morphological and functional lung MRI study. The alteration of the tissue density change in the corresponding lung area was detected in the FD ventilation-weighted image. Lack of gas-exchange in caused hypoxic vasoconstriction and the pulmonary blood was shunted to other parts of the lung parenchyma. Thus, a large perfusion defect in the affected lung region is visible in the DCE-MRI perfusion image, as well as in the FD perfusion-weighted image. The size and location of the defect correlates very well.

An example of post pneumonia tissue scaring in another patient is shown in figure 4.33.

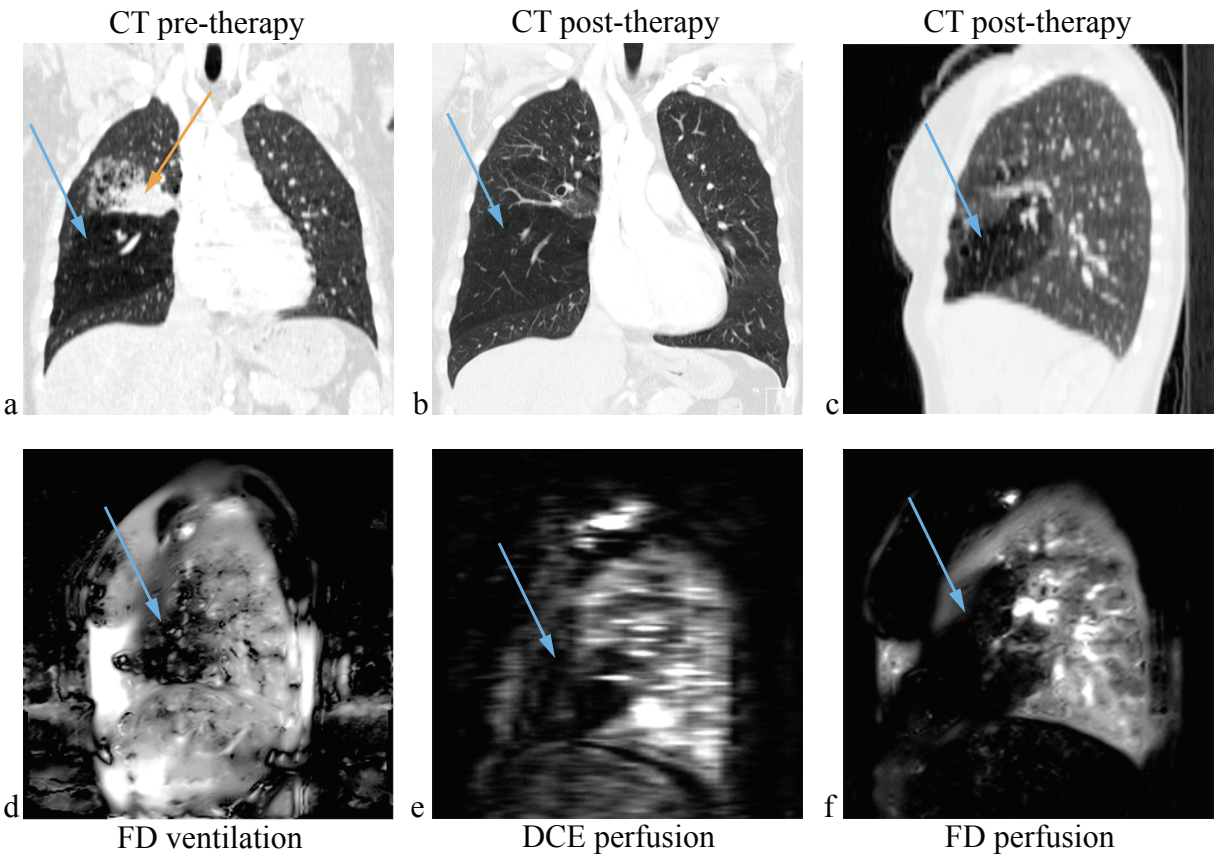

Figure 4.32: *Coronal CT image (a) acquired during the first examination (18.06.2009) shows lung inflammation (orange arrow) in the upper lobe of the right lung. Image (a) and CT images (b,c) obtained during the second examination (10.09.2009) shows air-trapping in the middle lobe of the right lung (blue arrows). The FD ventilation-weighted image shows alteration of the density change (d) in the destructed lung region and perfusion defect caused by hypoxic vasoconstriction in this region in the DCE-MRI image, as well as in the FD perfusion-weighted image (blue arrows).*

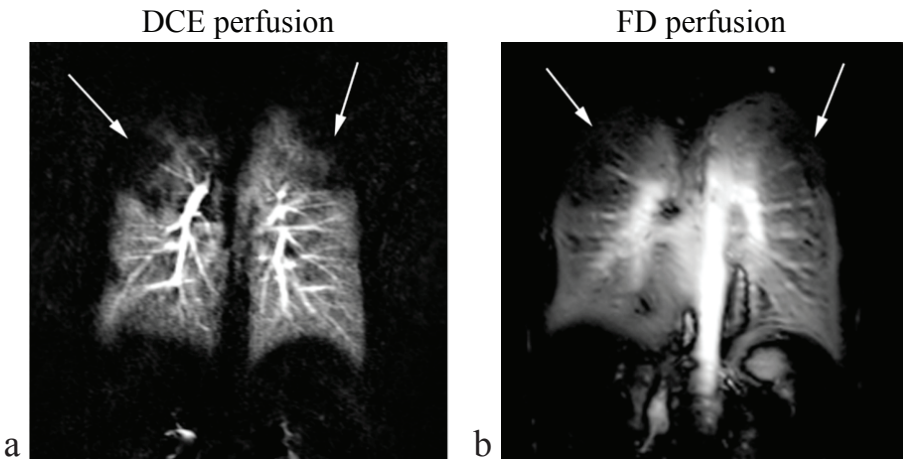

Figure 4.33: *DCE-MRI (a) and FD-MRI (b) perfusion images obtained for corresponding slices in a 32 year old female patient with post-pneumonia tissue destruction (arrows) in the upper lobes in both lungs.*

4.8.4 Bronchial cancer

Figure 4.33 shows images obtained in a 58 years old female patient with bronchial cancer (stage IIIA, T3 N1 M0). The tumor is located in the upper lobe of the right lung in morphological SSFP images. FD-MRI perfusion-weighted image shows huge perfusion defect in the upper lobe of the right lung in the region of tumor. In the coronal subtraction DCE-MRI image created, the tumor appears to be unperfused. The sagittal DCE-MRI shows no perfusion in tumor and in the upper lobe of the right lung.

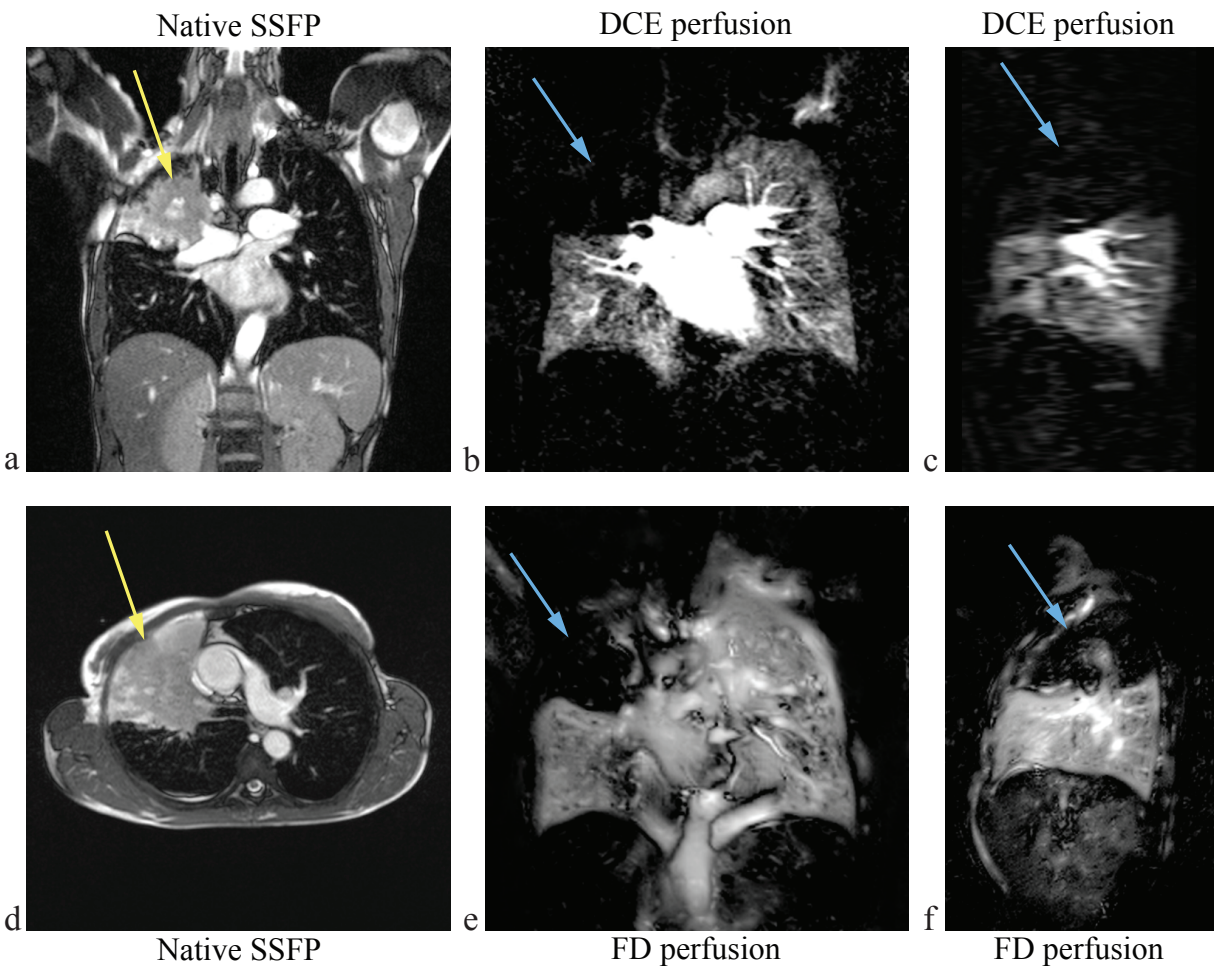

Figure 4.34: *Native SSFP images in coronal (a) and transverse (d) orientation show huge bronchial tumor in the upper lobe of the right lung (yellow arrows). DCE-MRI perfusion images in coronal (b) and sagittal (c) orientation show perfusion defect in the whole upper lobe of the right lung. The same perfusion defects are visible in FD-MRI images in coronal (e) and sagittal (f) orientation (blue arrows).*

4.8.5 Chronic Obstructive Pulmonary Disease

COPD is a progressive medical condition comprising three related diseases, chronic bronchitis, chronic asthma, and emphysema. Thickening of the walls of the airways leads to narrowing and obstruction of the airways. In emphysema the alveoli are permanently enlarged due to the destruction of the alveolar walls. As a result, the overall elasticity of the lung is reduced causing the bronchioles to collapse and obstruct the air flow out of the alveoli. Moreover, the passageways may be also plugged with mucus. For this reason, COPD is characterized by reduced forced vital capacity (FVC), as well as forced expiratory volume in one second (FEV1). Regional enlargement of the alveoli enlargement, as well as air trapping lead to alterations of the local density change caused by the contraction of the tissue in comparison to regions with healthy lung parenchyma.

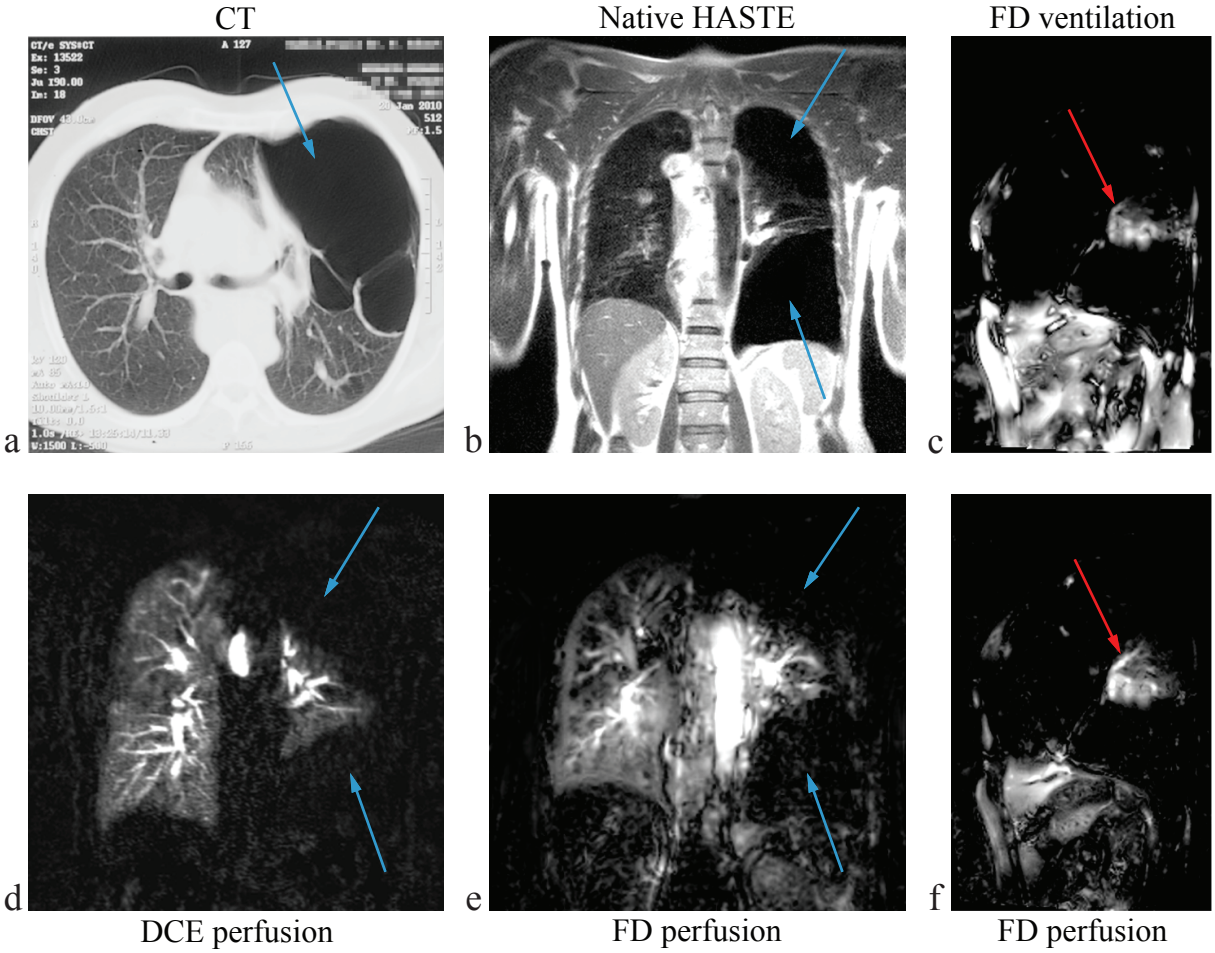

Figure 4.35: *The transverse CT image (a) and the coronal morphological MRI (b) acquired using HASTE sequence in a 55 years old male patient with COPD shows extensive destruction of the lung parenchyma (arrows). Perfusion defect in destructed lung regions is shown by arrows in DCE-MRI (d), as well as in the FD perfusion-weighted image (e). The sagittal FD ventilation- and perfusion-weighted images shows that change of the density in the pulmonary parenchyma and blood flow occurs only in the sixth segment of the left lung (red arrows).*

An example of data acquired in COPD patients using different imaging techniques is shown in this section. A transverse CT scan and a coronal morphological MR image (Fig. 4.35) acquired in patient a 55 years old male patient with severe COPD show extensive destruction of the pulmonary parenchyma in the left lung. Large perfusion defects in corresponding regions are visible in the coronal DCE-MRI and FD perfusion-weighted images. Sagittal FD ventilation- and perfusion-weighted images show lung parenchyma density change and blood flow in the sixth segment of the left lung.

4.9 Validation of FD-MRI in an animal experiment

This section presents results from a validation experiment of FD-MRI technique in animals. The experiments were performed as a part of a multimodal study organized in cooperation between the German Cancer Research Center in Heidelberg and the University Clinic Schleswig-Holstein in Kiel. The goal of the study was to compare qualitatively and quantitatively techniques for the assessment of pulmonary perfusion and ventilation using different imaging modalities i.e. CT, MRI, SPECT/CT.

4.9.1 Measurement protocol

Seven domestic pigs were examined. Prior to measurements each animal was sedated and artificially ventilated through the whole examination. The workflow of the study is shown in figure 4.36. The first measurement was performed in CT (Sensation, Siemens Healthcare, Erlangen, Germany) to acquire high resolution morphological data. The images were acquired separately in expiratory and inspiratory phases.

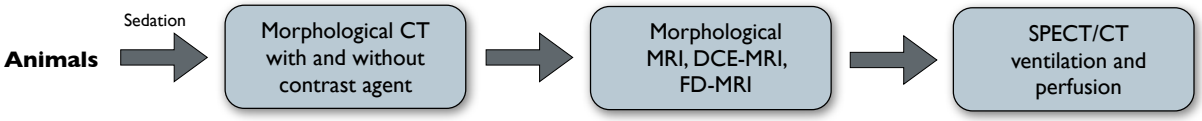

Figure 4.36: *Workflow of the animal study.*

The examination was continued in a 1.5 T whole-body MR scanner (MAGNETOM Avanto, Siemens Healthcare, Erlangen, Germany) using an identical set of transmit and receiver coils as in case of human patients. The MR measurements comprised (among other protocols) in chronological order: morphological scans; acquisition of five coronal slices numbered from posterior (S1) to anterior (S5) using the FD-MRI protocol; intravenous administration of the contrast agent in form of gadopentetate dimeglumine (Magnevist, Bayer Vital, Germany) in dose of 0.05 mmol/kg body weight at rate of $2-5$ mL/s and followed by DCE-MRI acquisitions using TWIST sequence.

The last part of the examination took place in SPECT/CT (Symbia T, Siemens Healthcare, Erlangen, Germany) to acquire the lung ventilation and perfusion data. The aerosol radionuclide ^{99,m}Tc (Technegas) was used for ventilation imaging. The measurement of pulmonary perfusion was assessed by injection of ^{99,m}Tc macroagreggated albumin (Tc-MAA). After the whole examination the animals were euthanized.

4.9.2 Quality assessment and comparison of FD-MRI against other techniques

All time-resolved bSSFP data sets were successfully acquired. The data were registered and postprocessed by generation of perfusion- and ventilation-weighted images. Figure 4.38 shows an example set of FD-MRI images obtained in five coronal slices in an animal.

The lung area was manually segmented for every acquired time-resolved data set. The average SNR in the lung parenchyma within all animals and slices calculated using the formulas from section 4.6.2 was 30.28 ± 13.35. Mean values of the signal intensity in the lung parenchyma, amplitude of signal change caused by respiration and blood flow measured within all slices and all animals were: $\mu(SI) = 31.59 \pm 9.34$, $\mu(A_R) = 8.64 \pm 4.22$, and $\mu(A_C) = 2.77 \pm 0.86$, respectively.

Influence of the gravitational force on the distribution of the pulmonary parenchyma and blood in the lungs was observed in all animals. Figure 4.37 shows averaged signal intensity measured in the segmented lungs for all animals as a function of slice position in the anterior-posterior direction.

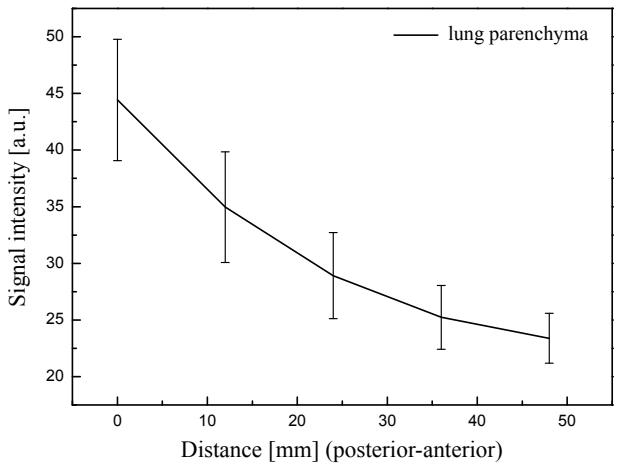

Figure 4.37: *Diagram shows the dependence between the signal intensity measured in the lung parenchyma and position in the posterior-anterior direction.*

Two examples presents accidentally detected pathologies in animals. Data obtained in these animals was used to check whether the defects in the lung parenchyma are detectable with different functional imaging techniques.

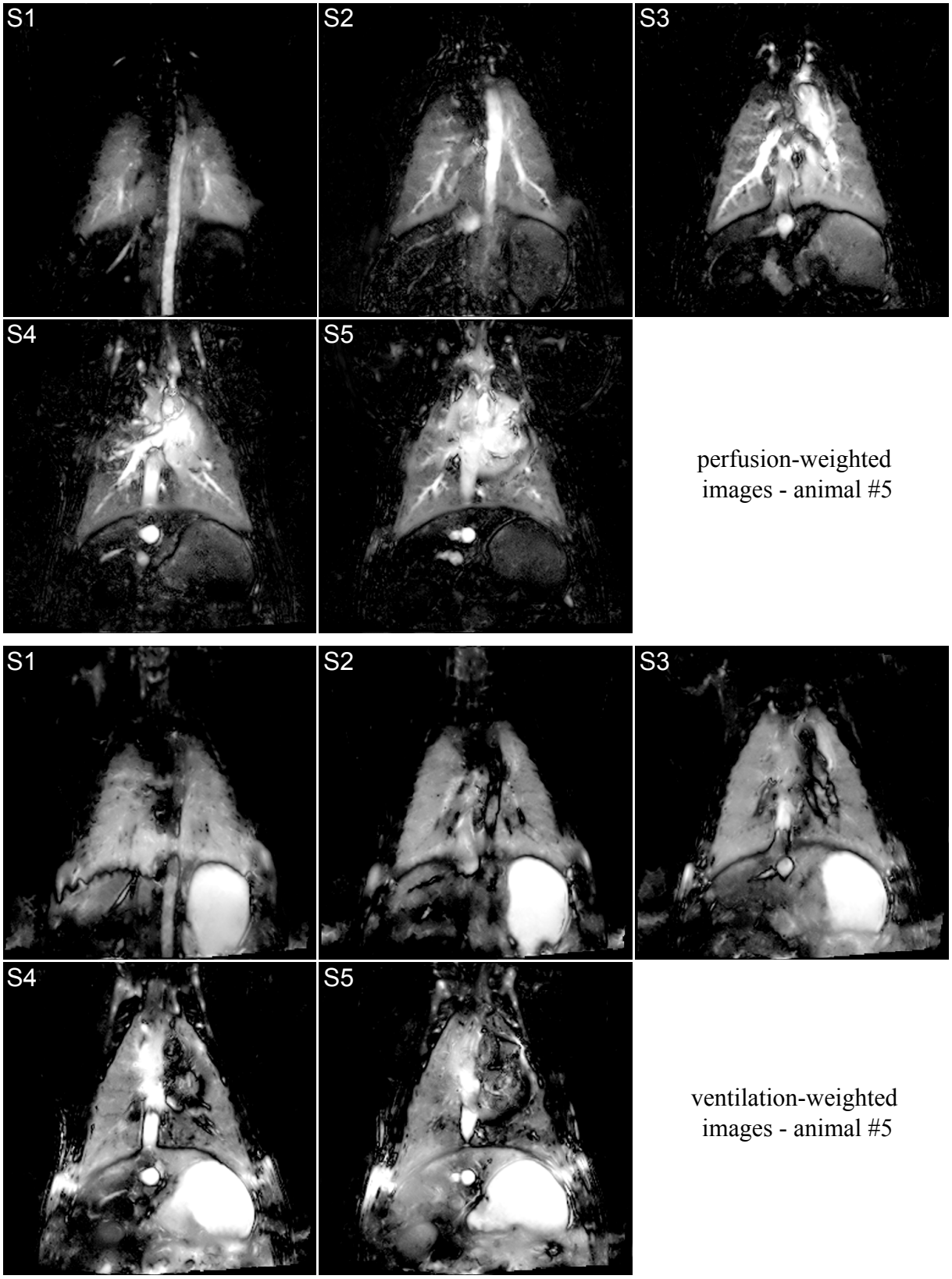

Figure 4.38: *The upper array shows FD perfusion-weighted images, and the lower array corresponding FD ventilation-weighted images obtained from a pig in five coronal slices.*

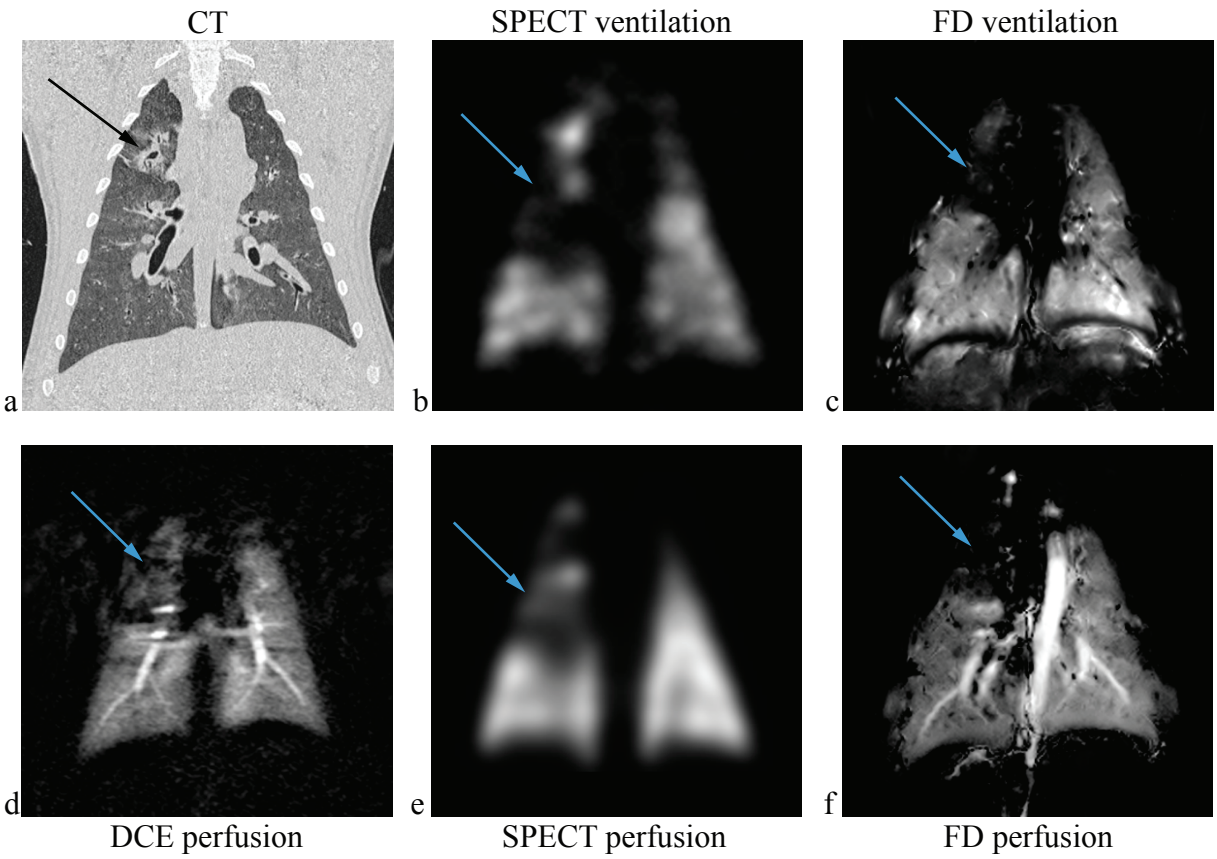

Figure 4.39: *Coronal images obtained in the animal #3. The CT scan (a) shows a parenchymal defect in the upper lobe of the right lung (black arrow). The affected region was unventilated, which is noticeable in the SPECT ventilation image (b). Alteration of the density change in the pulmonary parenchyma is visible in the FD ventilation-weighted image (c). The DCE-MRI (d), SPECT perfusion (e) and FD perfusion-weighted images shows that the defected lung region was unperfused.*

Figure 4.39 show coronal images acquired in the animal #3 in an identical anatomical position using CT, DCE-MRI, FD-MRI, and SPECT. A parenchymal defect is visible in the upper lobe of the right lung in the CT image. Perfusion images obtained with DCE-MRI, SPECT, and FD-MRI show a defect in the corresponding lung region. The SPECT image show lack of ventilation in this lung area. Moreover, an alteration of the parenchyma density change is noticeable in the FD ventilation-weighted image.

A second example (Fig. 4.40) show coronal images obtained in the animal #6. A region with air-trapping was detected in the right lung in the CT scan comparing the images acquired in respiratory expiration and inspiration. The mean signal intensity in the region with air-trapping measured for a single slice position was -702.63 ± 34.89 HU, while in the healthy tissue was -548.65 ± 53.55 HU. The SPECT ventilation image shows that this lung area was unventilated, probably due to mucus plugging of a bronchus. The FD ventilation-weighted shows as expected that the density change of the lung parenchyma in this area is lower that in the healthy tissue. As a result of a hypoxic vasoconstriction, the pulmonary blood flow has decreased in the region

with air-trapping (see section 2.4.6). This is clearly visible in the DCE-MRI, SPECT perfusion image and FD perfusion-weighted image.

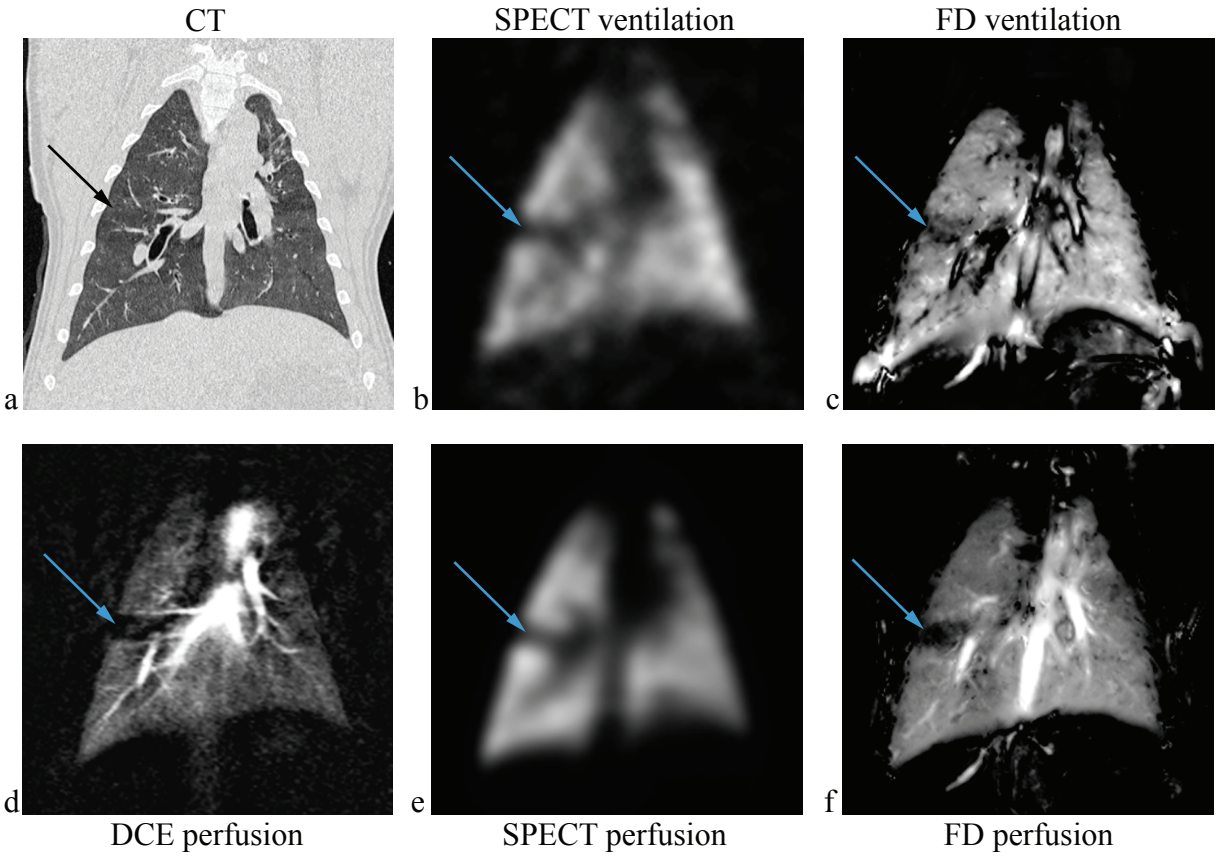

Figure 4.40: *Coronal images acquired in the animal #6. The CT scan shows a region with air-trapping (black arrow). A ventilation defect was detected in the SPECT ventilation image (b). The density change in this lung region was decreased, which is visible in the FD ventilation-weighted image (c). As a result of Euler-Liljestrand mechanism the blood was shunted to regions with healthy pulmonary parenchyma from the region with the trapped air. Perfusion defects are visible in DCE-MRI, SPECT and FD-MRI perfusion images.*

4.9.3 Measurements with a thorax phantom

Apart from the study in animals, measurements with a thorax phantom containing plastinated lungs extracted from a pig (artiCHEST, PRO design GmbH, Heiligkreuzsteinach, Germany) were performed. A mechanical system simulated diaphragm movement in the phantom. The respiratory frequency was set to 0.167 Hz. One coronal data set was acquired with the bSSFP sequence. The SNR measured in the manually segmented lungs was 11.47 ± 1.26. The lungs were not perfused and the signal intensity change in the lung parenchyma was modulated only with the respiratory frequency. Figure 4.41 shows the thorax phantom lying on an MR table, and the FD ventilation-weighted image obtained from an MR data set.

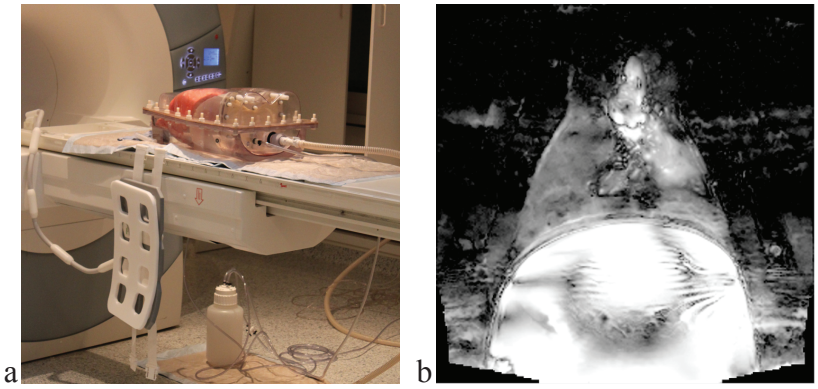

Figure 4.41: *Thorax phantom (a) containing plastinated pig lungs. Coronal FD ventilation-weighted image (b) obtained from the data measured in the phantom.*

4.10 Validation of FD-MRI in humans - initial results

THIS SECTION SHOWS the initial validation results of FD-MRI against ^{129}Xe-MRI in humans. The measurements were performed in cooperation with the Department of Biomedical Engineering of the University of Virginia in Charlottesville. Figure 4.35 images obtained in a 55 years old female with COPD. Information about the regional ventilation was assessed by ^{129}Xe-MRI using 2D spiral sequence. Unventilated lung areas, which are blocked by mucus, or where the air flow is obstructed by collapse of bronchiole provide no signal in the ventilation image. However, not only the healthy lung tissue, but also the affected by emphysema is shown as bright areas in this image.

The measurement of ventilation were followed by imaging of ^{129}Xe diffusion in intraalveolar spaces. This examination allowed producing map of the apparent diffusion coefficient (ADC) and gave supplementary functional information. The mean ADC was 0.050 ± 0.016 cm^2/s.

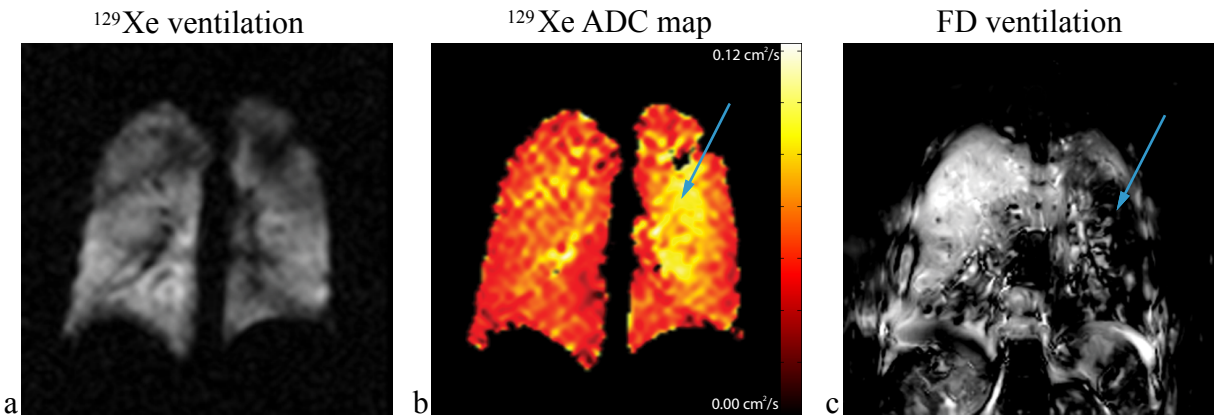

Figure 4.42: *Images obtained in a 55 years old female patient with COPD. The ^{129}Xe MRI ventilation image (a) was acquired using 2D spiral sequence. The region in the left lung affected by emphysema is characterized by high values in the ADC map (b), while in the FD ventilation-weighted image (c) shows decrease of the signal intensity (blue arrows). All images were acquired in the identical slice position. (^{129}Xe images courtesy of J. Mugler, UVA, Charlottesville, Virginia, USA)*

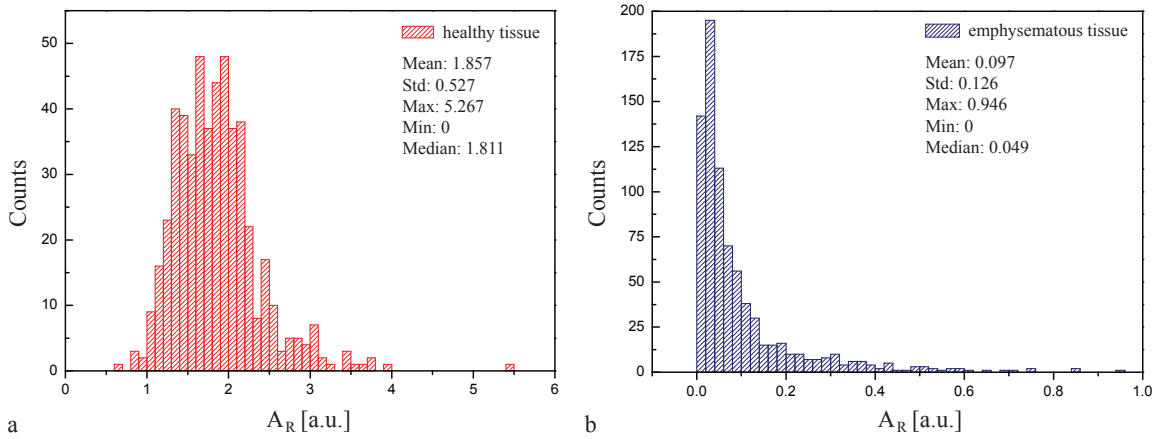

Figure 4.43: *The histograms show distributions of A_R values from two ROIs drawn in healthy tissue (a) and emphysematous tissue (b), respectively. The size of each ROI was* 20 cm^2.

Regions of emphysematous changes in the left lung are characterized by high ADC values, due to the less restricted diffusion of gas particles in enlarged and destructed alveoli. The same emphysema regions in the FD ventilation-weighted image have decreased amplitude of parenchyma density change A_R, and can be differentiated from a healthy tissue.

Figure 4.43 shows histograms obtained in healthy and emphysematous tissue for a ROI drawn in the FD ventilation-weighted image. The histograms presents different distributions of A_R estimated for these ROIs.

Chapter 5

Discussion

Time-resolved MRI of the lung

The major difficulties of MRI of the lung parenchyma were described in section 3.2. In lung MRI, due to the fast signal dephasing, respiratory motion, cardiac pulsation, short acquisition times, or the application of triggering techniques is required. Several studies have shown a potential of a bSSFP pulse sequence for morphological and dynamic MR imaging of the lung at a low magnetic field of $0.2 - 0.35$ T [Deimling, 2000; Zapke et al., 2006], as well as at a magnetic field of 1.5 T [Topf et al., 2005; Failo et al., 2009].

One of the goals of this work was to numerically simulate and further optimize the bSSFP sequence for time-resolved MRI of the lung in a 1.5 T MR-scanner. The optimizations resulted in a significant improvement in the visualization of the pulmonary parenchyma and vasculature.

The main requirement of the bSSP dynamic MR acquisition was a short acquisition time (TA) of a single image. This was achieved using a combination of a single-shot acquisition of the whole k-space, parallel imaging technique, and a high bandwidth to sample the k-space at a very short echo time (TE). The most widely used techniques in the clinical routine are GRAPPA [Griswold et al., 2002] and SENSE [Pruessmann et al., 1999]. Both provide nearly identical reconstruction quality, however, pMRI with GRAPPA is beneficial in regions with low spin density, e.g. like lungs, where accurate coil sensitivity maps may be difficult to obtain [Heidemann et al., 2003]. In case of acquisitions of coronal images, GRAPPA technique with a relatively high acceleration factor = 3 for a given coil setup (see section 3.1) was used. Acquisitions in a sagittal orientation were performed with GRAPPA factor = 2 and reduced phase field of view of $60 - 70\%$. Since the images were acquired in free breathing, the auto-calibration signal lines (ACS) were measured prior to every single image scan. An initial ramp of 10 linearly increasing RF excitation pulses applied before the acquisition block was necessary to avoid oscillations of the magnetization vector [Deshpande et al., 2003], although it resulted in longer TA per image. Nevertheless, TA in order of 100 ms was achieved for a resolution of 128×128, which significantly reduced motion-related artifacts. Thus, a major source of artifacts was the pulsation of the aorta and heart.

As a consequence of the application of parallel imaging, the number of sampled k-space lines was reduced from 128 to 48 per image. It was shown that the steady-state in a bSSFP sequence is reached after about $T_1T_2/(TR(T_2+2T_1))$ RF excitation pulses [Vassiliadis and Sergiadis, 1993]. Thus, all measurements were performed in a transient-state of the magnetization vector. It is concluded that the contrast of the bSSFP images is proportional to $M0\sqrt{T_2/T_1}$. However, in case when the acquisition time of an image is shorter than the time required to approach the steady-state, the image can be weighted by a combination of proton-density and T_2/T_1 contrasts [Huang et al., 2002]. According to Scheffler and Hennig [2003] the signal decay between RF excitation pulses in the bSSFP sequence at the echo time (TE) is weighted with $\exp(-TE/T_2)$ rather than $\exp(-TE/T_2^*)$ and the magnetization refocusing appears at $TE = TR/2$ for $T_1, T_2 > TR$. However, signal intensity measured at TE after the excitation pulse depends also on the distribution of the intravoxel dephasing in the lung tissue that was simulated by Martirosian et al. [2006].

As predicted, a very strong dependence between the TE and the signal intensity in the lung tissue at the magnetic field of 1.5 T was observed. The maximal signal intensity of the lung parenchyma, as well as a maximal difference between signal intensity between expiratory and inspiratory phases was obtained for submillisecond values of TE (Fig. 4.1a). The loss of SNR at a high bandwidth was estimated theoretically and measured in the lung parenchyma (Fig. 4.4a). However, the high bandwidth was required to achieve fast k-space sampling. The inter-echo spacing was reduced to 1.9 ms by application of a high bandwidth of 1302 Hz/px in combination with an asymmetric echo sampling. The value of $s = 0.4$ of the asymmetric sampling factor was found to be optimal, which corresponds to the minimal TE of 0.8 ms. Further reduction of the asymmetric sampling factor would decrease the TE, affecting the image reconstruction process and resulting in severe blurring artifacts in the frequency encoding direction. One of the common problems of bSSFP acquisitions is related to its sensitivity to magnetic field inhomogeneities and susceptibility differences. The Frequency Response Function (FRF) of bSSFP sequence shows a periodical minima occurring at certain frequency offsets (Eq. 3.12). The shape of the FRF for bSSFP sequence in a transient-state was simulated and presented in figure 4.1b. Since the frequency offsets at which the minima occur is inversely proportional to TR, a very short inter-echo spacing used in bSSFP sequence helped avoiding the banding artifacts within a FOV.

Application of a centric k-space sampling scheme and the introduction of intervals TW between each image acquisition increased significantly the signal in comparison to other sampling schemes e.g. for linear sampling, or acquisitions with no intervals (see Fig. 4.3). The drawback of the centric sampling was the enhancement of the pulsation artifacts in the presence of pulmonary arteries and heart. Intervals TW allowed for partial recovery of the longitudinal magnetization, as well as for the inflow of fresh unsaturated blood into the slice where the acquisition took place. This imaging scheme enhanced the measured signal from the lung parenchyma when compared with a continuous data acquisition; on the other hand, the image sampling rate was decreased. An interval in a range of $150 - 200$ ms was used to acquire data for functional lung MRI. Minimization of the TW can be used to increase the image sampling rate up to 10 frames/s and applied for breathing maneuver studies.

The simulations of the bSSFP sequence, as well as the experimental results presented in the

section 4.1 have shown that the maximal signal intensity in the lung tissue was observed for high values of the flip angle above 70°. Thus, the major concern regarding the dynamic acquisition was the possible exceedance of maximal allowable specific absorption rate (SAR). A reduction of the SAR was obtained by application of the parallel imaging technique, which decreased a number of RF excitation pulses during every image acquisition. Moreover, the time intervals TW introduced between image acquisitions lowered the RF power deposition per unit of time. Implementation of a variable flip angle for the centric k-space sampling scheme could also be beneficial to reduce the SAR.

The slice thickness of 10 mm was sufficient to obtain high signal intensity in children and young adults. The parenchyma density decreases with the age [Van Dyk et al., 1982; Long et al., 2005]. Thus, for adults the slice thickness was increased to 15 mm. Larger slice thickness reduces the quality of images because of partial volume effects. Acquisition of a 2D time-resolved data set was limited to one minute, in order to be able to cover the whole chest volume in about 10 minutes.

Postprocessing of time-resolved MR data

Non-rigid registration of time-resolved MR data was used to correct the shape of the lung for every acquired image with respect to a reference image. This procedure enabled an analysis of signal intensity changes of corresponding lung areas along the time domain of the MR data sets. One of the most important advantages of the algorithm is the fact that it is fully automatic and does not require the extraction of anatomical landmarks, which would be very demanding for a large amount of data. The local cross-correlation similarity criterion used by the algorithm is quite robust to, noise and to the local variation of signal intensities observed in dynamic MR scans. Moreover, a very simple parametrization of the registration process allowed finding universal value σ describing the width of the Gaussian regularization operator by measuring peak signal-to-noise ratio between registered images and a reference image (see Fig. 4.13). All dynamic bSSFP lung data were registered using the optimal value of $\sigma = 0.5$. Visual comparison between images registered using different values of σ was shown in figure 4.14. Best results of image registration were typically obtained by selecting a reference image acquired halfway through the inspiration or expiration phase.

A main limitation of the registration procedure is the fact that it was applied in two dimensions. During the respiration, the predominant movement, and volume change of the thorax are resulting from the diaphragmatic motion. Additionally, chest wall expansion results in an anterior-posterior motion. However, for coronal data sets it has limited significance because of the relatively large slice thickness of $10 - 15$ mm. Dynamic acquisition of 3D data sets may solve this limitation in future and allow applying the registration in all three spatial dimensions. In case of sagittal images, the movement in the normal direction to an imaging plane is not noticeable. Acquisition of transverse images was not performed because movement of the lung out of the imaging slice in the apical-basal direction cannot be neglected.

Deformation fields can be exported from registered images as shown in figure 4.15. It was confirmed that a deformation field calculated between two coronal images acquired in expiration and inspiration shows high amplitude of deformation along the vertical direction. The deformation was especially noticeable in the basal regions of the lung, which confirms that these areas are more extended during respiration than the apical regions of the lung. It should be noticed that the deformation was also calculated for other body regions. Contraction and movement of unventilated body regions into areas of different coil sensitivity cause a local change of the signal intensity. Therefore, these regions may appear visible in FD ventilation-weighted images. Further studies should be performed to validate the image registration comparing it with other techniques enabling calculations of lung parenchyma deformation, for instance, grid-tagging [Chen et al., 2001].

A spectral analysis of the registered MR data was performed using two different approaches. The first approach was based on the Fourier decomposition (FD), while the second on the wavelet analysis (WA). Both were applied pixel-wise along the temporal direction of the acquired data sets. Examples of ventilation- and perfusion-weighted images acquired in a healthy volunteer were shown in figures 4.16 and 4.17. The images obtained using both spectral analysis methods show similar homogeneous distribution of lung parenchyma density change and pulmonary perfusion.

The important factor for the quality of the ventilation and perfusion-weighted images calculated using FD method is the stability of breathing and heart rate during the measurement. The FD method requires an assumption that the sampled signal is stationary. A modified Lujan formula (Eq. 4.2) was used to describe the time-course of signal change in the lung parenchyma. The effect of respiratory and cardiac frequency variations during the measurement were observed by an analysis of signals using short-time Fourier transform (STFT). Irregular rates cause widening or splitting of the spectral lines located at respiratory and cardiac frequencies. Wide spectral lines require integration of a larger frequency range; hence more noise is added to calculated images. In case of spectral line splitting, automatic detection of respiratory and perfusion frequency ranges containing highest signal energy can be impeded. This problem was partly solved employing calculation of a power spectrum of signal, which mathematically corresponds to signal autocorrelation prior to the application of the FFT.

The analysis of non-stationary signals requires specific tools, which surpass classical Fourier analysis. In this work, the feasibility of signal analysis using wavelets to obtain functional information has been shown. The WA tends to do very well in separating slow and fast processes like in this case, respiratory and heart cycles. An orthogonal Daubechies D4 wavelet was used for the DWT and the inverse DWT. A low-pass property of the D4 wavelet was used to produce a rough approximation of the signal change with filtered out the cardiac signal component. Standard deviation around the baseline of this approximated signal branch was corresponding to changes of the signal intensity caused by parenchyma contraction or expansion in a given voxel. The detail branches obtained using high-pass property of the D4 wavelet were used to calculate faster signal oscillations caused by blood flow. Further studies should be the focus on construction of an optimized wavelet mother function, which would better fit to the time-course of signal changes in the lung parenchyma. Thresholding was used in the wavelet domain to smooth and remove some wavelet coefficients of the measured signal, which can help in reducing the noise content.

The thresholding could also be applied in the spatial domain using 2D DWT. A main drawback of WA technique is longer computation time required for postprocessing of the data. However, this method could be successfully applied in case of high respiratory frequency instabilities providing images of better quality. Furthermore, application of WA helps overcoming the problem of overlapping between frequency bands, which can be problematic for standard Fourier analysis in case of misfortune combination of respiratory and cardiac frequency harmonics. Since this method was developed during the last period of this work, all ventilation- and perfusion-weighted images obtained in patients were postprocessed using FD technique.

Technical and medical reproducibility of FD-MRI

In order to verify the technical and medical reproducibility of FD-MRI, a study in a group of seventeen healthy non-smoking volunteers was performed. Each volunteer was examined twice using identical imaging protocol in an interval of one day. Coronal bSSFP multi-slice data sets obtained on the first and second day were acquired in corresponding anatomical locations using identical sequence parameters. Anatomical MR scans performed at the beginning of each examination were used to reproduce the slice positioning.

Ventilation- and perfusion-weighted images obtained in healthy volunteers showed no significant regional alterations in the distribution of signal change caused by respiration A_R and by blood inflow A_C within the lung parenchyma. It was noticed that the quality of images acquired in the supine position in posterior thoracic regions is superior to of those obtained in anterior thoracic regions. In case of perfusion-weighted images the quality is influenced by the presence of pulsation artifacts and heart motion, which are more distinct in paracardiac regions. Motion of the chest wall decreased significantly the quality of ventilation-weighted images acquired in anterior regions. Moreover, the abdominal structures are often visible in the ventilation-weighted images as a result of motion and high signal intensity of these organs. One of the possible solutions to this problem is to use an image generated at the zero-frequency (Eq. 4.17) as a weighting mask suppressing body regions with a high signal intensity.

Other factors influencing the image quality were: size of a volunteer, density of lung parenchyma as a function of age and regularity of a breathing cycle. Furthermore, it was observed that better image quality is obtained by avoiding aliasing artifacts and locating the arms of a volunteer above the head during MR acquisitions.

Analysis of ROIs was performed on the registered bSSFP data and ventilation- and perfusion-weighted images. Three different parameters: mean signal intensity $\mu(SI)$, mean signal intensity changes caused by respiration $\mu(A_R)$, and blood inflow $\mu(A_C)$ were calculated for manually segmented areas in the lung parenchyma for every slice. Values of these parameters obtained on the first and second day of the study were compared by application of statistical methods described in section 4.6.3. No significant difference in the distributions of $\mu(SI)$, $\mu(A_R)$, and $\mu(A_C)$ was found. Moreover, a strong correlation between these values measured on the first and the second day of the study was observed (table 4.2), which proofs a good technical reproducibility. Effect of

gravitational force on the distribution of $\mu(SI)$, $\mu(A_R)$, and $\mu(A_C)$ along the anterior-posterior direction was calculated (table 4.3). The slope of $\mu(SI)$ equal to $5.1 \pm 0.6\%/\text{cm}$ was found to be close to the value of $4.9\%/\text{cm}, P < 0.0001$ reported by Hopkins et al. [2007]. Higher signal intensity in posterior thoracic regions improved image quality acquired in these areas.

Another aim of the study was to collect information about stability of respiratory and cardiac frequencies, as well as their variabilities at the first and the second day of the study. To do so, the volunteers were asked to breathe freely. No significant difference between the distribution of respiratory and cardiac frequencies measured on the first and the second day was observed. Distributions of first and second harmonics of respiratory (ω_{R1}, ω_{R2}) and cardiac frequencies (ω_{C1}, ω_{C2}) were used to calculate probabilities of overlapping between peaks in frequency spectra. Because of limited imaging rate, the second harmonic of cardiac frequency harmonic was aliased into spectra. Overlapping of cardiac and respiratory frequencies would make it impossible to separate the information about perfusion and ventilation. The probability of the most critical event - overlapping of ω_{R1} and ω_{C2} was estimated to be very low ($P = 0.004$, see table 4.4) in the group of healthy volunteers.

Functional images obtained in this group of volunteers served as a reference point for analysis of images acquired in patients with pulmonary diseases. The data helped differentiating between artifacts appearing in images and relevant physiological information.

Comparison between FD-MRI and DCE-MRI perfusion imaging

Aim of this study was to compare FD-MRI and DCE-MRI in a group of cystic fibrosis (CF) patients. Eight CF patients were examined with an extended MR study protocol containing dynamic scans using bSSFP sequence. The wide spread of the patients' age (1 - 23 years) allowed getting data of different severity of the disease. The parameter TW of the bSSFP sequence was reduced to 120 ms to cover higher cardiac and respiratory frequency range than in healthy adult volunteers. FD-MRI and DCE-MRI perfusion images were radiologically evaluated using a dedicated field-based scoring system presented in section 4.7.2. The pattern of perfusion defects in images acquired using both methods was found to be very similar. A good correlation $\rho_{all} = 0.82$, $P < 0.05$ (Spearman rank test) was determined between corresponding FD and DCE perfusion images. The strongest correlation was in the right lung and in the upper lung fields. Paracardiac regions showed the weakest correlation, as a result of pulsation artifacts and cardiac motion (table 4.6).

Very high signal intensity, was observed in children, especially in the alveolar phase of the lung development due to high density of lung parenchyma [Long et al., 2005]. The average SNR measured in pulmonary parenchyma was 50.99 ± 21.52 significantly higher than in adult volunteers. The major challenge for imaging this group of patients was high cardiac and respiratory frequency, thus the acquisition rate was increased to 4 images/second. Moreover, spontaneous coughing during the measurements may cause severe motion, which may be difficult to compensate by the image registration.

As a recommendation of the contrast agent manufacturer, the administration of intravenous contrast agent was limited to the patients older than one year and not at risk for renal failure. However, application of FD-MRI is possible in this group of patients where DCE-MRI is not recommended, and allows obtaining information about regional lung function (Fig. 4.28).

In conclusion, FD-MRI can be a good alternative for DCE-MRI especially in CF patients. In this group of patients the follow-up is long, thus non-contrast-enhanced perfusion imaging method could be a choice to avoid risks associated with frequent exposition to contrast media.

Clinical examples

In several examples it was shown that FD-MRI can be successfully applied to evaluate the lung function in patients with different pulmonary diseases including cystic parenchymal defect, pulmonary embolism, pneumonia with air-trapping, bronchial cancer, cystic fibrosis, and COPD. Along with the FD-MRI, DCE-MRI, morphological MR or CT scans were available. Further studies should be focused on certain groups of patients to evaluate clinical relevance of the FD technique.

Validation of the FD-MRI against other imaging modalities

In addition to the validation study in cystic fibrosis patients, FD-MRI technique was compared with other well-established clinical imaging modalities in animal experiments. Seven pigs were examined using morphological CT, morphological MRI, DCE-MRI, FD-MRI, and SPECT perfusion and ventilation scans. The animals were sedated and artificially ventilated during every measurement, thus the respiratory frequency was constant. This allowed generating high quality ventilation-weighted images as showed in figure 4.38. No significant alterations in the distribution of parenchyma density and perfusion were visible in healthy animals. The average SNR of bSSFP images was in the same range in pigs and healthy volunteers, 30.28 ± 13.35 and 26.9 ± 5.3, respectively. The influence of the gravitational force on the distribution of pulmonary parenchyma was also observed in animals (Fig. 4.37).

Accidentally, two animals showed regional defects in ventilation and perfusion caused by atelectasis (Fig. 4.39) and air-trapping (Fig. 4.40). These defects were visible in corresponding anatomical regions in all images obtained using different modalities.

Results obtained during this study in healthy animals can be used as a reference for animal experiments, where an obstruction of a bronchus and blockage of pulmonary artery can be used to produce a controlled pathology, and validate FD-MRI against other modalities.

Tests performed in a thorax phantom with plastinated pig lungs showed that, the SNR obtained in the lung parenchyma *ex vivo* was 11.47 ± 1.26, which is much lower than in pig lungs *in vivo*. A diaphragm motion was simulated by a mechanical system, thus the lungs were contracted and expanded with a constant frequency. A reason for the weak signal intensity is lack of pulmonary

blood in the plastinated lung parenchyma. This suggests that the signal in ventilation-weighted images in vivo consists of two components, the lung tissue and the pulmonary blood.

Apart from the animal studies, this work presents also initial results from a validation study between FD-MRI and hyperpolarized ^{129}Xe-MRI. Figure 4.42 presents ^{129}Xe-MRI ventilation image, ^{129}Xe ADC map, and FD ventilation-weighted image obtained in a COPD patient. It was suggested that the regions, with high values of ADC correlate with regions with low values of A_R in the FD ventilation-weighted image. However, further studies are required to collect more information to prove the statistical significance of the proposed hypothesis. Moreover, as shown in histograms (Fig. 4.43), a statistical analysis can be used to differentiate between healthy and emphysematous tissue, and may allow to obtained additional quantitative information.

Advantages and disadvantages of FD-MRI / WA-MRI

The following paragraphs summarize main advantages and disadvantages of FD/WA-MRI techniques in comparison with other available functional lung imaging modalities.

One of the most important advantages concerning the MR based techniques in general is associated with the fact, that this modality offers a possibility of repetitive examinations without ionizing radiation. This is especially important for patients requiring long periods of follow-up, and allows minimizing a cumulative radiation dose received during a life-span. MRI offers also a wider variety of available techniques for assessment of lung function. In section 3.3 a short review of selected ventilation and perfusion MRI methods was presented. Every MR based method allows for evaluation of the functional information from a different perspective, thus the physiological information it provided may vary.

The advantage of FD/WA-MRI over other MR techniques is no requirement for administration of intravenous contrast agents or gaseous tracers. Moreover, this technique does not rely on triggered acquisitions, is well tolerated by patients, and a multi-slice chest coverage can be performed in a clinically reasonable time of ten minutes.

Table 5.1: *Functional lung imaging modalities. Notation used in table: V - ventilation, P - perfusion, "V" or "P" - ventilation or perfusion related information, respectively, and a three point grade scale: 0 (low), + (moderate), ++ (high).*

Modality	Function	Radiation	Toxicity	Technical effort	Resolution
CT	V/P	++	0/+	0	++
SPECT	V/P	++	+	+	0
^{3}He-MRI	V	0	0	++	++
^{129}Xe-MRI	V/"P"	0	+	++	++
DCE-MRI	P	0	+	+	++
O_2-MRI	V	0	0	+	+
FD/WA-MRI	"V"/P	0	0	0	+

Implementation of this method on a clinical MR scanner is simple and inexpensive. The main disadvantages of this method are: spatial resolution lower than in ^{3}He and ^{129}Xe-MRI; fact that is does not provide a direct information about ventilated lung regions, but about regional parenchyma density instead, and difficulties in the quantification of pulmonary perfusion.

Table 5.1 presents a list of selected imaging modalities allowing for spatially resolved measurement of lung function, as well as scores assigned with regard to the amount of toxicity or radiation associated with an examination, technical effort, and spatial resolution of images.

Chapter 6

Summary and outlook

The goal of this work was to develop a novel approach for non-contrast-based imaging of regional pulmonary function. It has been demonstrated that using time-resolved non-triggered MR data acquisitions it is possible to observe signal intensity changes in the lung parenchyma modulated with respiratory and cardiac frequencies. The MR scans were performed with a multi-slice 2D balanced steady-state free-precession (bSSFP) sequence [Oppelt et al., 1986] in a 1.5 T whole-body MR-scanner. The bSSFP sequence has been already shown to be a promising technique for dynamic lung imaging by few researchers [Rupprecht et al., 2003; Topf et al., 2005; Zapke et al., 2006]. A series of experiments was conducted to optimize the sequence parameters and imaging schemes. The pulse sequence uses a submillisecond echo time sampling ($TE \approx 0.8$ ms) combined with a parallel imaging technique GRAPPA [Griswold et al., 2002] and single-shot acquisitions, which are necessary to enhance the signal intensity of the pulmonary tissue. Application of image registration of the acquired MR data was mandatory to correct for the respiratory and cardiac motion [Chefd'hotel et al., 2002]. Two different methods of spectral analysis of the registered MR data based on Fourier decomposition (FD) and wavelet analysis (WA), were developed and implemented to obtain spatial-resolved ventilation- and perfusion-related information [Deimling et al., 2008; Bauman et al., 2009, 2010a].

The most important advantages of the proposed functional imaging technique are: avoidance of the risk related with exposure to ionizing radiation, which is the main problem of current standard nuclear medicine techniques (scintigraphy and SPECT), and the fact that the method is not dependent on the administration of any intravenous contrast agents or gaseous tracers. Moreover, the technique requires only minimal patient compliance and does not rely on ECG or respiratory triggering during image acquisitions.

In order to show the feasibility of FD-MRI and WA-MRI a group of volunteers was examined. Furthermore, a study on a group of seventeen healthy volunteers was performed to test the medical and technical reproducibility of the FD method. Statistical analysis, as well as radiological evaluation of ventilation- and perfusion-weighted images confirmed the assumption that the technique is reproducible.

Since the acquisition time required to cover the whole chest volume using the bSSFP sequence is in less than 10 minutes, FD-MRI can be successfully included into a standard clinical MR lung

imaging protocol. Comparison between the perfusion images obtained using FD-MRI and DCE-MRI was performed in a group of cystic fibrosis (CF) patients showing a good correlation between the both methods. Validation of the FD technique against other imaging modalities including CT, DCE-MRI, SPECT/CT was conducted in animal experiments. Moreover, this work includes several clinical examples, where different imaging modalities (CT, morphological MRI, DCE-MRI, ^{129}Xe-MRI) were combined with FD-MRI. It was successfully applied in patients with chronic obstructive pulmonary disease (COPD), cystic fibrosis, bronchial cancer, pulmonary embolism, pneumonia, and parenchymal cystic defect yielding useful functional information.

The MRI technique presented in this work can be applicable in groups of chronically ill patients, especially young adults and children requiring long-term periods of follow-up, and patients where the administration of contrast media is medically problematic or impossible, due to allergic reactions, or the risk of development of nephrogenic systemic fibrosis [Grobner, 2006].

Further studies in this field should be focused on two different aspects. The first aspect will involve improvements of the pulse sequence and imaging scheme to increase the signal intensity measured in the lung parenchyma, as well as temporal resolution of dynamic MR scans; reduction of the specific absorption rate (SAR) during bSSFP acquisitions using e.g. a variable flip angle technique; possible extension of the technique to time-resolved 3D acquisition combined with the development of new postprocessing and elastic image registration methods; further developments of wavelet based spectral analysis.

The second aspect concerns the validation of FD/WA-MRI technique against other modalities, especially ventilation imaging techniques based on hyperpolarized gas imaging (^{3}He-MRI and ^{129}Xe-MRI); evaluation of a clinical impact of the proposed techniques and its applicability as an alternative noninvasive lung examination. An important improvement in the technique will be a development of quantification models for FD/WA ventilation- and perfusion-weighted images. Ability to quantitatively differentiate between healthy and pathological tissue would be of great importance for radiological diagnostics.

One of the interesting future perspectives of FD/WA-MRI is its application in measurements of tumor perfusion in patients with lung cancer. In images obtained using DCE-MRI the tumor tissue is normally characterized by a delayed perfusion [Hintze et al., 2010]. Figure 6.1 shows time course of signal intensity in a ROI measured in tumor, and a result of subtraction of an image acquired during the signal enhancement in the ROI and before contrast agent administration. In current FD/WA perfusion-weighted images, change of the signal intensity in the tumor mass caused by blood pulsation is too low to be visible on a spatially resolved level. After averaging over a larger area in the tumor, the signal intensity change caused by perfusion is noticeable (Fig. 6.1c). Improvements in the sensitivity and spatial resolution of this method may allow studying the tumor perfusion providing a valuable functional information.

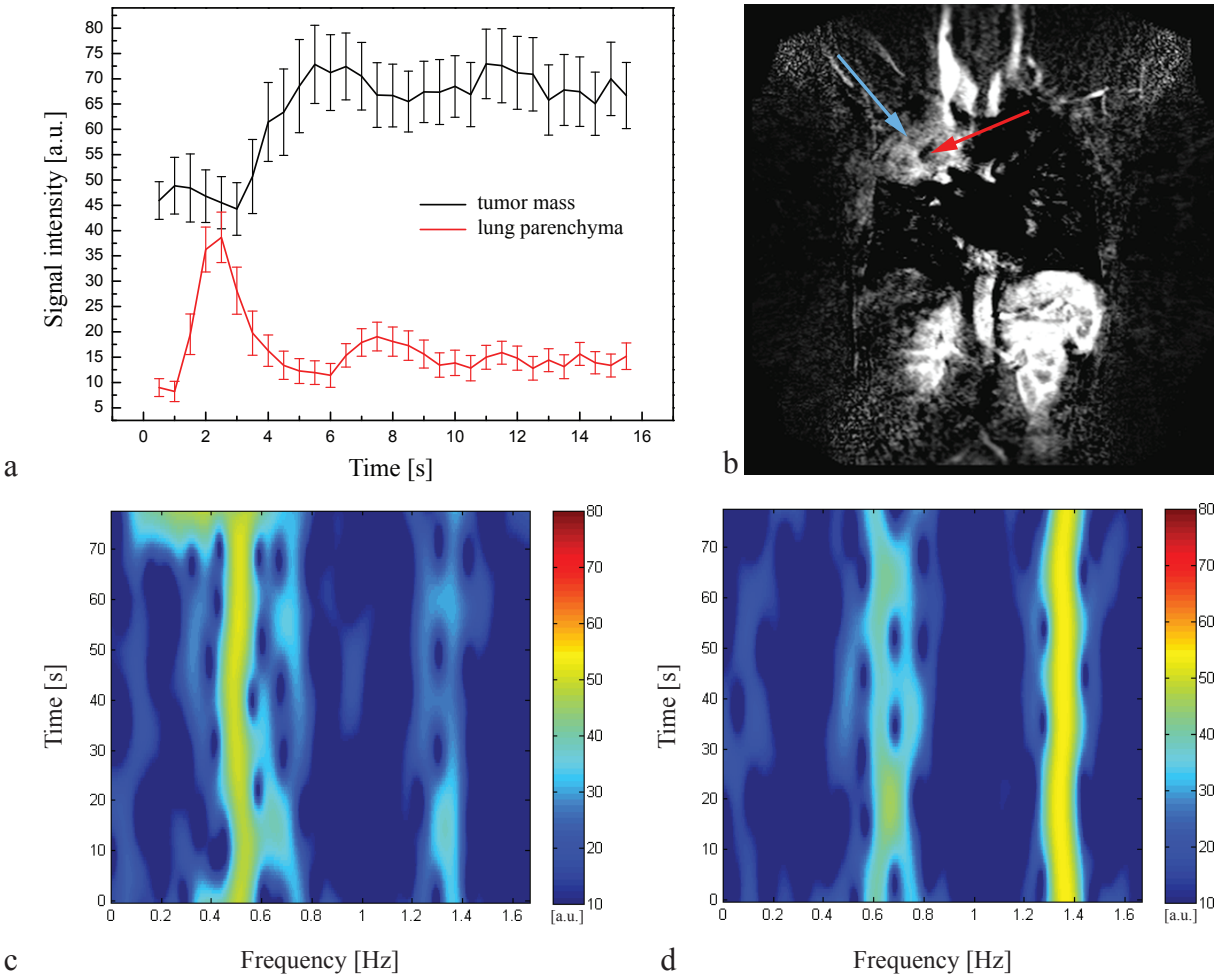

Figure 6.1: *Diagram (a) shows the time-course of a signal intensity from a ROI drawn in the tumor tissue in DCE-MRI time-resolved data set. Signal enhancement in the tumor tissue visible in DCE-MRI perfusion image (b) is shown by a blue arrow. Notice that the necrotic mass in the inner region of tumor stays unperfused (red arrow). Spectrograms (c) and (d) show amplitude of measured frequency components using FD-MRI technique in the tumor mass (right lung), and healthy lung parenchyma (left lung), respectively. The frequency components of the cardiac cycle are visible in the spectrogram measured in the tumor.*

Bibliography

Abragam, A.: *Principles of Nuclear Magnetism.* Oxford University Press, New York, 1961.

Addison, P. S., Walker, J. and G., Rodrigo C.: Time-Frequency Analysis of Biosignals. *IEEE Eng Med Biol Mag*, 28(5): 14–29, 2009.

Akay, M.: *Time Frequency and Wavelets in Biomedical Signal Processing.* John Wiley & Sons, 2001.

Albert, M. S., Cates, G. D., Driehuys, B., Happer, W., Saam, B., Springer, C. S. and Wishnia, A.: Biological magnetic resonance imaging using laser-polarized 129Xe. *Nature*, 370: 199–201, 1994.

Altes, T. A., Powers, P. L., Knight-Scott, J., Rakes, G., Platts-Mills, T. A., de Lange, E. E., Alford, B. A., Mugler, J. P. and Brookeman, J. R.: Hyperpolarized 3He MR lung ventilation imaging in asthmatics: preliminary findings. *J Magn Reson Imaging*, 13: 378–384, 2001.

Appelt, S., Baranga, A. B., Erickson, C. J., Romalis, M. V., Young, A. R. and Happer, W.: Theory of spin-exchange optical pumping of 3He and 129Xe. *Phys Rev A*, 58(2): 1412–1439, 1998.

Ardeshir Goshtasby, A.: *2-D and 3-D Image Registration for Medical, Remote Sensing, and Industrial Applications.* Wiley Press, 2005.

Bachert, P., Schad, L. R., Bock, M., Knopp, M. V., Ebert, M., Grossmann, T., Heil, W., Hofmann, D., Surkau, R. and Otten, E. W.: Nuclear magnetic resonance imaging of airways in humans with use of hyperpolarized 3He. *Magn Reson Med*, 36: 192–196, 1996.

Bankier, A. A., O'Donnell, C. R., Mai, V. M., Storey, P., De Maertelaer, V., Edelman, R. R. and Chen, Q.: Impact of lung volume on MR signal intensity changes of the lung parenchyma. *J Magn Reson Imaging*, 20: 961–966, 2004.

Bauman, G., Dinkel, J., Puderbach, M. and Schad, L. R.: Time-resolved lung perfusion- and ventilation-weighted MRI by Wavelet Analysis. *Proceedings of the 18th Annual Meeting of ISMRM, Stockholm, Sweden*, 2010a.

Bauman, G., Eichinger, M., Deimling, M., Niemann, A., Mall, M., Schad, L. R. and Puderbach, M.: Non-Contrast-Enhanced lung perfusion MRI in comparison to Contrast-Enhanced MRI perfusion in young cystic fibrosis patients. *Proceedings of the European Congress of Radiology, Vienna, Austria*, 2010b.

Bauman, G., Puderbach, M., Deimling, M., Jellus, V., Chefd'hotel, C., Dinkel, J., Hintze, C., Kauczor, H. U. and Schad, L. R.: Non-contrast-enhanced perfusion and ventilation assessment of the human lung by means of fourier decomposition in proton MRI. *Magn Reson Med*, 62: 656–664, 2009.

Becker, E. D.: *High Resolution NMR: Theory and Chemical Applications.* Elsevier Science, 1999.

Bernstein, M. A., King, K. F. and Zhou, X. J.: *Handbook of MRI Pulse Sequences.* Elsevier Academic Press, 2004.

Berthezene, Y., Vexler, V., Clement, O., Muehler, A., Moseley, M. E. and Brasch, R. C.: Contrast-enhanced MR imaging of the lung: assessments of ventilation and perfusion. *Radiology*, 183: 667–672, 1992.

Blaimer, M., Breuer, F., Mueller, M., Heidemann, R. M., Griswold, M. A. and Jakob, P. M.: SMASH, SENSE, PILS, GRAPPA: how to choose the optimal method. *Top Magn Reson Imaging*, 15: 223–236, 2004.

Bloch, F., Hansen, W. W. and Packard, Martin: Nuclear Induction. *Physical Review*, 69(3-4): 127, 1946.

Bolar, D. S., Levin, D. L., Hopkins, S. R., Frank, L. F., Liu, T. T., Wong, E. C. and Buxton, R. B.: Quantification of regional pulmonary blood flow using ASL-FAIRER. *Magn Reson Med*, 55: 1308–1317, 2006.

Bracewell, R. N.: *The Fourier Transform And Its Applications.* McGraw-Hill Companies, third Edition, 1999.

Brau, A. C. and Brittain, J. H.: Generalized self-navigated motion detection technique: Preliminary investigation in abdominal imaging. *Magn Reson Med*, 55: 263–270, 2006.

Brooks, R. A. and Di Chiro, G.: Magnetic resonance imaging of stationary blood: a review. *Med Phys*, 14: 903–913, 1987.

Buehrer, M., Curcic, J., Boesiger, P. and Kozerke, S.: Prospective self-gating for simultaneous compensation of cardiac and respiratory motion. *Magn Reson Med*, 60: 683–690, 2008.

Buxton, R. B., Frank, L. R., Wong, E. C., Siewert, B., Warach, S. and Edelman, R. R.: A general kinetic model for quantitative perfusion imaging with arterial spin labeling. *Magn Reson Med*, 40: 383–396, 1998.

Carr, H. Y. and Purcell, E. M.: Effect of Diffusion on Free Precession in Nuclear Magnetic Resonance Experiments. *Physical Review*, 94(3): 630–638, 1954.

Chefd'hotel, C., Hermosillo, G. and Faugeras, O.: A variational approach to multimodal image matching. *Proceedings of the IEEE Workshop on Variational and Level Set Methods in Computer Vision, ICCV Workshop, Vancouver, British Columbia, Canada*, 2001.

Chefd'hotel, C., Hermosillo, G. and Faugeras, O.: Flows of diffeomorphisms for multimodal image registration. *Proceedings of the IEEE International Symposium on Biomedical Imaging, Washington, DC, USA*, 2002.

Chen, Q., Jakob, P. M., Griswold, M. A., Levin, D. L., Hatabu, H. and Edelman, R. R.: Oxygen enhanced MR ventilation imaging of the lung. *MAGMA*, 7: 153–161, 1998.

Chen, Q., Main, V. M., Bankier, A. A., Napadow, V. J., Gilbert, R. J. and Edelman, R. R.: Ultrafast MR grid-tagging sequence for assessment of local mechanical properties of the lungs. *Magn Reson Med*, 45: 24–28, 2001.

Cooley, J. W. and Tukey, J. W.: An algorithm for the machine calculation of complex fourier series. *Mathematics of Computation*, 19: 297–301, 1965.

Damadian, R., Goldsmith, M. and Minkoff, L.: NMR in cancer: XVI. FONAR image of the live human body. *Physiol. Chem. Phys.*, 9: 97–100, 1977.

Daubechies, I.: Orthonormal bases of compactly supported wavelets. *Comm Pure Appl Math*, 41: 909–996, 1988.

Deimling, M.: True FISP imaging of lung parenchyma at 0.2 T. *Proceedings of the 8th Annual Meeting of ISMRM, Denver, Colorado, USA*, 2000: 2002, 2000.

Deimling, M., Jellus, V., Geiger, B. and Chefd'hotel, C.: Time resolved lung ventilation imaging by Fourier decomposition. *Proceedings of the 16th Annual Meeting of ISMRM, Toronto, Canada*, 2008: 2639, 2008.

Deshpande, V. S., Chung, Y. C., Zhang, Q., Shea, S. M. and Li, D.: Reduction of transient signal oscillations in true-FISP using a linear flip angle series magnetization preparation. *Magn Reson Med*, 49: 151–157, 2003.

Diederich, S. and Lenzen, H.: Radiation exposure associated with imaging of the chest: comparison of different radiographic and computed tomography techniques. *Cancer*, 89: 2457–2460, 2000.

Donnelly, L. F., MacFall, J. R., McAdams, H. P., Majure, J. M., Smith, J., Frush, D. P., Bogonad, P., Charles, H. C. and Ravin, C. E.: Cystic fibrosis: combined hyperpolarized 3He-enhanced and conventional proton MR imaging in the lung–preliminary observations. *Radiology*, 212: 885–889, 1999.

Donoho, D. L. and Johnstone, I. M.: Ideal denoising in an orthonormal basis chosen from a library of bases. *C R Acad Sco Paris A*, 319: 1317–1322, 1994.

Ebert, M., Grossmann, T., Heil, W., Otten, W. E., Surkau, R., Leduc, M., Bachert, P., Knopp, M. V., Schad, L. R. and Thelen, M.: Nuclear magnetic resonance imaging with hyperpolarised helium-3. *Lancet*, 347: 1297–1299, 1996.

Edelman, R. R., Hatabu, H., Tadamura, E., Li, W. and Prasad, P. V.: Noninvasive assessment

of regional ventilation in the human lung using oxygen-enhanced magnetic resonance imaging. *Nat. Med.*, 2: 1236–1239, 1996.

Eichinger, M., Puderbach, M., Fink, C., Gahr, J., Ley, S., Plathow, C., Tuengerthal, S., Zuna, I., Müller, F. M. and Kauczor, H. U.: Contrast-enhanced 3D MRI of lung perfusion in children with cystic fibrosis–initial results. *Eur Radiol*, 16: 2147–2152, 2006.

Failo, R., Wielopolski, P. A., Tiddens, H. A., Hop, W. C., Mucelli, R. P. and Lequin, M. H.: Lung morphology assessment using MRI: a robust ultra-short TR/TE 2D steady state free precession sequence used in cystic fibrosis patients. *Magn Reson Med*, 61: 299–306, 2009.

Fink, C., Bock, M., Puderbach, M., Schmaehl, A. and Delorme, S.: Partially parallel three-dimensional magnetic resonance imaging for the assessment of lung perfusion–initial results. *Invest Radiol*, 38: 482–488, 2003.

Fink, C., Puderbach, M., Bock, M., Lodemann, K. P., Zuna, I., Schmaehl, A., Delorme, S. and Kauczor, H. U.: Regional lung perfusion: assessment with partially parallel three-dimensional MR imaging. *Radiology*, 231: 175–184, 2004.

Finn, J. P., Nael, K., Deshpande, V., Ratib, O. and Laub, G.: Cardiac MR imaging: state of the technology. *Radiology*, 241: 338–354, 2006.

Fischer, A., Pracht, E. D., Arnold, J. F., Kotas, M., Flentje, M. and Jakob, P. M.: Assessment of pulmonary perfusion in a single shot using SEEPAGE. *J Magn Reson Imaging*, 27: 63–70, 2008.

Fitzgerald, T. N., Muto, A., Kudo, F. A., Pimiento, J. M., Constable, R. T. and Dardik, A.: Emerging vascular applications of magnetic resonance imaging: a picture is worth more than a thousand words. *Vascular*, 14: 366–371, 2006.

Ganong, W. F.: *Review of Medical Physiology.* McGraw-Hill Companies, 21. Edition, 2003.

Gast, K. K., Puderbach, M. U., Rodriguez, I., Eberle, B., Markstaller, K., Knitz, F., Schmiedeskamp, J., Weiler, N., Schreiber, W. G., Mayer, E., Thelen, M. and Kauczor, H. U.: Distribution of ventilation in lung transplant recipients: evaluation by dynamic 3He-MRI with lung motion correction. *Invest Radiol*, 38: 341–348, 2003.

Gee, J., Sundaram, T., Hasegawa, I., Uematsu, H. and Hatabu, H.: Characterization of regional pulmonary mechanics from serial magnetic resonance imaging data. *Acad Radiol*, 10: 1147–1152, 2003.

Gentile, T.R. and McKeown, R. D.: Spinpolarized nuclei with an arclamppumped neodymium-doped lanthanum magnesium hexaluminate laser. *Phys Rev A*, 47(1): 456–467, 1993.

Gibson, R. L., Burns, J. L. and Ramsey, B. W.: Pathophysiology and management of pulmonary infections in cystic fibrosis. *Am. J. Respir. Crit. Care Med.*, 168: 918–951, 2003.

Griswold, M. A., Jakob, P. M., Heidemann, R. M., Nittka, M., Jellus, V., Wang, J., Kiefer, B.

and Haase, A.: Generalized autocalibrating partially parallel acquisitions (GRAPPA). *Magn Reson Med*, 47: 1202–1210, 2002.

Griswold, M. A., Jakob, P. M., Nittka, M., Goldfarb, J. W. and Haase, A.: Partially parallel imaging with localized sensitivities (PILS). *Magn Reson Med*, 44: 602–609, 2000.

Grobner, T.: Gadolinium–a specific trigger for the development of nephrogenic fibrosing dermopathy and nephrogenic systemic fibrosis? *Nephrol. Dial. Transplant.*, 21: 1104–1108, 2006.

Haacke, E. M., Brown, R. W., Thompson, M. R. and Venkatesan, R.: *Magnetic Resonance Imaging: Physical Principles and Sequence Design.* J. Wiley & Sons, New York, 1999.

Haage, P., Karaagac, S., Spuentrup, E., Adam, G. and Guenther, R. W.: MR-Bildgebung der Lungerventilation mittels aerosolierter Gadolinium-Chelate. *Fortschr Roentgenstr*, 175: 187–193, 2003.

Haage, P., Karaagac, S., Spuentrup, E., Truong, H. T., Schmidt, T. and Guenther, R. W.: Feasibility of pulmonary ventilation visualization with aerosolized magnetic resonance contrast media. *Invest Radiol*, 40: 85–88, 2005.

Haase, A., Frahm, J., Matthaei, D., Hanicke, W. and Merboldt, K. D.: FLASH imaging. Rapid NMR imaging using low flip-angle pulses. *Journal of Magnetic Resonance (1969)*, 67(2): 258–266, 1986.

Hahn, E. L.: Spin Echoes. *Physical Review*, 80(4): 580, 1950.

Hargreaves, B. A., Vasanawala, S. S., Pauly, J. M. and Nishimura, D. G.: Characterization and reduction of the transient response in steady-state MR imaging. *Magn Reson Med*, 46: 149–158, 2001.

Harris, R. K.: *Encyclopedia of Nuclear Magnetic Resonance.* John Willey & Sons, Chichester, UK, 1996.

Hatabu, H., Alsop, D. C., Listerud, J., Bonnet, M. and Gefter, W. B.: T2* and proton density measurement of normal human lung parenchyma using submillisecond echo time gradient echo magnetic resonance imaging. *Eur J Radiol*, 29: 245–252, 1999a.

Hatabu, H., Gaa, J., Kim, D., Li, W., Prasad, P. V. and Edelman, R. R.: Pulmonary perfusion: qualitative assessment with dynamic contrast-enhanced MRI using ultra-short TE and inversion recovery turbo FLASH. *Magn Reson Med*, 36: 503–508, 1996.

Hatabu, H., Gaa, J., Tadamura, E., Edinburgh, K. J., Stock, K. W., Garpestad, E. and Edelman, R. R.: MR imaging of pulmonary parenchyma with a half-Fourier single-shot turbo spin-echo (HASTE) sequence. *Eur J Radiol*, 29: 152–159, 1999b.

Hatabu, H., Tadamura, E., Levin, D. L., Chen, Q., Li, W., Kim, D., Prasad, P. V. and Edelman, R. R.: Quantitative assessment of pulmonary perfusion with dynamic contrast-enhanced MRI.

Magn Reson Med, 42: 1033–1038, 1999c.

Heidemann, R. M., Griswold, M. A., Kiefer, B., Nittka, M., Wang, J., Jellus, V. and Jakob, P. M.: Resolution enhancement in lung 1H imaging using parallel imaging methods. *Magn Reson Med*, 49: 391–394, 2003.

Hennig, J., Nauerth, A. and H., Friedburg: RARE Imaging: A Fast Imaging Method for Clinical MR. *Magn Reson Med*, 3: 823–833, 1986.

Hermosillo, G.: *Variational Methods for Multimodal Image Matching.* Universite de Nice, 2002.

Hersman, F. W., Ruset, I. C., Ketel, S., Muradian, I., Covrig, S. D., Distelbrink, J., Porter, W., Watt, D., Ketel, J., Brackett, J., Hope, A. and Patz, S.: Large production system for hyperpolarized 129Xe for human lung imaging studies. *Acad Radiol*, 15: 683–692, 2008.

Hinshaw, W. S., Bottomley, P. A. and Holland, G. N.: Radiographic thin-section image of the human wrist by nuclear magnetic resonance. *Nature*, 270: 722–723, 1977.

Hintze, C., Stemmer, A., Bock, M., Kuder, T. A., Risse, F., Dinkel, J., Prüm, H., Puderbach, M., Fink, C., Biederer, J. and Kauczor, H. U.: A hybrid breath hold and continued respiration-triggered technique for time-resolved 3D MRI perfusion studies in lung cancer. *Rofo*, 182(1): 45–52, 2010.

Hopkins, S. R., Henderson, A. C., Levin, D. L., Yamada, K., Arai, T., Buxton, R. B. and Prisk, G. K.: Vertical gradients in regional lung density and perfusion in the supine human lung: the Slinky effect. *J. Appl. Physiol.*, 103: 240–248, 2007.

Huang, T. Y., Huang, I. J., Chen, C. Y., Scheffler, K., Chung, H. W. and Cheng, H. C.: Are TrueFISP images T2/T1-weighted? *Magn Reson Med*, 48: 684–688, 2002.

Jakob, P. M., Hillenbrand, C. M., Wang, T., Schultz, G., Hahn, D. and Haase, A.: Rapid quantitative lung (1)H T(1) mapping. *J Magn Reson Imaging*, 14: 795–799, 2001.

Jakob, P. M., Wang, T., Schultz, G., Hebestreit, H., Hebestreit, A. and Hahn, D.: Assessment of human pulmonary function using oxygen-enhanced T(1) imaging in patients with cystic fibrosis. *Magn Reson Med*, 51: 1009–1016, 2004.

Kauczor, H. U.: *MRI of the Lung.* Springer, Berlin, Heidelberg, 2009.

Kauczor, H. U., Hofmann, D., Kreitner, K. F., Nilgens, H., Surkau, R., Heil, W., Potthast, A., Knopp, M. V., Otten, E. W. and Thelen, M.: Normal and abnormal pulmonary ventilation: visualization at hyperpolarized He-3 MR imaging. *Radiology*, 201: 564–568, 1996.

Keener, J. and Sneyd, J.: *Interdisciplinary Applied Mathematics: Mathematical Physiology.* Springer, New York, Inc., 1998.

Korosec, F. R., Frayne, R., Grist, T. M. and Mistretta, C. A.: Time-resolved contrast-enhanced 3D MR angiography. *Magn Reson Med*, 36: 345–351, 1996.

Landwehr, P., Schulte, O. and Lackner, K.: Mr imaging of the chest: mediastinum and chest wall. *Eur Radiol*, 9: 1737–1744, 1999.

Latchaw, R. E., Yonas, H., Pentheny, S. L. and Gur, D.: Adverse reactions to xenon-enhanced CT cerebral blood flow determination. *Radiology*, 163: 251–254, 1987.

Lauterbur, P. C.: Image Formation by Induced Local Interactions: Examples Employing Nuclear Magnetic Resonance. *Nature*, 242(5394): 190–191, 1973.

Leupold, J.: *Neue Methoden zur frequenzselektiven Kernspintomographie mit TrueFISP - Sequenzen.* Dissertation, Kapitel 3, Freiburg, Germany, 2005.

Levin, D. L., Chen, Q., Zhang, M., Edelman, R. R. and Hatabu, H.: Evaluation of regional pulmonary perfusion using ultrafast magnetic resonance imaging. *Magn Reson Med*, 46: 166–171, 2001.

Levitt, M. H.: *Spin Dynamics: Basics of Nuclear Magnetic Resonance.* John Wiley & Sons, New York, USA, 2008.

Levitzky, E. D.: *Lange physiology series: Pulmonary Physiology.* The McGraw-Hill Companies, 7. Edition, 2007.

Ley, S., Puderbach, M., Risse, F., Ley-Zaporozhan, J., Eichinger, M., Takenaka, D., Kauczor, H. U. and Bock, M.: Impact of oxygen inhalation on the pulmonary circulation: assessment by magnetic resonance (MR)-perfusion and MR-flow measurements. *Invest Radiol*, 42: 283–290, 2007.

Lipson, D. A. and van Beek, J. R.: *Functional Lung Imaging (Lung Biology in Health and Disease.* Taylor & Francis Group, 2005.

Ljunggren, S.: A simple graphical representation of Fourier-based imaging methods. *Journal of Magnetic Resonance*, 54(2): 338–343, 1983.

Lohberger, F., Amann, A. and Schad, L. R.: Radial MRI of the human lung. *Proceedings of the 14th Annual Meeting of ISMRM, Seattle, Washington, USA*, 2006.

Long, F. R., Williams, R. S. and Castile, R. G.: Inspiratory and expiratory CT lung density in infants and young children. *Pediatr Radiol*, 35: 677–683, 2005.

Lujan, A. E., Larsen, E. W., Balter, J. M. and Ten Haken, R. K.: A method for incorporating organ motion due to breathing into 3d dose calculations. *Med Phys*, 26: 715–720, 1999.

Mai, V. M. and Berr, S. S.: MR perfusion imaging of pulmonary parenchyma using pulsed arterial spin labeling techniques: FAIRER and FAIR. *J Magn Reson Imaging*, 9: 483–487, 1999.

Mai, V. M., Tutton, S., Prasad, P. V., Chen, Q., Li, W., Chen, C., Liu, B., Polzin, J., Kurucay, S. and Edelman, R. R.: Computing oxygen-enhanced ventilation maps using correlation analysis.

Magn Reson Med, 49: 591–594, 2003.

Mallat, S. G.: A Theory for Multiresolution Signal Decomposition: A Wavelet Representation. *IEEE Transactions on Pattern Analysis and Machine Intelligence*, 11: 674–693, 1989.

Mansfield, P.: Multi-planar image formation using NMR spin echoes. *J Phys C*, 10: 55–58, 1977.

Marcus, J. T., Korporaal, J. G., Rietema, H., Boonstra, A. and Vonk Noordegraaf, A.: MRI estimation of dynamic regional lung ventilation, derived from pulmonary density changes during respiration. *Proceedings of the 15th Annual Meeting of ISMRM, Berlin, Germany*, 2007: 2777, 2007.

Martirosian, P., Boss, A., Fenchel, M., Deimling, M., Schäfer, J., Claussen, C. D. and Schick, F.: Quantitative lung perfusion mapping at 0.2 T using FAIR True-FISP MRI. *Magn Reson Med*, 55: 1065–1074, 2006.

Meiboom, S. and Gill, D.: Modified spin-echo method for measuring nuclear relaxation times. *Rev. Sci. Intr.*, 29: 688–91, 1958.

Mentore, K., Froh, D. K., de Lange, E. E., Brookeman, J. R., Paget-Brown, A. O. and Altes, T. A.: Hyperpolarized HHe 3 MRI of the lung in cystic fibrosis: assessment at baseline and after bronchodilator and airway clearance treatment. *Acad Radiol*, 12: 1423–1429, 2005.

Middleton, H., Black, R. D., Saam, B., Cates, G. D., Cofer, G. P., Guenther, R., Happer, W., Hedlund, L. W., Johnson, G. A. and Juvan, K.: MR imaging with hyperpolarized 3He gas. *Magn Reson Med*, 33: 271–275, 1995.

Molinari, F., Eichinger, M., Risse, F., Plathow, C., Puderbach, M., Ley, S., Herth, F., Bonomo, L., Kauczor, H. U. and Fink, C.: Navigator-triggered oxygen-enhanced MRI with simultaneous cardiac and respiratory synchronization for the assessment of interstitial lung disease. *J Magn Reson Imaging*, 26: 1523–1529, 2007.

Montgomery, A. B., Paajanen, H., Brasch, R. C. and Murray, J. F.: Aerosolized gadolinium-DTPA enhances the magnetic resonance signal of extravascular lung water. *Invest Radiol*, 22: 377–381, 1987.

Mueller, C. J., Loeffler, R., Deimling, M., Peller, M. and Reiser, M.: MR lung imaging at 0.2 T with T1-weighted true FISP: native and oxygen-enhanced. *J Magn Reson Imaging*, 14: 164–168, 2001.

Mugler, J. P., Brookemann, J. R., Maier, T., De Lange, E. E. and Bogorad, P. L.: Regional measurement of the 3He diffusion coefficient in the human lung. *Proceedings of the 6th Annual Meeting of ISMRM, Sydney, Australia*, 1998.

Mugler, J. P., Driehuys, B., Brookeman, J. R., Cates, G. D., Berr, S. S., Bryant, R. G., Daniel, T. M., de Lange, E. E., Downs, J. H., Erickson, C. J., Happer, W., Hinton, D. P., Kassel, N. F., Maier, T., Phillips, C. D., Saam, B. T., Sauer, K. L. and Wagshul, M. E.: MR imaging

and spectroscopy using hyperpolarized 129Xe gas: preliminary human results. *Magn Reson Med*, 37: 809–815, 1997.

Naish, J. H., Parker, G. J., Beatty, P. C., Jackson, A., Young, S. S., Waterton, J. C. and Taylor, C. J.: Improved quantitative dynamic regional oxygen-enhanced pulmonary imaging using image registration. *Magn Reson Med*, 54: 464–469, 2005.

Napadow, V. J., Mai, V., Bankier, A., Gilbert, R. J., Edelman, R. and Chen, Q.: Determination of regional pulmonary parenchymal strain during normal respiration using spin inversion tagged magnetization MRI. *J Magn Reson Imaging*, 13: 467–474, 2001.

Netter, F. H., Dalley, A. H. and Myers, J.M.: *Atlas der Anatomie des Menschen.* Thieme, Stuttgart, New York, 2000.

Nikiel, A., Palasz, T., Suchanek, M., Abboud, A., Sinatra, A., Olejniczak, Z., Dohnalik, T., Tastevin, G. and Nacher, P-J.: Metastability exchange optical pumping of 3He at high pressure and high magnetic field for medical application. *The European Physical Journal - Special Topics*, 144: 255–263, 2007.

Nikolaou, K., Schoenberg, S. O., Brix, G., Goldman, J. P., Attenberger, U., Kuehn, B., Dietrich, O. and Reiser, M. F.: Quantification of pulmonary blood flow and volume in healthy volunteers by dynamic contrast-enhanced magnetic resonance imaging using a parallel imaging technique. *Invest Radiol*, 39: 537–545, 2004.

Ohno, Y., Chen, Q. and Hatabu, H.: Oxygen-enhanced magnetic resonance ventilation imaging of lung. *Eur J Radiol*, 37: 164–171, 2001.

Oppelt, A., Graumann, R., Barfuss, H., Fischer, H., Hartl, W. and Schajor, W.: FISP: eine neue schnelle Pulssequenz fuer die Kernspintomographie. *Electromedica*, 54: 15–18, 1986.

Parzen, E.: On the estimation of probability density function. *Ann Math Statist*, 33: 1065–1076, 1962.

Patz, S., Hersman, F. W., Muradian, I., Hrovat, M. I., Ruset, I. C., Ketel, S., Jacobson, F., Topulos, G. P., Hatabu, H. and Butler, J. P.: Hyperpolarized (129)Xe MRI: a viable functional lung imaging modality? *Eur J Radiol*, 64: 335–344, 2007.

Petersson, J., Sanchez-Crespo, A., Larsson, S. A. and Mure, M.: Physiological imaging of the lung: single-photon-emission computed tomography (SPECT). *J. Appl. Physiol.*, 102: 468–476, 2007.

Pracht, E. D., Arnold, J. F., Wang, T. and Jakob, P. M.: Oxygen-enhanced proton imaging of the human lung using T2. *Magn Reson Med*, 53: 1193–1196, 2005.

Pracht, E. D., Fischer, A., Arnold, J. F., Kotas, M., Flentje, M. and Jakob, P. M.: Single-shot quantitative perfusion imaging of the human lung. *Magn Reson Med*, 56: 1347–1351, 2006.

Pruessmann, K. P., Weiger, M., Scheidegger, M. B. and Boesiger, P.: SENSE: sensitivity encoding

for fast MRI. *Magn Reson Med*, 42: 952–962, 1999.

Puderbach, M., Eichinger, M., Gahr, J., Ley, S., Tuengerthal, S., Schmähl, A., Fink, C., Plathow, C., Wiebel, M., Müller, F. M. and Kauczor, H. U.: Proton MRI appearance of cystic fibrosis: comparison to CT. *Eur Radiol*, 17: 716–724, 2007a.

Puderbach, M., Hintze, C., Ley, S., Eichinger, M., Kauczor, H. U. and Biederer, J.: MR imaging of the chest: a practical approach at 1.5T. *Eur J Radiol*, 64: 345–355, 2007b.

Purcell, E. M., Torrey, H. C. and Pound, R. V.: Resonance Absorption by Nuclear Magnetic Moments in a Solid. *Physical Review*, 69(1-2): 37, 1946.

Richard, J. C., Janier, M., Lavenne, F., Tourvieille, C., Le Bars, D., Costes, N., Gimenez, G. and Guerin, C.: Quantitative assessment of regional alveolar ventilation and gas volume using 13N-N2 washout and PET. *J. Nucl. Med.*, 46: 1375–1383, 2005.

Roach, P. J., Bailey, D. L. and Harris, B. E.: Enhancing lung scintigraphy with single-photon emission computed tomography. *Semin Nucl Med*, 38: 441–449, 2008.

Roberts, D. A., Gefter, W. B., Hirsch, J. A., Rizi, R. R., Dougherty, L., Lenkinski, R. E., Leigh, J. S. and Schnall, M. D.: Pulmonary perfusion: respiratory-triggered three-dimensional MR imaging with arterial spin tagging–preliminary results in healthy volunteers. *Radiology*, 212: 890–895, 1999.

Roche, A., Malandain, G., Pennec, X. and Ayache, N.: Multimodal image registration by maximization of the correlation ratio. *Technical report 3378, INRIA*, 1998.

Ruppert, K., Mata, J. F., Brookeman, J. R., Hagspiel, K. D. and Mugler, J. P.: Exploring lung function with hyperpolarized (129)Xe nuclear magnetic resonance. *Magn Reson Med*, 51: 676–687, 2004.

Rupprecht, T., Kuth, R., Deimling, M. and Wagner, M.: Functional lung imaging by MRI - is there a simple solution for a complex problem? *Proceedings of the 11th Annual Meeting of ISMRM, Toronto, Canada*, 2003: 1371, 2003.

Ruset, I. C., Ketel, S. and Hersman, F. W.: Optical pumping system design for large production of hyperpolarized. *Phys. Rev. Lett.*, 96: 053002, 2006.

Ruth, U., Hof, T., Schmidt, J., Fick, D. and Jänsch, H. J.: Production of nitrogenfree, hyperpolarized 129Xe gas. *Appl Phys B*, 68: 93–97, 1999.

Scheffler, K. and Hennig, J.: Is TrueFISP a gradient-echo or a spin-echo sequence? *Magn Reson Med*, 49: 395–397, 2003.

Semelka, R. C., Kelekis, N. L., Thomasson, D., Brown, M. A. and Laub, G. A.: HASTE MR imaging: description of technique and preliminary results in the abdomen. *J Magn Reson Imaging*, 6: 698–699, 1996.

Senden, T. J., Moock, K. H., Gerald, J. F., Burch, W. M., Browitt, R. J., Ling, C. D. and Heath, G. A.: The physical and chemical nature of technegas. *J. Nucl. Med.*, 38: 1327–1333, 1997.

Shiotani, S., Sugimura, K., Sugihara, M., Kawamitsu, H., Yamauchi, M., Yoshida, M., Kushima, T., Kinoshita, T., Endoh, H., Nakayama, H., Kajitani, M. and Wada, M.: Diagnosis of chest wall invasion by lung cancer: useful criteria for exclusion of the possibility of chest wall invasion with MR imaging. *Radiat Med*, 18: 283–290, 2000.

Slichter, C. P.: *Principles of Magnetic Resonance.* Springer Verlag, Berlin, 1989.

Sodickson, D. K. and Manning, W. J.: Simultaneous acquisition of spatial harmonics (SMASH): fast imaging with radiofrequency coil arrays. *Magn Reson Med*, 38: 591–603, 1997.

Song, G. and Zhao, R.: Three novel models of threshold estimator for wavelet coefficients, in: Tang Y. et al. Lecture Notes in Computer Science. *Proceedings of WAA 2001, Hong Kong, China*, 145–150, 2001.

Stadler, A., Jakob, P. M., Griswold, M., Barth, M. and Bankier, A. A.: T1 mapping of the entire lung parenchyma: Influence of the respiratory phase in healthy individuals. *J Magn Reson Imaging*, 21: 759–764, 2005.

Stanisz, G. J., Odrobina, E. E., Pun, J., Escaravage, M., Graham, S. J., Bronskill, M. J. and Henkelman, R. M.: T_1, T_2 Relaxation and Magnetization Transfer in Tissue at 3T. *Magn Reson Med*, 54: 507–512, 2005.

Stavngaard, T., Søgaard, L. V., Mortensen, J., Hanson, L. G., Schmiedeskamp, J., Berthelsen, A. K. and Dirksen, A.: Hyperpolarized 3He MRI and 81mKr SPECT in chronic obstructive pulmonary disease. *Eur. J. Nucl. Med. Mol. Imaging*, 32: 448–457, 2005.

Stock, K. W., Chen, Q., Hatabu, H. and Edelman, R. R.: Magnetic resonance T2* measurements of the normal human lung in vivo with ultra-short echo times. *Magn Reson Imaging*, 17: 997–1000, 1999.

Sundaram, T. A. and Gee, J. C.: Towards a model of lung biomechanics: pulmonary kinematics via registration of serial lung images. *Med Image Anal*, 9: 524–537, 2005.

Swift, A. J., Wild, J. M., Fichele, S., Woodhouse, N., Fleming, S., Waterhouse, J., Lawson, R. A., Paley, M. N. and Van Beek, E. J.: Emphysematous changes and normal variation in smokers and COPD patients using diffusion 3He MRI. *Eur J Radiol*, 54: 352–358, 2005.

Thews, G.: *Physiologie der Menschen.* Springer, Berlin, Heidelberg, New York, 1997.

Topf, H. G., Wagner, M., Kreisler, P., Deimling, M., Geiger, B., Chefd'hotel, C. and Rupprecht, T.: Measuring quantitativeregional lung ventilation by alveolar ventilation imaging (AVI) - phantom data and results of a feasibility study in 50 patients. *Proceedings of the 12th Annual Meeting of ISMRM, Kyoto, Japan*, 2004: 671, 2004.

Topf, H. G., Zapke, M., Kreisler, P., Deimling, M., Geiger, B., Chefd'hotel, C. and Rupprecht,

T.: 1.5 Tesla can do too - measuring quantitative regional lung ventilation by AVI (alveolar ventilation imaging) - phantom data and results of a feasibility study in 10 patients. *Proceedings of the 13th Annual Meeting of ISMRM, Miami, Florida, USA*, 2005: 46, 2005.

Twieg, D.: The k-trajectory formulation of the NMR imaging process with applications in analysis and synthesis of imaging methods. *Medical Physics*, 10(5): 610–621, 1983.

Unser, M. and Akram, A.: A Review of Wavelets in Biomedical Applications. *Proceedings of the IEEE*, 84: 626–638, 1996.

van Beek, E. J. and Hoffman, E. A.: Functional imaging: CT and MRI. *Clin. Chest Med.*, 29: 195–216, 2008.

Van Dyk, J., Keane, T. J. and Rider, W. D.: Lung density as measured by computerized tomography: implications for radiotherapy. *Int. J. Radiat. Oncol. Biol. Phys.*, 8: 1363–1372, 1982.

Vassiliadis, K. and Sergiadis, G.: The duration of transient in SSFP experiments. *Proceedings of the 1st Annual Meeting of ISMRM, New York, New York, USA*, 1208, 1993.

Vidal Melo, M. F., Layfield, D., Harris, R. S., O'Neill, K., Musch, G., Richter, T., Winkler, T., Fischman, A. J. and Venegas, J. G.: Quantification of regional ventilation-perfusion ratios with PET. *J. Nucl. Med.*, 44: 1982–1991, 2003.

Vlaardingerbroek, M. T. and den Boer, J. A.: *Magnetic Resonance Imaging. Theory and Practice.* Springer Verlag, Berlin, 2003.

Vogt, F. M., Eggbrecht, H. and Laub, G.: High spatial and temporal resolution MRA (TWIST) in acute aortic dissection. *Proceedings of the 15th Annual Meeting of ISMRM, Berlin, Germany*, 2007.

Von Euler, U. S. and Liljestrand, G.: Effect of Diffusion on Free Precession in Nuclear Magnetic Resonance Experiments. *Acta Physiol. Scand.*, 12: 301–320, 1946.

von Schulthess, G. K., Fisher, M. R. and Higgins, C. B.: Pathologic blood flow in pulmonary vascular disease as shown by gated magnetic resonance imaging. *Ann. Intern. Med.*, 103: 317–323, 1985.

Voorhees, A., An, J., Berger, K. I., Goldring, R. M. and Chen, Q.: Magnetic resonance imaging-based spirometry for regional assessment of pulmonary function. *Magn Reson Med*, 54: 1146–1154, 2005.

Wang, C., Altes, T. A., Mugler, J. P., Miller, G. W., Ruppert, K., Mata, J. F., Cates, G. D., Borish, L. and de Lange, E. E.: Assessment of the lung microstructure in patients with asthma using hyperpolarized 3He diffusion MRI at two time scales: comparison with healthy subjects and patients with COPD. *J Magn Reson Imaging*, 28: 80–88, 2008.

Weick, S., Oechsner, M., Blaimer, M., Breuer, F., Koestler, H., Dietbert, H., Beer, M. and

Jakob, P. M.: Self-gated 3D FLASH imaging of the human lung under free breathing using DC signals. *Proceedings of the 17th Annual Meeting of ISMRM, Honolulu, Hawaii, USA*, 2009.

Weiss, L. G.: Wavelet transforms for nonstationary signal processing. *Proc of SPIE annual meeting, Denver, USA*, 3813: 540, 1999.

Wells III, W., Viola, P., Atsumi, H., Nakajima, S. and Kikinis, R.: Multi-modal volume registration by maximization of mutual information. *Medical Image Analysis*, 1: 35–51, 1996.

White, P. G., Hayward, M. W. and Cooper, T.: Ventilation agents–what agents are currently used? *Nucl Med Commun*, 12: 349–352, 1991.

Wiedemair, W., Kroll, A., Kindl, P. and Schad, L. R.: Improvement of perfusion imaging of the human lung using retrospective gating. *Proceedings of the 15th Annual Meeting of ISMRM, Berlin, Germany*, 2007.

Wild, J. M., Paley, M. N., Kasuboski, L., Swift, A., Fichele, S., Woodhouse, N., Griffiths, P. D. and van Beek, E. J.: Dynamic radial projection MRI of inhaled hyperpolarized 3He gas. *Magn Reson Med*, 49: 991–997, 2003.

Wild, J. M., Schmiedeskamp, J., Paley, M. N., Filbir, F., Fichele, S., Kasuboski, L., Knitz, F., Woodhouse, N., Swift, A., Heil, W., Mill, G. H., Wolf, M., Griffiths, P. D., Otten, E. and van Beek, E. J.: MR imaging of the lungs with hyperpolarized helium-3 gas transported by air. *Phys Med Biol*, 47: N185–190, 2002.

Wild, J. M., Teh, K., Woodhouse, N., Paley, M. N., Fichele, S., de Zanche, N. and Kasuboski, L.: Steady-state free precession with hyperpolarized 3He: experiments and theory. *J. Magn. Reson.*, 183: 13–24, 2006.

Wild, J. M., Woodhouse, N. and Teh, K.: Single-scan acquisition of registered hyperpolarized (3)He ventilation and ADC images using a hybrid 2D gradient-echo sequence. *Magn Reson Med*, 57: 1185–1189, 2007.

Zapke, M., Topf, H. G., Zenker, M., Kuth, R., Deimling, M., Kreisler, P., Rauh, M., Chefd'hotel, C., Geiger, B. and Rupprecht, T.: Magnetic resonance lung function–a breakthrough for lung imaging and functional assessment? A phantom study and clinical trial. *Respir. Res.*, 7: 106, 2006.

Zhang, G., Dilling, T. J., Stevens, C. W. and Forster, K. M.: Functional lung imaging in thoracic cancer radiotherapy. *Cancer Control*, 15: 112–119, 2008.

List of Figures

List of Tables

List of Abbreviations

α	Flip angle
ADC	Apparent Diffusion Coefficient
ASL	Arterial Spin Labeling
bSSFP	Balanced Steady-State Free-Precession
BW	Bandwidth
CF	Cystic fibrosis
COPD	Chronic obstructive pulmonary disease
CT	Computed Tomography
CWT	Continuous Wavelet Transform
DCE-MRI	Dynamic Contrast Enhanced
DWT	Discrete Wavelet Transform
ECG	Electrocardiogram
FID	Free Induction Decay
FD	Fourier decomposition
FD-MRI	Fourier decomposition Magnetic Resonance Imaging
FFT	Fast Fourier Transform
FLASH	Fast Low Angle Shot
FOV	Field of View
GRAPPA	Generalized Autocalibrating Partially Parallel Acquisition
HASTE	Half-fourier Acquisition Single-shot Turbo Spin-Echo
MR	Magnetic Resonance
MRI	Magnetic Resonance Imaging
NMR	Nuclear Magnetic Resonance
NSF	Nephrogenic systemic fibrosis
PET	Positron Emission Tomography
pMRI	Parallel Magnetic Resonance Imaging
PSNR	Peak Signal-to-Noise Ratio
ROI	Region of Interest
RF	Radio Frequency
SAR	Specific Absorption Rate
SNR	Signal-to-Noise Ratio
SPECT	Single Photon Emission Computed Tomography
ST	Slice Thickness
STFT	Short-time Fourier transform
TA	Acquisition time

TE	Echo time
TR	Repetition time
TW	Time interval between image acquisitions
TWIST	Time-resolved Imaging with Stochastic Trajectories
WA	Wavelet analysis
WA-MRI	Wavelet analysis Magnetic Resonance Imaging
VIBE	Volumetric Interpolated Breath-hold Examination

Acknowledgements

The preparation of this document would not have been possible without the support and endless efforts of a large number of individuals and institutions. I would like to express my gratitude:

- first and foremost to my supervisor Prof. Lothar Schad for allowing me to join his team and work on this interesting topic, but especially for his valuable suggestions and guidance.
- Prof. Wolfgang Schlegel for the supervision and representation of my Ph.D. thesis at the Faculty.
- Michael Puderbach for his support, involvement in the project and assistance provided in numerous ways.
- to the members of my research group Armin Nagel, Sebastian Schmitter and Frederik Laun for their extremely important support for me as a new student. Furthermore, special thanks goes to my roommates Maja Sohlin, Thomas Gaaß, Moritz Zaiß, Moritz Berger, Andreas Lemke and Christian Matthies for their good humor and time spent in our office sharing helpful ideas through the last three years.
- Julien Dinkel, Christian Hintze and Monika Eichinger for their radiological expertise, generous practical support and hours of constructive discussions.
- Michael Deimling for his ideas.
- Katarzyna Cieślar, Christian Hintze, Thomas Gaaß, Michael Puderbach and Benjamin Schmitt who helped me with proof-reading.
- Prof. Wolfhard Semmler for admitting me to his department.
- Alema Bahtovic and Sabine Fritz who helped me in facing administrative problems.
- to all the other colleagues at the DKFZ for the professional and stimulating working atmosphere.
- to the medical technical assistants for their help and support with volunteer and patient measurements.
- Polarized Helium Imaging Lung Imaging Network "PHeLINET" and Marie Curie Research Training Networks for financing my dissertation.

Finally, I cannot end without thanking my family for all their endless love and support. Dziękuję wam bardzo. Furthermore, I want to thank Diane for the support, patience and understanding.